Durham E-Theses

A seismological study of the mantle beneath Iceland

Pritchard, Matthew James

A Seismological Study of the Mantle beneath Iceland

by

Matthew James Pritchard

A thesis submitted in partial fulfilment of the requirements for the degree of

Doctor of Philosophy.

Department of Geological Sciences

University of Durham

January 2000

Declaration

I declare that this thesis, which I submit for the degree of Doctor of Philosophy at the University of Durham, is my own work and not substantially the same as any which has previously been submitted at this or any other University.

Matthew James Pritchard.

Acknowledgements

Abstract

Iceland has long been thought to be underlain by a thermal upwelling, or plume, rising from deep within the mantle. This study tests this hypothesis, by

a) seeking evidence for a plume in the lower mantle in azimuth anomalies at the NORSAR array and

b) mapping the three-dimensional structure of the mantle beneath Iceland using teleseismic tomography and data from an Iceland-wide broadband seismometer network.

A temporary network of 30 digital broadband, three-component seismographs was deployed 1996-1998 to complement the existing, permanent seismic network on Iceland. This created a dense, well-distributed network. 3159 P-wave and 1338 S-wave arrival times were measured and inverted for velocity structure using the ACH method of teleseismic tomography.

The preferred models are well-resolved down to ~400 km, and reveal a low-velocity body with anomaly up to -2.9% in v_P and -4.9% in v_S beneath central Iceland. This persists throughout the entire model depth range. The amplitudes of the anomalies imply an excess temperature of 200-300 K relative to the surrounding mantle.

The morphology of the anomaly changes from cylindrical to tabular at 250-300 km depth, a feature that resolution tests suggest is real. This is consistent with the predictions of some convection models and suggests that the plume is restricted to the upper mantle.

Anomalies in v_P and v_S provide evidence for lateral flow of material beneath the Reykjanes Ridge to the southeast in the depth range 50-200 km. Similar anomalies are present beneath the Kolbeinsey Ridge to the north only beneath 160 km. This shows that flow outwards beneath the Kolbeinsey Ridge is blocked by the Tjörnes Fracture Zone above 160 km.

Azimuthal anomalies detected on the NORSAR array for rays travelling beneath Iceland at 1,500 km depth are consistent with a plume beneath Iceland at this lower-mantle depth with a Gaussian radius of 125 km and a strength of 1.5%. The observations do not serve as proof for such an anomaly because the solution is not unique.

v_P/v_S ratios are 1% high throughout most of the plume, and up to 3.2% high at depths of 100-300 km beneath central and east-central Iceland. This suggests that up to a few percent of melt pervades the entire plume.

TABLE OF CONTENTS

TABLE OF FIGURES

Chapter 1

Hotspots and Mantle Plumes

1. HOTSPOTS AND PLUMES

1.1 INTRODUCTION: HOTSPOTS AND PLUMES

1.1.1   The plume hypothesis

The bathymetry of the world's oceans is shown in Figure 1.1, which reveals several areas of elevated sea floor, such as seamounts and plateaux. These are not immediately explained in terms of the simple idea of rigid plates moving slowly over the Earth's surface.
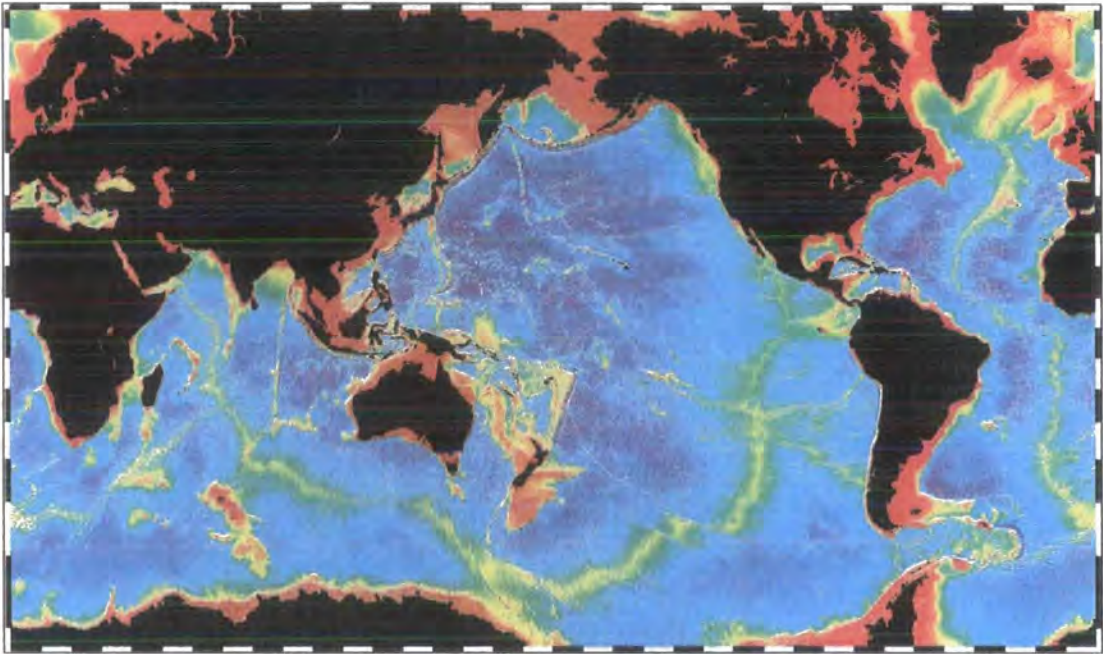
Figure 1.1 Global seafloor topography. Image from NOAA/Walter H. Smith/David T. Sandwell. Deep ocean floor is blue; mid-ocean ridges show as green and yellow; plateaux and continental shelves show as pink.

In addition, the excessive volcanism in the middle of some plates, such as at Hawaii and Yellowstone and at the mid-ocean ridge at Iceland, requires an explanation that involves some additional sub-lithospheric heat source. These areas have been termed "hotspots" (Wilson, 1963; Wilson, 1965; Morgan, 1971; Morgan, 1981). Up-welling convection currents in the mantle, or plumes, are thought to be the most likely cause. It was also proposed that plumes were the major driving force in plate motions (Morgan, 1971).

Alternative hypotheses involving stress and giant propagating cracks in the lithosphere have been discussed (Sleep, 1984), but the most widely favoured model involves relatively stationary, narrow plumes of hot material rising from the mantle

(Morgan, 1971; Morgan, 1972). Although their existence has been widely accepted with little supporting observational evidence, their depth of origin, physical properties and dimensions have remained the subject of considerable debate over the past three decades. It is only recently that significant advances have been made in providing observational evidence to support or reject the hypothesis.

1.1.2 Hotspot volcanism

The dating of lavas taken from islands in oceanic swells and seamount-chains reveals not only that these features are considerably younger than the oceanic lithosphere on which they reside, but that the ages of islands in such chains increase progressively, with distance from the present-day, or most recent, centre of volcanic activity. This is explained as resulting from the motion of a rigid plate over a heat source or "hotspot". Convective up-welling dynamically uplifts the overlying oceanic lithosphere, and produces melt which penetrates through the crust. A given site continues to be volcanically active until the motion of the plate has carried it away from the heat source, when it becomes extinct, cools and subsides. A new island then begins to form above the heat source. A chain of islands, atolls and seamounts remains as evidence of the passage of the plate over the hotspot. Many such hotspot tracks, consisting of linear chains of progressively older volcanic islands, have been identified worldwide, and their chronological and geometrical relationships have been used to determine the relative and absolute motions of the plates (e.g., Gripp & Gordon, 1990).

Hotspots are not confined to the centres of plates and their general proximity to constructive plate boundaries and especially mid-ocean ridges has been recognised (Morgan, 1971). Some examples of such oceanic hotspots are Tristan, Easter Island, Azores and Réunion. If the hotspot coincides with a spreading ridge, excessive igneous activity results in the formation of an oceanic plateau, such as that surrounding Iceland.

The interaction of hotspots with continental crust and rift zones is more complex, since continental crust usually has a more complex thermal, compositional and tectonic history than oceanic crust. Examples are the East African Plateau (Birt *et al.*, 1997), and the Yellowstone hotspot in Wyoming, USA, which is the cause of the Snake River Plain flood basalts.

1.1.3   Surface anomalies associated with hotspots

Hotspots are characterised by a several surface anomalies. These can extend up to 1000-2000 km from the centre of the hotspot, but are normally most pronounced directly over the presumed centre of the ascending plume. The large extent of the affected area has been attributed to a mushroom-shaped head of a thermal plume rising in the mantle which is deflected laterally. This raises the temperature of a vast area as it spreads out at the base of the lithosphere (White & McKenzie, 1989). Direct observational evidence for such "mushroom-heads" is lacking and in some cases, the distant effects attributable to plumes are quite localised. This implies active channelling of plume material along the base of plates, especially towards regions undergoing lower crustal extension (Kent, 1995).

Increased heat flow: Measurements at oceanic hotspots have revealed considerable increases in heat flow relative to surrounding lithosphere of equivalent age, for example 25% at the centre of the Cape Verde swell (Courtney & White, 1986). Hotspot areas are often characterised by hydrothermal activity, such as the geysers and hot springs that are found on Iceland and at Yellowstone.

Elevated bathymetry & topography: Hotspots are often characterised by broad uplift of the seafloor of up to 1000-2000 metres (White & McKenzie, 1989). Depending on the local tectonic regime and the thickness of the lithosphere, shallowing of the sea can sometimes be augmented by thickened crustal production at a rifted margin (e.g. Iceland), or a thick volcanic pile erupted directly over the centre of the hotspot (e.g. Hawaii, Figure 1.2). In the case of Hawaii, the volcanic pile acts as a load on the long-wavelength regional uplift, causing shorter-wavelength down-warping of the lithosphere.
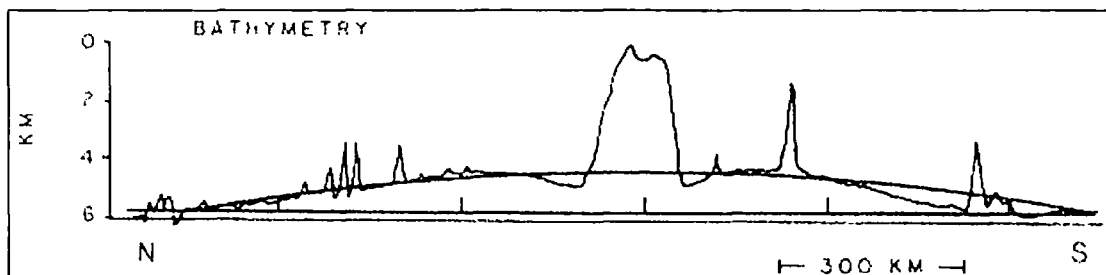
Figure 1.2 Bathymetry of the Hawaiian swell near Oahu (Watts, 1976; Crough, 1983; Sleep, 1992). The parabola has a halfwidth of 750 km and a height of 1.4 km, and a cross-sectional area of 1400 km^2.

Geoid & gravity anomalies: Small, positive anomalies in free-air gravity and geoid height occur over hotspots, because deflection of the surface of the seabed, and the presence of erupted lavas or thickened crust are a mass excess. However, the Bouguer anomaly is negative since the effect of the shallow mass excess is removed by reducing measurements to the same datum. A negative Bouguer anomaly indicates a mass deficit, which is due to hot, less dense material rising in the mantle below.

Geochemical anomalies: The flood basalts associated with hotspots are expected to contain a substantial proportion of upper and perhaps lower mantle material, and thus to be associated with a suite of trace element and isotopic geochemical anomalies. A summary is given by Saunders *et al.* (1992). The picture is not simple, however, especially as plumes may erupt through diverse types of lithosphere, including continental and oceanic plateau lithospheres and along spreading plate boundaries. Contamination from the lithosphere may thus occur and obscure geochemical patterns. Some flood basalts are even reported to show no geochemical plume signature (e.g., Karoo tholeiites), which may also indicate the difficulty of recognising such components.

Geochemical signatures suggested to be diagnostic of plume or asthenospheric components include low $^{87}Sr/^{86}Sr$, high ε-Nd and mantle-normalised Th/Nb, Rb/NB and Ba/Nb ratios less than one. Examples of basalt provinces that have such characteristics are the Deccan lavas, Madagascar and eastern Greenland. However, other element ratios such as K/Nb are highly variable between plumes and flood basalts, and difficult to explain. The K/Nb ratios that characterise basalts from Greenland, Iceland, Réunion and Madagascar range from 333 to as low as 50. The very low K content is difficult to explain with plume models. The much greater range of isotopic and trace element compositions in continental flood basalts compared with oceanic plateaux may be explained by strong contamination when the plume passes through the continental lithosphere, but nonetheless hinders the search for a reliable geochemical plume diagnostic.

The two geochemical features that are probably least ambiguous are (R.N. Thompson & D.G. Pearson, *pers. comms.*):

1. Helium isotopes. Helium 3 is enriched in magmas from plumes that are thought to have been generated from the lower mantle e.g., the Hawaiian plume.

2. In oceanic settings, radiogenic $^{187}Os/^{188}Os$ appears to be associated with plume basalts. This does not hold for continental plume basalts, however. Initial work on $^{186}Os/^{188}Os$ may be indicative of the involvement of the outer core in some plumes (e.g. Hawaii, Brandon *et al.*, 1998), but more work is needed to substantiate this.

1.1.4 Existence and origin of plumes

Hotspots are thought to be the surface expression of convective plumes rising from within the mantle (Morgan, 1971; Morgan, 1972). The question of whether these plumes originate in the lower mantle, as he proposed, are purely upper-mantle phenomena, or have some other explanation, remains yet to be resolved satisfactorily.

Relevant facts are:

• Hotspots move only very slowly compared with each other. Plate motions are often stated relative to a fixed "hotspot reference frame".

• Hotspots are long-lived and typically last for periods of the order of 100 Ma.

• Hotspots are often located at or near constructive plate boundaries (Morgan, 1971; Anderson *et al.*, 1992), but sometimes occur at other locations within plates. Their distribution is generally anticorrelated with destructive plate boundaries.

In order for hotspots to remain both active and relatively stationary with respect to each other for prolonged periods of time, there must be some significant, persistent thermal feature which tends to be located away from cooler regions of downwelling slabs in the mantle. But whether a plume originates from deep in the mantle, possibly at the core-mantle boundary, or is a purely upper-mantle convective feature, or some coupled lower- and upper-mantle phenomenon, remains unresolved. The formation of plumes may require a thermal boundary layer heated from below (Lay *et al.*, 1998). In this case, the two most plausible locations for this are at the 670-km discontinuity and the core-mantle boundary (CMB).

Arguments in favour of a core-mantle boundary origin: The theoretical temperature excess required to initiate a plume from a thermal boundary layer has been estimated to be 1000 K (Williams & Jeanloz, 1990; Boehler, 1993; Lay *et al.*, 1998). However, seismological modelling of temperature variations in the lower mantle (Nataf & Vandecar, 1993) and petrological modelling of plumes in the upper mantle (Watson & McKenzie, 1991) predict plume excess temperatures of less than 300 K. This is a major discrepancy, but one which can be overcome by invoking a chemical boundary at the base of the lowermost mantle in which densities are increased by 5-10 % compared with the overlying mantle (Farnetani, 1997). This reduces the required temperature excess to about 300 K.

D'' is the layer in the lowermost mantle immediately above the core. It is thought to act as a thermal boundary layer between the outer core and the mantle, and to have properties that differ significantly from the rest of the lower mantle. Kendall and Silver (Kendall & Silver, 1996) detected a high degree of seismic anisotropy within this layer, with vertically-polarised wave speeds reduced by several percent compared with those of horizontally-polarised waves. This may be caused by horizontal layering of oceanic slab remnants which form layers of partial melt there (Wysession, 1996).

Recent global tomography results show large-scale features interpreted as indicating mantle-wide convection. Linear regions, a few hundred kilometres wide and tens of thousands of kilometres long with seismic P-wave velocities elevated by about 0.5%, extend deep into the lower mantle as tabular features beneath several (though not all) regions where subduction has occurred in the last 180 Ma (van der Hilst *et al.*, 1997). Also, regions at the core-mantle boundary with ultra-low seismic velocities (Helmberger *et al.*, 1998; Wen & Helmberger, 1998) have a positive correlation with surface hotspots (Williams *et al.*, 1998). Some geochemical anomalies are thought to require a CMB source. Picritic lavas from Hawaii contain Osmium isotope characteristics for which the most viable explanation is the mixing of lowermost mantle material with that from the outermost core and the subsequent transport of this material to the surface (Brandon *et al.*, 1998). In terms of plume origin, this would strongly imply a lower-mantle source.

Arguments in favour of a 670-km discontinuity origin: Wide, low-velocity areas in the upper mantle modelled using high-resolution global seismic tomography have been interpreted as "vast domains of high temperature" (Anderson *et al.*, 1992). These have been termed "hot cells", and are consistent with geochemically anomalous domains of similar scale rather than point sources associated with thin, chimney-like plumes (Anderson, 1998). Hotspot swells are on a scale characteristic of the upper mantle (spherical harmonic degree *l*=6), rather than deep mantle convection, which corresponds to the scale of *l*=2 harmonics (Anderson *et al.*, 1992). It has also been argued that there is still no geophysical evidence that demands deep thermal perturbations beneath hotspots (Anderson *et al.*, 1992).

Geochemistry shows mixed evidence. Some surface rocks exhibit features which are explained by considerable input from upper-mantle material (Fitton *et al.*, 1997) and other evidence is thought to require the transport of lowermost mantle material to the surface (Brandon *et al.*, 1998).

Alternative theories: Theories which have competed strongly with those of Wilson (1963) and Morgan (1971) include mechanisms such as whole-Earth contraction by cooling, compaction and the extrusion of lavas. Others involve volcanoes erupting at the ends of giant propagating rifts (Sleep, 1984). A strong argument against that theory is that hotspot tracks have been observed to cross ridge axes in the Atlantic and Indian Oceans, which is not in agreement with the crack model, since giant propagating cracks would be expected to stop when they reached a free edge (Sleep, 1990). There are still problems with "conventional" plume theory, whether these plumes are considered to originate at the CMB or the 670-km discontinuity. Perhaps plumes do not all have the same origin. The simplistic age-distance relationships often quoted for hotspot oceanic islands do not always hold true (McNutt *et al.*, 1997). Contrary to the idea of plates drifting passively over a "blowtorch" plume, a "fossil" plume head, severed from its "tail", has been reported beneath the Brazilian shield (Vandecar *et al.*, 1995). The head of this plume appears to have remained fixed to the overlying lithospheric plate despite thousands of kilometres of plate motion from the still-active plume which now feeds the Tristan hotspot. This supports the theory that the regions where plumes *originate* do not move along with the overlying plate.

1.2 DETECTION & OBSERVATION OF PLUMES

Measurable, near-surface parameters that may cast light on the nature of plumes include bathymetric and topographic anomalies, heat flow, gravity and geoid anomalies. Models constructed from such measurements are non-unique, however and it has been argued that plumes are not *required* to explain the observations (Anderson *et al.*, 1992). Other, indirect methods of detecting plumes include modelling the effect of the thermal regime of the plume on sediments in surrounding regions, and seismic imaging of seaward-dipping reflector series thought to be associated with rifting in the presence of a plume. However, most plume models are based on geochemical and direct seismological evidence.

1.2.1   Geochemistry

Observations of age relationships along oceanic island chains can be made by comparing isotopic ratios in surface rocks. Islands and submerged seamounts were originally dated using palaeomagnetic measurements, and these observations formed a major part of hotspot theory. The surface extent of hotspots (and therefore the influence of the inferred plume) can be measured by mapping the spatial distribution of anomalies in isotope and trace element ratios in erupted basalts. Material in mantle plumes is isotopically distinct from that in the asthenosphere, which normally feeds mid-ocean ridges (Schilling, 1991), so the geochemical relationships in such anomalies provide evidence for the existence of plumes.

Normal mid-ocean ridge basalt (MORB) is generally depleted in large-ion lithophile elements (LILs), which have been removed by some prior stage of melt extraction. MORB has low isotopic ratios such as $^{87}Sr/^{86}Sr$ (Anderson *et al.*, 1992). Hotspot basalts, and those erupted at early stages of lithospheric break-up, are generally less depleted than MORB, implying an origin in, or at least mixing with, relatively "enriched" mantle with high LIL concentrations and high $^{87}Sr/^{86}Sr$ ratios. The range of values for these ratios is much greater than for MORB, which suggests a primitive, heterogeneous source. The implication is that enriched material from deep within the mantle is brought to the surface by plumes which penetrate through the relatively depleted asthenosphere. Time-variance of plume activity can be investigated by comparing isotope ratios in surface geology along with independently determined age relationships.

1.2.2   Seismology

A seismological observation of a plume "tail" in the deep mantle has been made by Nataf and Vandecar (1993), who measured travel time delays across the region containing the Bowie hotspot, west of Canada. These delays were attributed to a low-velocity region at ~700 km depth, which was inferred to represent a temperature excess of ~300 K.

However, there exist earlier studies which document significant velocity anomalies in the mantle, detected by measurements of delay times in regions which we now recognise as being plume sites (Tryggvason, 1964; Long & Mitchell, 1970). Core-reflected shear waves, identifying an ultra-low velocity zone and anisotropic fabric, suggest flow at the core-mantle boundary beneath Hawaii (Russell *et al.*, 1998). Corroborating evidence for anisotropy indicating flow and layering beneath areas of large-scale downwelling add weight to this argument (Kendall & Silver, 1996).

The relatively narrow expected tail of a plume in the mantle, and the low-magnitude of the velocity anomaly expected to characterise it, pose a problem for the resolution of global seismic tomography, which is of the order of 500-1000 km. This may explain why, despite significant, recent improvements in the method, it has not provided much evidence for plume-like features. Large-scale seismic tomography has revealed low compressional- and shear-wave velocities beneath both mid-ocean ridges and hotspots. Whereas those beneath ridges appear to be confined to the upper 100 km of the mantle, those beneath hotspots extend to several hundred kilometres depth (Zhang & Tanimoto, 1991), although the resolution of such features is low compared to smaller-scale regional studies. Recent global tomography results show some large-scale structures consistent with mantle-wide convection. Direct evidence of upwelling is less clear.

A problem for the seismological detection of plumes is the frequency-dependent wavefront-healing effect, whereby a time delay produced by the passage of a ray through a low-velocity region is counteracted by rays diffracted around the edge of the slow region which can arrive before the Fermat ray. The effect was shown to be small for the case of relatively small and smooth variations in velocity (Nataf & Vandecar, 1993), although a reduction in travel time delay of up to 40% has

been observed for S-waves passing through strong, narrow, low-velocity structures, by comparison with a model constructed using frequency-dependent amplitude variations (Allen *et al.*, 1999).

Regional, restricted-array tomography techniques, in which the receiver array is located directly over a "target volume" have the advantage that raypaths sample much of the target volume with sub-vertical trajectories, making maximum use of the low-velocity anomaly to produce larger integrated time delays which are easier to detect. This type of experiment has been shown to be successful in detecting and imaging low-velocity anomalies beneath a number of known hotspots. Teleseismic P-wave tomography has been applied to the Yellowstone (Iyer *et al.*, 1981) and Hawaii hotspots (Ellsworth, 1977; Ellsworth & Koyanagi, 1977). Beneath Yellowstone, a low-velocity anomaly was detected, interpreted as a body of up to 9% partial melt along the Snake River Plain, extending to a depth of 175-200 km. Beneath Hawaii little lateral inhomogeneity was detected. The small size of the network aperture meant that the structure was only resolved down to around 165 km. The results suggest that magma is supplied to the Hawaiian volcanoes by very narrow conduits and that the main seismic signature of the hotspot is below 75 km. Similar methods have been used in plume imaging experiments using teleseismic tomography, for example at the Rio Grande Rift (Slack *et al.*, 1996) and the French Massif Central (Granet *et al.*, 1995).

Ji and Nataf (1998) applied two-dimensional waveform tomography to scattered, long-period *P* waves in a search for vertical cylindrical structures in the lowest 1,000 km of the mantle beneath Hawaii. They observed a double feature 200 km north-west of Hawaii, which may indicate two plumes. However, the strength of this feature is 30 to 60 times greater than the expected effect of a 600 K thermal anomaly (which would give a v_p anomaly of -1.5%), so the physical interpretation of this result is problematical. Another method uses a synthetic model of P- and S-wave scattering caused by a vertical cylinder to predict waveform features which could be used in future observational experiments (Tilmann *et al.*, 1998). These include ray focussing effects and the excitation of secondary phases including a 25% increase in the amplitude of the transverse component relative to the radial component.

Indirect observation using the method of receiver function analysis has been applied to the upper mantle transition zone (Shen *et al.*, 1998). The excess temperature associated with a plume is predicted to displace the depths of the phase transitions at the 670- and 410-km seismic discontinuities upwards and downwards respectively, resulting in a small region where the transition zone is thinner by some 20 km relative to the surrounding mantle.

1.3 THE ICELAND PLUME : SUMMARY OF CURRENT KNOWLEDGE

1.3.1 Regional setting

Iceland straddles the mid-Atlantic ridge, the constructive boundary between the Eurasian and North American lithospheric plates at ~65°N. The mid-Atlantic ridge is a slow-spreading ridge, with an average full spreading rate of 18 mm a^{-1} (DeMets *et al.*, 1994). While the island of mainland Iceland is about 500 × 300 km in size, the large bathymetric plateau around Iceland is over 1000 km wide. The topographic anomaly rises to 3 km above the level of normal sea floor of this age and influences the spreading ridge as far south as the Charlie Gibbs fracture zone (CGFZ), some 1000 km away.
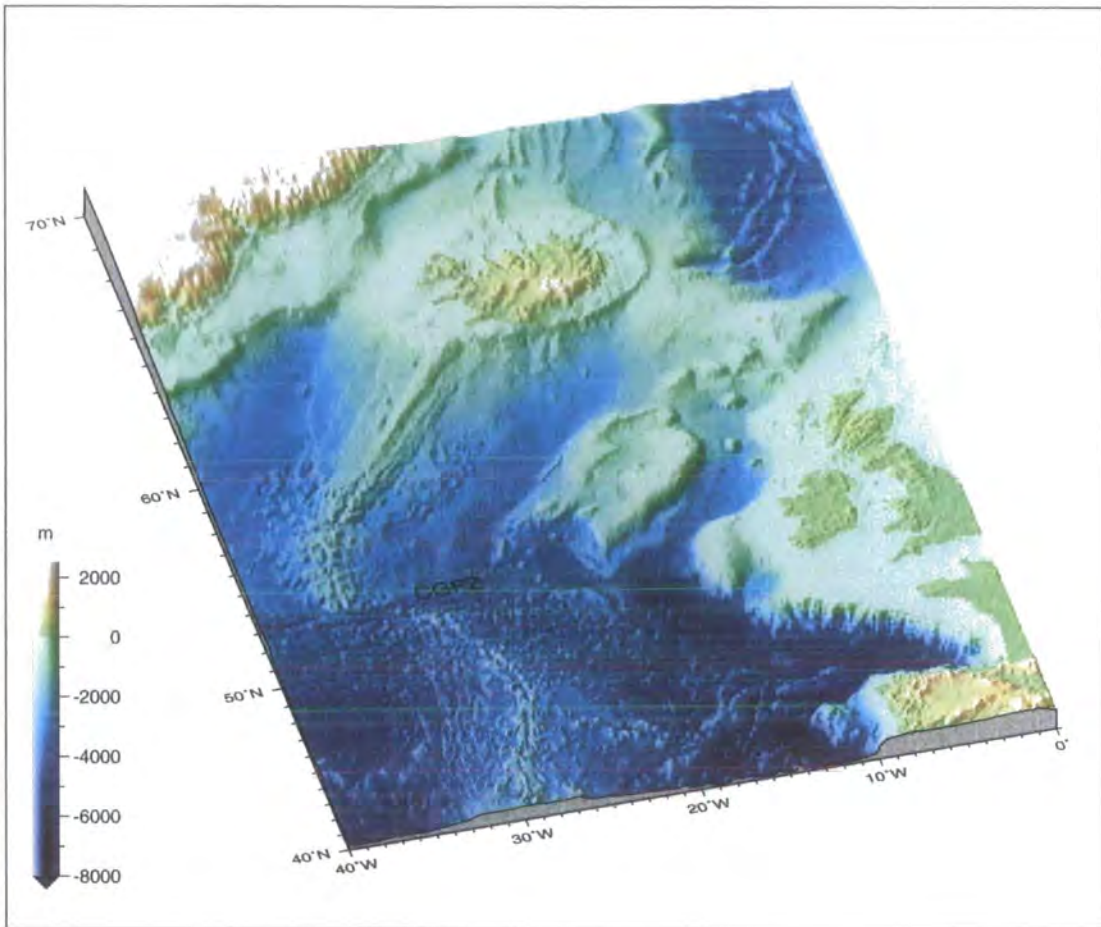
Figure 1.3 ETOPO5 Bathymetry and topography of the Iceland region. CGFZ = Charlie Gibbs fracture zone.

The thermal anomaly beneath Iceland is thought to have been present at least since the opening of the north Atlantic ocean some 55 Ma ago, and may have initiated the process (Morgan, 1981). The continued influence of the plume has been felt in the region ever since, implying a long-lived feature in the mantle. Some evidence points to time-dependent variations in the strength of the plume. Outward-propagating, V-shaped topography and gravity anomalies along the Reykjanes Ridge suggest temperature variations of around 30°C with a period of 5-10 Ma (White *et al.*, 1995), and along-axis variations in Pb isotopes support the idea of material from a pulsating plume interacting with the flow of asthenospheric mantle related to the spreading plate boundary (Hanan & Schilling, 1997).

1.3.2   The Iceland ridge-centred hotspot

Iceland is regarded as the type example of a ridge-centred hotspot, and evidence for the interaction of the Iceland hotspot with the spreading ridge is apparent from several observations. The apparent influence of the hotspot along the Reykjanes Ridge suggests lateral outward flow of plume-fed material beneath the ridge axis , and would explain the geochemical patterns such as decreases in Fe:Mg, Na:Ca ratios and incompatible trace element concentrations along the ridge away from Iceland (Schilling, 1973). Interestingly, the Kolbeinsey ridge north of Iceland does not appear to be influenced to such an extent, and it is possible that the Tjornes fracture zone in the north of Iceland acts as a barrier to the lateral flow of material from beneath Iceland. The Greenland-Iceland and Faroe-Iceland ridges are evidence that the thermal anomaly has been active beneath Iceland for a considerable time as the plates have spread apart. These ridges represent the track of the Iceland hotspot on either side of the spreading ridge.

The axis of the spreading ridge emerges on land at the Reykjanes peninsula in the south-west and continues east-north-eastwards as the Western Volcanic Zone (WVZ, Figure 1.4), one of three such rift zones which comprise rifts, fissure swarms and central volcanoes. The South Iceland Seismic Zone offsets the WVZ from the Eastern Volcanic Zone (EVZ), which includes the increasingly active volcanic centres of Grimsfjall and Barðabunga beneath the Vatnajökull glacier, the site of a sub-glacial eruption and jökulhlaup (glacial melt-water outburst) in 1996. The Krafla central volcano lies in the centre of the Northern Volcanic Zone to the north, which is itself terminated by the Tjörnes fracture zone (TFZ), a transform zone which connects the rift axis on land to the Kolbeinsey ridge, the continuation of the mid-Atlantic ridge north of Iceland.

There is evidence that the active spreading centre has shifted eastwards on the surface of Iceland over time (Saemundsson, 1979; Helgason, 1984; Eysteinsson & Hermance, 1985; Helgason, 1985; Hardarson *et al.*, 1997). The ridge is thought to have initially jumped eastwards to the Snaefelsnes zone at around 16 Ma (Saemundsson, 1979). A second jump moved the spreading centre to the Húnaflói-

Figure 1.4 Relief map of Iceland showing major tectonic and volcanic features. RR = Reykjanes ridge, KR = Kolbeinsey ridge, TFZ = Tjörnes fracture zone, W,E & NVZ = Western, Eastern and Northern Volcanic Zones, SISZ = South Iceland Seismic Zone, SZ = Snaefelsnes Zone, HSVZ = Húnaflói-Skagi Volcanic Zone. Vatnajökull and other glaciers are shown in blue.

Skagi Volcanic Zone in north-western Iceland and a third jump at 7-6 Ma moved the spreading centre to the NVZ (Helgason, 1984; Helgason, 1985). The centre of the hotspot is currently thought to be beneath east-central Iceland and to be moving eastwards with respect to the North American plate at about 1-2 cm a^{-1} (Nunns, 1983; Vogt, 1983). The location of the ridge is probably controlled by the underlying plume, and follows it as the plume migrates eastwards. This is also suggested by the large eastwards embayment which the ridge axis forms between the Reykjanes and the Kolbeinsey ridges (Figure 1.4).

1.3.3 Icelandic crust

Lively debate has been in progress for some time over two different models for the Icelandic crust. One model involves a thin, hot crust of around 10-15 km thickness, underlain by anomalously hot mantle with a significant percentage (~15%)

of partial melt (Pálmason, 1973; Pálmason & Saemundsson, 1974; Gebrande *et al.*, 1980). That model was supported by the original interpretation of the RRISP refraction profile (Reykjanes Ridge Iceland Seismic Profile) results (Angenheister *et al.*, 1980). Magnetotelluric measurements of the conductivity structure with depth (Beblo & Björnsson, 1980; Beblo *et al.*, 1983; Hersir *et al.*, 1984; Eysteinsson & Hermance, 1985), map a widespread, high-conductivity layer beneath most of Iceland. Interpreted as a thin layer of partially molten basalt at around 1,000-1,100°C, this layer was found at 10 km depth below the spreading ridge axis and at 20-30 km beneath older crust further away. An alternative explanation is that the low resistivity is due to zeolite minerals as observed in extrusives in the rift zones, rather than to large accumulations of melt (Smallwood *et al.*, 1998). High temperature gradients measured in boreholes support the hot-crust model, suggesting, by extrapolation, molten material at between 10 and 30 km depth.

Recent, high-resolution seismic work points to a thicker (20-35 km) and cooler crust (Zverev *et al.*, 1976; Bjarnason *et al.*, 1993; Staples *et al.*, 1997; Smallwood *et al.*, 1998), with melt present only in small, shallow, crustal magma chambers (Brandsdóttir & Menke, 1992; Menke & Levin, 1994; Menke & Sparks, 1995; Brandsdóttir *et al.*, 1997). Crucial to this debate are arguments over the existence and depth of a Moho beneath Iceland, and estimates of the temperatures of the lower and upper crust with respect to the basalt and gabbro solidi.

The RRISP seismic profiles across Iceland and the Reykjanes Ridge were originally interpreted as showing low shear-wave velocities and quality factors in the 10-15 km depth range, implying a thin crust underlain by partially molten material (Angenheister *et al.*, 1980). A subsequent re-interpretation suggested that the Moho is present at 35 km depth, and that the high attenuation observed was associated with shallow volcanism (Menke *et al.*, 1996). This implies that the crust beneath Iceland is both thick (30-35 km) and generally below the solidus temperature. This hypothesis was supported by reports of a Moho in other refraction seismic results (Brandsdóttir & Menke, 1992; Bjarnason *et al.*, 1993; Staples *et al.*, 1997) and from receiver function analysis, for example in the NVZ (Darbyshire *et al.*, 1997). There, a gradational Moho is observed, though considerable variation in crustal thickness is noted within northern Iceland. Evidence for a ubiquitous, sharp Moho is not found in

the Western Fjords area, where analysis of receiver functions and regional surface wave phase velocities revealed a zone of enhanced velocity gradient beneath only some of the stations, while others showed a velocity gradient increasing smoothly with depth (Du & Foulger, 1999). At the time of writing, the best available results from surface wave and receiver function work suggest that the depth to the v_P=7.8 km s^{-1} horizon varies from ~24 km to ~40 km over Iceland (G.R. Foulger, *pers. comm.*).

1.3.4 Gravity field

A map of the Bouguer gravity field of Iceland is given in Figure 1.5 and shows a negative anomaly of 20-40 mGal centred on the interior highlands, increasing to zero in the neovolcanic zones and to +20-40 mGal at the coasts (Thorbergsson *et al.*, 1990). This low appears at least roughly to coincide with the presumed centre of the hotspot. When compared to the Atlantic ocean basin as a whole, the Bouguer gravity field of Iceland is negative by approximately 350 mGal, and by approximately 150 mGal relative to the neighbouring Faroe-Iceland Ridge (Hermance, 1981). The anomaly can be divided into contributions from crustal and subcrustal effects. Comparisons with crustal structures and densities obtained from regional seismic studies suggested a significant component (~-430 mGal) of isostatic compensation from subcrustal material beneath the neovolcanic zone (Hermance, 1981).

1.3.5 Seismic phenomena

The mantle beneath Iceland has long been noted to cause significant time delays in teleseismic body waves (Tryggvason, 1964; Long & Mitchell, 1970; Bjarnason *et al.*, 1996), implying that wave speeds are lower beneath Iceland than in the surrounding mantle. These delays may even be greater than can be observed due to wavefront healing effects (Allen *et al.*, 1999). Shear-wave splitting can also contribute to these time delays, although only a limited number of observations from Iceland exist. The fast direction of splitting, thought to be associated with preferred orientation of upper mantle minerals such as olivine, was found to be between N20°W and N45°W (Bjarnason *et al.*, 1996), which does not correlate with likely flow patterns associated with a plume. However, the size of the time delays
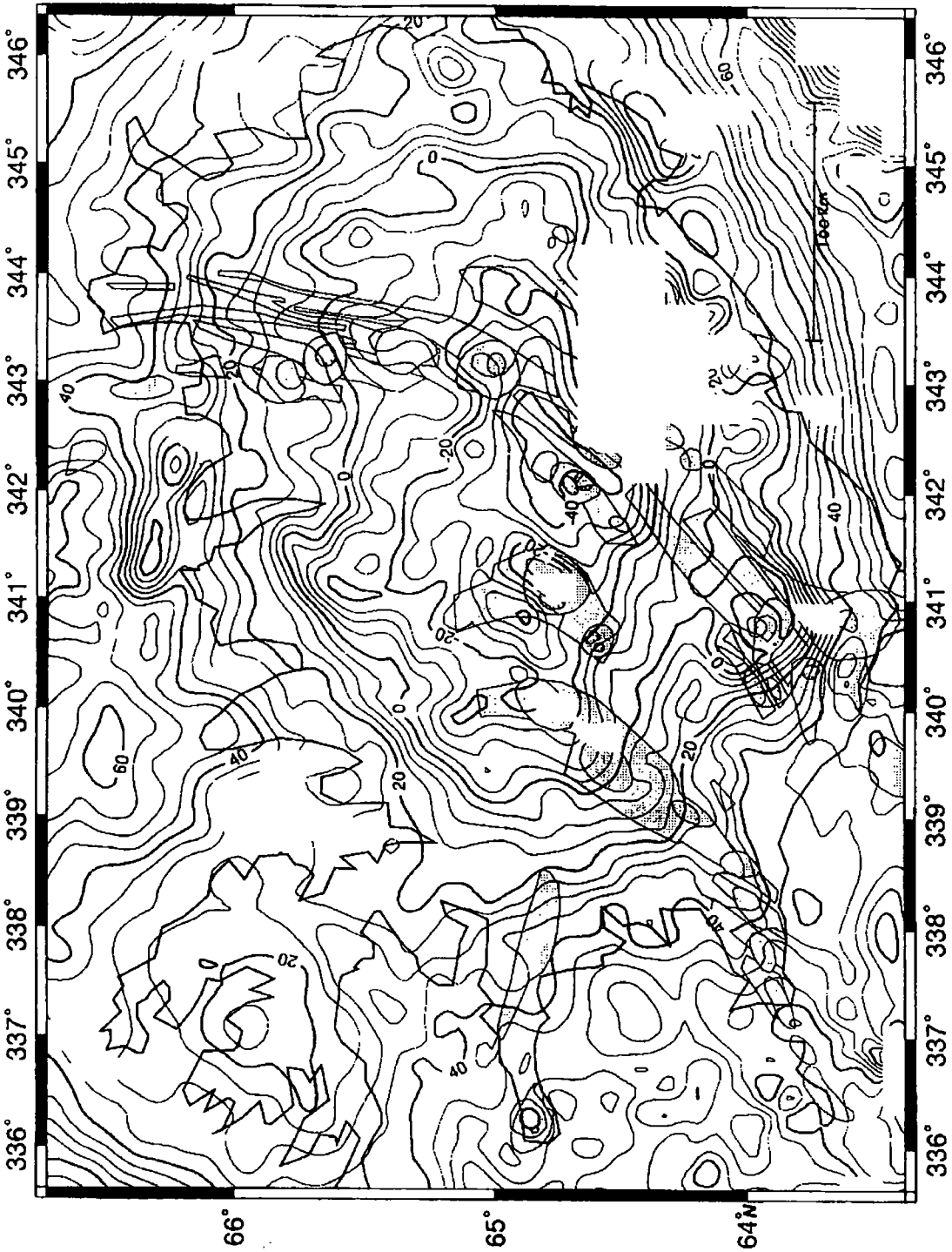
Figure 1.5 A Bouguer gravity map of Iceland (model CBA1, Fig 3.11 of Field (1994), using the dataset of Thorbergsson *et al.* (1990).

between the fast and slow S-waves (0.7-1.7 s) suggest a cause associated with mantle anisotropy, rather than crustal anisotropy which causes a much smaller degree of splitting (0.1-0.3 s) in the NVZ (Menke *et al.*, 1994). The splitting in the mantle is probably linked to the large-scale mantle flow field of the north Atlantic.

The first seismic image of the mantle beneath Iceland made using teleseismic tomography (Tryggvason, 1981; Tryggvason *et al.*, 1983) revealed a maximum anomaly of -3.9% P-wave velocity perturbation. The shape of the anomaly in the uppermost layer was found to correlate strongly with the southwest-northeast trend of the neovolcanic zone. The anomaly was strongest in the uppermost and lowermost layers, but weaker in the depth range 75-275 km, where the peak anomaly was around -1.6%.

More recently, Wolfe *et al.* (1997) provided the first S-wave model of the Iceland plume using teleseismic tomography. This model showed an anomaly shaped like a truncated cone, with maximum magnitudes of -2.1% for the P velocity perturbation, and -4.2% for S. In horizontal section at 300 km depth, the anomaly shape is best described by a radial Gaussian velocity function of radius 150-200 km. The anomaly was found to broaden with depth and to be persistent down to at least 400 km. These anomalies in P- and S-wave velocity suggest excess temperatures between 200-300 K, which support the idea of a hot, narrow plume rather than the broader, cooler structure predicted by some numerical models (Ribe *et al.*, 1995; Ito *et al.*, 1997). Support for the thin, hot plume model is also provided by frequency-dependent amplitude variations of teleseismic waves in the mantle beneath Iceland (Allen *et al.*, 1999). In this case, the model was optimised by a maximum S-wave velocity perturbation of -12% and Gaussian radius of 100 km.

Further discussion of the teleseismic tomography models of Tryggvason (1983) and Wolfe *et al.* (1997) is given in Chapter 6. There, their models are reproduced and compared with the results of this thesis.

The whole-mantle plume observed by Bijwaard & Spakman (1999) is slightly wider, having a radius of up to 250 km in the mantle, but supports the temperature contrast of between 200 and 300 K in the upper mantle Figure 1.6. This model provides evidence for extensive spreading of the plume head, which is inferred from a region 1200 km in diameter with P-wave velocities reduced by up to 2%. The

anomaly is much weaker (less than 0.5%) in the lower mantle. Those results also show considerable deviation of the plume conduit from the hypothesised vertical cylinder, and lateral branching which may indicate that the surface hotspot may not be stationary over time. Very recent, high-resolution global tomography work, published in December 1999, largely agrees with the results of Bijwaard & Spakman (1999) but suggests that the lower mantle structure is insignificant (Megnin & Romanowicz, 1999; Ritsema *et al.*, 1999).
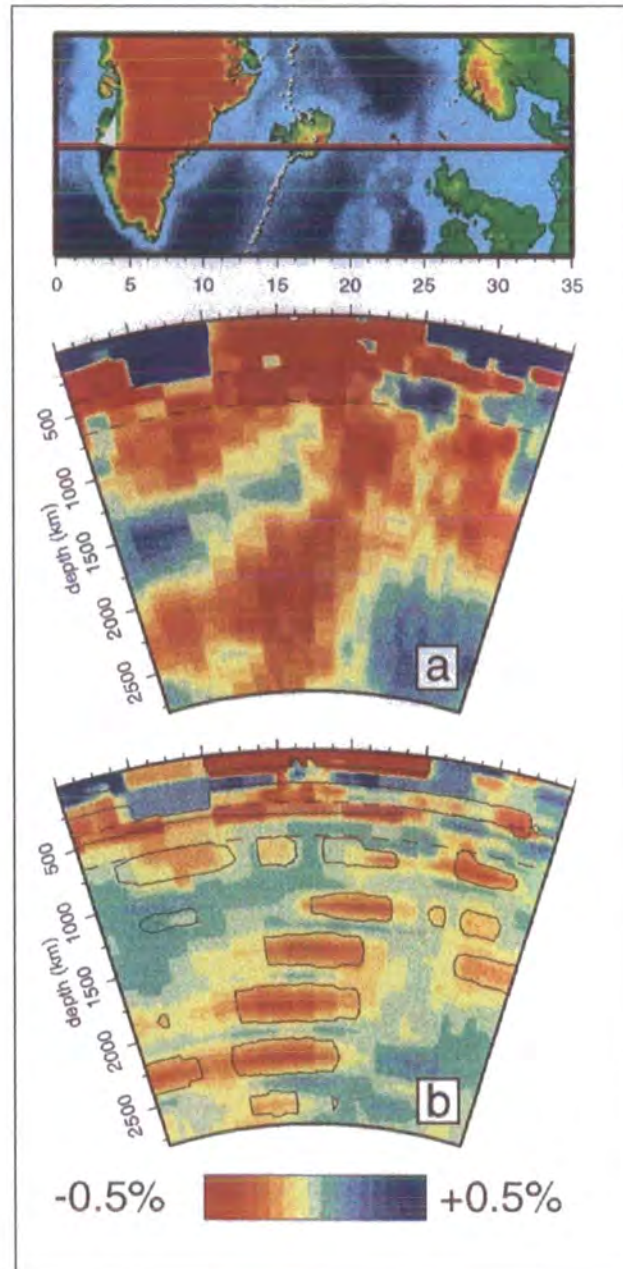
Figure 1.6 P-wave tomographic model of a whole mantle plume beneath Iceland (Bijwaard & Spakman, 1999). (a) shows observed results, (b) shows results from synthetic tests.

The thickness of crust predicted to be produced by a hot, narrow plume model over-estimates actual crustal thickness and the temperature contrast between Iceland and the rest of the spreading ridge (Wolfe *et al.*, 1997). Models have been reconciled with observed parameters by including the effects of dehydration (Ito *et al.*, 1999). The extraction of water from the mantle by partial melting beneath the spreading ridge leaves a residuum with a much higher viscosity, preventing active (buoyant) upwelling of material, and allowing only passive upwelling in response to plate spreading. This implies lower rates of melt production, which are more in line with observed values of crustal thickness.

1.3.6 Geochemistry

Iceland exerts considerable influence on the geochemistry of lavas produced along a 1000-km long section of the mid-Atlantic ridge. That such lavas are derived at least partly from primitive material from deep within the Earth is suggested by several geochemical parameters.

Lavas dredged from an axial profile along the Reykjanes Ridge show marked and regular decreases in K_2O, TiO_2, P_2O_5, La and other LIL concentrations with increasing distance south-west along the Reykjanes ridge (Schilling, 1973) (Figure 1.7), i.e., basalts on Iceland are relatively enriched, or less depleted, than MORB.
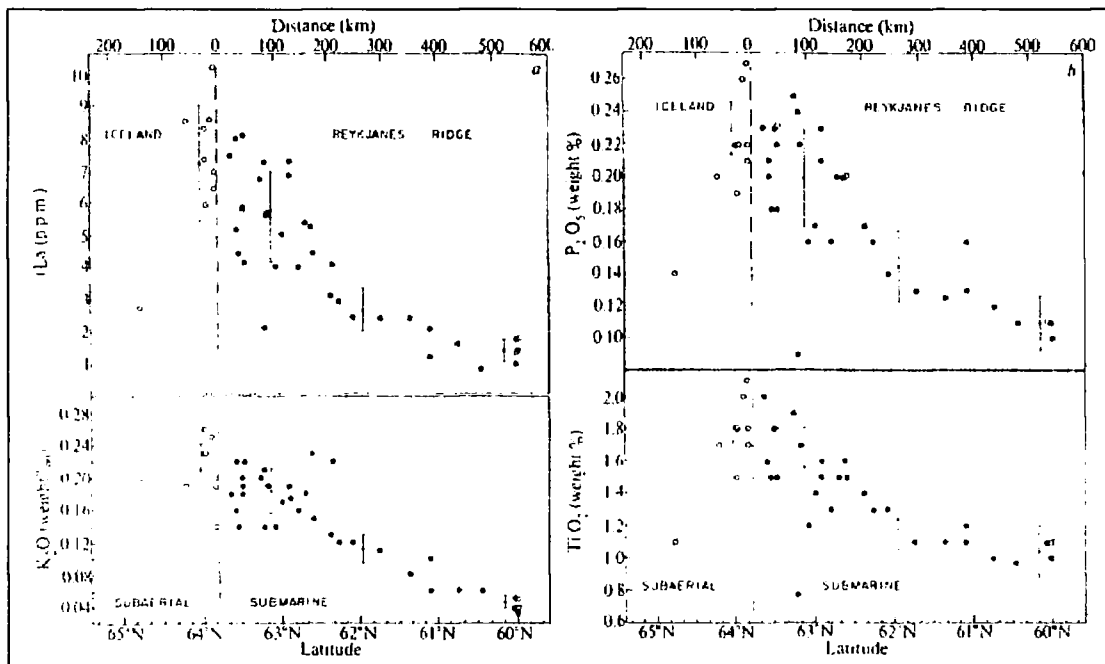
Figure 1.7 Geochemical trends along the Reykjanes ridge (Schilling, 1973).

There is considerable variation in these concentrations within basalts on Iceland, however (Sigvaldason *et al.*, 1974), suggesting that some mixing occurs between the primitive material and MORB-source mantle. Evidence for such mixing comes from isotopic ratios such as $^{87}Sr/^{86}Sr$, which decrease outwards along the ridge as the plume signature is "diluted" by mixing with Atlantic MORB asthenosphere (Hart *et al.*, 1973). Pb isotopic variations of lavas on Iceland suggests some grouping of lavas in space and time (Welke *et al.*, 1968) implying that there is temporal variation in the activity of the plume, perhaps involving pulsating activity (Hanan & Schilling, 1997). The outward-propagating V-shaped topographic and gravity anomalies along the Reykjanes Ridge have been explained in terms of temperature and flow-rate fluctuations of material flowing laterally away from the core of the plume (White *et al.*, 1995), again, consistent with pulsating plume activity.

The variations in Icelandic rock types from picrite to tholeiite to alkali basalt have been explained by the existence of two distinct source regions and mixing between them, or melts derived from them (Hards *et al.*, 1995). Other workers have suggested distinct zoning of the Icelandic plume head (Fitton *et al.*, 1997), with an axial zone of "Icelandic" mantle (i.e. primitive plume material) encapsulated in a shell of anomalously hot, but compositionally normal, MORB-source mantle. This last study has difficulty reconciling observations with the hypothesis of a plume originating solely from the lower mantle and instead suggests that at least part of the plume originated at the thermal boundary layer at the base of the upper mantle. This could be caused by a lower mantle plume which "stalls" at the 670 km discontinuity and initiates an upper-mantle plume. Alternatively, a plume that originates at the basally-heated boundary layer at the base of the upper mantle could entrain some lower-mantle in the plume conduit. There is strong evidence that at least some lower-mantle material is brought to the surface (Brandon *et al.*, 1998) and this is difficult to ignore in the light of supporting seismological evidence of CMB anomalies beneath plumes.

The lateral branching of the plume observed in the whole-mantle tomographic image of the Iceland plume of Bijwaard & Spakman (1999) may also be supported by geochemical evidence. Picrites (high MgO-content lavas) of early Tertiary age, representing "Iceland-like" plume material have been reported from

west Greenland, 4-5 Ma older than the onset of volcanism in east Greenland, normally associated with the beginning of Icelandic plume activity. Picrites are thought to be restricted to the region above the hot axial conduit of a plume, and therefore it is unlikely that these lavas are erupted merely in the (hypothetical) broad "mushroom-head" of the plume. This suggests that a lateral branch of the plume may have been focussed in this area. It is argued that the plume centre could not have migrated fast enough from west Greenland to its known position beneath east Greenland at the start of the main plume activity. This would have required a migration rate ~20 times that of the next 58 Ma.

These observations may also support the idea of a lower-mantle "mega-plume" which spawns major and minor "sub-plumes" in the upper mantle. Numerical modelling of lower-mantle mega-plumes has demonstrated that smaller, more localised plumes can form in the upper mantle, allowing hotspots to vary in plume flux whilst being fed from a relatively stable thermal boundary layer at the CMB (Thompson & Tackley, 1998).

1.4 QUESTIONS TO BE ANSWERED

Several questions regarding the role of plumes in mantle convection and surface tectonics and volcanism remain. Some of these may be summarised as follows:

What is a plume, in terms of measurable physical parameters? What is the observational evidence that plumes fit theoretical models of axisymmetric, cylindrical thermal currents rising from some source in the mantle? Can we infer physical properties such as excess temperature, width, depth extent and up-welling rate from physical observations?

Are plumes required by surface observations? Can surface observations be explained by models other than plumes? How reliable and realistic are the models we construct?

What is the role of plumes in plate-driving forces? Do plumes actively pull plates apart (explaining their proximity to many constructive plate margins), or is plate separation above plumes merely a passive process in response other forces? The latter would suggest some independence of surface tectonics from mantle convection.

What is the depth of origin of plumes? Do plumes originate at the core-mantle boundary, or some other thermal boundary layer such as the 670-km seismic discontinuity? Are convection currents in the lower and upper mantle connected, or does the transition zone act as a barrier, restricting convection to lower and upper "compartments"?

Does plume activity vary with time? Observations of surface morphology and geochemistry seem to suggest some variability with time. Is there any evidence for this from direct observations of plumes in the mantle?

1.5 AIMS OF THIS STUDY

The primary aim of this study is to test the hypothesis that Iceland is underlain by a plume, and to determine its extent and seismic structure. The approach used is:

- To investigate the signature of a possible plume in the lower mantle at around 1,500 km depth from seismic ray paths which pass beneath Iceland to Norway and Scotland and to use these observations to place constraints on the size and strength of any such plume at this depth,

- To record and analyse seismic body waves arriving in Iceland and measure relative arrival times to identify seismic waves which may been slowed down by travelling through anomalously hot and/or partially molten material,

- To map the seismic P- and S-wave structure of the mantle beneath Iceland with the highest resolution of studies to date, using teleseismic travel-time tomography, and to interpret the results along with information about quality and reliability in terms of temperature variation and convective state,

- To compare these results with other previous studies and to test the quality of those results.

Chapter 2

Azimuth Anomaly Study

2. AZIMUTH ANOMALY STUDY

2.1   BACKGROUND

Teleseismic *P* waves passing near convective plumes in the mantle are refracted horizontally, causing anomalies in their propagation directions that can be measured by wide seismometer arrays. Waves from seismically active areas in the eastern Pacific and western north America to an array in Norway (NORSAR) and a seismic network in Scotland pass beneath Iceland at depths of about 1,200 to 1,900 km. The arrival azimuths of seismic waves at NORSAR can thus place upper bounds on a plume in the mid-mantle beneath the Iceland region. The signal is weak, a result that is not dissimilar from those of other studies that seek evidence for the Iceland plume in the lower mantle. However, this is a novel approach and the results add to the sparse information available about the lower mantle beneath Iceland.

2.2   THE NORSAR SEISMIC ARRAY

The 100-km aperture Norwegian Seismic Array (NORSAR) in southern Norway was operated from the 1960s to the 1980s to conduct research on detecting and identifying nuclear explosions. NORSAR and other, similar arrays enabled seismologists to improve signal-to-noise ratios, by summing signals from sensors that were spaced widely enough so that the noise was largely incoherent. These arrays had another capability of greater scientific importance: the relative arrival times at different sensors could give direct measurements of the arrival directions (slowness vectors) of seismic waves. Such measurements were found to differ substantially from the directions predicted by standard tables, because of the effects of lateral variations in Earth structure. Although it is not possible to invert observed slowness anomalies from a single array to determine three-dimensional structure uniquely, it is possible to draw some general conclusions. At NORSAR, *P* waves from earthquakes throughout the world had observed slowness vectors that were systematically displaced eastward by about 1 s/°, an effect that could be attributable to lateral variations in the crust and/or upper mantle directly beneath the array, which affect waves from all directions similarly. On the other hand, the slowness anomalies sometimes changed rapidly with the locations of the earthquakes. Such anomalies must arise much further from the array, although the location cannot be determined with any precision using a single array.

The most rapidly varying slowness vector anomaly at NORSAR occurred for earthquakes in middle America, whose waves approach NORSAR from the WNW (Sheppard, 1973). This anomaly was originally attributed to structure in the upper mantle beneath the earthquakes. However, these waves also pass beneath Iceland at a distance of about 1,500 km from NORSAR, raising the intriguing possibility the anomaly might be related to structure beneath Iceland, in the depth range 1,600-1,900 km. If seismic rays pass near a low-velocity plume, the first arrivals will be refracted horizontally so that they pass to either side of it, and the range of azimuths measured by the array will be greater than the range of great-circle azimuths to the epicentres. Just such an effect was seen in the NORSAR data by Sheppard (1973).

Data from a single array can provide information about the direction of an anomalous structure. Here, data from a network in southern Scotland is used in an attempt to improve spatial constraints. If an anomaly could be detected from two directions, then its location could be determined by triangulation.

2.3   DATA

2.3.1   Experiment geometry

The data used in this study consist of teleseismic *P*-wave arrival times measured from vertical-component seismograms recorded on the NORSAR array and a collection of stations of the UK seismic network in southern Scotland. The experiment geometry is shown in Figure 2.1. Both arrays are located within 15° of Iceland. Body waves from teleseisms at epicentral distances of between 70° (e.g., earthquakes in Alaska observed in Scotland) and 85° (e.g., earthquakes in middle America observed at NORSAR) pass through the mantle beneath Iceland at depths of approximately 1,200-1,700 km and 1,600-1,900 km, respectively. The ray paths cross, providing an experimental geometry capable of locating the position of an anomaly, if one exists.

2.3.2   Data from NORSAR

The NORSAR dataset comprises teleseisms from the central America region (array-to-event azimuth range 260°-320°) that were recorded during the years 1973-1976 (Figure 2.2). During this period, NORSAR consisted of 22 six-station subarrays, had an aperture of about 100 km, and could resolve slowness within about

0.06 s/°, or 0.6° in azimuth. All stations had identical, vertical, short-period, Hall-Sears HS-10-1/ARPA seismometers (Bungum *et al.*, 1971). Data were digitised at each subarray at a sampling rate of 20 sps and transmitted to the main data processing centre by telephone line.

I extracted seismograms from a selection of the largest events (Table 2.1) from the archive of digital data on magnetic tape at the NORSAR data processing centre. I digitally filtered these (passband 0.5-2.0 Hz) and measured *P*-phase arrival-time differences at different sensors by visual correlation of coherent peaks or troughs relative to the first cycle. Only the clearest of these relative arrivals were measured. Where possible, an arrival was picked from at least one sensor in each subarray for each event. Typically, about 20 of the 22 subarrays provided reliable picks for each event.

Table 2.1 Events recorded at NORSAR (data from ISC Bulletin)

Lat	Lon	d/km	Date	Origin	Mb	Δ (°)	Region
5.23°N	75.82°W	110	1973/04/24	18:42:31.5	5.3	83.8	COLOMBIA
19.97°N	73.05°W	24	1973/08/03	15:44:25.5	5.2	69.7	HAITI REGION
18.26°N	96.58°W	75	1973/08/28	09:50:39.1	6.6	82.2	VERA CRUZ, MEXICO
5.27°N	78.08°W	30	1973/09/16	08:21:37.9	5.3	84.9	SOUTH OF PANAMA
19.42°N	104.98°W	56	1973/10/18	10:49:39.3	6.0	84.8	NEAR COAST OF JALISCO, MEXICO
9.51°N	83.95°W	34	1974/02/28	20:20:10.4	5.8	84.0	COSTA RICA
14.52°N	91.64°W	106	1974/04/10	22:43:00.5	5.4	83.3	GUATEMALA
15.61°N	95.26°W	33	1974/06/25	05:01:01.2	5.2	84.0	NEAR COAST OF OAXACA, MEXICO
15.54°N	95.33°W	23	1974/06/25	08:44:45.3	5.4	84.1	NEAR COAST OF OAXACA, MEXICO
7.51°N	77.50°W	54	1974/07/13	02:20:24.6	5.5	82.6	PANAMA-COLOMBIA BORDER REGION
7.24°N	77.55°W	23	1974/07/13	23:08:42.6	5.3	82.9	PANAMA-COLOMBIA BORDER REGION
17.06°N	98.42°W	63	1974/07/18	19:21:26.3	5.5	84.1	GUERRERO, MEXICO
4.32°N	76.84°W	91	1974/08/24	02:47:31.1	5.7	85.1	COLOMBIA
2.72°N	71.37°W	44	1974/09/27	04:09:01.6	5.5	83.8	COLOMBIA
7.18°N	77.76°W	40	1975/01/25	02:08:41.8	6.0	83.1	PANAMA-COLOMBIA BORDER REGION
15.68°N	91.72°W	226	1975/02/03	01:03:26.6	5.3	82.3	MEXICO-GUATEMALA BORDER REGION
16.47°N	98.86°W	17	1975/04/23	11:14:49.3	5.9	84.8	NEAR COAST OF GUERRERO, MEXICO
29.49°N	113.40°W	30	1975/07/08	09:37:28.9	5.6	79.0	GULF OF CALIFORNIA
16.24°N	94.07°W	79	1975/08/19	14:57:11.6	5.6	82.9	OAXACA, MEXICO
14.65°N	93.48°W	15	1975/08/22	23:08:14.2	5.2	84.0	NEAR COAST OF CHIAPAS, MEXICO
6.96°N	77.67°W	27	1975/08/25	03:57:18.1	5.2	83.2	NEAR WEST COAST OF COLOMBIA
7.55°N	77.50°W	0	1975/11/21	01:14:55.6	5.8	82.6	PANAMA-COLOMBIA BORDER REGION
14.70°N	90.63°W	27	1976/02/06	18:19:21.4	5.6	82.7	GUATEMALA
21.63°N	106.60°W	43	1976/02/09	21:29:57.0	5.6	83.5	OFF COAST OF CENTRAL MEXICO
17.45°N	100.65°W	48	1976/06/07	14:26:39.9	6.0	84.7	GUERRERO, MEXICO
7.41°N	78.04°W	3	1976/07/11	20:41:47.9	6.1	83.0	PANAMA
7.06°N	78.15°W	37	1976/07/11	20:58:24.3	5.4	83.3	PANAMA
7.24°N	78.29°W	15	1976/07/12	14:43:08.6	5.4	83.3	PANAMA
7.42°N	78.02°W	16	1976/07/13	01:26:07.3	5.2	83.0	PANAMA
7.41°N	78.01°W	27	1976/07/14	01:32:34.6	5.4	83.0	PANAMA
7.41°N	78.11°W	43	1976/07/15	00:35:33.6	5.3	83.0	PANAMA
19.35°N	104.67°W	69	1976/07/17	09:02:14.7	5.2	84.8	NEAR COAST OF JALISCO, MEXICO
4.93°N	82.59°W	33	1976/07/24	10:43:22.5	5.4	87.4	SOUTH OF PANAMA
18.81°N	101.06°W	93	1976/09/05	20:11:39.2	5.3	83.7	GUERRERO, MEXICO
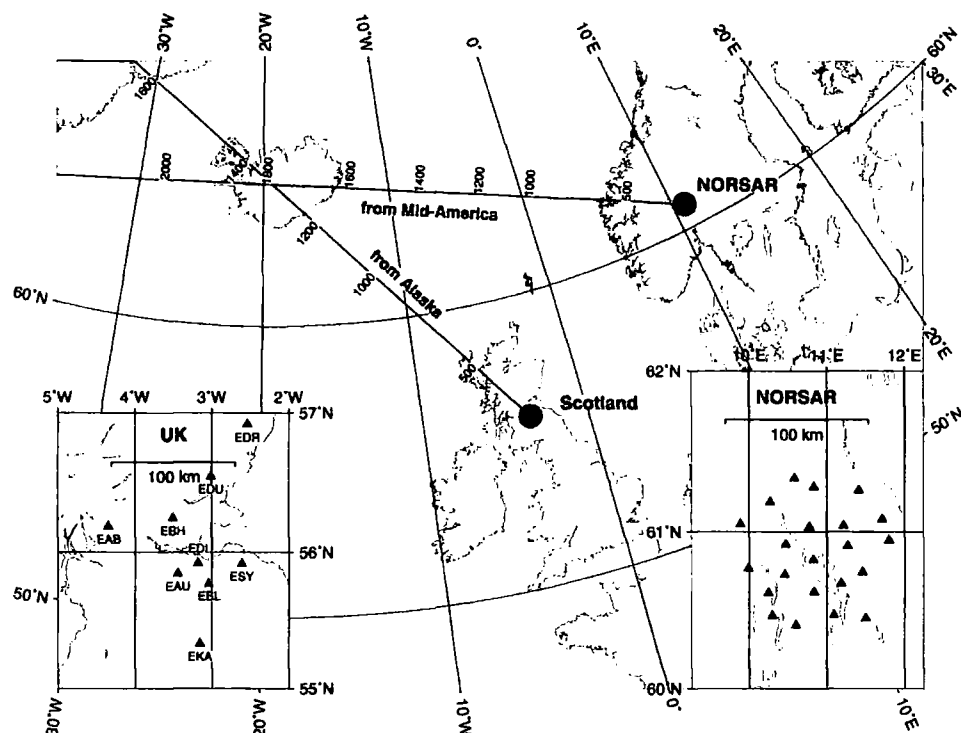
Figure 2.1 Map showing the NORSAR array and network of seismic stations in Scotland used in this study. Triangles on insets show locations of seismic stations (Scotland) and subarray centres (NORSAR). Lines show great circles along which waves approach the arrays, with numbers indicating the depths, in km, of rays from typical epicentral distances (70° for the Scottish stations; 85° for NORSAR).
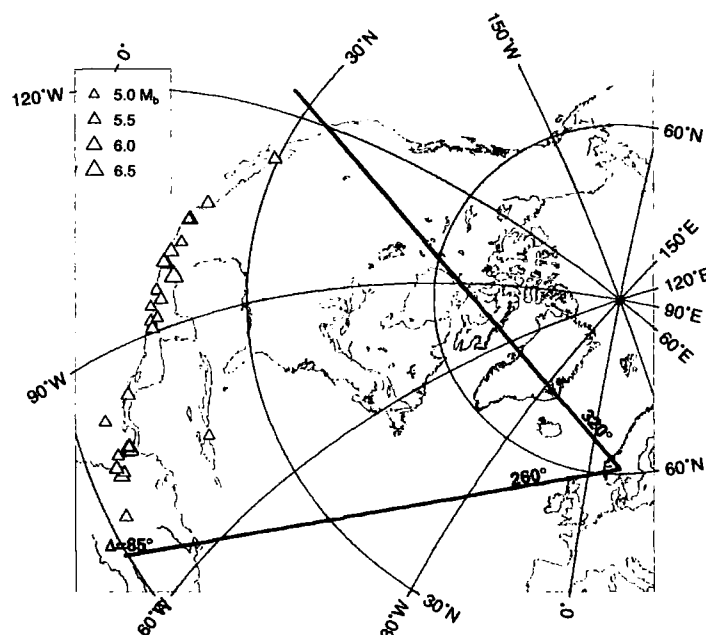
Figure 2.2 Map showing events used in this study, recorded at NORSAR between 1973 and 1976. Lines shown bound the array-to-event azimuth range 260°-320°. Typical epicentral distance is 85°.

2.3.3 Data from the Scottish network

An array of the aperture of NORSAR is not available in the UK, the Eskdalemuir, Scotland array being only 20 × 20 km in size. Such an array is too small to assess azimuth anomalies accurately. Thus a subset of the seismic network operated by the British Geological Survey (BGS) in the UK was used as an array (Figure 2.1).

Stations of the Scottish network have vertical, short-period Wilmore Mk II/III seismometers, and data are relayed by FM analogue telemetry to Edinburgh. BGS personnel regularly measure *P*-wave arrival times from paper playouts (D. Galloway, BGS, *pers. comm.*) and report them to the International Seismological Centre (ISC), which publishes them in monthly Bulletins and distributes them in computer-readable form. A group of stations was selected for this analysis which covers an area similar to that of NORSAR, and *P* arrival times were extracted from the ISC CD-ROMs for the period 1984-1994. The teleseisms used were in the region from Vancouver Island through Alaska to the Aleutian Islands (array-to-event azimuth range 300°-360°) (Figure 2.3, Table 2.2)
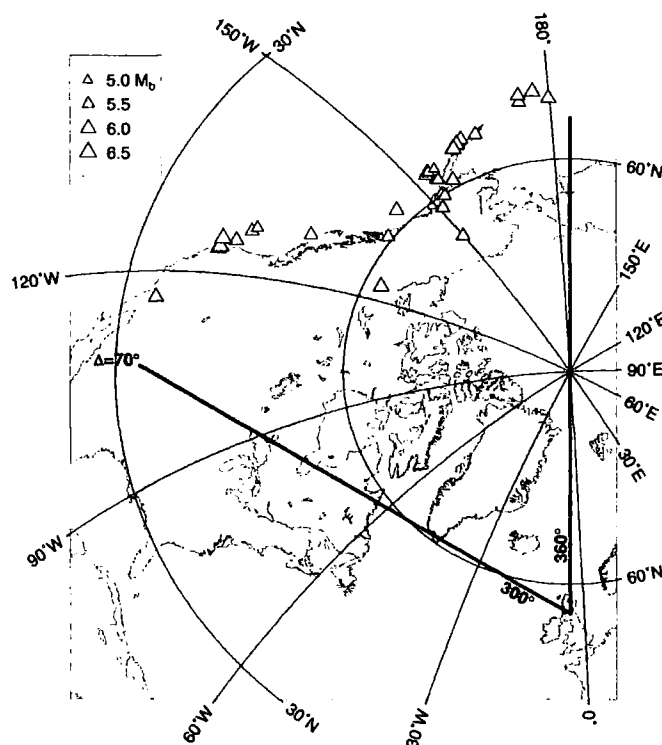
Figure 2.3 Map showing events used in this study, recorded at Scottish seismic stations between 1984 and 1994. Lines shown bound the array-to-event azimuth range 300°-360°. Typical epicentral distance is 70°.

Table 2.2 Events recorded in Scotland (data from ISC Bulletin)

Lat	Lon	d/km	Date	Origin	Mb	Δ (°)	Region
66.22°N	149.98°W	12	1985/03/09	14:08:04	5.8	55.4	ALASKA
43.50°N	127.62°W	10	1985/03/13	19:34:57	5.9	70.1	OFF COAST OF OREGON
62.19°N	124.27°W	6	1985/12/23	05:16:03	6.2	53.3	NORTHWEST TERRITORIES, CANADA
51.42°N	174.84°W	5	1986/05/07	20:43:28	5.9	72.5	ANDREANOF ISLANDS, ALEUTIAN IS.
56.39°N	152.86°W	17	1986/06/19	09:09:10	5.9	65.1	KODIAK ISLAND REGION
56.19°N	153.40°W	31	1986/09/12	23:57:15	6.0	65.3	KODIAK ISLAND REGION
61.45°N	150.85°W	60	1987/04/18	02:01:37	5.7	59.9	SOUTHERN ALASKA
51.26°N	179.88°W	26	1987/05/06	04:06:15	6.1	72.9	ANDREANOF ISLANDS, ALEUTIAN IS.
54.20°N	162.66°W	33	1987/06/21	05:46:10	6.0	68.6	ALASKA PENINSULA
56.19°N	153.69°W	33	1987/07/24	05:25:11	5.5	65.4	KODIAK ISLAND REGION
57.74°N	142.94°W	10	1988/03/06	23:14:36	6.1	61.8	GULF OF ALASKA
54.29°N	165.58°W	104	1989/05/19	02:21:56	5.9	68.9	FOX ISLANDS, ALEUTIAN ISLANDS
57.80°N	154.29°W	43	1989/06/16	10:51:17	5.6	64.0	KODIAK ISLAND REGION
58.85°N	156.83°W	210	1990/05/01	16:12:21	6.0	63.3	ALASKA PENINSULA
59.34°N	136.67°W	10	1990/07/11	15:14:03	5.7	59.0	SOUTHEASTERN ALASKA
54.59°N	161.59°W	28	1991/05/30	13:17:43	6.2	68.1	ALASKA PENINSULA
42.19°N	125.65°W	11	1991/07/13	02:50:14	6.1	70.5	OFF COAST OF OREGON
50.65°N	130.06°W	10	1992/04/06	13:54:40	5.9	64.7	VANCOUVER ISLAND REGION
40.36°N	124.05°W	15	1992/04/25	18:06:04	6.2	71.5	NEAR COAST OF NORTHERN CALIFORNIA
40.51°N	124.25°W	20	1992/04/26	07:41:41	5.8	71.4	NEAR COAST OF NORTHERN CALIFORNIA
40.47°N	124.36°W	22	1992/04/26	11:18:26	6.4	71.5	NEAR COAST OF NORTHERN CALIFORNIA
34.25°N	116.48°W	1	1992/06/28	11:57:35	6.1	73.5	SOUTHERN CALIFORNIA
50.46°N	174.93°W	10	1992/08/19	00:57:40	6.0	73.5	ANDREANOF ISLANDS, ALEUTIAN IS.
43.94°N	128.33°W	20	1992/08/21	01:02:18	5.5	69.9	OFF COAST OF OREGON
59.66°N	152.97°W	108	1993/03/19	12:20:50	5.1	62.0	SOUTHERN ALASKA
56.26°N	155.01°W	25	1993/04/16	04:09:19	5.2	65.5	ALASKA PENINSULA
55.00°N	160.39°W	32	1993/05/13	11:59:47	6.3	67.6	ALASKA PENINSULA
55.01°N	160.56°W	30	1993/05/25	23:16:42	6.2	67.6	ALASKA PENINSULA
50.18°N	177.45°W	3	1993/11/11	00:28:31	6.2	73.9	ANDREANOF ISLANDS, ALEUTIAN IS.
60.17°N	153.11°W	124	1993/11/20	19:24:51	5.6	61.5	SOUTHERN ALASKA
40.44°N	125.69°W	10	1994/09/01	15:15:53	6.5	72.0	OFF COAST OF NORTHERN CALIFORNIA

Table 2.3 Dataset statistics

	NORSAR	Scotland
No. of events used	34	31
Average no. of picks per event	19.9	6.9
Total no. of picks	678	214

2.3.4   Analysis of arrival times

Arrival times for each event were examined and outliers removed. Where the relative observed arrival time (arrival time – mean arrival time for the event) differed by more than an emprically-selected threshold (0.78 s) from the value predicted by a computer program using the tau-p method of Buland & Chapman (1983) and the IASP91 Earth model (Kennett & Engdahl, 1991), the datum was rejected. Events with fewer than 4 reliable arrival times were also rejected, because this is the minimum number that provides redundancy in a plane-wave fit. Table 3 gives statistics for the assembled data.

Plane waves were fitted by least-squares to the relative arrival times for each event to obtain the horizontal slowness vector *p*. Because different subsets of stations were used for different events, it is possible for near-array structure to introduce noise into these results (Berteussen, 1975). Experiments using different sets of stations indicated that this effect is small (around ±0.75°). In order to reduce it still further, station corrections were applied to the observed times before fitting plane waves. The correction for each station was computed by averaging the misfit between the predicted and observed times over all events.

2.4   RESULTS

2.4.1   NORSAR

Figure 2.4 shows the NORSAR results plotted in slowness space. It is similar to the corresponding part of Figure II-9 of Sheppard (1973). Waves from events due west of NORSAR arrive nearly from the expected great-circle azimuth, whereas waves from the northwest arrive from directions about 7° too far to the northwest.

Figure 2.5 shows the same data, plotted in the form of azimuth anomalies as a function of azimuth. This representation is appropriate because the primary effect of a vertical plume is to change the azimuthal component of the slowness vectors, while leaving the radial component relatively unaffected. Error bars show the approximate accuracy of the measurements, assuming an aperture of 100 km and timing uncertainties of 0.05s. Also shown is the theoretical azimuth anomaly for a plume of velocity contrast of -1.5% and Gaussian diameter 250 km, with a "DC shift" applied to achieve the best fit to the observations.
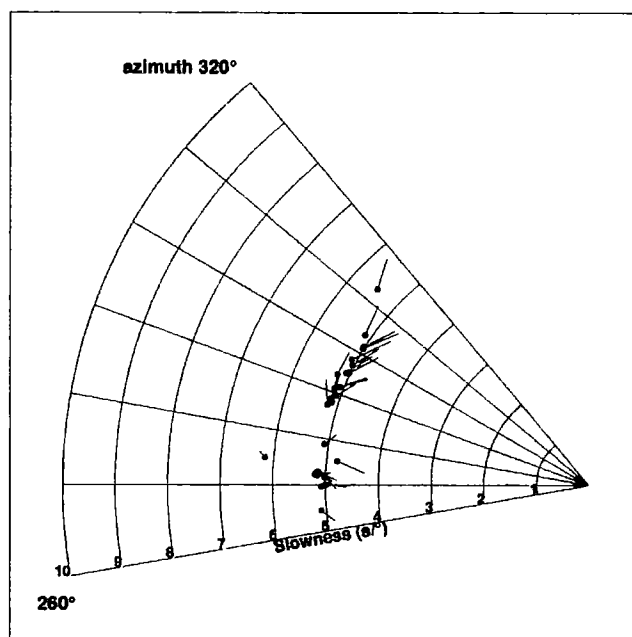
Figure 2.4 Slowness vectors observed at NORSAR for *P* phases from earthquakes in middle America, as measured in this study. Dots are slownesses predicted from ISC hypocentres and the tau-p computer programs of Buland & Chapman (1983), which use the IASP91 Earth model (Kennett & Engdahl, 1991). Lines join these values to the observed slownesses. These results are similar to those of Sheppard (1973).
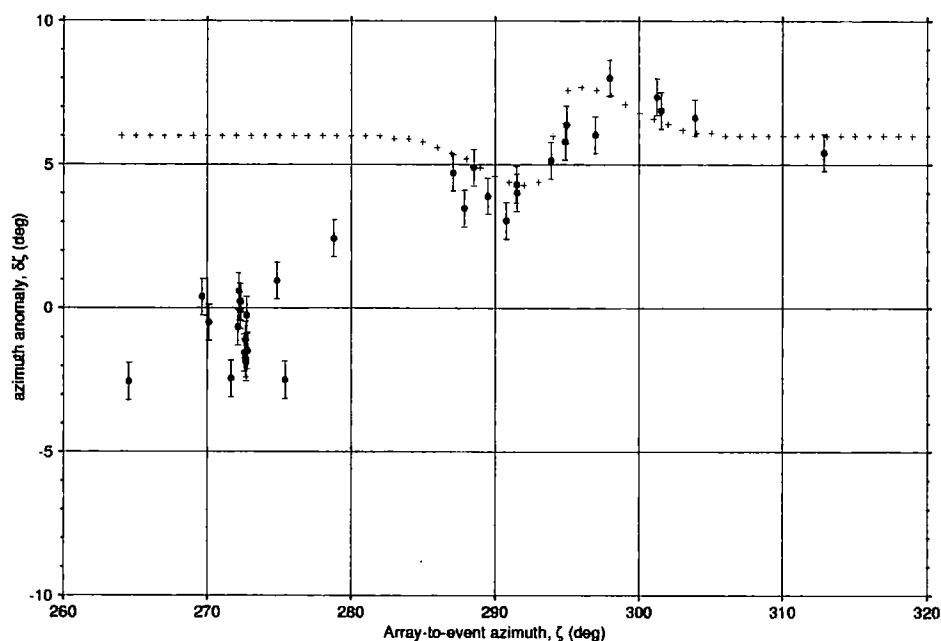
Figure 2.5 *P*-phase azimuth anomalies (dots, with error bars) observed at NORSAR for earthquakes in middle America (same data as shown in Fig. 4). Positive values indicate waves arriving from greater (more northerly) azimuths than the great circle to the epicentre. Crosses indicate anomalies predicted using a synthetic plume model.

The dominant features are the increase in arrival azimuth anomaly with event-to-station azimuth and the rapid change in these azimuth anomalies for event-to-station azimuths between 265° and 300°. The azimuthal range covered by this feature, 30° or more, is much too large to be caused by a plume beneath Iceland. If it is caused by a structure 1,600 km from NORSAR (the approximate distance to Iceland), then the structure is at least 800 km in diameter, which is far greater than expected, e.g. Wolfe *et al.* (1997); Ji & Nataf (1998); Shen *et al.* (1998); Allen *et al.* (1999). It is possible that this feature could be associated with the large free-air gravity anomaly present in the north Atlantic region. The great width of this anomaly could be explained as a deeper source than those associated with the near-surface effects of the Reykjanes Ridge. It is also possible that this strong effect could have some contribution from azimuthally-varying lateral inhomogeneities beneath the array.

A second-order feature of the azimuth anomalies occurs for azimuths between about 287° and 300°, and, as discussed below, has approximately the shape expected for the effect of a plume. Because of observational error and the larger-scale azimuth anomaly discussed above, and because of the non-unique nature of the problem, it is not possible to associate this feature with a plume with certainty, or to infer the properties of any possible plume very accurately. Indeed, similar, rapid variations in slowness vectors could be caused by velocity structures other than a plume and in the data of Sheppard (1973), there were such rapid variations in directions from NORSAR not associated with known hotspots. It is possible, however, to use these observations to place a bound on the strength (wave-speed perturbation) and diameter of a plume, if one exists in the mid-mantle beneath the Iceland region.

It might be appropriate to remove a trend (linear, for example) from the azimuth anomalies of Figure 2.5 before interpreting them. Doing this will reduce the amplitude of the anomaly in the range 287°-300°, and thus the magnitude of the wave-speed perturbation in the hypothetical causative plume, without affecting its position significantly. However, because an upper bound is sought for the wave-speed anomaly in the plume, no such trend is removed here.
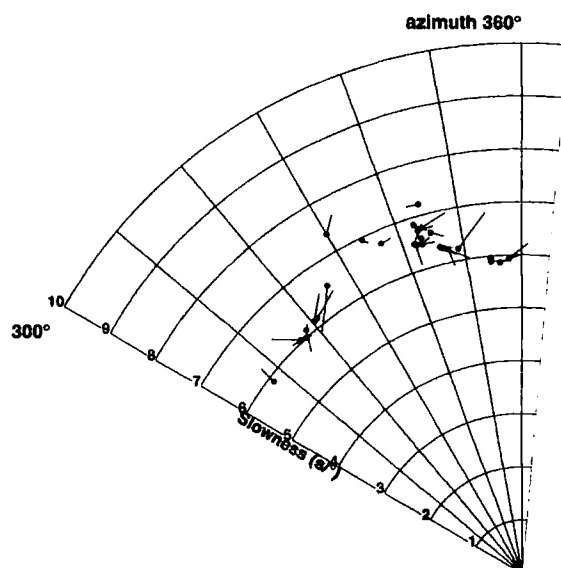
Figure 2.6 Slowness vectors observed in Scotland for *P* **phases from earthquakes in the Vancouver Island, Alaska and the Aleutian Islands regions. Plotting conventions are the same as used in Figure 2.4.**
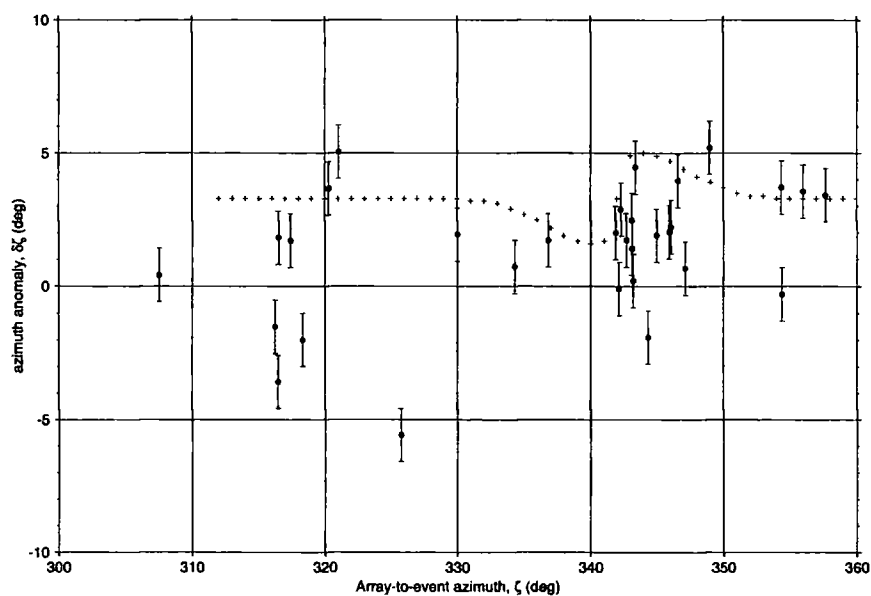
Figure 2.7 *P*-**phase azimuth anomalies observed in Scotland (same data as shown in Figure 2.6) overlain with a theoretical curve for a plume of 1.5% velocity contrast and Gaussian diameter 250 km. Plotting conventions are the same as used in Figure 2.5.**

2.4.2   *Scotland*

Figures 2.6 and 2.7, which are similar to Figures 2.4 and 2.5 respectively, show the observations from Scotland in slowness space and in the form of azimuth anomalies as a function of great-circle azimuth. The scatter in these data is larger

than for the NORSAR data, because of the poorer quality of the arrival time measurements from the Scottish network.

2.5   INTERPRETATION

2.5.1   *Plume model*

It is instructive to compare the observed anomalies with the expected effect of a plume. The compressional-wave speed v_p near a vertical plume could be approximated by the analytical function:

$$v_p = v_0 - \delta v \exp\left(-r^2/a^2\right)$$

(2.1)

where r is distance from the plume axis, v_0 is the wave speed far from the plume, δv is the maximum wave-speed perturbation, and a, the Gaussian radius, is the distance at which the perturbation falls to $\delta v/e$. No vertical variation is included. The horizontal wave-speed gradient near the plume refracts rays horizontally, causing them to arrive from azimuths different from those of the great circles to the epicentres. If the radius of the plume, a, is small compared to the epicentral distance and if $\delta v \ll v_0$ (so that the total deviation of the ray is much less than a radian), then the azimuth anomaly caused by the plume is

$$\delta \zeta \approx \left[1 - \frac{\Delta_P}{\Delta}\right] \frac{\delta v}{v_0} f\left(\frac{(\zeta - \zeta_P)\Delta_P R_E}{a}\right),$$

(2.2)

where Δ is the (angular) epicentral distance, Δ_P is the distance from the array to the plume, ζ is the great-circle azimuth from the array to the epicentre, ζ_P is the azimuth from the array to the centre of the plume, R_E is the radius of the Earth, and f is a function that depends on the form of the wave-speed anomaly. In other words, the azimuth anomaly, as a function of azimuth, has a characteristic shape, with an amplitude proportional to the fractional wave-speed perturbation associated with the plume, and to the fraction of the path length that lies between the epicentre and the plume, and a width proportional to the angle subtended by the plume at the array. From symmetry considerations, f is an odd function. Figure 2.8 shows the shape of f for the Gaussian anomaly of equation 2.1, which was determined by numerical ray-tracing using the bending method (Julian & Gubbins, 1977).
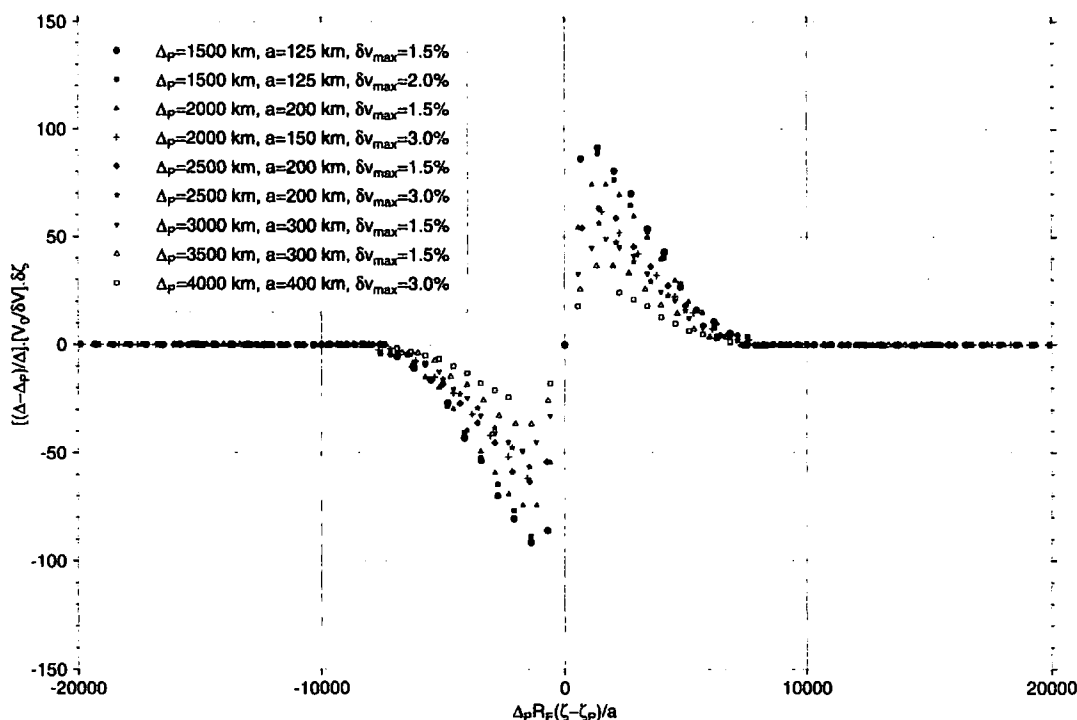
Figure 2.8 Theoretical azimuth anomalies for vertical plumes with Gaussian wave-speed perturbations of equation 2.1, plotted in dimensionless form. The abscissa is the dimensionless difference between the great-circle azimuth to the epicentre and the azimuth to the plume. The ordinate is the dimensionless azimuth anomaly caused by the plume.

2.5.2 Comparison with data

A theoretical azimuth-anomaly curve like that of Figure 2.8 is shown superimposed on the NORSAR data in Figure 2.5. The position of the anomaly has been placed in the Iceland region ($\Delta_P \approx 1,500$ km) and width of the anomaly has been chosen to fit the data. The magnitude of the anomaly has been made as large as possible, while remaining consistent with the data. As discussed above, removing a large-scale trend from the data would result in a weaker anomaly, so the curve shown gives an upper bound on the magnitude of the anomaly. The anomaly is centred at an azimuth of 295°, and has a width of about 20° and an amplitude of about 4°. These values correspond to a relative wave-speed perturbation, $\delta v / v_0$, in the plume of 1.5% and a plume Gaussian diameter, $2a$, of about 250 km. This diameter is consistent with the results of other seismological studies of plumes.

Figure 2.7 shows a similar curve superimposed on the Scottish data. The diameter and magnitude of the theoretical curve are the same as those used for Figure

2.5. The centre of the anomaly is placed at an azimuth of 342°, where there is marginal evidence for a signal of the expected shape and strength. It is clear, however, that the data are too noisy and sparse to enable the expected signal to be either confidently located or ruled out. The geographical context of these results is shown in Figure 2.9.
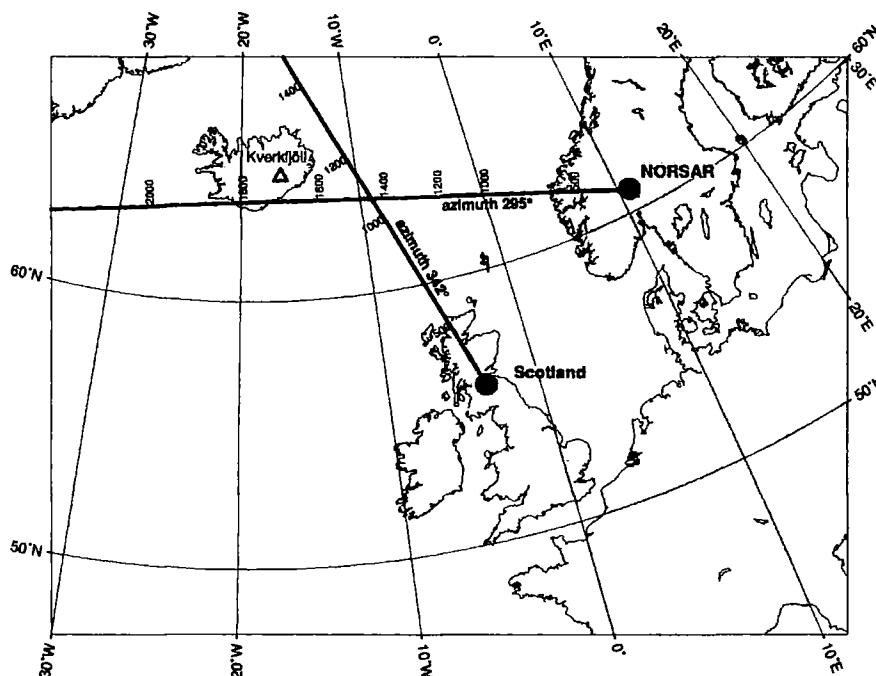
Figure 2.9 Map showing surface projections of array-to-event azimuths of the best estimate of the centre of the anomaly, deduced from modelling of the NORSAR and Scotland data. A possible, but poorly constrained estimate for the centre of the plume is beneath the point at which the lines cross. Depth annotations in km as used in Figure 2.1.

2.6   DISCUSSION AND CONCLUSIONS

For a simple, vertical, cylindrical plume in the mid-mantle beneath Iceland, anomalies in the arrival directions of teleseismic P waves recorded at NORSAR place an upper bound of 250 km on the Gaussian diameter at a depth of ~1,500 km and an upper bound of 1.5% on the wave speed contrast. Data from a network of stations in Scotland are of poor quality and add little to this result. Without further constraints, it is difficult to constrain the location of the surface projection of the possible plume. A possible location may be at approximately 63.5°N, 9°W, ~300 km southeast of the coast of Iceland. A wider plume would produce a broader anomaly at NORSAR, and a stronger plume would produce a greater anomaly amplitude.

It must be emphasised that the fit to the data is not unique. The source of the anomaly could be more distant than the Iceland region. Parameter space was searched by modelling a suite of plumes of various strengths and widths and at various distances, that could cause an anomaly of the size observed at NORSAR. Bodies with realistic velocity contrasts of up to a few percent would have to be wider and deeper if more distant from NORSAR, reaching a diameter of 600 km at 3,000 km distance (i.e. beneath Greenland) and 800 km at 4,000 km distance (i.e. beneath Newfoundland).

Global tomography has the potential to identify such alternative bodies. Recent global tomography work (Bijwaard *et al.*, 1998; Bijwaard & Spakman, 1999) provides an image of the large-scale velocity structure beneath Iceland, Greenland and Newfoundland. In the lowermost mantle, velocities beneath Newfoundland are generally high. At mid-mantle depths a plume-like anomaly is resolved beneath the area southeast of Iceland in the depth range 600-1,500 km. This anomaly appears to broaden with depth to the west where it extends beneath Greenland in the depth range 2,000 - 2,500 km. These results strongly suggest that the plume model used here is a simplification, but they also suggest that the approach in modelling a low wave-speed body in the mid-mantle beneath the Iceland region is reasonable. A tentative location for this plume, southeast of Iceland at mid-mantle depths, is consistent with those global tomography results, which further suggest that, if all or part of the anomaly found in the NORSAR data is caused by a low-velocity body further away than Iceland, beneath the Greenland region, then such a body is continuous with the Iceland plume.

2.7 SUMMARY

- Azimuth anomalies of teleseismic P waves arriving at the NORSAR array in Norway show features which can be modelled by a plume at a depth of 1,500 km, southeast of Iceland.

- If the anomaly is due to a vertical, cylindrical plume, upper limits of 125 km for the Gaussian radius and 1.5% for the velocity reduction can be placed by the data. The solution is not unique and bodies at other distances and with other strengths would also fit the data.

- ISC bulletin data from a seismic network in Scotland are of too poor quality to enable confident identification of a similar anomaly, if one exists, or triangulation on the causative body.

Chapter 3

The Iceland Hotspot Project: Data Acquisition

3. THE ICELAND HOTSPOT PROJECT: DATA ACQUISITION

3.1 TELESEISMIC TOMOGRAPHY EXPERIMENT GEOMETRY

Teleseismic tomography enables a three-dimensional image of the subsurface to be made using relative delay times of teleseismic waves recorded at instruments placed vertically above the volume of interest. In order to sample the volume of interest sufficiently, rays from a broad range of directions and slownesses are required, as is a dense network of stations. Regular station spacing is desirable for all methods of teleseismic tomography, as it improves the homogeneity of ray sampling (Evans & Achauer, 1993). In this case, stations from two complementary seismic networks were used: a permanent network operated by the Icelandic Meteorological Office (Veðurstofa Íslands), and the temporary Hotspot network, deployed as part of the Iceland Hotspot Project. An average station spacing of approximately 50-75 km was achieved, which provides the best station coverage to date for an experiment of this type in Iceland.

3.1.1 SIL network

3.1.1.1 History & Layout

The South Iceland Lowlands (SIL) project was initiated in 1988 to provide facilities for earthquake prediction research in the South Iceland Seismic Zone (SISZ). The SIL seismic network has been collecting data since 1990, and a nearly complete record exists of all earthquakes in the Iceland region down to magnitude 0 (Stefánsson *et al.*, 1993).

The current SIL network now extends beyond the original SISZ area in the south-west of Iceland, and was recently extended by the addition of a group of five stations (GRA, GRI, GRS, GIL, REN) in the north (Figure 3.1). Broadband sensors for these stations were provided by the University of Cambridge, using funding from the Natural Environment Research Council (NERC). Even with these additional stations, the SIL stations cover only a small part of Iceland. Details of those stations used in the tomography experiment are given in Appendix 1.

3.1.1.2 Instrumentation

The present SIL network has increased in size considerably since the original
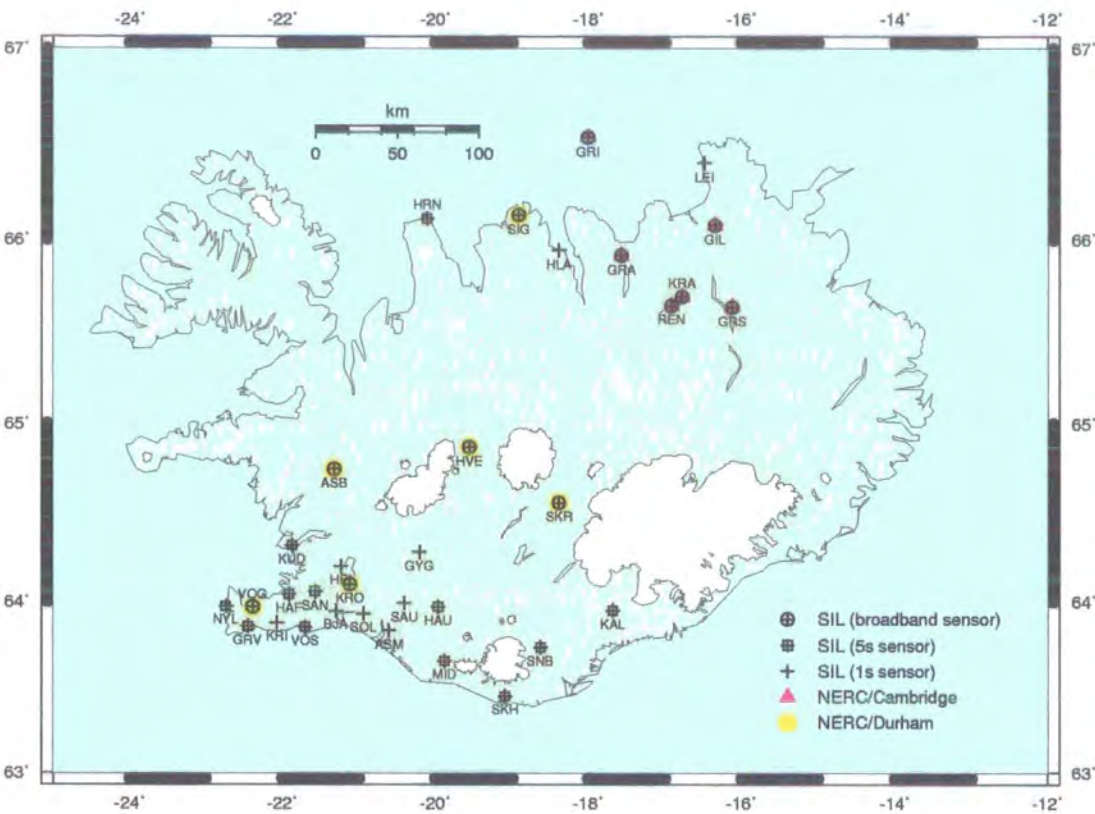
Figure 3.1 The SIL network.
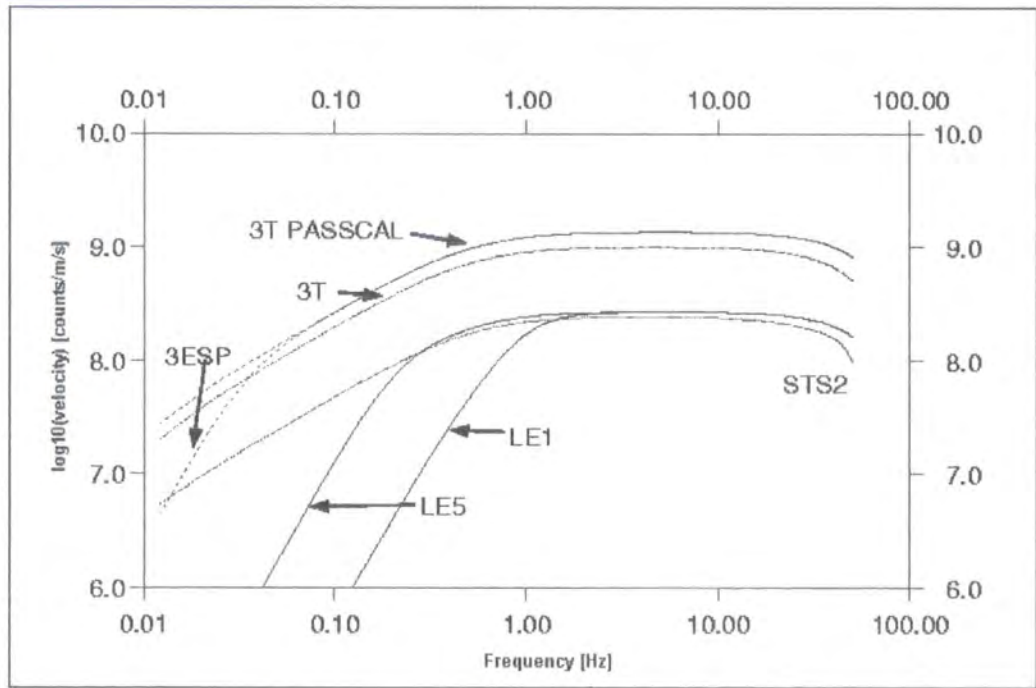
Figure 3.2 Frequency response of SIL sensors (Rögnvaldsson, 1997). 3T, 3T PASSCAL and 3ESP are Guralp instruments, LE1 and LE5 are Lennartz 1 Hz and 5 Hz instruments, STS2 is Streckeisein STS-2.

8 stations, which were equipped with short-period seismometers. The network now consists of a mixture of sensor types. Short-period sensors at six SIL stations (ASB, HVE, KRO, SIG, SKR & VOG) were temporarily replaced by broadband sensors as part of the Hotspot project. The frequency response curves for instruments of the SIL network are shown in Figure 3.2.

For this study, only data recorded at the SIL broadband stations were used, since sensors at these stations are mostly of the same type as those used by the Hotspot network, namely Guralp CMG-3T and CMG-3ESP. One station (ASB) has a Streckeisen STS-2 sensor, which has a response curve of similar shape over a common range of frequencies (0.03-30 Hz). The resulting network of over 40 broadband stations provided excellent coverage for tomography purposes.

All sensors are 3-component. Each station is equipped with an acquisition system consisting of a 16-bit gain-ranging digitiser, a Global Positioning System (GPS) synchronised clock, and a 32-bit UNIX computer connected by X25 telephone link to Veðurstofa headquarters in Reykjavík. Data are initially sampled at 400 samples/s and then filtered and resampled at 100 or 20 samples/s as required. A typical SIL seismic station is shown in Figure 3.3.
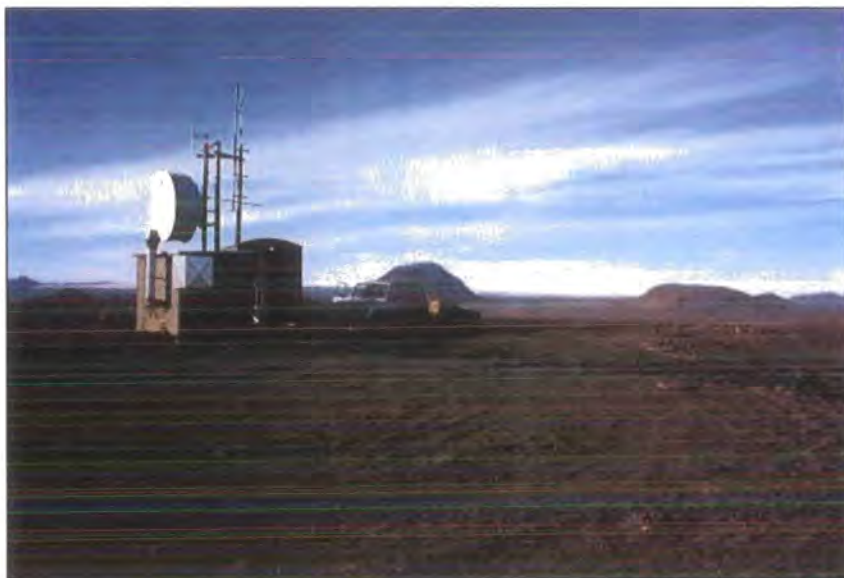
Figure 3.3 SIL seismic station SKR, showing the station hut with telemetry equipment. Stations are run by the Icelandic Meteorological Office and relay meteorological as well as seismic data to the headquarters in Reykjavík.

The SIL network was designed primarily for detecting and recording local earthquakes. This has determined the layout of the network, but the established event-detection system, the recent installation of broadband instruments at several stations, as well as the existing subset of instruments of 5 s period, make the network a useful source of regional and teleseismic data.

As part of the Hotspot project, a system for saving teleseisms was developed and implemented. Notification of a teleseismic event is received from the U.S. National Earthquake Information Center (NEIC) by e-mail, the relevant portions of data are extracted from a ring buffer (Stefánsson *et al.*, 1993), resampled to 20 sps and stored online as "AH"-format seismogram files. Each file contains the seismograms for the vertical (Z), north-south (N) and east-west (E) components, and is given a filename which includes the station name and the data time. An extensive dataset now exists and is freely available on the internet from Veðurstofa Íslands at http://www.vedur.is/ .

3.1.1.3 Timing

The internal clocks of the recording system computers are kept synchronous by the GPS receiver attached to each system. Clock corrections are applied automatically by the SIL system, so seismogram timings are kept accurate to within 0.5 ms.

3.1.1.4 Data collection

Each station records data continuously, and performs on-line phase detection based on simple signal-to-noise ratio characteristics. The detected signal is then scanned to obtain the exact onset time of the detected phases, and a "phase log" entry is written, containing information such as maximum amplitude, azimuth and spectral parameters. Phase logs are relayed by telephone line to Veðurstofa Íslands headquarters in Reykjavík, where event association is made automatically, using the multi-station information. Relevant sections of waveform data are then requested from each station.

Since the main function of the SIL network is to record local earthquake data, which is of higher dominant frequency than teleseismic data, the main data stream is

recorded at 100 sps. For teleseismic work, however, where dominant frequencies are lower, 20 sps is adequate, and conserves storage space.

Earthquakes recorded on the SIL network are listed in a catalogue file `televents.lib` (Appendix 2), stored in the directory `/eq/YYYY/teleseism/` (YYYY=year) on the computer network at Veðurstofa Íslands. This file gives the directory structure in which the relevant seismogram files can be found. Files are grouped by event, and for this study, only the 20 sps data for broadband stations were extracted.

3.1.2   The Hotspot network

3.1.2.1 Introduction

The Hotspot network was deployed as part of this study during the summer of 1996, and is, to date, the largest temporary broadband seismic network that has ever been operated in Iceland (Figure 3.4). The whole project was funded by the UK Natural Environment Research Council (NERC) and the US National Science Foundation (NSF). The network was designed to complement the permanent SIL network, by filling in gaps in the existing station coverage. Large areas of the country in the north-west, east, and the interior had little or no coverage by SIL stations. In some cases, notably the Snaefelsnes peninsula, the installation of the Hotspot network was the first time that earthquake recording equipment had been deployed for any length of time.

A station worthy of particular mention is that at Grímsfjall (station HOT23), on a nunatak on the Vatnajökull glacier. This station provided much-needed data to fill in the large gap in station coverage made by Europe's largest glacier. The logistics of siting and maintaining stations in the hostile environment of the interior of Iceland have meant that, in the past, sites such as this have not been possible. However, the station proved to be very useful and, within a month of being installed, recorded the seismic activity associated with the September 1996 eruption of the Gjalp subglacial volcano. Other stations sited in the uninhabited interior of Iceland (stations HOT24, 25, 26, 27 and 28) provided unprecedented data coverage in these areas, and were, on the whole, remarkably reliable considering the harsh environmental conditions.

A team of workers from the University of Durham (UK), Princeton University, NJ (USA), the US Geological Survey, Veðurstofa Íslands and technical staff from the IRIS-PASSCAL (Program for Array Seismic Studies of the Continental Lithosphere) group at the Lamont-Doherty Earth Observatory, New York, USA, took part in a 4-month fieldwork project in the summer of 1996 to install the stations in Iceland (Table 3.1). The stations recorded for two years, so careful planning was needed to ensure that the equipment would survive the notorious Icelandic climate and require the minimum of service visits, which, in some cases, meant driving for several days across glaciers and snow in specialist vehicles with professional guides.

Table 3.1 Personnel involved with network deployment fieldwork in 1996.

Name	Affiliation
Matt Pritchard	University of Durham
Gillian Foulger	University of Durham
Bruce Julian	U.S. Geological Survey
Guust Nolet	Princeton University
W. Jason Morgan	Princeton University
Richard Allen	Princeton University
Kristín Vogfjörð	Princeton University
Pálmi Erlendsson	Veðurstofa Íslands
Sturla Ragnarsson	Veðurstofa Íslands
Paul Friberg	IRIS-PASSCAL
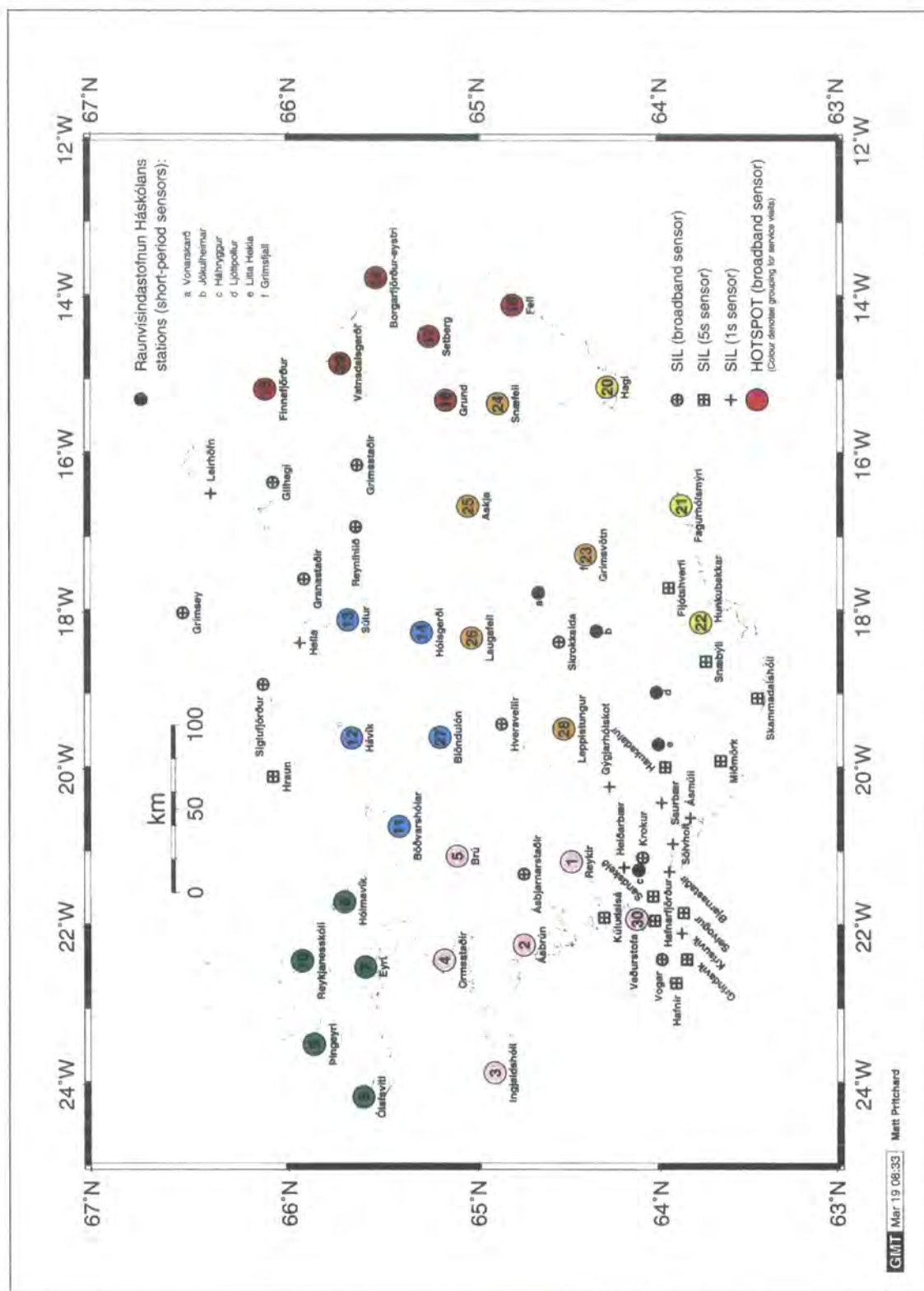
Figure 3.4 Map of seismic stations in Iceland. Coloured symbols show temporary Hotspot stations deployed during this experiment. Different colours denote logistic groups (see text for details). Black symbols represent SIL and University of Iceland (Raunvísindastofnun Háskólans) stations (stations a-f).

3.1.2.2 Instrumentation

Field equipment was supplied by the IRIS-PASSCAL consortium, based at the time at Lamont-Doherty Earth Observatory, New York. REFTEK Data Analysis Systems (DASs) were used to record to 0.66 - 1.2 Gbyte disks. GPS clocks provided timing.

All sensors were Guralp, 3-component, broadband digital seismometers, of three types: CMG-3T, CMG-40T and CMG-3ESP. The three types of sensors differ slightly in their response to low frequencies. CMG-3T sensors have a fairly flat (i.e. constant) response for periods of up to 100 s, while CMG-40T and CMG-3ESP sensors are flat to 50 s. The instruments also differ slightly in their susceptibility to higher frequency noise. Because of this, the CMG-3T sensors were deployed, where possible, at stations where there was particularly good acoustic coupling, or at least low noise levels, such as station HOT13 (Súlur), where the equipment was deployed in the WWSSN (World-Wide Standardised Seismic Network) vault. The CMG-40T sensors are slightly more susceptible to noise than the CMG-3ESP sensors, but are more compact instruments, and were thus best suited to sites where a pit had to be dug to bedrock, or where there was little space for the sensor.

3.1.2.3 Network layout and installation

Initially, the task was to choose locations on the basis of optimal station coverage, maintaining an even station spacing and avoiding large gaps in the coverage. Having identified a potential site area, we then assessed it in terms of several logistical factors, namely:

- Availability of mains electricity

- Accessibility (winter and summer)

- Geology (availability of surface bedrock)

- Cultural and natural noise sources (e.g., proximity to roads, generators, rivers etc.)

Harsh weather conditions in Iceland, particularly in winter, mean a hostile environment for electronic equipment and make outdoor fieldwork difficult.

Consequently, as many stations as possible were installed in farm out-buildings or in the cellars of buildings, where there was access to continuous mains power. 60-Amp hr lead-acid battery packs were provided as backup in case of power failure. In many cases, sites were available which enabled sensors to be placed either directly on bedrock, or on concrete floors underlain by bedrock.

In order to maintain coverage in the central part of Iceland, however, several stations had to be sited in the uninhabited, interior wilderness where access is considerably more difficult and where mains electricity is not available. In many areas, the only buildings are wooden mountain huts. For these stations, power was provided by sets of 30-Watt solar panels, connected to large banks of eight 150-amp hr lead-acid batteries. Details of the 30 Hotspot stations and their locations are given in Appendix 3.

Once the necessary equipment had been shipped to Iceland, it was first "huddle tested" to ensure correct operation. This involved setting up and running several acquisition systems side-by-side indoors. Faulty equipment could be easily identified by comparing the recordings. Correctly functioning equipment was distributed in lorry consignments to locations around the island, ready to be collected by the field parties, who drove out in smaller service vehicles, and taken to individual stations.

An installation timetable was drawn up by G. R. Foulger, which allowed approximately 2 days per station, and time for driving between Reykjavík and the station groups. Icelandic roads are mostly gravel outside of the Reykjavik area, and driving conditions can be hazardous, even in good weather (Figure 3.5). The large distances and poor road conditions involved meant that journeys were often very lengthy.

After installing the stations, each field party revisited the site after around 7-10 days to check that equipment was operating correctly and to obtain sample data which could be quality-controlled. In some cases, problems such as excessive local noise were identified on examination of this first set of data, and remedial steps taken. For example, the sensor at station HOT05 (Brú) was moved to a quieter location once it was discovered that a nearby generator was swamping the data with noise. A list of the equipment used at a typical station is given in Appendix 4.

Figure 3.5 Fording a river en route to station HOT28 (Leppistungur). The road is marked out by yellow stakes leading up the hill. These mark the location of the road when it is snow-covered. This type of obstacle is typical for roads in the uninhabited interior of Iceland.

3.1.2.4 Station setup instructions

In order to ensure that stations were set up in a standard and consistent manner, they were set up according to the instruction sheet given in Appendix 5. A typical station was set up as follows:

1) Pit preparation. Many stations had good facilities for housing the sensor indoors on a concrete floor set on bedrock. However, if the sensor had to be installed outdoors, it was important to ensure that the pit was adequately drained. If possible, the pit was dug on a slope, ideally with a depth of about 0.75 m to bedrock. A cement pad was laid in the bottom of the pit, a ceramic tile embedded level in it and marked with the direction of local magnetic north. A drainpipe was installed, draining downhill to the surface (Figure 3.6). Two large inverted buckets were used as the vault walls. A hole was cut in the rims of these to allow the seismometer cable to run out. A layer of loft insulation, placed between the two buckets, served to slow temperature changes which affect the response of the instruments.

2) Power. The power supply was first connected to the "battery" terminal strip on the power board. Next, the battery was connected to the same terminal on the power board, in parallel with the power supply. The DAS power cable (2 m, grey) was then connected to the "station" strip on the power board. The 5 m double grey cable was

then attached to the "station" strip on the power board, and the plug connected to the mains.

3) Seismometer. The seismometer was positioned on the tile or floor with the brass pointer oriented towards magnetic north (Figure 3.6). The seismometer feet were then unlocked by turning the brass screws anticlockwise. The seismometer could then be levelled by adjusting the three feet and checking the levelling bubble on the top surface of the instrument. Once levelled, the feet were locked in position and the north orientation checked once more.

The single cable was then connected to the seismometer, and fastened to the handle with a cable tie so that a sharp pull would not move the seismometer. The levels were then re-checked, and the protective covers (screws and rubber "O-rings") were removed from the locking control holes and the masses unlocked using a special six-sided tool. The covers were then replaced. At this point, the other end of the single cable was plugged into the "sensor" port of the breakout box.

Figure 3.6 (Left) Seismometer pit after initial preparation, showing base of concrete poured onto bedrock, surrounded by boulders and with a ceramic tile mounted as a flat base for the sensor. The black drainage pipe prevents the pit from flooding. (Right) Guralp CMG-40T seismometer positioned on ceramic tile in base of pit.

4) Data Acquisition System (DAS) The grey power cable was connected from either power port on the DAS to the disk, and the black SCSI cable was used to make the data connection to either SCSI port. At this point, the GPS antenna was erected in a place with a clear view of the sky (Figure 3.7). The antenna was mounted on a metal bracket designed to fit on the side of a roof as shown. The fitting had to be sturdy enough to withstand high winds, and the cable had to be fixed securely in place.

Figure 3.7 Installing the GPS antenna on the roof of a building at station HOT19 (Fell).

The antenna was connected to the "COMM" port on the DAS using the grey GPS cable. The single grey cable that was attached to the power board in step 2c (Appendix 5) was then connected to a free power port on the DAS. The black data connection cable was connected into the "CH4-6" port on the DAS.

5) Parameter loading/setup Parameters from the table given in Appendix 6 were loaded into the DAS using the Epson Hand Terminal (EHT) or, if preloaded, checked

against values in the table to make sure that all stations were set up correctly and consistently.

Figure 3.8 Epson EHT being used to load parameters into the DAS (upper left grey unit) at station HOT08 (Ólafsvíti). Also visible is the connected field disk and breakout box (next to DAS), battery and spare field disk on floor. The Seismometer is beneath the insulation on the right.

A "stomp test" was carried, which is a coarse test to check that each of the 3 sensor components is recording. A member of the field party provided a small "seismic" source by jumping, and the resulting signal output is examined on the screen of the EHT. Once this had been performed, a station setup report was completed..

3.1.2.5 Recording parameters for seismic data

The REFTEK instruments were set up to record three data streams, each consisting of three channels: vertical (4), north-south (5) and east-west (6). The north-south sensor was orientated to local magnetic north. This was done because the magnetic declination varies significantly over Iceland, and making the correction at

the data processing stage is less prone to error than attempting to do it in the field. The declination for each station is given in Appendix 3.

Each data stream had an associated set of parameters which were loaded into the REFTEK DAS from the EHT at the time of installation. Parameters for the three data streams are given in Appendix 6.

Data stream 3, which recorded at 100 sps, was an event-triggered data stream designed for the detection and recording of local events. Data stream 2 recorded continuously at 1 sps and was intended to provide a means of scanning the dataset by days at a time to search for events with good-quality surface waves, work which is ongoing at Princeton University. Data stream 1 recorded continuously at 20 sps, and is the data stream from which teleseismic events for this study were later extracted.

3.1.2.6 Timing

Accurate timing is essential to any seismograph system, particularly when the data of interest consist of relative measurements of seismic wave arrival times, as is the case with teleseismic delay-time tomography. The internal clocks of the REFTEK DASs are relatively primitive and drift strongly. They need to be corrected at regular intervals to ensure a sufficiently accurate, synchronised time base for the seismic network. GPS provides a suitable solution.

Each DAS had a GPS antenna which was mounted where it was well exposed to the sky. The distribution of the ~30 GPS satellites around the Earth ensures that at least 4 satellites are above the horizon at any point on the Earth's surface at any time. The primary function of the system is to provide navigation for military vehicles and personnel. In addition to positional data, each satellite broadcasts the time, which could be received by an antenna connected to the DAS. The primary and secondary functions of the GPS system are thus reversed when used for seismology in this way, since a useful by-product of using the GPS system is that accurate station locations are obtained. The DASs were set up to attempt to obtain a time estimate from the GPS system every hour ("locking on"). If this was achieved, the DAS clock was re-synchronised to GPS time by skewing the clock rate (in the case where the correction was small) or applying a time "jerk". In most cases, lock was achieved, but there were times when a considerable time passed during which no lock could be obtained.

This can occur, for example, when the antenna becomes obscured by snow, and in this case the gradual drift of the internal clock was unchecked until the next "lock".

All system operations of the DAS are automatically kept in a log file, so that the behaviour of the recording system can be examined once the disk has been retrieved from the field. The log file lists the time of every clock lock, along with the value of the jerks applied to the REFTEK internal clock. In this way, corrections can be made to time measurements from seismograms, in the period covered by the logfile, by interpolating between the two clock locks before and after the pick time. Typical clock corrections applied were of the order of 500-1000 µsec, though occasionally, problems with GPS clocks meant that time clocks received no synchronising lock from the satellites for long periods. Diagrams showing performance of station GPS clocks are given in Appendix 7.

3.1.2.7 Maintenance procedure

Stations were divided into logistic groups in particular areas of Iceland that could be visited in one 3- or 4-day trip from the project headquarters at Veðurstofa Íslands. The coloured symbols in Figure 3.4 denote the following groups:

- SW Iceland   Pink

- Western Fjords   Green

- North Iceland   Cyan

- SE Iceland   Yellow

- E Iceland   Red

- Interior (Highlands)   Orange

Stations were visited at regular intervals during the two-year deployment by staff from Veðurstofa Íslands (funded by NERC grant GST/02/1238) or by other Hotspot project members on fieldwork in Iceland. The frequency with which each station was visited depended on the type of station and its accessibility. This also governed the size of disk deployed at a particular station. Larger disks (1,020 or 1,200 Mb) were left at stations which were difficult and/or expensive to reach, while

smaller disks (540 Mb) were used at stations that could be visited easily and frequently. A station typically recorded around 10 Mb per day, so a 540 Mb disk would typically last ~50 days, while a 1,200 Mb disk would last ~120 days. The timetable for servicing the stations took account of the sizes of disks at particular stations. The stations in the uninhabited interior were generally visited at least once every three months with a generator, because the batteries often needed charging. Lack of power was the most serious cause of data loss at those stations.

Service visits involved swapping the field disk with an empty one, as well as carrying out a set of tests to check that the recording system was in working order. Any problems that could be fixed on the spot were attended to, and any equipment known or found to be malfunctioning was swapped with spares carried by the service party and returned to Reykjavík for repair and/or return to the equipment supplier.

3.1.2.8 Data extraction

Data on disks brought back from the field were extracted and archived at the project headquarters in Reykjavík. This was done using computer hardware supplied by the IRIS-PASSCAL equipment pool and installed on the local area network at Veðurstofa Íslands. It included two Sun workstations, three, 9 Gbyte disks and four 4-mm DAT drives.

Each batch of field disks was first dumped to DAT tape and converted from the data blocks written by the DAS into miniseed format using the program `ref2mseed`. These files were then written to workstation disk and sample files inspected visually to detect problems. The program `ref2mseed` also generated the DAS log files, which were then written to tape, grouped by day. On a monthly basis, time windows corresponding to events of interest were extracted and stored on-line by means of a set of shell scripts written by B.R. Julian. The list of events of interest was constructed by consulting the global earthquake catalogue produced by the U.S. Geological Survey. Potentially interesting events were defined using the criteria given in Table 3.2, applied to the "ehdr" list of the National Earthquake Information Center. Data for selected events were then extracted for a time window starting 200 seconds before the predicted arrival time.

Table 3.2 Epicentral distance and magnitude thresholds used as criteria for initial data extraction.

Epicentral distance (°)	Minimum magnitude above which events were extracted
30	5
20	4
10	3

Files for the extracted events were cut and spliced by a program called qmerge, (Doug Neuhauser, U.C. Berkeley, *pers. comm.*). qmerge deals with data gaps, overlaps, clock rates, etc., and the final output is the set of seismogram files for all three components for the appropriate time period. The file is labelled with the station number and channel name, e.g. HOT24.4.m. All the files for an event were then written to DAT tape and distributed to the co-operating research groups (Durham, Princeton, and the U.S.G.S.). The events used in the tomography study are a subset of the saved events and are described in Chapter 4

3.2 SUMMARY

- The network used for the teleseismic tomography study experiment comprised stations from two networks, the permanent SIL network operated by the Icelandic Meteorological Office and a temporary network of 30 stations deployed for two years as part of this study. The final distribution of stations used is shown in Figure 3.9.

- The temporary network returned 86% of the targeted data for the two-year period 1996-1998. It delivered ~200 Gbytes of high-quality broadband data including over 2,400 events with $M \geq 5.0$ and 730 events at distances less than 20° with $M \geq 3.0$. Station performance statistics are shown in Appendix 21.
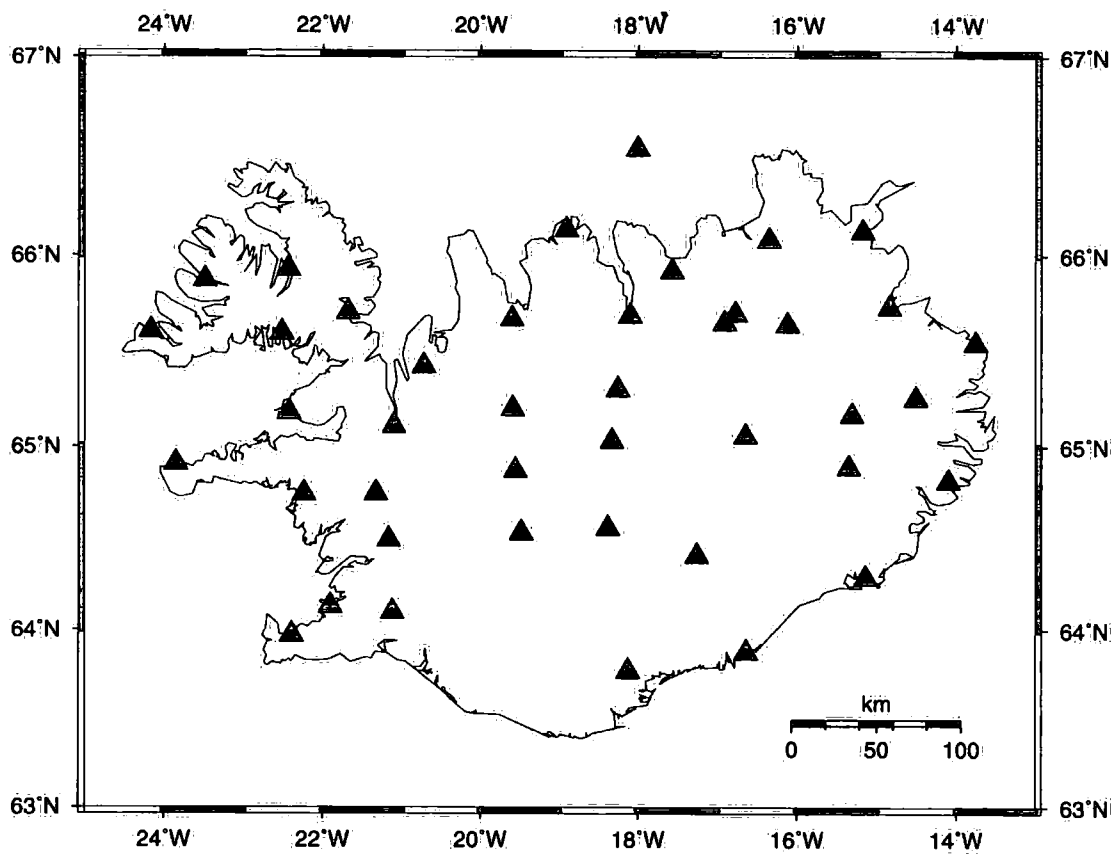
Figure 3.9 Configuration of seismic stations used in tomography study.

Chapter 4

Processing of SIL & Hotspot Teleseismic Data

4. PROCESSING OF SIL & HOTSPOT TELESEISMIC DATA

4.1   DATA PREPARATION

4.1.1   Extraction of data from archive

4.1.1.1 Data from the SIL network.

Data from the SIL network were available on 4 mm DAT tape at Durham, and by internet connection via FTP (File Transfer Protocol) from the computer network at Veðurstofa Íslands.

Seismograms are stored there by event in the directory structure, and the file `televents.lib` (Appendix 2) lists the directory location for each event. Once events of interest had been identified, the corresponding data files were copied to the same directory as the corresponding Hotspot data in Durham.

Only data recorded at 20 sps were used. Sometimes it was not possible to obtain SIL data for a particular event, for one of several reasons. Occasionally, data had simply not been stored. The SIL system only archives data from its ring-buffer if it matches particular criteria of magnitude, epicentral distance and other parameters. For unknown reasons, it was sometimes the case that only 100 sps data were available, covering only the first part of the seismogram immediately following the first P arrival. These data were not used for the sake of consistency, and because it was considered more efficient to devote time to extracting event datasets where complete seismograms were available, enabling both P and S arrival times to be measured.

4.1.1.2 Data from the Hotspot network.

Archived Hotspot seismograms were available via FTP from the IRIS-PASSCAL field computers, which were housed at Veðurstofa Íslands and connected to the internet via that computer network. These data were periodically archived to 4 mm DAT "event tapes" which contained data grouped by event for several weeks at a time, and were sent to Durham by post.

Event tapes contained incomplete data for particular events, as they were invariably created before data from the entire network had been collected from the field for every event. The event data occupied little space compared with the

continuous data, however, and was therefore all kept on disk for most of the two-year monitoring period. Extraction of a particular event from the event tapes was time-consuming as the data were often spread over two or three tapes. In the summer of 1998, the event data were therefore re-written to "mother event tapes" which contained all the data for each event on the same tape, and thus provided a much more convenient archive of all events.

Until the arrival of the mother event tapes (by which time, a large amount of the data for this study had already been extracted and processed), the most efficient way of extracting data associated with events of interest was as follows. A table of contents (`tocfile`) was created for each event tape, which listed all the files on the tape. These `tocfiles` were stored together in a single directory and were read by the script *tocsearch.pl* (Appendix 8) which listed the directory and data files associated with a particular event. The directory name (defined at the time of construction of the data archive) was normally obvious from the list of available directories for that day, but could be found by adding the predicted travel time for the first P arrival to the listed origin time. For example, data for an event at origin time 12:24:26 on day 123 of 1997, with a P travel time of 724 seconds might be stored in directory

```
E1997.123/123630/Mseed/
```

The command

```
tocsearch.pl E1997.123 123630
```

would list all the relevant files on any tape, along with the number of the event tape on which each file was to be found. Individual tape lists could then be created, for a set of events, to drive tape jobs that extracted the required files.

Data were copied to disk in a directory structure similar to that used on Hotspot data tapes, i.e.

```
(user's path)/EYYYY.DDD/HHMMSS/Mseed/
```

4.1.2   File format conversion

It was decided to adopt the widely-used Ad-Hoc (AH) format for processing the data, since there exist many useful tools for manipulating data in this format. The SIL data were already available in AH format, with each file containing all 3 seismogram components (Z, N and E). The picking program used, `dbpick` (Harvey & Quinlan, 1996), requires that each seismogram be contained in a separate file, so the AH program `ahsplit` was used to split the SIL files into three. The vertical, north-south and east-west component files were then identified by the suffixes BHZ, BHN and BHE respectively.

Hotspot data were stored on the archive tapes in miniseed format, with each component in a separate file. The program `ms2ah` (D. Neuhauser, *pers. comm.*) was used to translate these to AH format. This program also added station location information from the file `hotstns.dat` to the AH file headers.

The resulting AH files were then stored, along with the corresponding SIL data, into the directories with the naming convention:

```
(user's path)/EYYYY.DDD/HHMMSS/
```

4.1.3   Database creation

In order to use the picking program `dbpick` (Harvey & Quinlan, 1996), it is first necessary to create a database for each event, using the program `ah2db` (Harvey & Quinlan, 1996), which produces a set of files, each with the prefix `dbname`, where `dbname` is a user-defined name. In this case, I used the SIL event prefix, or some appropriate time label of the form HH:MM:SS, which would distinguish events sharing the same day. The file `dbname.wfdisc` lists the seismogram files and their locations for the event, along with other information such as the start and end time of the trace, sample rate, and component. The files `dbname.site`, `dbname.sitechan` and `dbname.instrument` list the station locations, components used at each station and sensor information, respectively. These files were created in a different directory, one per day, in an area of disk space which was backed up regularly. The convention used for naming these directories was:

```
/usr/local/seismic/hotspot/pritchard/hotspot/db/YYYY/HOT/DDD/
```

The original seismogram files were stored in an un-backed-up area as backup resources were limited and these data could easily be restored in the event of an irretrievable disk crash.

Lists of station locations and channel names were produced from individual database files, (which did not usually include all the stations), and stored in the files HOTSPOT.site and HOTSPOT.sitechan. These files contained information for all stations in the network, including SIL stations.

4.1.4 Event matching

A full list of hypocentre locations was collected during the course of the experiment from the U.S. Geological Survey QED (Quick Epicenter Determination) lists. I made these into yearly origin table database files (named YYYY.origin) using the program qed2origin (Harvey & Quinlan, 1996). For each event database (i.e. collection of files named dbname.*), a symbolic link was made to the YYYY.origin file. This was named dbname.origin, and stored with the other dbname.* files, enabling hypocentre coordinates and origin time to be incorporated into the database of information for each event. Individual events are listed in the YYYY.origin file with a unique origin identifier (orid), of the form YYDDDEEE, for example, 97123002, which is the second event listed for day number 123 of year 1997. Each event used in this study was allocated such an orid, which was then used to refer to the event and obtain hypocentre information at any stage. In a handful of cases, events were included whose details were not included in the QED listing. Additional records were added manually for these events, using hypocentre information from the U.S.G.S. Preliminary Determination of Epicenters (PDE) list.

4.1.5 Rotation of seismograms

The hypocentre information in the files YYYY.origin was used to rotate the 3 recorded components, namely the vertical [Z or 4], north-south [N or 5], and east-west [E or 6], into the source-related components vertical [Z or 4], radial [R] and transverse [T]. This was performed using the program ahrotate (B.R. Julian, *pers. comm.*).

First, corrections had to be applied for the fact that HOTSPOT sensors were aligned to *local* magnetic north. The script dbrot.pl (Appendix 9), for each station

in turn (listed in the file dbname.wfdisc), constructed the ahrotate command lines with the appropriate options, using hypocentre information appropriate to each orid, and sensor orientations in the file HOTSPOT.sitechan. Rotated seismograms were thus produced using the correct sensor orientations. The radial and transverse component files were stored in the same directory as the other seismogram files, and the program ah2db was run again to add their details to the corresponding event database.

4.2   DELAY TIME MEASUREMENT

4.2.1   Filtering

Teleseisms recorded at stations in Iceland are polluted by high levels of oceanic microseismic noise. This noise is most prominent at frequencies of around 0.3 Hz. Other sources of noise, such as wind, also degrade the signal. High attenuation beneath Iceland reduces the signal-to-noise ratio further, with the effect that only relatively large or deep teleseisms produce clear seismograms in Iceland. However, during the 2-year deployment of the HOTSPOT seismic network, sufficient earthquakes of suitable signal quality occurred worldwide to enable a large dataset of arrival times to be assembled.

In previous work, it has been noted that teleseismic arrivals in Iceland display little energy above 1 Hz for P waves and 0.2 Hz for S waves (Wolfe *et al.*, 1997). Here, it was found that first P arrivals are often clear when filtered in the frequency range 0.5 - 2.0 Hz, while later arrivals tend to be swamped by noise in this frequency range. In many cases, even the first arrival is obscured at this relatively high frequency band, only to be clear at the much lower frequency range of (typically) 0.05-0.1 Hz. Since resolution is limited to signal wavelength, it is necessary to pick at frequencies as high as possible. Typical P waves propagating through the mantle beneath Iceland would have a velocity of ~8.5 km/sec. The wavelength of such waves would be ~8.5 km at around ~1 Hz, ~17 km at around ~0.5 Hz, but ~113 km at ~0.075 Hz. Thus, picking at such low frequencies would considerably reduce the structural detail obtainable.

S arrivals could rarely be seen at frequencies as high as 0.1-1.0 Hz, so the majority of S picks were made in the lower frequency band of around 0.05-0.1 Hz.

One disadvantage of manually picking arrivals in frequency ranges as low as this is that the arrivals are more emergent and thus picking errors are larger. Picks made in these frequency ranges therefore have a larger uncertainty than those at higher frequencies. This effect, rather than poor correlation between individual waveforms, was the dominant factor in determining overall pick uncertainty, so a set of picks for a particular phase, picked at a particular frequency was assigned the same uncertainty value.

Picks were made using the program *dbpick*. Filtering was applied on-screen, at the time of picking, using a set of user-defined filters available within *dbpick*. These were listed in a file .dbpickrc, which is stored in the same directory as the database files, or in the user's home directory. From this set, at least one filter could usually be found to reveal clear waveforms. If necessary, further filters could be defined by using the seismogram viewer *pq1*, which allows filters to be constructed interactively, with visual reference to the frequency spectrum, and the parameters transferred to .dbpickrc for use with *dbpick*.

4.2.2   Phase identification

dbpick enables phases to be identified on-screen. Seismograms for the event are loaded, and the user can choose to display traces for a particular channel, e.g. vertical channel 4 (Figure 4.1). The user selects an event by reference to its orid number. *dbpick* then retrieves the relevant hypocentre coordinates from the dbname.origin file, and the station coordinates from the dbname.site file (created by *ah2db*). Traces can then be sorted according to epicentral distance, which is helpful in identifying phases as they propagate across the network of stations (Figure 4.2).

Arrival times for common phases can be estimated within *dbpick* using a specified standard Earth model. In this case, the IASP91 model (Kennett & Engdahl, 1991) was used (Appendix 10) with the "tau-p" travel time algorithms (Buland & Chapman, 1983). Traces can then be time-shifted to align the predicted first P arrival, which is helpful for matching waveform shape between stations. Markers for other phases can also be displayed (Figure 4.3).
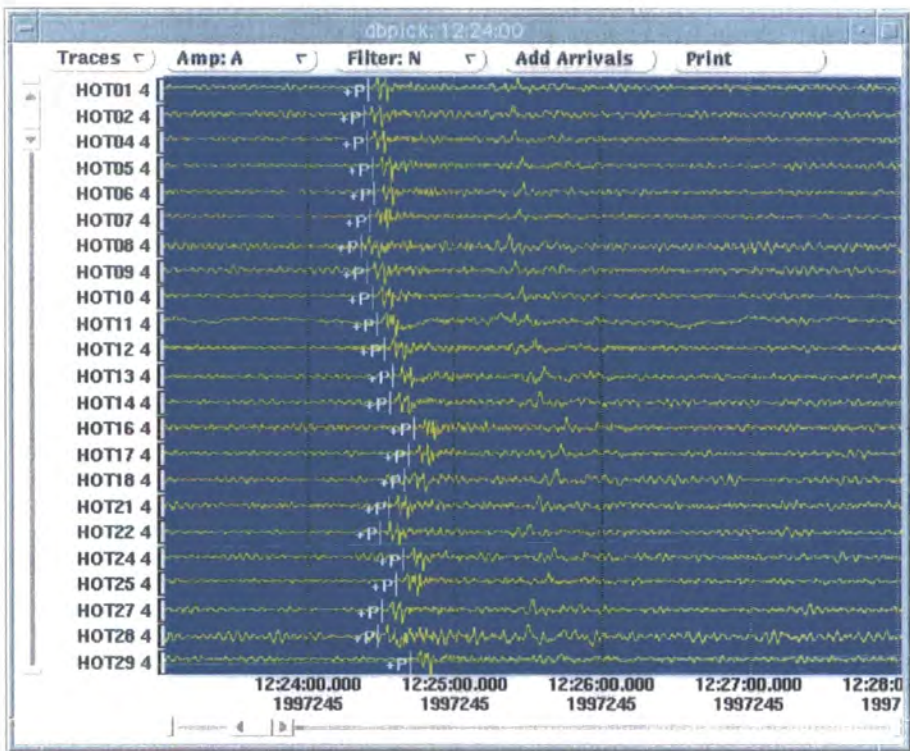
Figure 4.1 Vertical seismograms for a teleseismic event displayed using **dbpick**. Markers show predicted arrival time based on the IASP91 Earth model (Appendix 10).
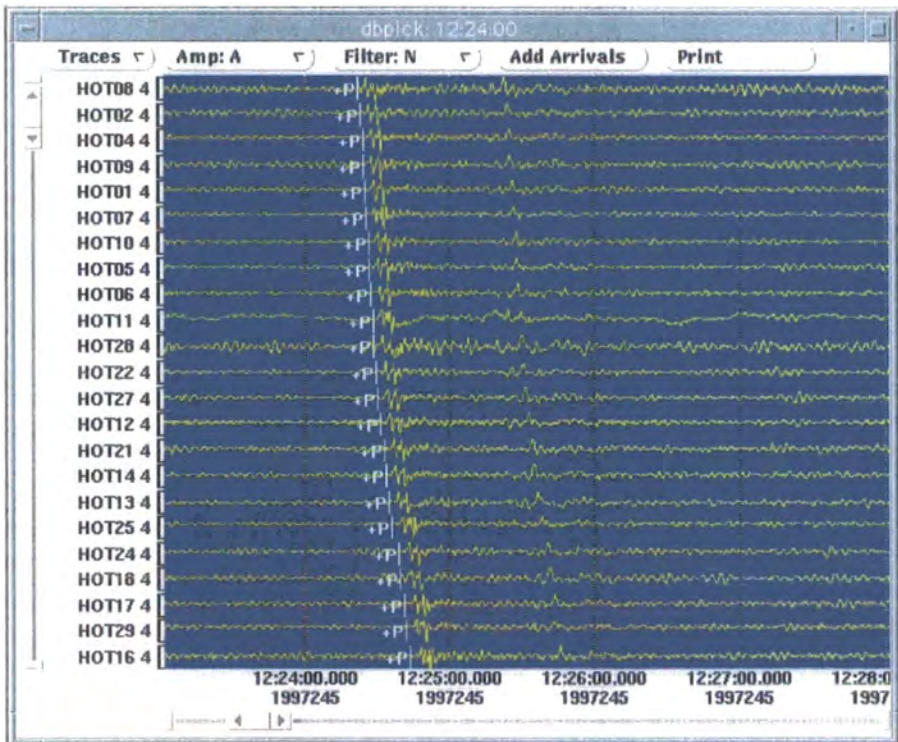
Figure 4.2 Seismograms sorted in order of epicentral distance, using hypocentre information from the U.S.G.S. QED earthquake listing.
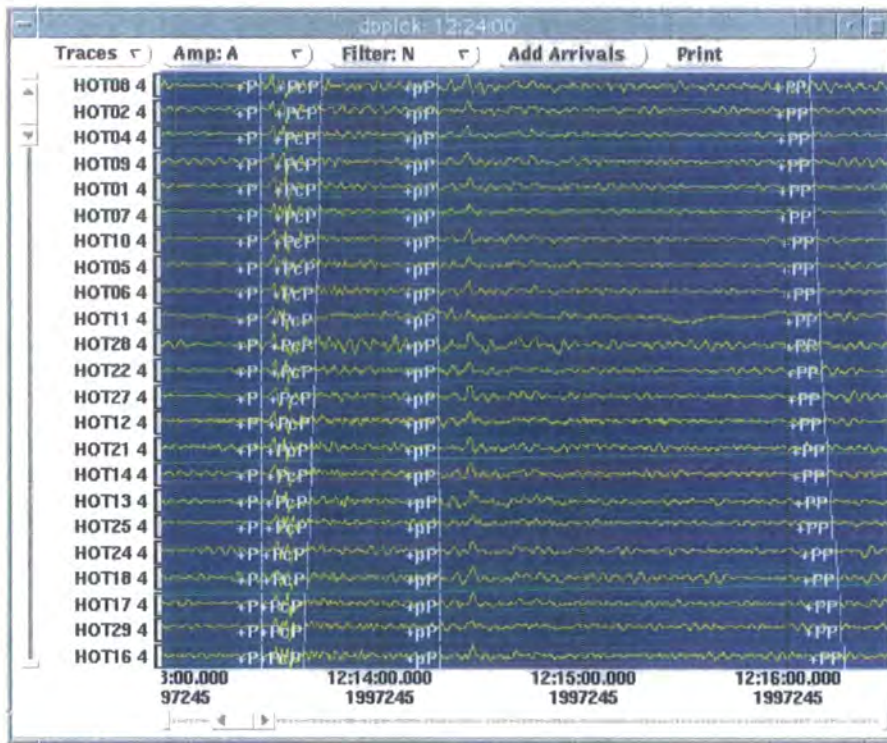
Figure 4.3 Seismograms aligned according to the arrival time for the first P wave, predicted using the IASP91 model. Markers for later phases pP, PcP and PP are also displayed.

The use of on-screen markers for predicted phase arrival times was found to be very useful, as it is a quick and reliable way of making sure that the set of observed arrivals has the correct phase slowness. Such phase identifications can also be verified by fitting a plane wave to the arrivals and calculating the slowness.

4.2.3   Picking

All picks were made by hand using *dbpick*, on one channel only for a particular phase. P arrivals were picked on the vertical channel (4 or Z), while S arrivals were picked on whichever component provided the clearest waveforms. This was usually R or T but occasionally the N-S (5 or N) or E-W (6 or E) components, depending on the phase of interest. For example, SKS is not present in the transverse component (T) in an isotropic Earth.

Picks were made by visually correlating, on screen, the best and earliest representative peak or trough across the network. An initial pick was made, at a low magnification, so that several traces could be seen at a time, to avoid cycle-skipping (Figure 4.4).
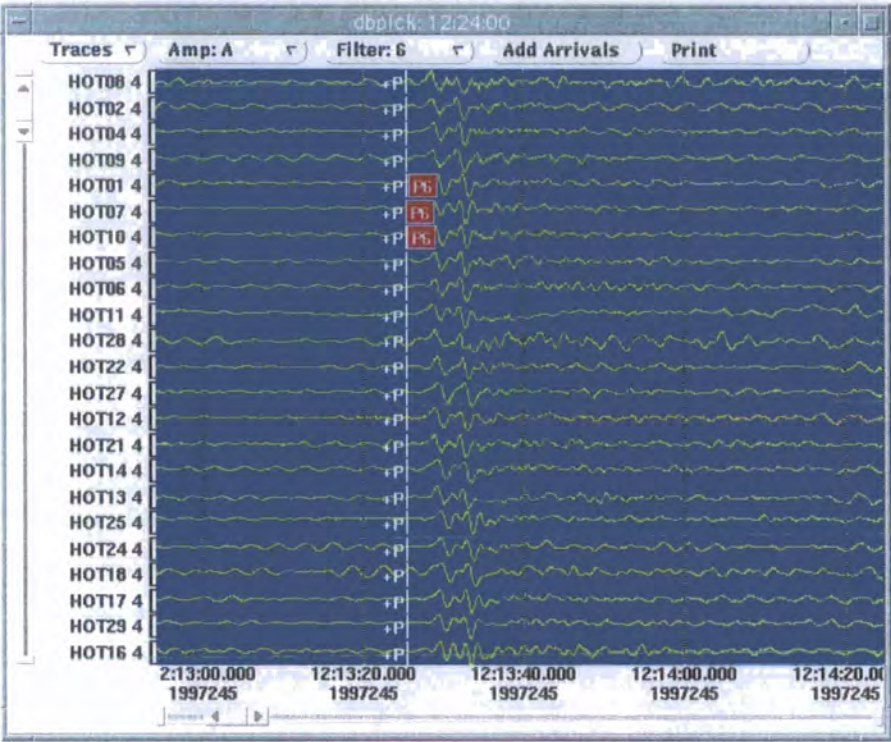
Figure 4.4 Traces filtered using pre-defined filter 6 (0.1-1.0 Hz), and initial picks made at low magnification labelled with the identifier P6. The right-hand edge of the arrival flag indicates the pick position.
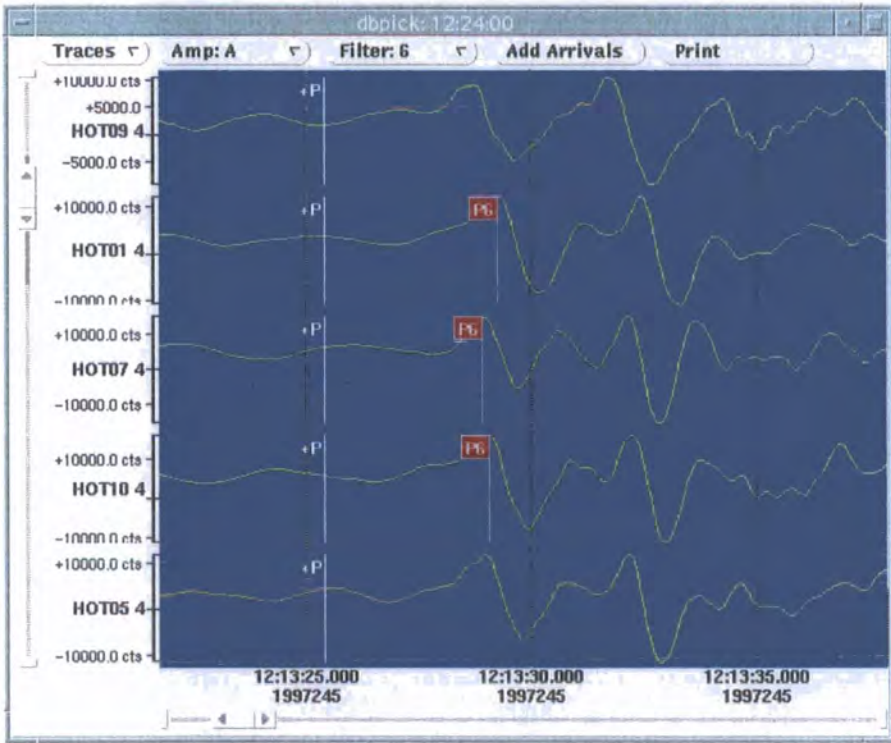
Figure 4.5 Final picks made at high magnification.

Once the correct peak or trough had been selected, it was magnified to enable the correct position on the peak or trough to be fine tuned (Figure 4.5). With the traces arranged in order of epicentral distance and aligned by first P arrival, gross outliers (e.g. from misidentifying the correct cycle) could be identified by their anomalous position with respect to other picks. Clock corrections had not yet been applied at this stage, so it is possible that some outliers may yet have remained.

As each pick was made, *dbpick* displayed a flag indicating its position. The user can annotate this with a text label. The pick was automatically recorded in the file dbname.arrival as a record with fields for the station name, channel name and pick time, stored as the number of seconds since 00:00:00 on 1st January 1970. This file is updated instantly with subsequent adjustments to the pick time, and picks can be deleted and re-made at will.

4.2.4   Clock corrections

Clock corrections were applied to individual pick times after the picking process. This was more accurate than adjusting the start times of whole traces in the seismogram file header. The main reason for this is that a correction is obtained for the instantaneous error at the pick time, rather than at the start time of the seismogram file. It is also better seismological practice to store uncorrected seismogram files, since future improvements in knowledge of the clock errors can then be applied.

Log files produced by the Hotspot DAS recorders list each instance of the GPS receiver obtaining a clock lock. A typical sample of a log file is shown in Appendix 11. The entry for each clock lock is accompanied by the value and sign of the clock correction which was applied to the recorder's internal clock to synchronise it with GPS time. The script *getcron.awk* (Appendix 12) was used to extract these clock locks from individual log files, which typically covered several weeks. These were written to a single file for each station which thus documented all clock locks and corrections for the entire duration of the deployment of that station. These are shown graphically in Appendix 7.

It can be seen that the performance of the GPS clocks varied considerably between stations, and that while clocks at some stations required little correction,

clocks at other stations show much more erratic behaviour, requiring corrections up to ±50 ms.

The `perl` script `clockcor.pl` was used to run the clock correction routine `hotclock` (Appendix 13) on each event database. This program is called with the time of the pick, and returns the clock correction to be applied. This is done by searching for the two times nearest to the pick time among the available, listed clock lock times and interpolating between the two corresponding corrections. The clock correction was added to the pick time to obtain the corrected time. This was then written to the file `dbname.picks`, produced by copying the file `dbname.arrival` but replacing the pick time with the corrected time.

4.2.5   Calculation of relative delay times

Teleseismic tomography models variations in travel time about some average Earth model. In this case, the IASP91 model was used as a reference Earth model. For source j and receiver $i=1,...I_j$ the travel time residuals are (Evans & Achauer, 1993)

$$r_{ij} = t_{Obs_{ij}} - t_{Calc_{ij}} \tag{4.1}$$

where $t_{Obs_{ij}}$ is the observed arrival time and $t_{Calc_{ij}}$ is the corresponding predicted arrival time according to the IASP91 travel time tables for the identified phase. These "absolute" travel time residuals contain contributions from errors in hypocentre location and origin time, as well as differences between the reference Earth model and the actual. Errors from the first two sources are nearly constant across the receiver network if this is small compared to the raypath length. They can be removed by forming relative residuals rr_{ij}, either by subtracting some reference residual, $r_{Ref,j}$, or, as was done in this study, the weighted mean of the residuals for that source:

$$rr_{ij} = r_{ij} - r_{Ref,j} \tag{4.2}$$

or

$$rr_{ij} = r_{ij} - \sum_{i=1}^{I_j} w_{ij} r_{ij} \bigg/ \sum_{i=1}^{I_j} w_{ij} \tag{4.3}$$

where w_{ij} is a weighting term derived from the pick uncertainty. The mathematical development of the ACH method is described in Chapter 5.

The procedure described above was implemented using the `perl` script `ach.pl` (Appendix 14), which produces as output the relative residuals in the format required by the ACH program. An example of the output of `ach.pl` is given in Appendix 15. In order to obtain the predicted travel time and phase slowness, which are required by the ACH input program for the basic, 1-dimensional raytracing, `ach.pl` calls the programs `taup_time` and `taup_slow` (Appendix 16), which use the tau-p method (Buland & Chapman, 1983). This method relies on a parameterised version of a standard Earth model to produce phase arrival times and slowness estimates for an event at a given epicentral distance and source depth. The slowness and travel time estimates produced by this program at this stage were used only as preliminary values, since they relied on epicentre locations from the U.S.G.S. QED listing, which is less accurate than Preliminary Determination of Epicentres (PDE) list. This is also from the U.S.G.S., but is released several months later as more data become available to provide better-constrained hypocentre locations. Errors in relative travel time and slowness caused by the difference in these two estimates will be small, because subtracting a reference or mean residual from each time almost removes the effect of error in the hypocentre location.

The QED values were later replaced with PDE values and travel times and slownesses re-calculated to ensure that the most reliable data were used in calculating the actual relative delay times used in the inversion. In order to do this, the data file produced by `ach.pl` was passed to another script, `pickdb_azbin_data.pl` (Appendix 17) which reformatted the data into a tabular form which could be used for subsequent data quality control procedures. At a later stage in this study, more flexible travel-time and slowness prediction programs became available (Crotwell *et al.*, 1999). These rely on the same method (Buland & Chapman, 1983) but are easier to use and are able to predict times and slownesses for a greater range of phases. Using the final PDE list of hypocentres, the script `tpred_unix.pl` (Appendix 18) called these programs and appended the relevant data to the tables. These could then be re-formatted for input to the ACH programs by the script `remake_ach.pl` (Appendix 19).

4.3   DATA QUALITY CONTROL

Tomographic inversion requires input data of high quality, so after the compilation of the initial dataset of relative arrival times, a number of steps were taken to identify and eliminate outliers.

A commonly-used method of checking for outliers in the data is to group delay times by station, and plot the delays at that station in azimuth-slowness space. The aim of this method is to identify outliers by noting data points which are very different from neighbouring points. For example, if a delay time at a particular slowness and azimuth point is positive, yet lies within a group of negative delays, then it is identified as suspicious, checked and deleted if found to be a blunder. One serious problem with this method is that it is very difficult to apply objective criteria to the identification of outliers, and the removal of data points re-adjusts the entire data set, requiring many iterations of the procedure. It was found to be relatively ineffective at identifying outliers in this study.

I designed a different method of outlier identification, which was more effective. The set of delay times was first divided into "bins" in azimuth-slowness space. (Figures 4.6 and 4.7). For each bin, relative residuals were then be plotted relative to some datum. The ACH program makes delays relative to the mean delay for each event, but this is not useful as a comparison in this case, since we need to compare delays for all stations, for each bin and for all events. Thus, delays should be made relative to one of two other values, either the mean residual for that aziumuth-slowness bin, or the mean residual for each station, for that azimuth-slowness bin. Initially, the former was used to plot graphs of delay times, with the intention of eliminating data which exceeded the mean value by some empirically-determined threshold which represented the maximum reasonable delay time. However, the "signal" contained in the data in the form of delays at some stations relative to others, is not properly treated when using this datum as the reference. A better datum is the mean for each station for that azimuth-slowness bin. Better still is the median, since it is less sensitive to large outliers than the mean. "Spidergrams" were plotted for each azimuth slowness bin and data falling outside the threshold values were labelled.
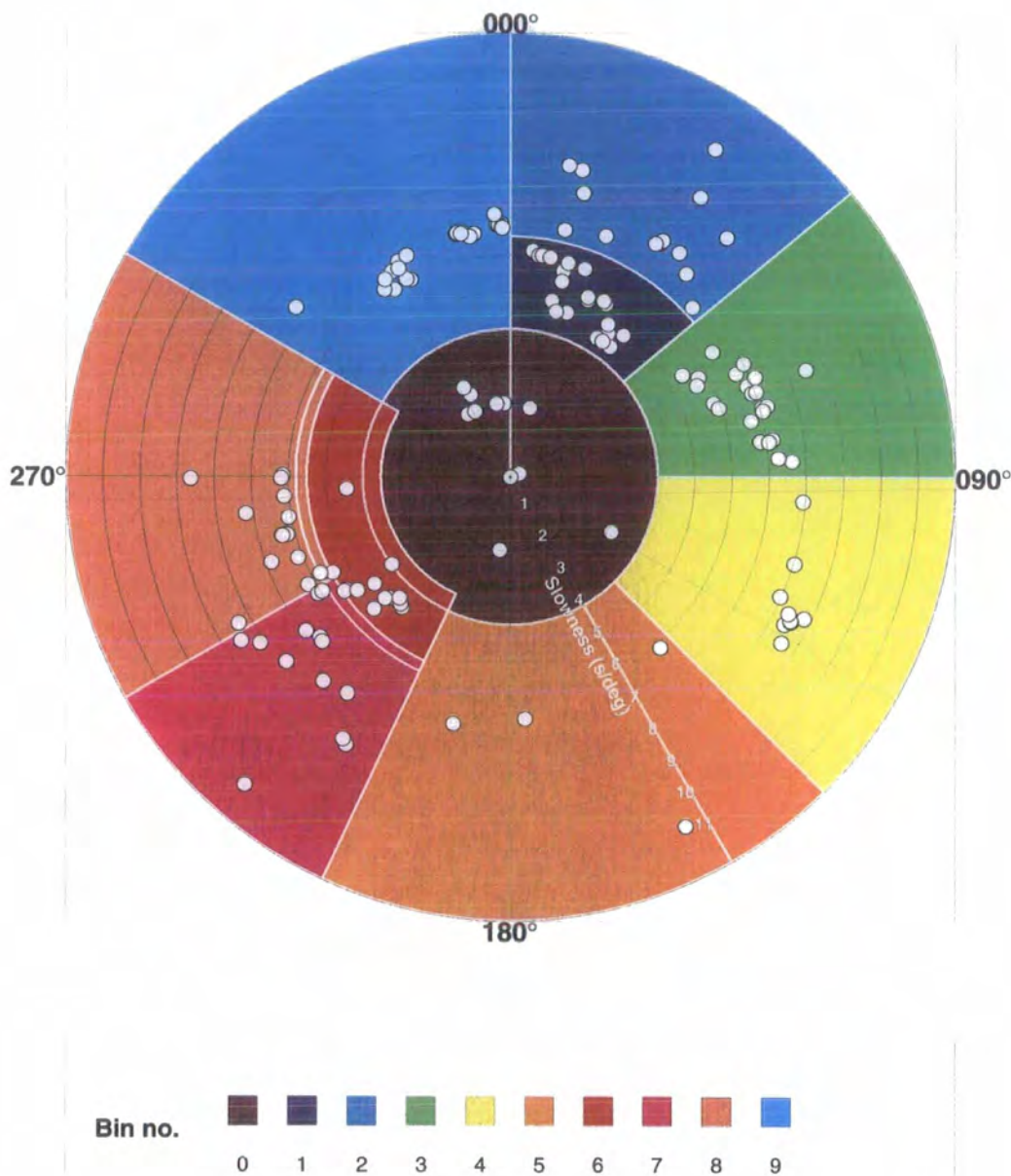
Figure 4.6 Events in the P dataset divided into "bins" in azimuth-slowness space.
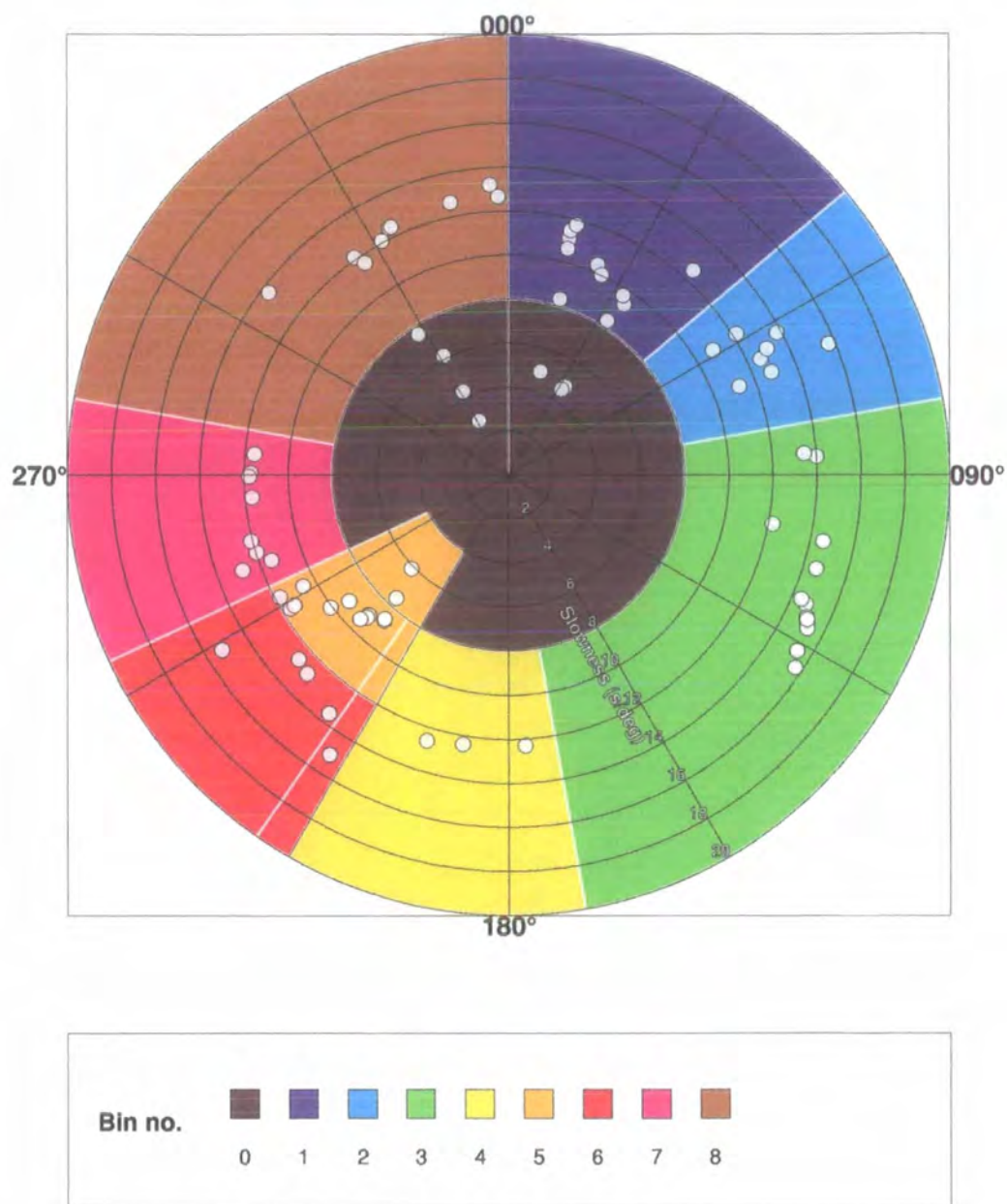
Figure 4.7 As for Figure 4.6 but for the S dataset.
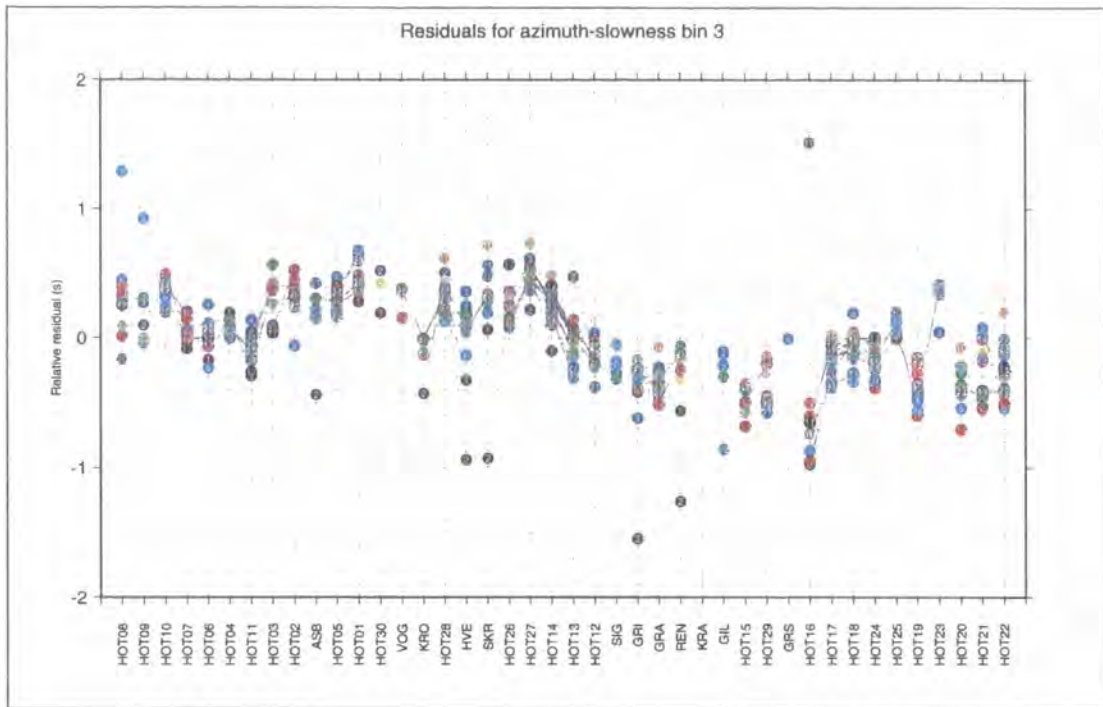
Figure 4.8 Example of a spidergram used to define outliers. Each circular dot represents one pick, numbered by event, and grouped by station along the horizontal axis. Outliers defined in this way are ringed in red.

Windows of median-value ±0.6s for P and ±1.5s for S were selected empirically the limits of the central "core" of picks at each station within each bin. Picks falling outside these windows were then identified and eliminated. The scripts `plot_azbin_delays_[ps]_stnmed` (Appendix 20) were used to plot successive sets of such spidergrams which, after two iterations, had filtered out the worst outliers from the dataset while leaving the form of the delay variation between stations intact.

4.4 SUMMARY

- Seismograms of suitable events recorded at the SIL and Hotspot networks were extracted from archive media, converted to a common file format, and organised in to event databases.

- These seismograms were rotated, bandpass filtered and relative phase arrival times picked by hand using an interactive picking program. Subsequent data quality control eliminated outliers from the set of arrival times.

- The final dataset used for tomographic inversion comprised 3,159 P-wave arrivals from 113 events (160 phases), and 1,338 S-wave arrivals from 66 events (73 phases) (Figure 4.9), (Appendix 22).
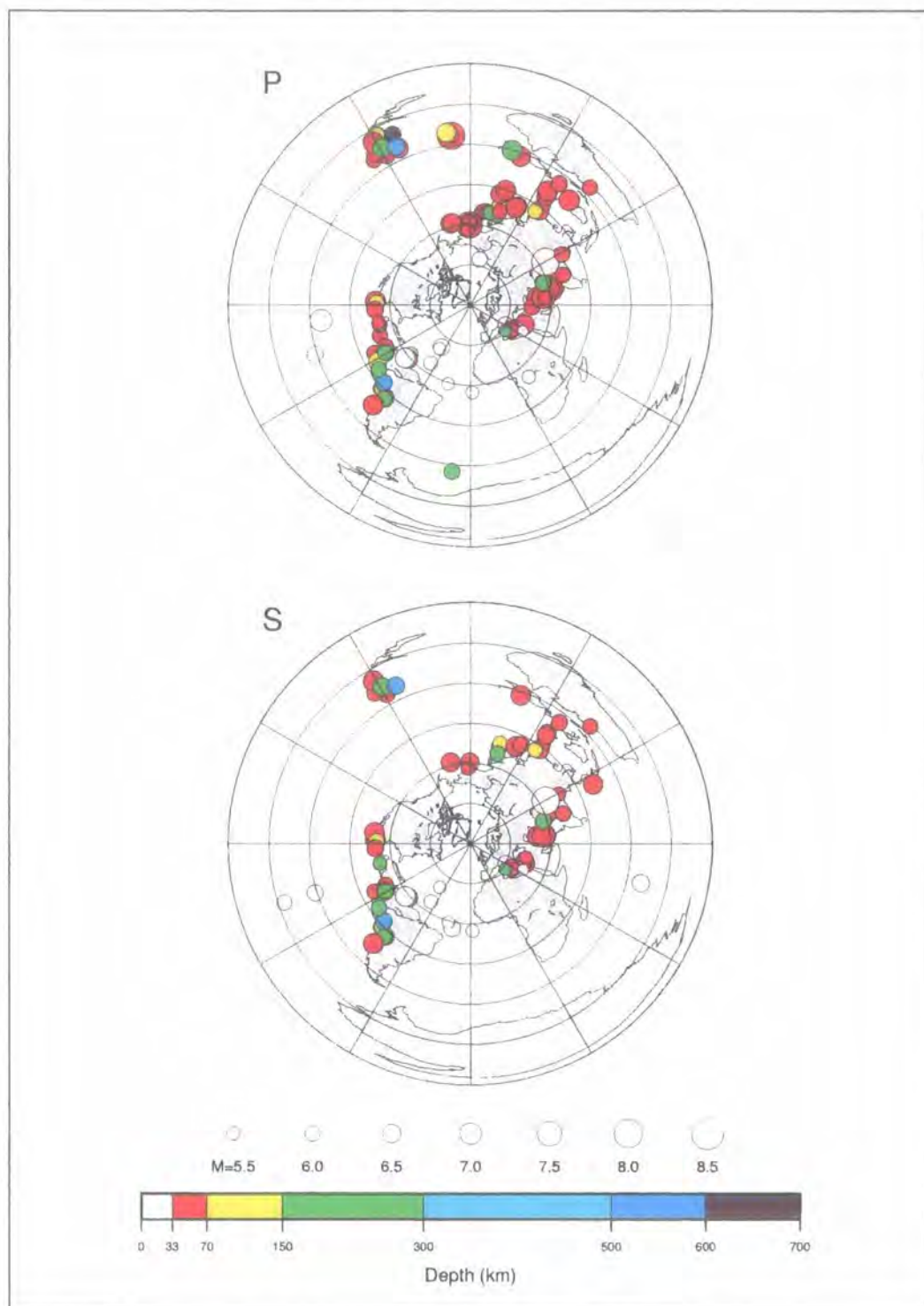
Figure 4.9 Events used for the tomographic inversion. Dots show location of epicentre, with the size proportional to magnitude and the colour representing the depth.

Chapter 5

Method and Results

5. METHOD AND RESULTS

5.1 METHOD

5.1.1 Background to the ACH method of teleseismic tomography

The ACH damped least-squares inverse method (Aki et al., 1977) is one of the most widely-used methods of teleseismic tomography, and is named after those who formulated it while working at the NORSAR seismic array in Norway in the 1970s. Despite its age and simplicity, it is still widely used as it is both robust and reliable. Its primary use has been for velocity tomography, but derivatives of the method have been applied to attenuation and anisotropy (Ward & Young, 1980; Young & Ward, 1980). A comprehensive description and guide for use, along with a discussion of the capabilities and limitations of the method is given by Evans & Achauer (1993). A brief summary only is given here.

The earliest ACH inversions were carried out during investigations of the lithosphere beneath NORSAR (Aki et al., 1977) and other seismic arrays (Aki et al., 1976; Husebye et al., 1976). Other early studies such as magma chamber imaging experiments at Yellowstone (Zandt, 1978; Iyer et al., 1981) and Hawaii (Ellsworth, 1977; Ellsworth & Koyanagi, 1977) demonstrated the potential of teleseismic data for subsurface imaging and revealed the presence of small-scale heterogeneities whilst, particularly in the case of the latter study, furthering understanding of the stability of the inversion scheme. An early tomographic study of Iceland (Tryggvason, 1981; Tryggvason et al., 1983) confirmed the presence of a low-velocity anomaly beneath the island. Many other studies have made use of the method and contributed to the wealth of literature on its use. Some examples are the studies of the Kenya Rift (Achauer et al., 1994; Kaspar & Ritter, 1997), the Rio Grande Rift (Slack et al., 1996) and the French Massif Central (Granet et al., 1995; Granet et al., 1995).

5.1.2 Principles & assumptions

In common with many tomography schemes, the ACH method is based on a number of simplifying assumptions that reduce the physical problem down to a manageable system of linear equations. ACH is a "restricted array" method, that is, the network of seismic recorders does not span the entire distance from source to

receiver (as with local earthquake tomography), so only part of the raypath is contained in the target volume. Consequently, only this final portion of the raypath can be modelled, with a standard 1-dimensional Earth model used to represent everywhere outside the target volume.
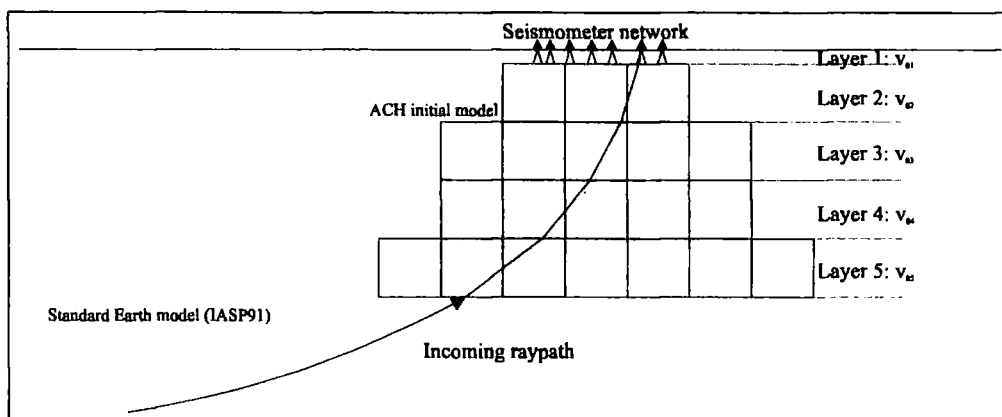
Figure 5.1 ACH experiment geometry. Receiver stations at the surface are shown by solid black triangles above the target volume. The top layer of the model is treated differently, with each receiver assigned a separate "block" (open triangles). Grey blocks denote those "hit" by an incoming teleseismic ray.

Layers of constant velocity are divided into regularly-shaped blocks, for each of which a velocity perturbation is found relative to the initial velocity for that layer, using teleseismic travel time residuals recorded at the seismometer network above the target volume. The top layer is treated differently, with each receiver assigned a separate "block". Blocks in the first layer represent the conical volume enclosed by the final portions of the raypaths approaching a receiver from below.

One of the key assumptions of the ACH method is that the time residuals generated outside the target volume, i.e. between the seismic source and the point of entry of a ray into the target volume, which result from errors in seismic source parameters and anomalous structure outside the target volume, are approximately constant for all stations in the network. The validity of this assumption has been questioned (Masson & Trampert, 1997), and indeed, heterogeneities placed just outside the target volume in synthetic studies are shown to introduce spurious anomalies into the result at the edges of the model (Evans & Achauer, 1993). These shortcomings merely serve to highlight the dangers, common to all tomographic methods, of over-interpretation of the resulting model, especially at its extremities of

depth and lateral extent, where sampling and resolution is poor. Despite its known limitations, ACH is a reliable and robust inversion method which is relatively efficient in terms of computing resources, whose behaviour is well-documented and understood, and which is known to produce geologically reasonable results when used correctly.

5.1.3 Correction of an error

The implementation of the method used in this study is that developed by Evans & Achauer (1993), and is the result of continual incremental improvements over the years in the light of experience by many workers. An error in the treatment of azimuths was found in the program during the course of this study, and a correction was made to the program. In its original form, the ACH method computes ray paths using the same station-to-epicentre azimuth, in local coordinates, for all stations observing a particular earthquake. This is equivalent to approximating the wavefront on the ground to a straight line in the local coordinate system. The variant of ACH used here (Evans & Achauer, 1993), attempts some improvement on this approximation by using the true spherical azimuth at each station. Because of the convergence of meridians, this practice introduces into each azimuth an error equal to the difference between the local grid direction and the true azimuth which, at high latitudes (e.g., ~65 °N in the case of Iceland) can greatly exceed the errors related to wavefront curvature that motivated the modification. A corrected version of the program was used in this study (Julian *et al.* 1999, see enclosure).
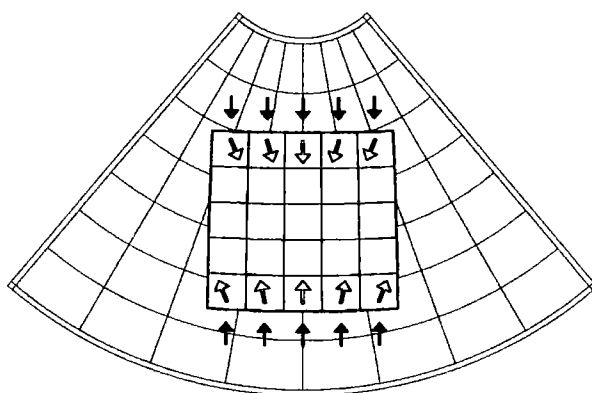
Figure 5.2 Relation between global (spherical) and local (Cartesian) coordinates, at a northern latitude. Black arrows show directions of approach of seismic waves from earthquakes at epicentral distances of 90° to the north and south. White arrows show artificial distortion of wavefronts that occurs if directions in the local rectangular grid are identified with directions specified in the spherical grid. From Julian *et al.* (1999) (see enclosure).

5.1.4 Mathematical formulation

The mathematical principles are described by many authors (e.g. Evans & Achauer, 1993) and summarised here. The travel time perturbation δt resulting from a fractional velocity variation δV about a starting model V_0 along the section of raypath ds is given by

$$\delta t = -\int_{Ray} \frac{1}{V_0} \frac{\delta V}{V_0} ds$$

(5.1)

In the implementation of ACH used here, refraction due to δV is disregarded. This approximation is appropriate in the case of relatively small δV (Aki, 1993) which is the case expected for the structure beneath Iceland. Previous studies have found the magnitude of δV to be less than 5% (Tryggvason *et al.*, 1983; Wolfe *et al.*, 1997). In cases where larger velocity perturbations are expected, the resulting refraction is significant and so the system becomes non-linear, requiring more sophisticated raytracing (Steck & Prothero, 1991).

First, we parameterise the target volume by dividing it into layers of constant velocity, and then further divide these layers into blocks, each assigned the quantity

$$\delta m_k = -\frac{\delta V}{V_0} \delta_k,$$

(5.2)

where δm_k represents a slowness perturbation for block k, and the Dirac delta function δ_k (1 inside the block; 0 outside) restricts the spatial scope of this parameter to the block in question. Thus, we have

$$\frac{\delta t}{\delta m_k} = -\int_{Ray} \frac{1}{V_0^2} \frac{\delta V}{\delta m_k} ds$$

(5.3)

for a total of K blocks (with the capital letter representing the maximum of the index). Similarly, the input travel time residuals are, for a given source $j=1,...,J$ and receiver $i=1,...,I$,

$$r_{ij} = dO_j + \sum_{k=1}^{K} \left(-\int_{base}^{receiver\,i} \frac{1}{V_0^2} \frac{\delta V}{\delta m_k} ds \right) \delta m_k + e_{ij}$$

(5.4)

where e_{ij} is an error term, and the source term dO_j has been introduced because absolute velocity and other unresolvable terms may be present in the data. We

abbreviate the parenthesised part to a_{ijk}, the partial derivatives. It can be shown that a_{ijk} is also the unperturbed travel time of ray ij inside block k. We now drop the error term, making the relation approximate, and introduce weighting by the estimated error of r_{ij}, (called σ_{ij} and normalised by the mean error $\bar{\sigma}$):

$$\frac{\bar{\sigma}}{\sigma_{ij}} r_{ij} = \sum_k \frac{\bar{\sigma}}{\sigma_{ij}} a_{ijk} \delta m_k + \frac{\bar{\sigma}}{\sigma_{ij}} dO_j .$$

(5.5)

Premultiplied by $(\bar{\sigma}/\sigma_{ij})[a_{ij1} \quad \dots \quad a_{ijK} \quad 1]^T$, summed over i, and expanded, this becomes

$$\sum_{i=1}^{I_j} \begin{pmatrix} w_{ij} a_{ij1} r_{ij} \\ \vdots \\ w_{ij} a_{ijK} r_{ij} \\ w_{ij} r_{ij} \end{pmatrix} = \sum_{i=1}^{I_j} \begin{pmatrix} w_{ij} a_{ij1} a_{ij1} & \cdots & w_{ij} a_{ij1} a_{ijK} & w_{ij} a_{ij1} \\ \vdots & & \vdots & \vdots \\ w_{ij} a_{ijK} a_{ij1} & \cdots & w_{ij} a_{ijK} a_{ijK} & w_{ij} a_{ijK} \\ w_{ij} a_{ij1} & \cdots & w_{ij} a_{ijK} & w_{ij} \end{pmatrix} \begin{pmatrix} \delta m_1 \\ \vdots \\ \delta m_K \\ dO_j \end{pmatrix}$$

(5.6)

where $w_{ij} = \bar{\sigma}^2 / \sigma_{ij}^2$.

Here, we introduce the dummy block index, l, and make the contractions:

$$\bar{r}_j = \sum w_{ij} r_{ij} , \quad \bar{a}_{jk} = \sum w_{ij} a_{ijk} \quad \text{and} \quad \bar{w}_{ij} = \sum w_{ij} \quad \text{(summing from } i=1 \text{ to } I_j\text{)}$$

We obtain

$$dO_j = \frac{\bar{r}_j}{\bar{w}_j} - \sum_{l=1}^{K} \frac{\bar{a}_{jl}}{\bar{w}_j} \delta m_l .$$

(5.7)

Separation of the dO_j parameter is completed by substituting (5.7) back into the kth equation 5.6, giving

$$\sum_{i=1}^{I_j} \left[w_{ij} a_{ijk} \left(r_{ij} - \frac{\bar{r}_j}{\bar{w}_j} \right) \right] = \sum_{i=1}^{I_j} \sum_{l=1}^{K} \left[w_{ij} \left(a_{ijk} a_{ijl} - \frac{\bar{a}_{jk} \bar{a}_{jl}}{\bar{w}_j^2} \right) \right] \delta m_l$$

(5.8)

for each source. We now sum over all J sources and note that the sum over l is a matrix multiplication. This yields the familiar form of the least-squares problem

$G m = b$

(5.9)

where $m = (\delta m_1, \dots, \delta m_K)^T$. The kth element of b is the left hand part of (5.8) in square brackets, and the kl^{th} element of G is the right hand part in square brackets, each summed over i and j. Equation 5.9 is solved by damped least squares, using the damping constant θ^2,

$$\hat{m} = \left(\mathbf{G} + \theta^2 \mathbf{I}\right)^{-1} b \; . \tag{5.10}$$

We now represent **G** and **b** in terms of *d*, a vector of $N_{Obs} = \sum I_j$ observed

residuals r_{ij}, **A**, (the $N_{Obs} \times K$ matrix of a_{ijk} terms) and (**W-P**), a weighting and

parameter separation matrix. The ACH inverse is thus represented as

$$\hat{m} = \left[\mathbf{A}^T(\mathbf{W}-\mathbf{P})\mathbf{A} + \theta^2 \mathbf{I}\right]^{-1} \mathbf{A}^T(\mathbf{W}-\mathbf{P})d \tag{5.11}$$

where **W** is a diagonal matrix of w_{ij} weights and **P** is the symmetric block matrix

whose j^{th} block is given by

$$\mathbf{P}_j = \frac{1}{\overline{w}_j} \begin{pmatrix} w_{1j}w_{1j} & \cdots & w_{1j}w_{I_j j} \\ \vdots & & \vdots \\ w_{I_j j}w_{1j} & \cdots & w_{I_j j}w_{I_j j} \end{pmatrix} . \tag{5.12}$$

Equation 5.11 is equivalent to the familiar solution (5.10) to the damped

least-squares problem and is the solution of

$$\mathbf{A}m = \mathbf{d} \tag{5.13}$$

with parameter separation and weighting described by (5.7).

The relationship between the inversion result $\hat{m}$ and the representation of the

"real" Earth in *m* is described by the resolution matrix, **R**

$$\hat{m} = \mathbf{R}m \tag{5.14}$$

which is given by

$$\mathbf{R} = \left[A^T(\mathbf{W}-\mathbf{P})\mathbf{A} + \theta^2 \mathbf{I}\right]^{-1} \mathbf{A}^T(\mathbf{W}-\mathbf{P})\mathbf{A} \; . \tag{5.15}$$

We may also attempt to quantify the significance of the inversion result by

computing the standard errors associated with the modelled velocity perturbations

$\hat{m}$. These are the square root of the diagonal elements of the covariance matrix **C**,

where

$$\mathbf{C} = \sigma_r^2 \left[\mathbf{A}^T(\mathbf{W}-\mathbf{P})\mathbf{A} + \theta^2 \mathbf{I}\right]^{-1} \mathbf{R} \; . \tag{5.16}$$

and σ_r is the data variance remaining after inversion.

5.1.5   Creation of initial model

The choice of initial model is an important step, since it is the approximation

of the real Earth to which we are comparing the result of our observations. Without

further analysis (such as detailed raytracing through the resulting model) measures of quality such as variance reduction only compare the output model to the initial model, so it is important that it is an acceptable approximation of reality.

Several parameters are involved in defining the initial model for an ACH inversion, the most important of which are discussed below. Other parameters can also be set and are described in the documentation for the program `thrd` (J.R. Evans, *pers. comm.*)

Model centre

The location of the model centre, specified in latitude and longitude, defines the centre of the coordinate system in which the target volume is parameterised. Suitable choices are the centre of the seismometer array or the coordinates of the station nearest the centre. Since the grid of blocks is defined in kilometres north, south, east and west from this point, a position in the resulting output model should be interpreted as angular position from the model centre.

Number of layers & thickness of each layer

These define a) the depth extent and b) the coarseness of the parameterisation of the target volume. The absolute restriction on depth extent is that all rays must enter the target volume through the base and not through the sides. Thus the model cannot extend deeper than the turning points of the shallowest rays in the dataset, i.e. rays from the nearest seismic sources. In practice, however, the limit below which structure cannot be retrieved is the depth at which the ray bundles begin to diverge and cross-firing of rays is not achieved. Below this level, blocks are sampled only from restricted directions, and the sources of velocity perturbations cannot be unambiguously located. It is a requirement of the method that blocks are sampled well from the best possible distribution of directions in azimuth-slowness space.

The layer thicknesses are governed by the need to achieve good ray density within the layers and the need for rays to spend as much time as possible "sampling" each block, but the model should not be over-simplified by having layers that are too thick. Evans & Achauer (1993) recommend the following:

1. A good starting thickness is 1.5 times the block width. A suitable block width is approximately the average station spacing.

2. Layer boundaries should be perturbed so that the travel time of a vertical ray through each layer is approximately equal.

3. Layer boundaries should be placed at the known major discontinuities in velocity structure.

Initial layer velocities

The initial velocities for all blocks in a layer should be obtained from a standard Earth model. Some average value should be used for the depth range of the layer.

Role of the top layer

The first (topmost) layer is treated differently, assigning one block to each receiver (Ellsworth, 1977). This is appropriate where the receiver spacing is not entirely regular. In such a case, rays overlap insufficiently between receivers in the first layer, so a grid of "normal" blocks would leave many blocks without crossing rays. The top layer serves to absorb strong heterogeneities in near-surface velocity, which may be due to factors such as weathering, faults and fractures, igneous intrusions, shallow crustal magma chambers, and other features which would contaminate the deeper structure.

Variations in elevation across the seismic network can be accommodated by setting options in the ACH model file. These define whether or not to correct residuals for station elevation and whether rays should be traced to the true elevation.

Block dimensions & number of blocks along north and east axes

The block size should be chosen as the best compromise between several factors such as the scale of anomalies in the target volume, the density of rays, computational constraints, receiver spacing and signal wavelength. The block size should not be smaller than the shortest wavelength of signals in the input data, since anomalous structures on a scale much shorter than a wavelength will behave as an equivalent homogeneous body with some average properties (Aki *et al.*, 1977). A sensible starting block width near the surface is the mean receiver spacing (Evans & Achauer, 1993). The lateral extent of each layer must be set so that all rays enter the model from the base, and that rays are contained within the model from there upwards. The resulting shape is a wide, downward-broadening "Mayan pyramid" block structure (Figure 5.3).
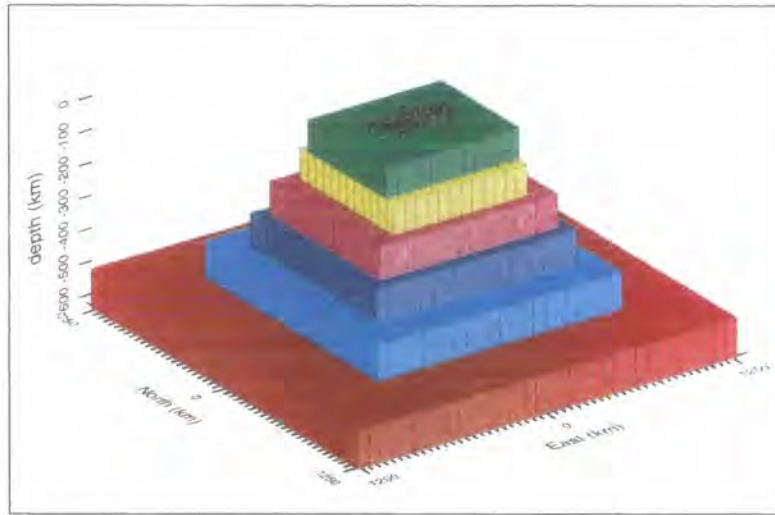
Figure 5.3 Typical 3-dimensional ACH initial model showing the downward-broadening "Mayan pyramid" structure necessary to enclose the ray bundle from teleseismic events. This example has blocks 75 km wide and layers of ~100 km thickness, perturbed to produce roughly equal vertical travel times between layers. The 10-km thick "special first layer" is shown, with one block assigned to each receiver.

Care should be taken to "trim" unnecessary additional blocks from the edge of the model, since there is a finite (compiler- and memory-dependent) limit to the total number of blocks that can be used in a model. This is best achieved by trial and error using the hitcount map (i.e. the number of rays sampling each block) that is included in the output of `thrd`, the ACH program. This is particularly important for the wide, lower layers of models if they have small block sizes and thin layers, since many thousands of blocks are then required to fill the study volume.

Damping parameter

The damping parameter (θ^2, equation 5.10) is selected empirically, by finding that which results in the optimum trade-off between squared model length and residual variance (Evans & Achauer, 1993). This is combined with examination of a set of output models using different damping to determine which are persistent features and which disappear at high damping values. A damping parameter is sought which neither over-damps real anomalies nor over-fits noise in the data set.

The damping parameter is scaled appropriately when treating layer-thinned models. Damping multiplies (increases) the model length, as does the greater number of blocks associated with thinned models. Thus, the damping parameter must be scaled down for thinner models by approximately the same factor by which the

number of modelled blocks is increased. The effect of damping is to cause model length *and* data misfit to be minimised in the least-squares sense in the same step in the inversion.

5.1.6   Layer thinning and horizontal smoothing

For vertical smoothing, the layer-thinning approach of Evans & Achauer, (1993) is followed, whereby a first model of relatively thick layers is compared to models of equal depth extent but successively thinned layers in order to investigate vertical smoothing. This enables "smoother" initial models to be used, since the greater number of layers allows closer matching of the standard Earth model being used.

Horizontal smoothing requires a different approach, since we have already seen that there is a lower limit on horizontal block size: horizontal "block narrowing" is not analogous to vertical layer-thinning. Instead, an offset-and-averaging scheme is employed, whereby an original output model is offset by $1/n$ times the block size along each axis and recomputed in each of these n^2 "offset-models". The average of these is known as the "pseudo-model" and is usually seen to improve the model significantly. One effect is to mitigate the "disappearing anomaly" artifact noted by Ellsworth (1977), whereby a small anomaly of approximately the size of one block may disappear if it is divided over adjacent blocks in the same layer. Offset-and-averaging may, however, reduce the magnitude of spatially small anomalies (Evans & Achauer, 1993), so it is important to compare the original model with the offset-and-averaged result.

5.1.7   Model quality measures

The resolution matrix of the inversion result describes how clearly we have "seen" the Earth, but only as parameterised in our starting model. However, merely to strive for large, positive diagonal elements of **R** does not necessarily lead to the best result, since the diagonals are largest and most positive for wide blocks. Coarse parameterisation may *not* be the best representation of the Earth that can be gained from the inversion, and may lead to artifacts which are not represented in **R**. In fact, a better representation of the true Earth may be gained from using a damped model with thinner layers. In the case of ACH, damping smears anomalies vertically since most of the rays are subvertical, so splitting the model into thinner layers, while

producing a more realistic result, will reduce the *magnitude* of the diagonal elements of **R**. If the same pattern of values is maintained, however, this implies that the resolution kernels are well behaved. The "volume metric" method of Evans & Achauer (1993) gives a useful interpretation of the resolution matrix of layer-thinned models. This is a way of representing the information in **R** other than the diagonal element that is relevant to a particular block. It is a measure of the shape and size of the 3-dimensional volume over which damping has smeared the anomaly, and can be used to verify that the layer-thinned model has preserved the equivalent **R**-diagonal value of a particular volume of space in the model. The method is normally applied to a handful of locations in a model which are representative of the range of expected resolution qualities, to give insight into the overall model quality.

The volume metric for block k is computed by sorting elements in the kth column of the resolution matrix (of which the element in the kth row is the diagonal element for that block) in descending order of magnitude, and summing elements until some predefined value is reached. Those elements that contribute to the sum indicate blocks over which the anomaly in block k has been smeared. For example, if the first few elements of column 336 (the column which contains resolution information for block 336) are, in descending order, are 0.58, 0.20, 0.14, 0.02 and the corresponding row numbers are 336, 168, 504, 672 respectively, and we wish to find the volume metric at the equivalent diagonal element value of 0.8, we sum the elements until the value of 0.8 is reached. In this case, blocks 336, 168 and 504 represent the volume metric. Plotting these blocks in three-dimensional view reveals their spatial relationship, and gives, in effect, the "impulse response" of the system at the location in question.

5.2   RESULTS

5.2.1   *Naming convention for ACH models*

A suite of models was used in this experiment to compare the effects of initial parameterisation on the resulting tomographic image. The models were named according to a system which identifies the block configuration as well as the damping parameter used. Models were stored on disk in directories named according to the block configuration, described in Table 5.1. After selection of the damping parameter (section 5.2.4), the actual model name was constructed according to the convention in Table 5.2. The model configuration prefix is made up of three parts, for example p_10_75a, which denotes a P-wave model with a "special first layer" of 10 km thickness, and blocks 75 km wide. This was stored in directory p_10_75a, where the "a" suffix denotes a thick-layered configuration, "at" a thinned configuration with half-thickness layers, and "at3" a thinned configuration with one-third-thickness layers. The actual model name, for example p_10_75_400 includes the value of the damping parameter used, in this case, 400.

Table 5.1 Naming conventions for ACH block configurations (directory names)

P-wave models	50-km models	75-km blocks	100-km blocks
Full thickness layers	p_10_50a	p_10_75a	p_10_100a
1/2 thickness layers	p_10_50at	p_10_75at	p_10_100at
1/3 thickness layers	p_10_50at3	p_10_75at3	p_10_100at3
S-wave models			
Full thickness layers	s_10_50a	s_10_75a	s_10_100a
1/2 thickness layers	s_10_50at	s_10_75at	s_10_100at
1/3 thickness layers	s_10_50at3	s_10_75at3	s_10_100at3

Table 5.2 Naming conventions for ACH models used.

P-wave models	50-km models	75-km blocks	100-km blocks
Full thickness layers	p_10_50_400	p_10_75_400	p_10_100_400
1/2 thickness layers	p_10_50_225	p_10_75_225	p_10_100_225
1/3 thickness layers	p_10_50_161	p_10_75_161	p_10_100_161
S-wave models			
Full thickness layers	s_10_50_400	s_10_75_400	s_10_100_400
1/2 thickness layers	s_10_50_225	s_10_75_225	s_10_100_225
1/3 thickness layers	s_10_50_161	s_10_75_225	s_10_100_161

5.2.2   Initial models used

The block structures for the initial models used in the inversions are shown in Figure 5.4, Figure 5.5 and Figure 5.6. The names used here represent the model configuration before selection of the damping parameter. For both P- and S-wave inversions, initial models were created with 50-, 75- and 100-km width blocks, using a common 7-layer structure for the initial "thick-layer" models. These models all had a 10-km thick "special" first layer, in which each receiver was assigned its own block.
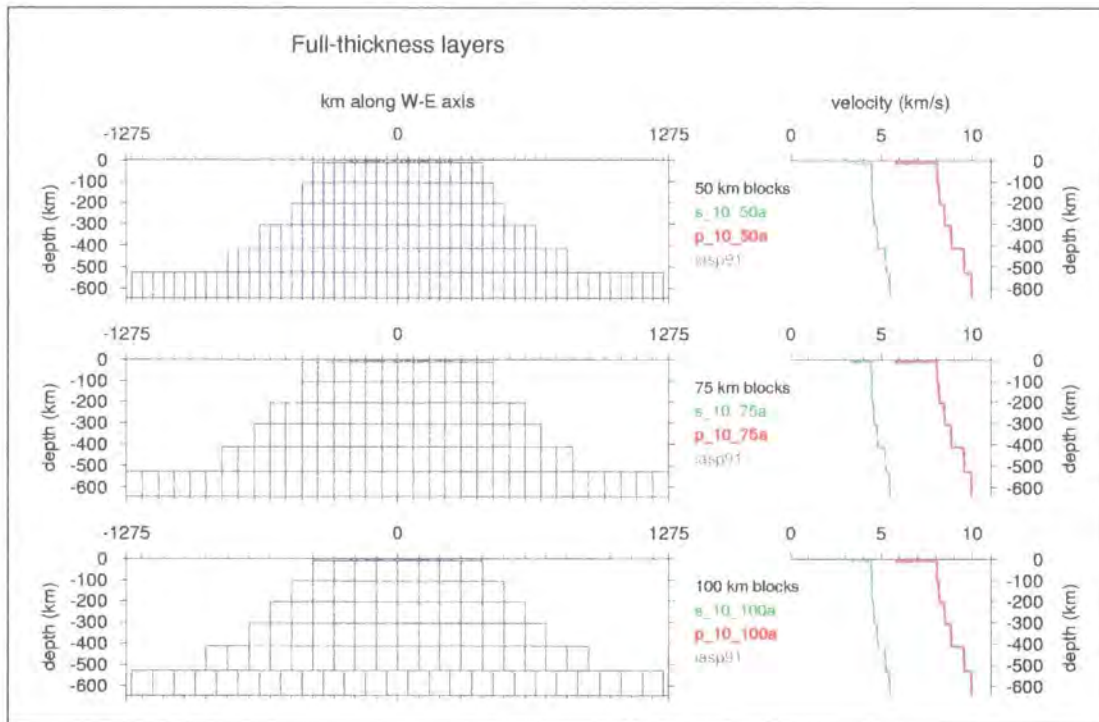
Figure 5.4 West-east cross sections of block structures for ACH initial models with 7, full-thickness (100 km) layers. Velocity profiles are shown on the right, plotted in the same colour as the model filename, and are overlain on the velocity profile of the IASP91 model (Kennett & Engdahl, 1991) from which they were derived.

These models represent the coarsest parameterisation of the true Earth used in the study, but serve as adequate starting models to which subsequent layer-thinned models can be compared. An example of a model file is given in Appendix 23. No velocity information other than the IASP91 model is used in these starting models, since it is the variation from this standard model that we seek. For the purposes of raytracing within the inversion, the models were designed so that the upper-mantle discontinuity at ~410 km coincides with a layer boundary. It was found in this study

that the recommendation of ensuring roughly equal vertical travel time between layers should override that of attempting to place layer boundaries at major velocity discontinuities in the Earth. Significant instability resulted from attempting to place a boundary at the Moho by placing a thinner (~30-km) layer between a thin "special first layer" and a stack of ~100-km layers. Removal of the thin layer immediately remedied the instability.

The velocity for each layer in the initial model was defined as the velocity in the standard Earth model at the midpoint of the depth range of the layer. At crustal levels, the velocity profiles in Figure 5.4 deviate most substantially from the IASP91 profile, because crustal variations occur on a smaller vertical scale than can be accommodated in this thick-layered starting model. Trial runs suggested that the ACH tomography result is largely insensitive to the absolute value of velocities used in the initial model, which are less important for coherency between models than maintaining constancy of vertical travel time between layers. Nevertheless, it is logical to attempt to parameterise the Earth as accurately as possible. Figures 5.5 and 5.6 show the improvement in smoothing the of velocity profile that is gained by using thinner layers, along with the significant increase in number of blocks and hence computational demand.

5.2.3   *Geographical distribution of delay times*

The input data used for the ACH inversion is the set of relative travel time delays (equation 5.4). If an upcoming ray encounters a region of lower-than-average seismic velocity, compared to a ray which travels via an adjacent path which is unaffected, the travel time for the affected ray will increase, and its arrival time on the surface will be correspondingly late at the receiver station, relative to the unaffected ray. The reverse is true for a region of increased seismic velocity. In this study, we ignore resulting refraction effects. If we map the distribution of delays across the network of receivers, we obtain a first indication as to the nature of anomalies within the target volume. This is done by dividing the ray set into station-to-event azimuth (or backazimuth) "bins" and obtaining an average delay for each station, for each arrival direction. The results for the P and S datasets are shown in Figures 5.7 and 5.8.
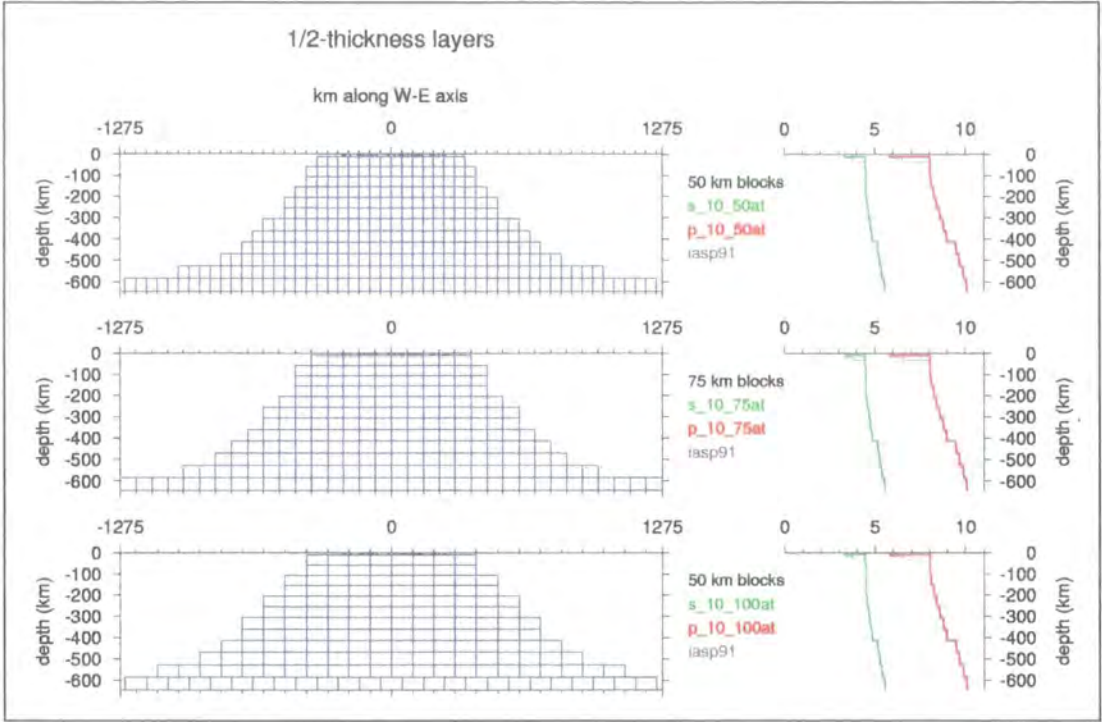
Figure 5.5 As for Figure 5.4 except for half-thickness-layer (~50 km) models.
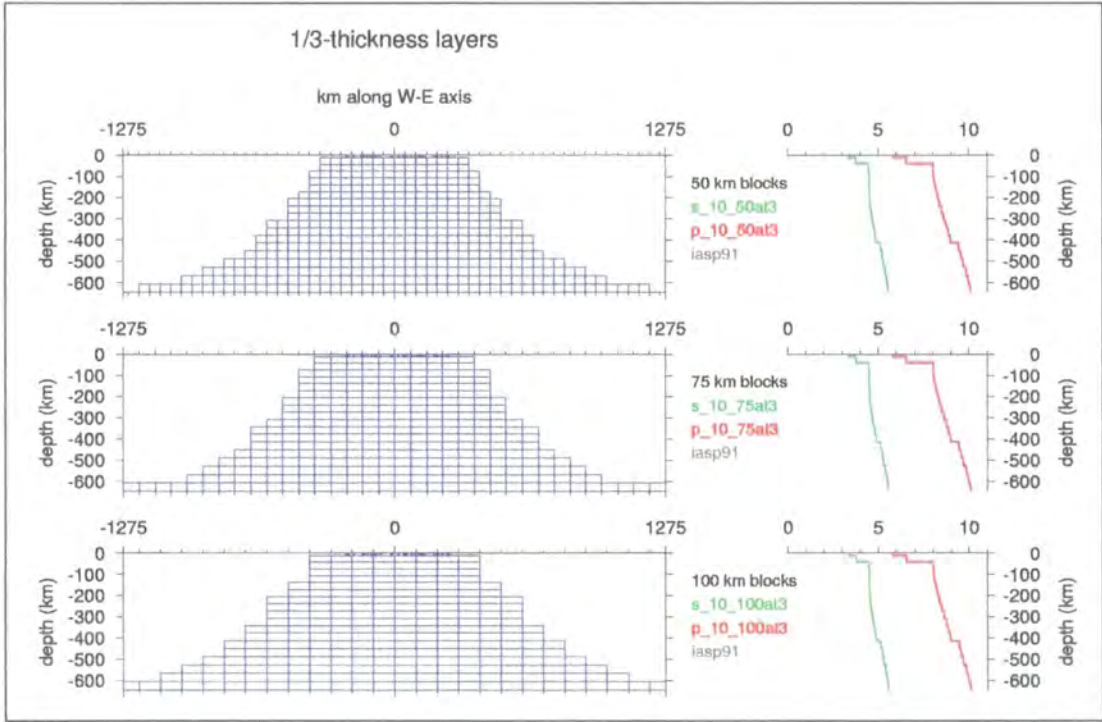
Figure 5.6 As for Figure 5.4 except for one-third-thickness-layer (~33 km) models.
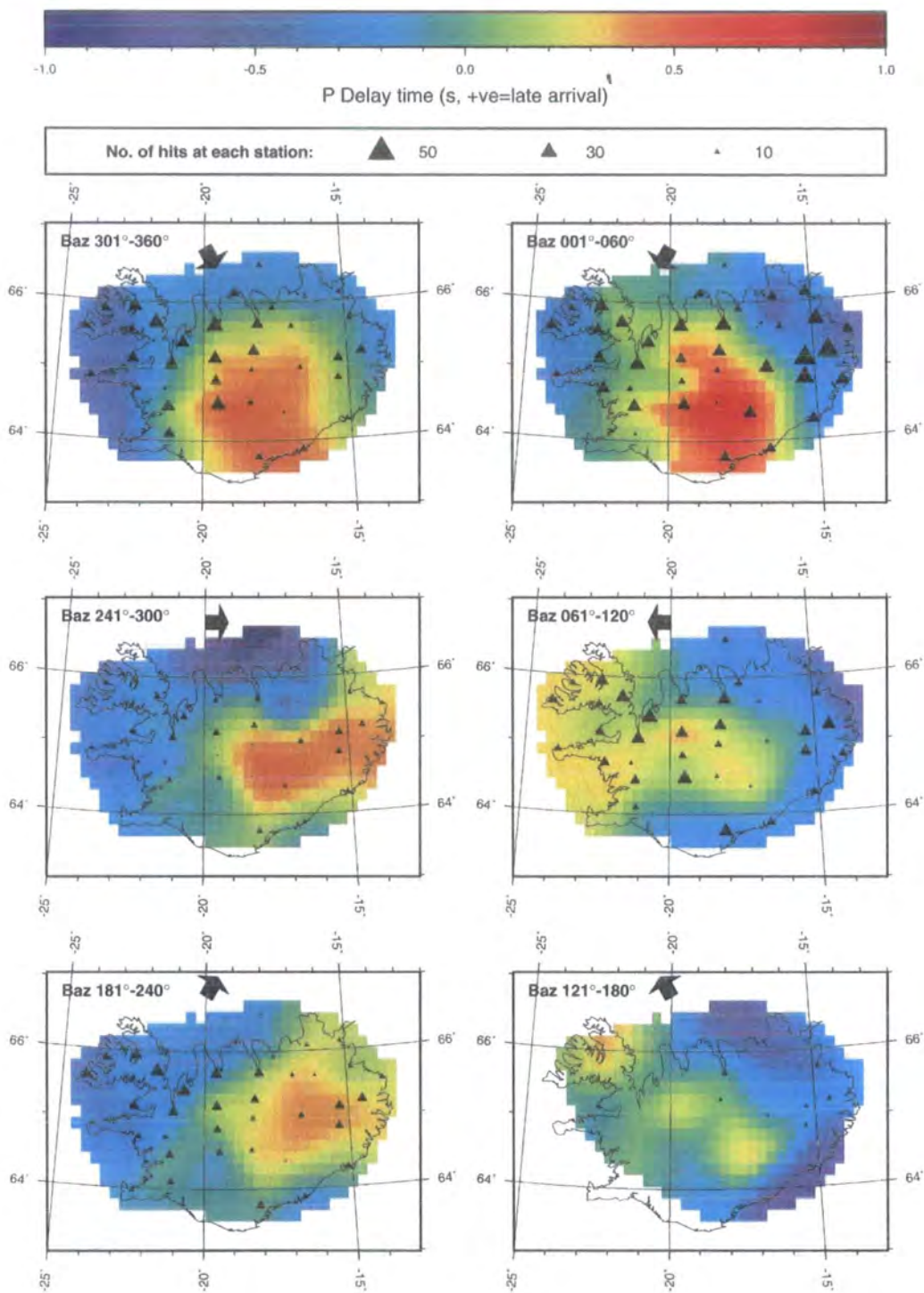
Figure 5.7 "Shadow" plots of delays from backazimuth ranges in the P-wave dataset. Yellow and red areas denote areas where average arrival times for a particular station are later than predicted, relative to other stations, while blue areas indicate relatively early arrivals. Black triangles indicate station locations and have a size proportional to the number of data at that receiver.
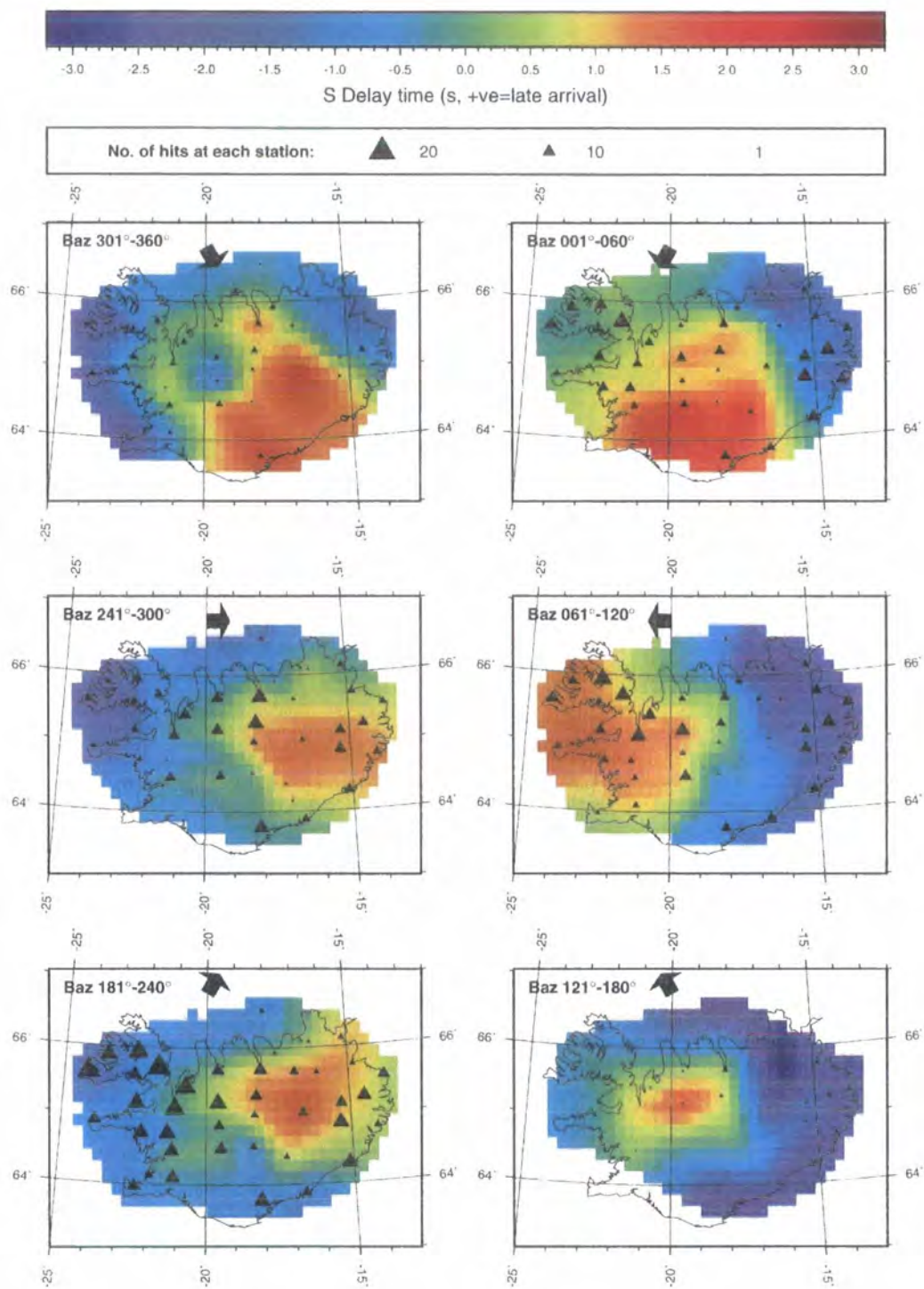
Figure 5.8 Same as Figure 5.7 except for the S-wave dataset. The colour scale has been multiplied by a factor of 3.2.

These plots illustrate the significant time delay associated with rays passing beneath Iceland, for rays from all azimuths. This confirms earlier observations of teleseismic delay times beneath Iceland (e.g. Long & Mitchell, 1970). The lack of rays from south-eastern backazimuths may contribute to the slightly weaker anomaly from that direction, but the result from other directions is strikingly consistent between P and S. Late arrivals are consistently found on the opposite side of Iceland from the arrival direction, e.g. rays from the south-west produce late arrivals at stations in the north-east. This suggests that the source of the anomalies is of limited lateral extent, located centrally beneath Iceland and exhibits some symmetry. This late-arrival "shadow" is likely to have been "cast" by a central region of low velocity.

The peak magnitude of these mean relative delay times is around 1 second for P and around 3 seconds for S. Some of this delay may well be attributable to differences in elevation between stations in the network, since these delay times are not corrected for station elevation at this stage. Stations in the highland interior of Iceland have elevations up to 1,760 m (at Grímsfjall, station HOT23). The elevation correction is performed later by the ACH inversion program. However, the result remains significant when we consider that low-lying stations e.g. those close to the coast, also have large residuals for rays from appropriate backazimuths. We may thus infer that these delays result from a low-velocity feature beneath the surface.

5.2.4 Damping parameter selection

The damping parameter has to be set for each initial model. This parameter is important, since it determines how much we require the final solution to fit to the data. Ideally, we wish to preserve the "real" features of the result, while avoiding over-fitting the model to noise in the data. This can be achieved by producing a set of models from a common initial model, varying only the damping parameter, and selecting a value which provides the best trade-off between residual variance (i.e. the fit of the resulting model to the data) and the squared length of the model vector $\hat{m}$.

Table 5.3 Comparison of 7-layer models for damping parameter selection.

P models						S models					
Model prefix	Damping parameter, θ	Squared model length	Data variance (s^2)	Residual variance (s^2)	Variance improvement (%)	Model prefix	Damping parameter, θ	Squared model length	Data variance (s^2)	Residual variance (s^2)	Variance improvement (%)
p_10_50_ (50 km blocks)	50	0.18	0.25	0.03	88.97	s_10_50_ (50 km blocks)	50	1.03	13.27	0.92	93.04
	100	0.12	0.25	0.03	87.90		100	0.66	13.27	1.07	91.91
	200	0.08	0.25	0.03	86.48		200	0.43	13.27	1.26	90.48
	300	0.06	0.25	0.04	85.47		300	0.33	13.27	1.40	89.47
	400	0.05	0.25	0.04	84.66		400	0.28	13.27	1.51	88.65
	600	0.04	0.25	0.04	83.38		600	0.22	13.27	1.68	87.34
	800	0.03	0.25	0.04	82.34		800	0.18	13.27	1.82	86.29
p_10_75_ (75 km blocks)	50	0.15	0.18	0.03	84.56	s_10_75_ (75 km blocks)	50	0.77	3.51	0.41	88.43
	100	0.10	0.18	0.03	83.73		100	0.50	3.51	0.44	87.60
	200	0.06	0.18	0.03	82.54		200	0.31	3.51	0.47	86.49
	300	0.05	0.18	0.03	81.65		300	0.24	3.51	0.50	85.69
	400	0.04	0.18	0.03	80.93		400	0.20	3.51	0.52	85.06
	600	0.03	0.18	0.04	79.79		600	0.15	3.51	0.56	84.06
	800	0.02	0.18	0.04	78.89		800	0.12	3.51	0.59	83.28
p_10_100_ (100 km blocks)	50	0.15	0.16	0.03	80.23	s_10_100_ (100 km blocks)	50	0.68	2.69	0.42	84.35
	100	0.10	0.16	0.03	79.27		100	0.41	2.69	0.44	83.53
	200	0.06	0.16	0.04	77.96		200	0.24	2.69	0.47	82.51
	300	0.04	0.16	0.04	77.02		300	0.18	2.69	0.49	81.83
	400	0.03	0.16	0.04	76.27		400	0.14	2.69	0.50	81.30
	600	0.02	0.16	0.04	75.15		600	0.11	2.69	0.52	80.52
	800	0.02	0.16	0.04	74.31		800	0.09	2.69	0.54	79.93

Table 5.3 shows output from thick-layered (7-layer) models for the three block sizes using a suite of damping values. Choosing the optimum trade-off is subjective. Damping trade-off curves for these models are shown in Figures 5.9 and 5.10.
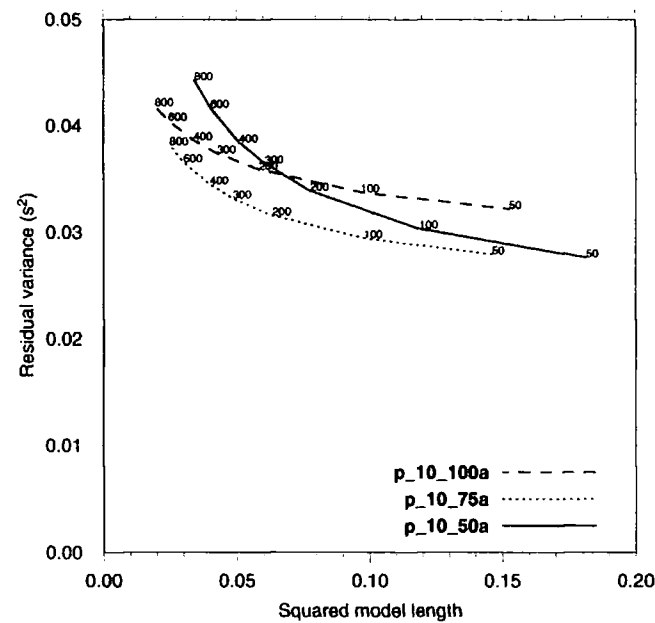
Figure 5.9 Damping trade-off curves for 7-layer P wave models.
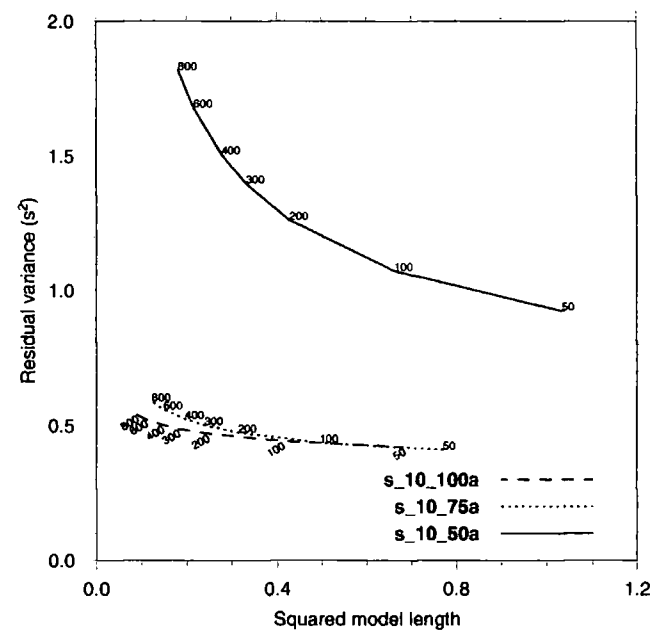
Figure 5.10 Damping trade-off curves for 7-layer S-wave models.

A reasonable trade-off is achieved for all the models with a damping parameter of 400 s^2/%^{2}, although this is subjective and depends to some extent on the plotting axes used for comparing models of different block size. The suitability of this value was later verified by checking that it did not distort significant features, i.e. those which persist between models using stronger damping. In this manner, 400 was found to be reasonable value to use for all the 7-layer initial models.

When selecting damping values for layer-thinned models, it must be appreciated that the damping parameter multiplies the length of the model, while the greater number of blocks also increases model length. A sensible approach is therefore to divide the damping parameter by approximately the same factor by which the number of modelled blocks has increased. For example, the number of modelled blocks in the 75-km block width, 7-layer model is 728, while this increases to 1,281 for the 13-layer model (50-km thick layers) and to 1,814 for the 19-layer model (33-km thick layers), giving damping parameters for these thinned models of 225 and 161 respectively. The numbers of blocks in the 50- and 100-km block width models increase in the same way, so that the damping parameters for these models must also be scaled by the appropriate factors. The damping parameters used were therefore 400 $s^2/\%^2$ for the 7-layer 100-km layer models, 225 $s^2/\%^2$ for 13-layer, 50-km layer models and 161 $s^2/\%^2$ for 19-layer, 33-km layer models.

The S-wave model s_10_50a exhibits unusual behaviour in that the residual variance remains very high compared to the other models. This may indicate that the lower limit of horizontal resolution is above the block size of 50 km used for this model.

5.2.5   The best result

The rest of this chapter describes a suite of inversions performed with different block widths and layer thicknesses, with and without offset-and-averaging. The preferred final model is the best compromise between too coarse a spatial parameterisation of the study volume, which under-uses the data, and too fine a parameterisation, resulting in a noisy result. The best results were offset-and-averaged models using 75-km wide blocks and layers 50 km thick (models p_10_75_225_av and s_10_75_225_av).

5.2.6   Thick-layered models

Figures 5.11 - 5.13 show horizontal sections through P-wave models p_10_100a, p_10_75a and p_10_50a, which represent models with 100-, 75- and 100-km block widths respectively, and which share the same initial thick-layered vertical structure. Figures 5.14 - 5.16 show the vertical cross sections through these models to a depth of 600 km. Figures 5.17 - 5.22 show the equivalent results for S-wave models s_10_100a, s_10_75a and s_10_50a.
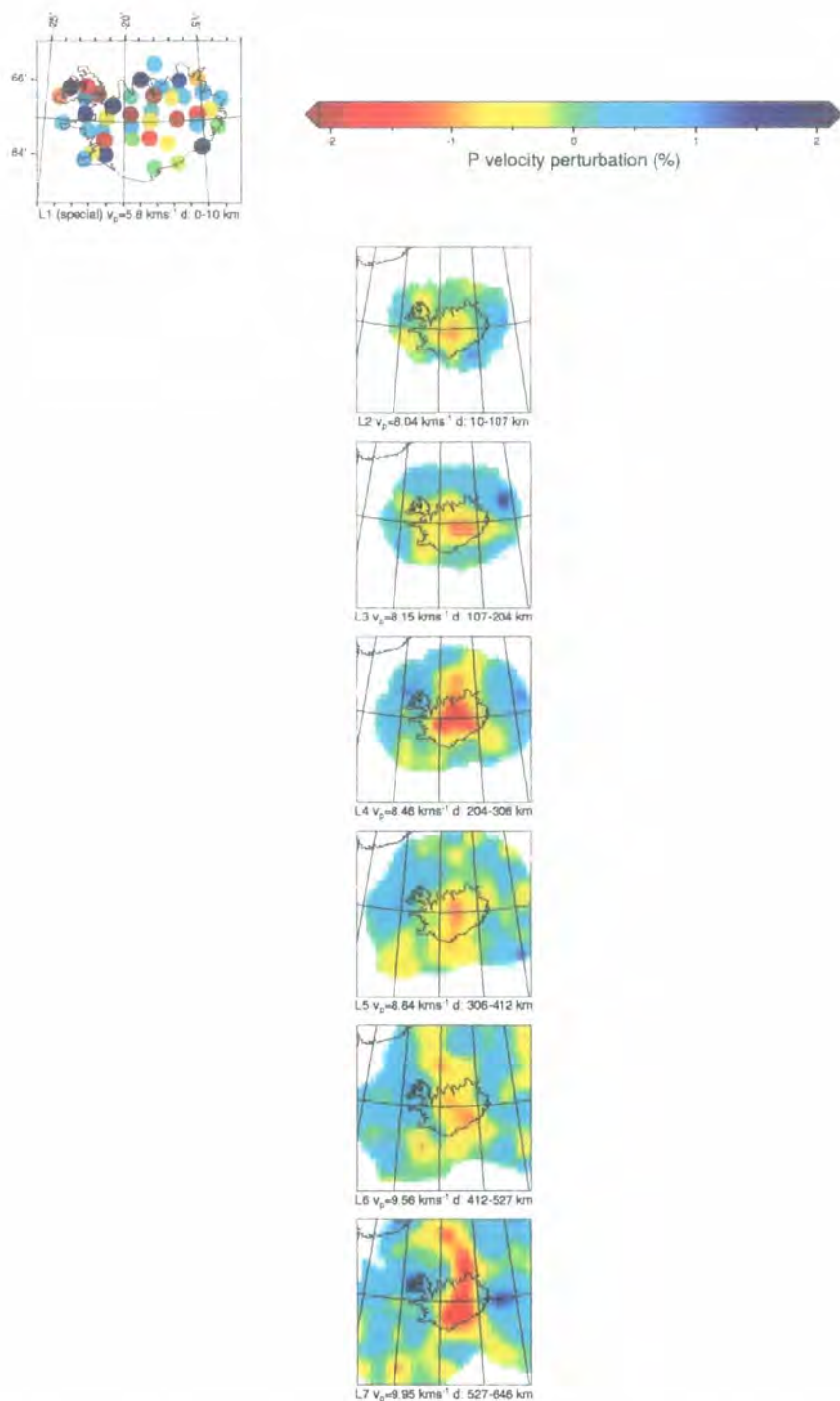
Figure 5.11 Horizontal sections through model p_10_100_400, showing the percent velocity perturbation of the modelled blocks relative to the initial velocity for each layer. The maps are plotted in azimuthal equidistant projection, thus preserving the angular and distance relationships between block centres (defined in kilometres east or north from a reference point) and the geographical location of the model centre. White areas of the maps represent regions with too few hits per block (<5) to be modelled. Perturbations for the "special first layer" are shown as circles at each station.

L1 (special) v_p=5.8 kms⁻¹ d: 0-10 km

P velocity perturbation (%)

L2 v_p=8.04 kms⁻¹ d: 10-107 km

L3 v_p=8.15 kms⁻¹ d: 107-204 km

L4 v_p=8.46 kms⁻¹ d: 204-306 km

L5 v_p=8.84 kms⁻¹ d: 306-412 km

L6 v_p=9.56 kms⁻¹ d: 412-527 km

L7 v_p=9.95 kms⁻¹ d: 527-646 km
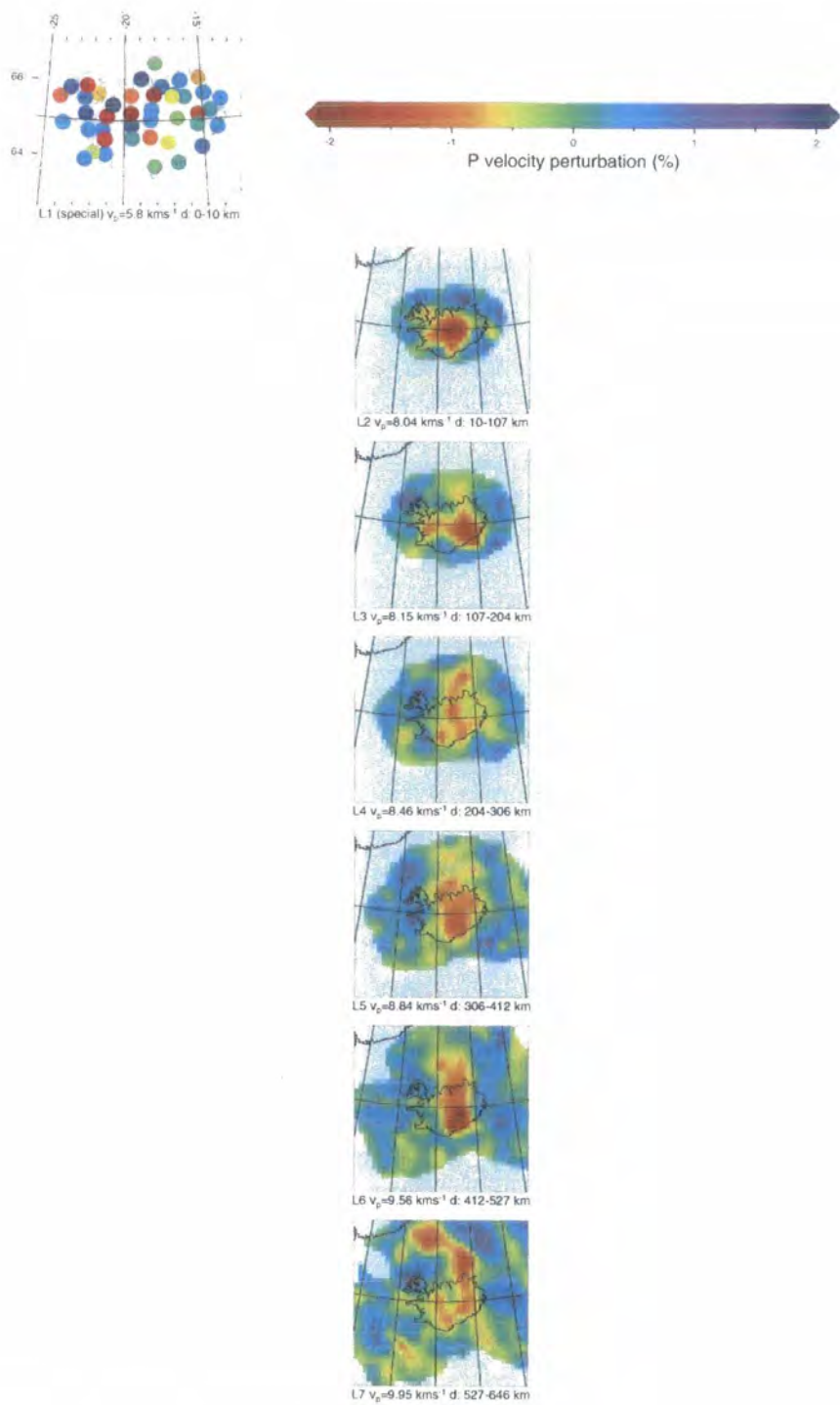
Figure 5.12 As for Figure 5.11 except for model p_10_75_400.
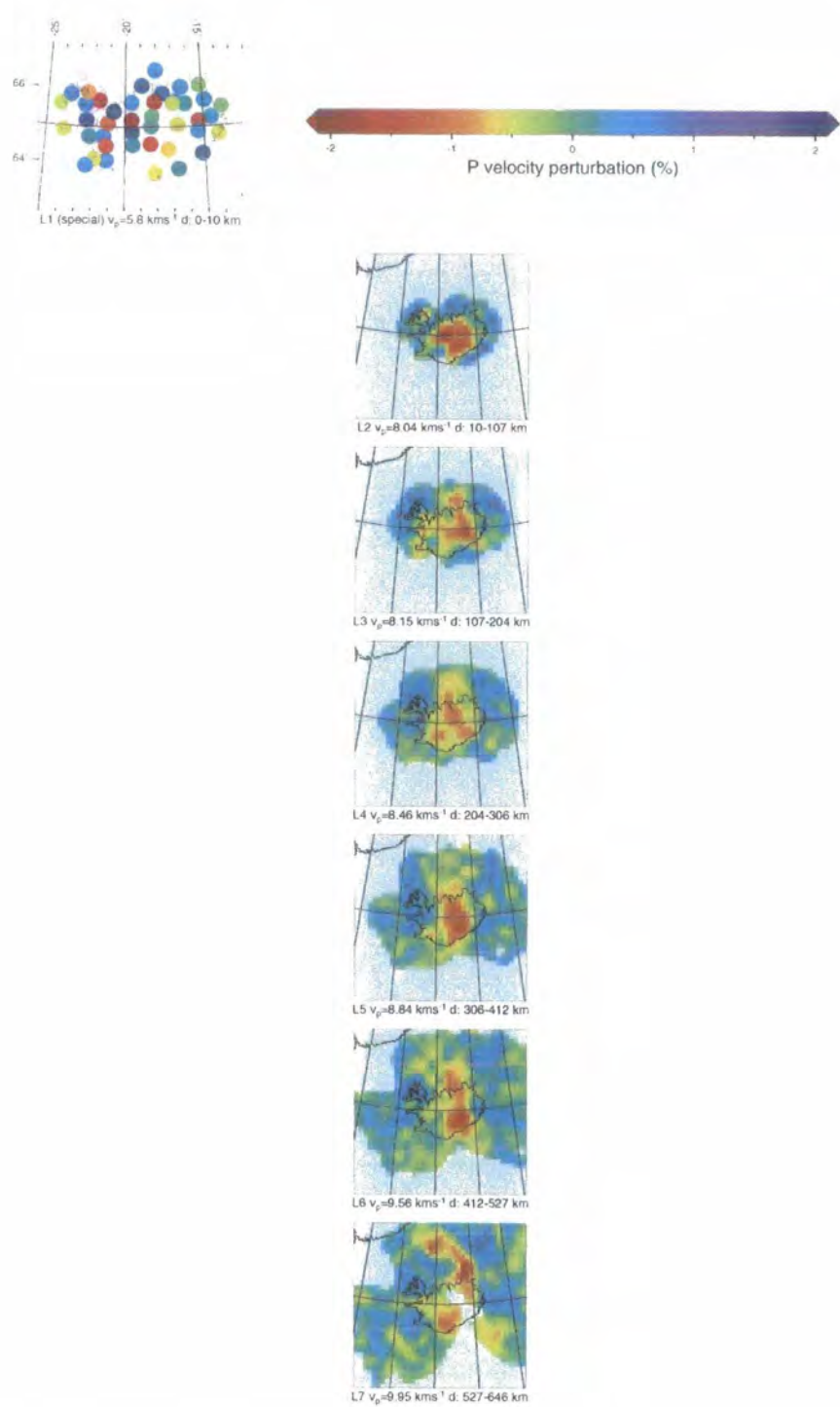
Figure 5.13 As for Figure 5.11 except for model p_10_50_400.
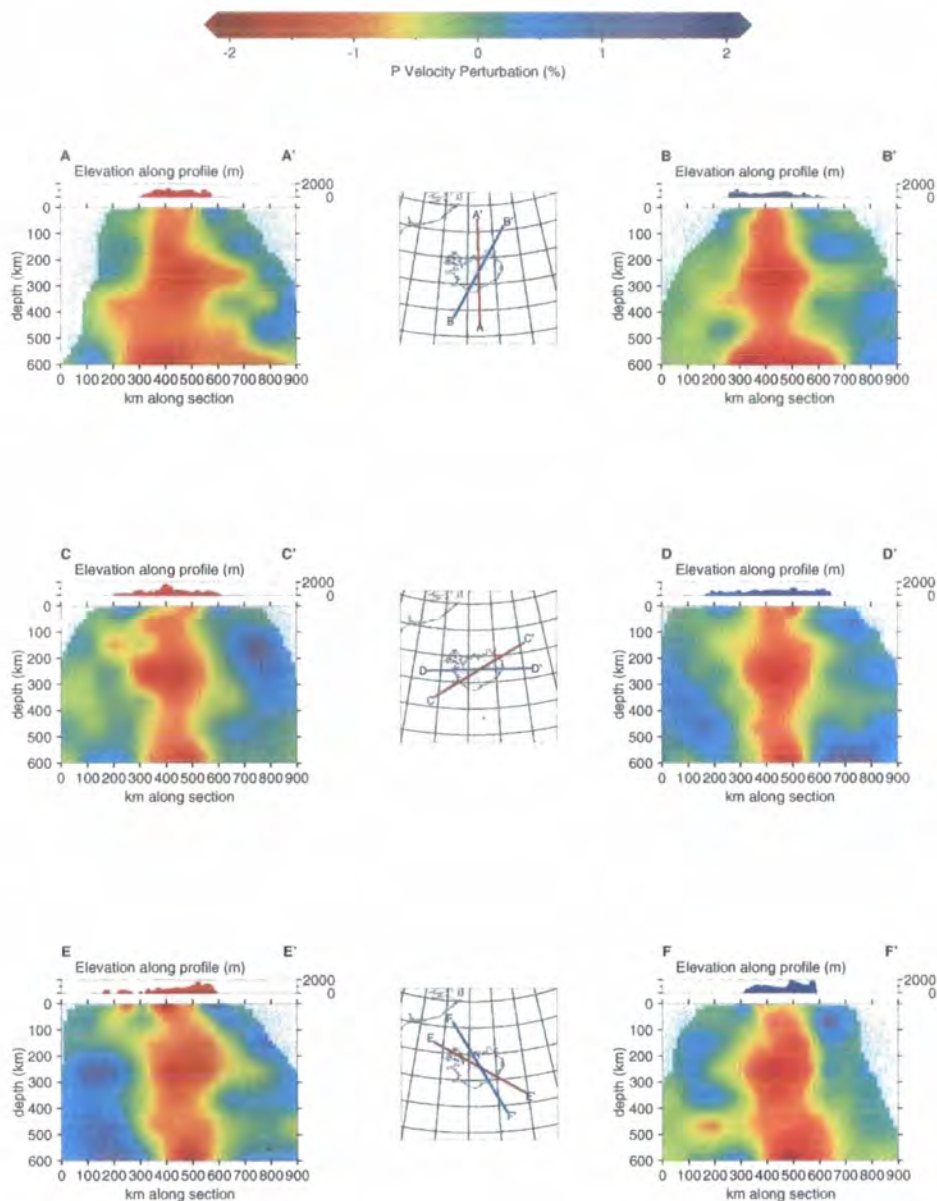
Figure 5.14 Vertical sections through model p_10_100_400 taken along profiles at 30° intervals. The elevation profile along the line of each section is given above the section plot and the locations of the lines of section are shown in the maps in the centre column.

Figure 5.15 As for Figure 5.14 except for model p_10_75_400.
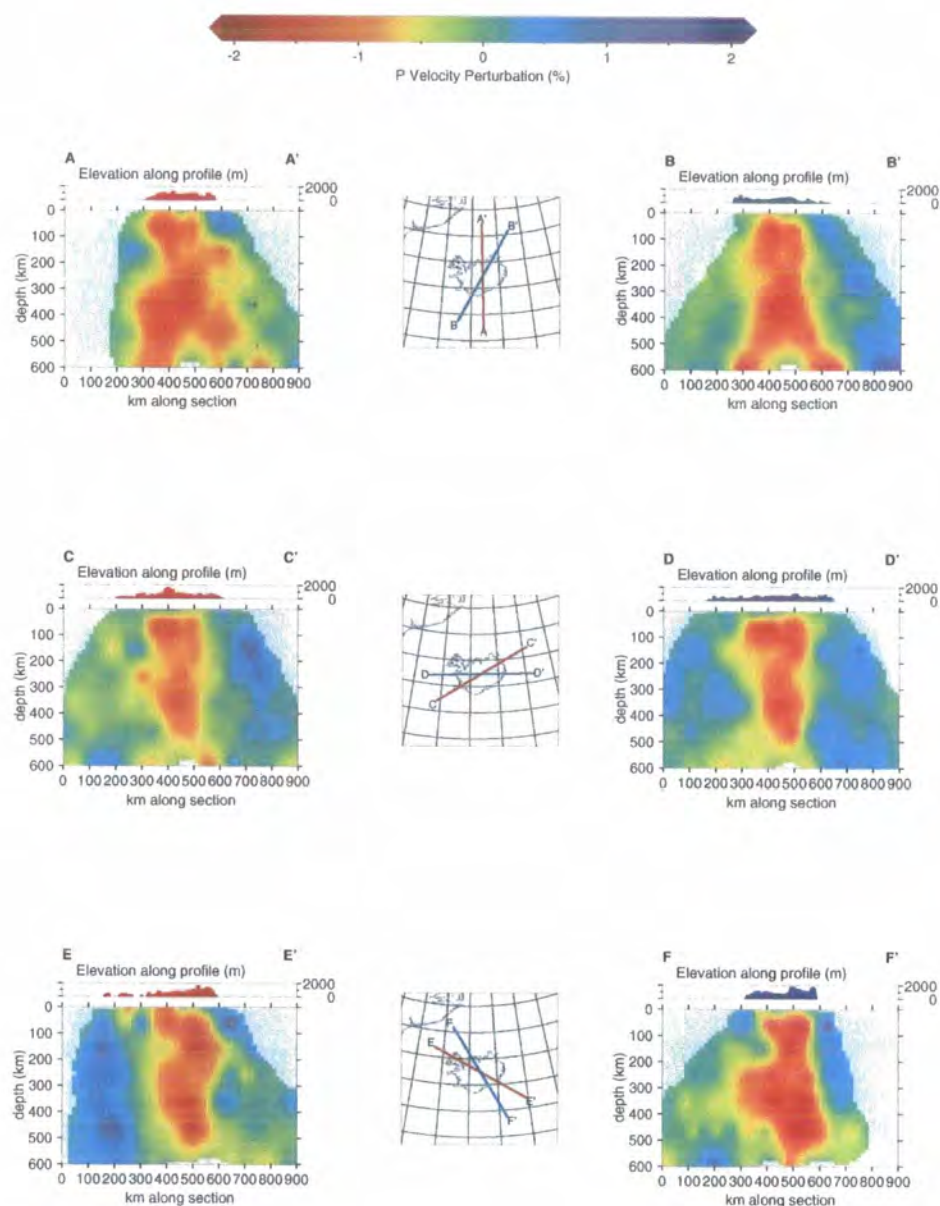
Figure 5.16 As for Figure 5.14 except for model p_10_50_400.
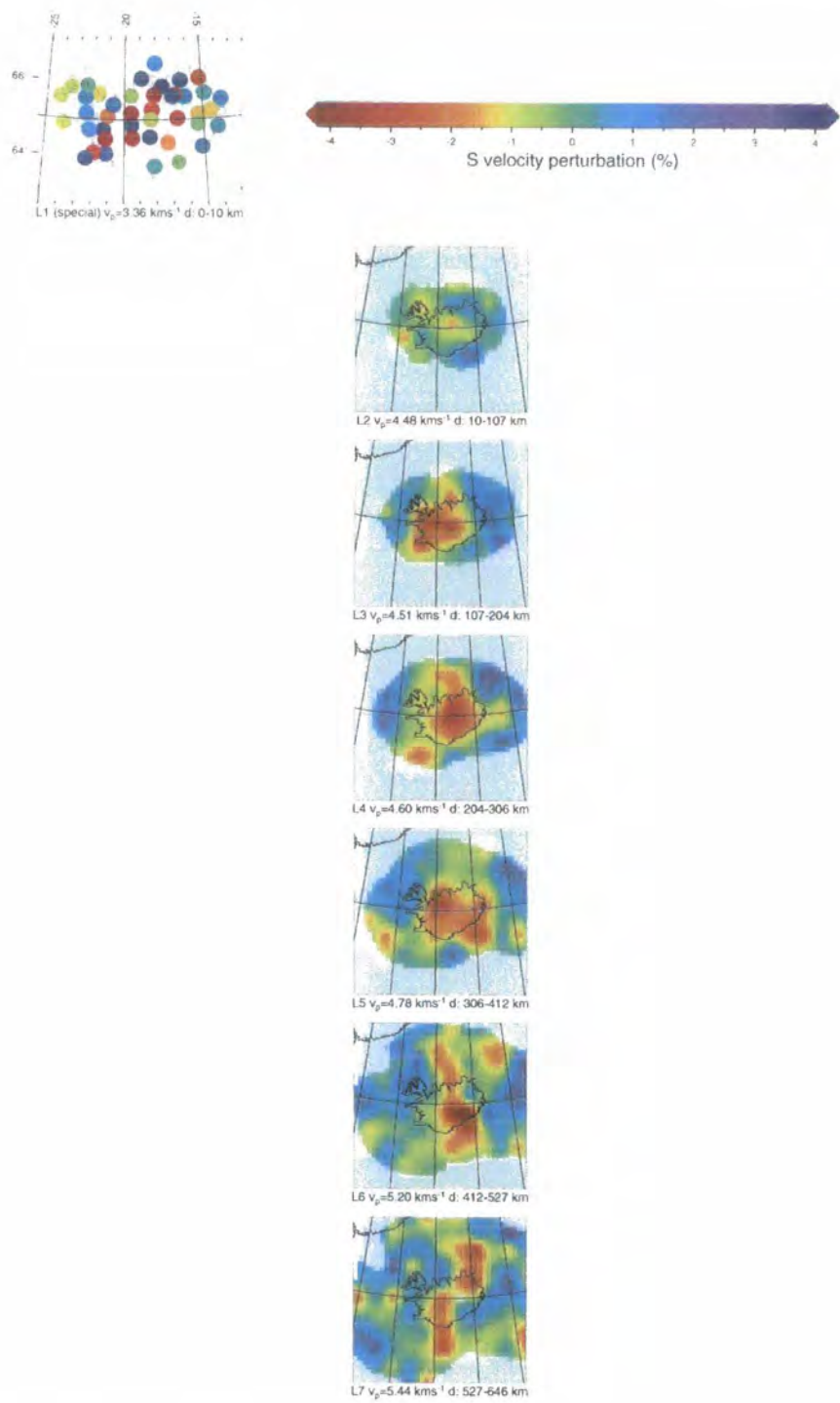
Figure 5.17 As for Figure 5.11 except for model s_10_100_400.
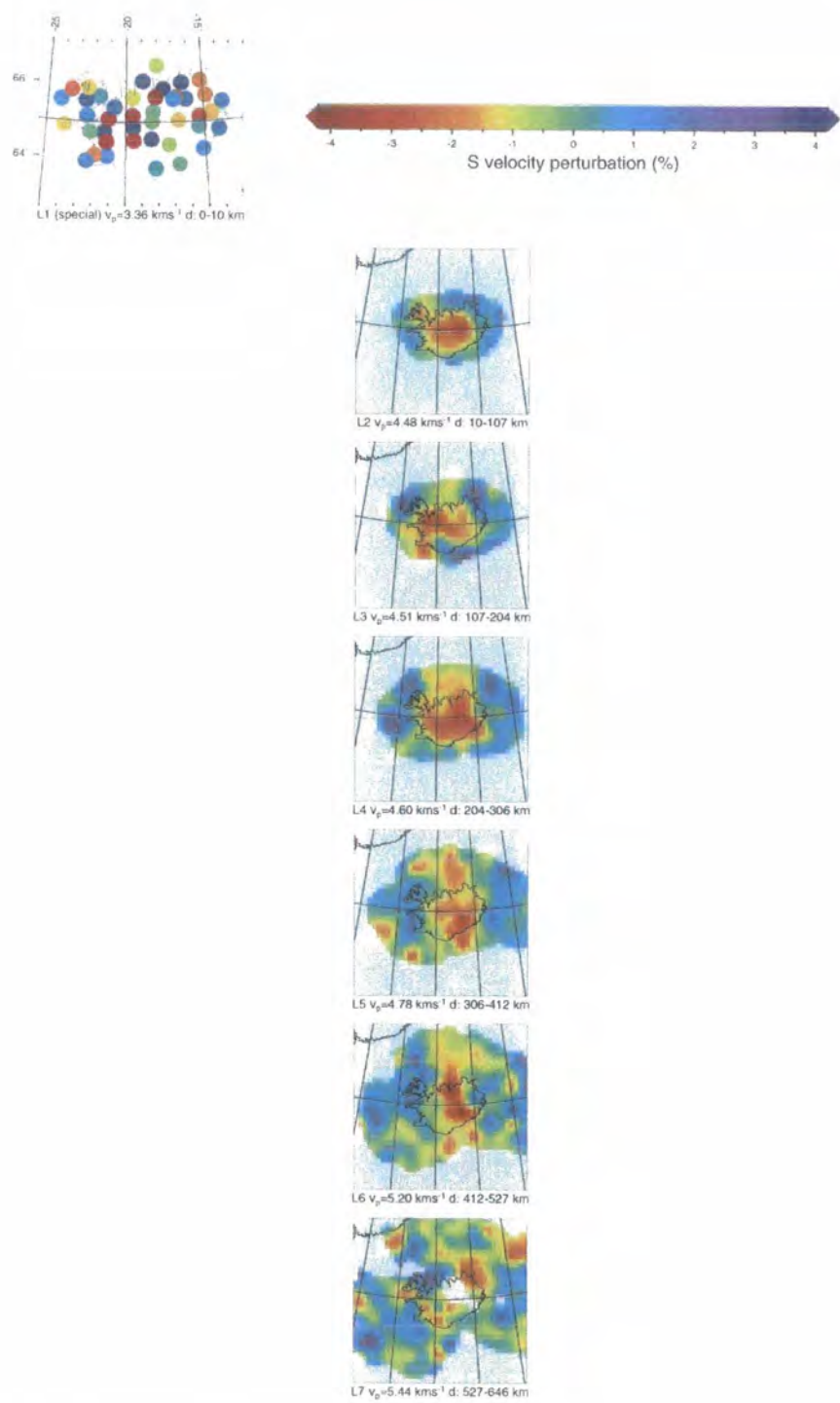
Figure 5.18 As for Figure 5.11 except for model s_10_75_400.
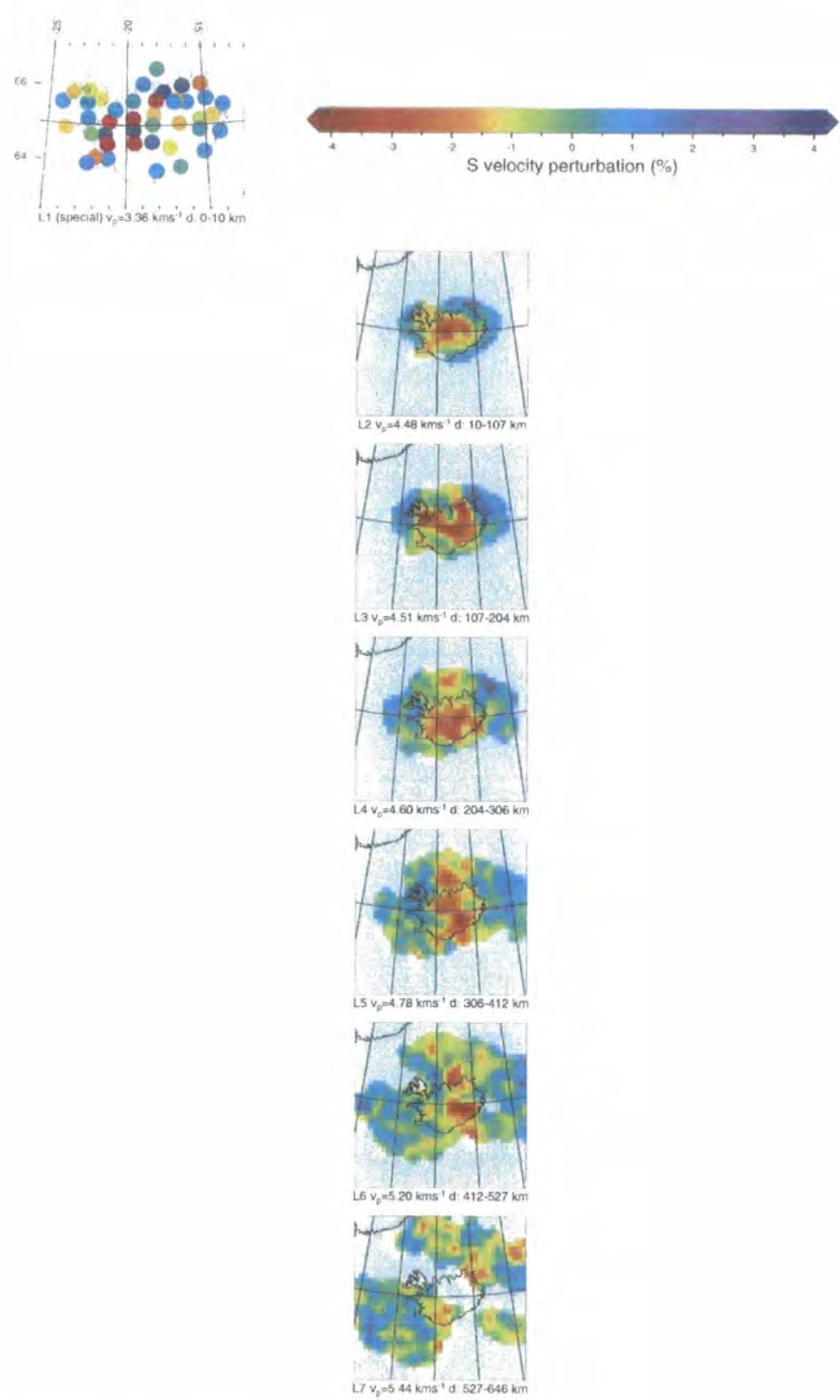
Figure 5.19 As for Figure 5.11 except for model s_10_50_400.
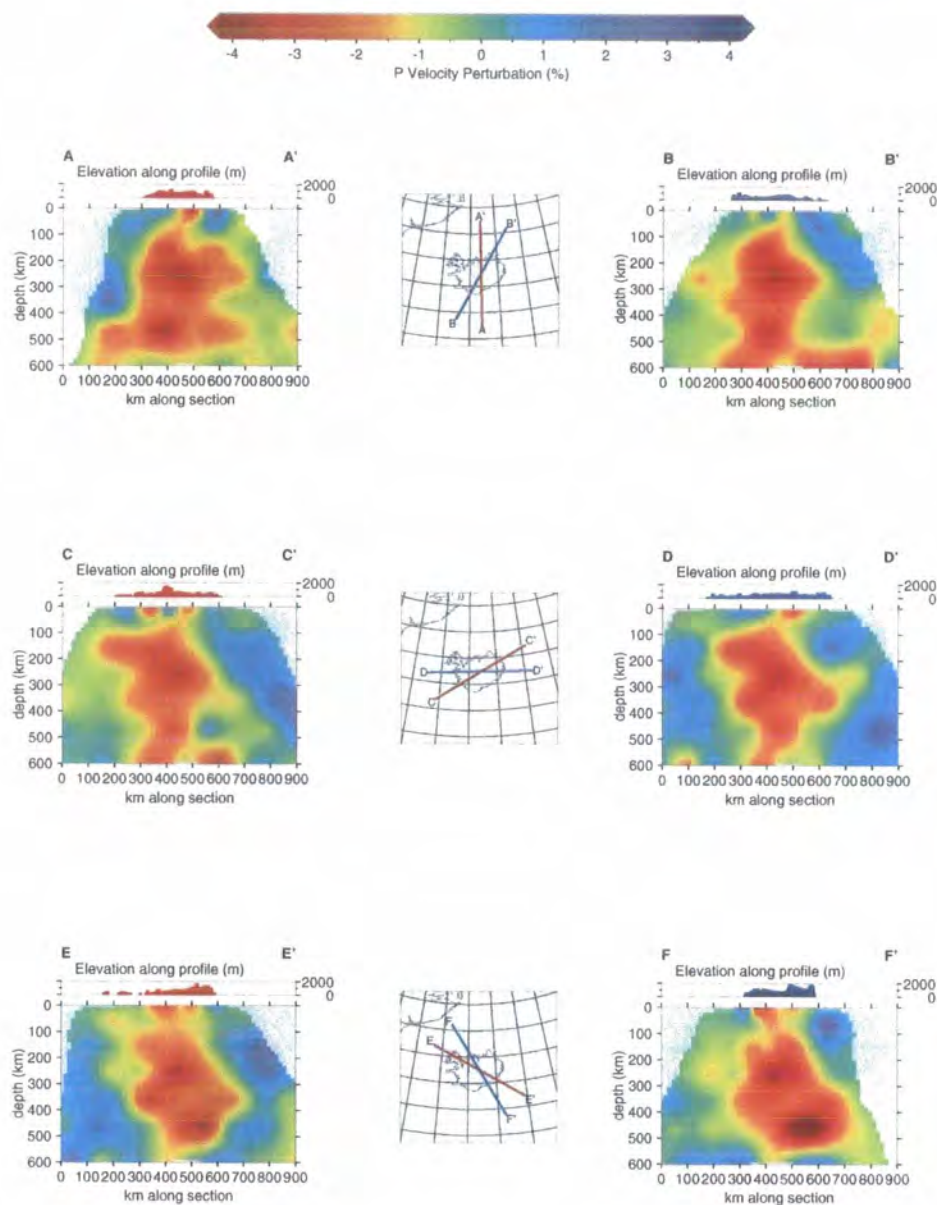
Figure 5.20 As for Figure 5.14 except for model s_10_100_400.
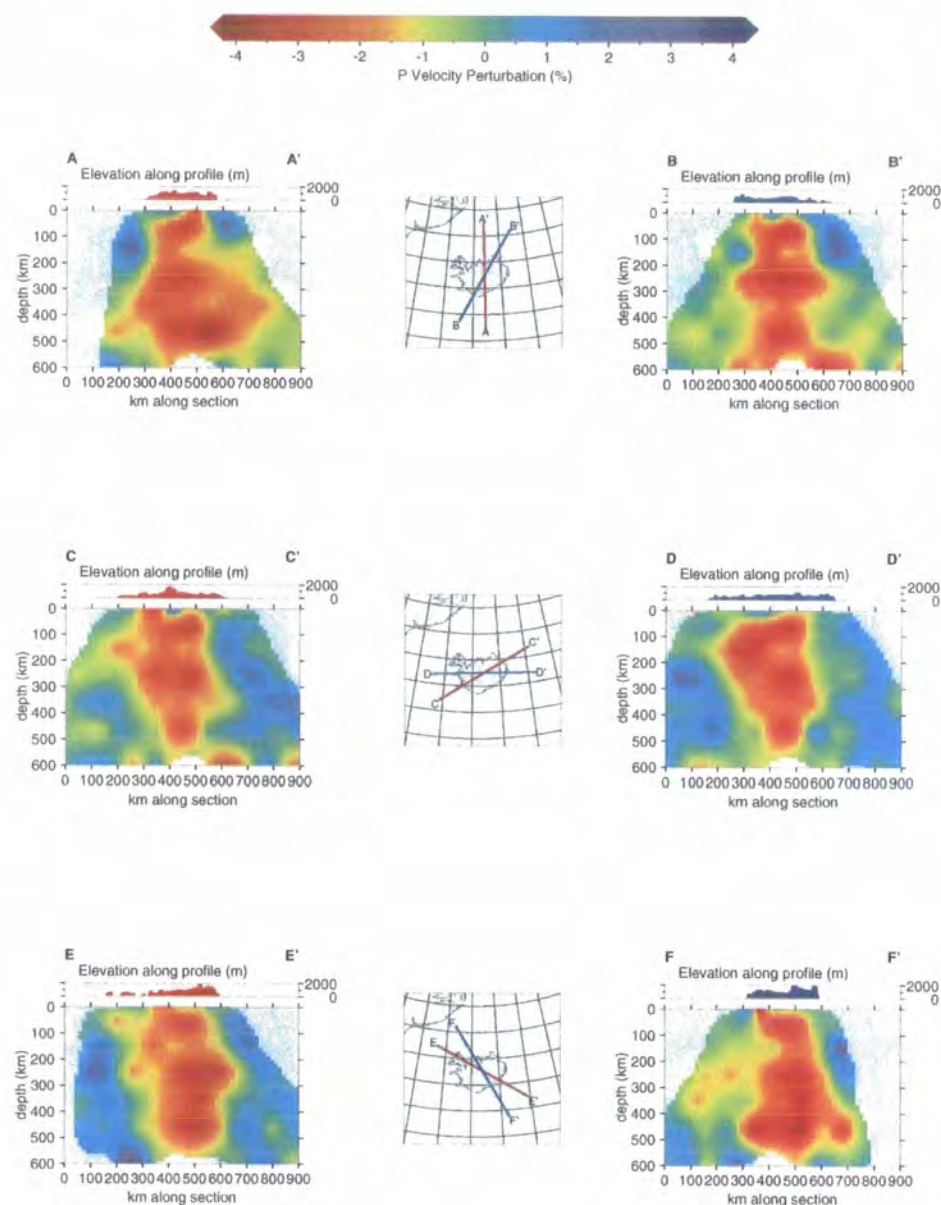
Figure 5.21 As for Figure 5.14 except for model s_10_75_400.
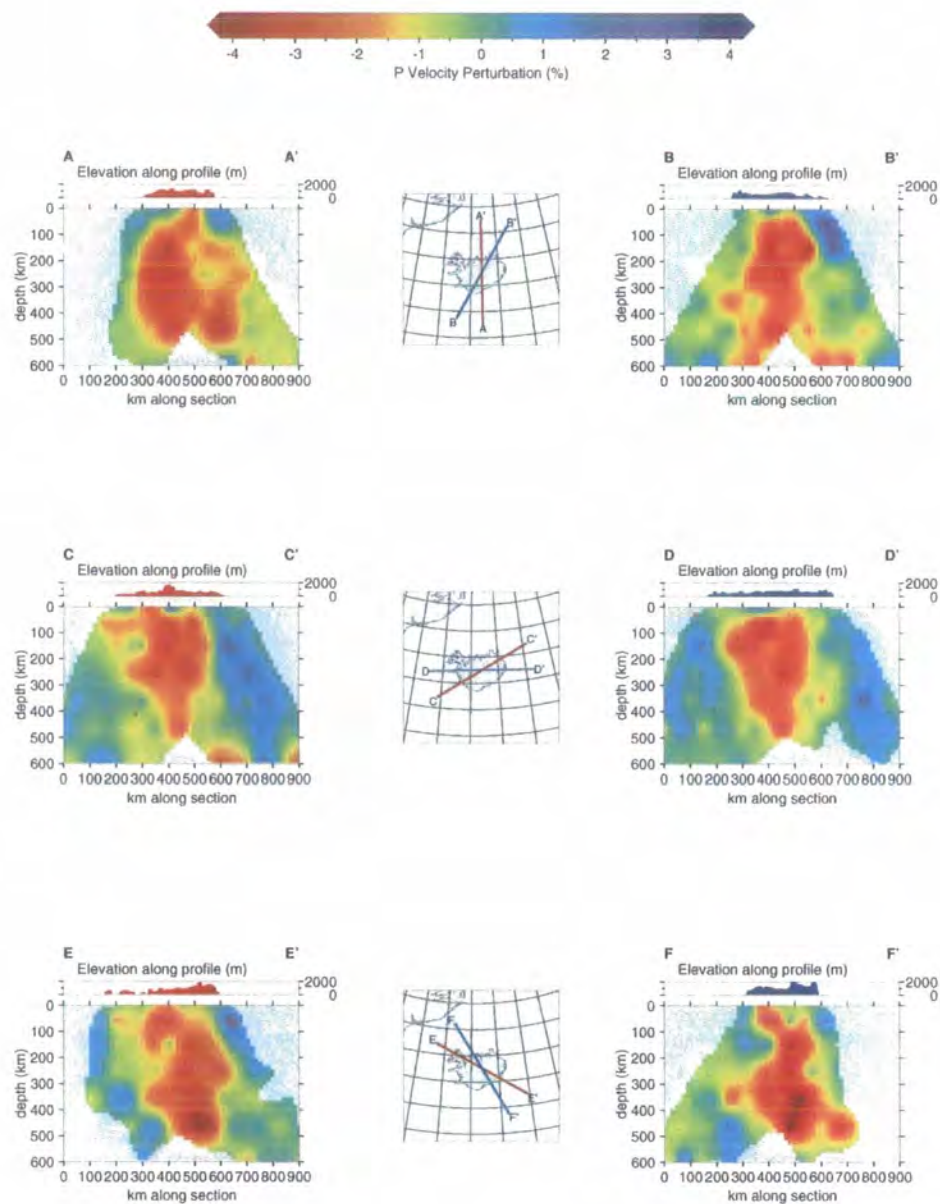
Figure 5.22 As for Figure 5.14 except for model s_10_50_400.

The most striking, first-order feature of these models is a prominent negative velocity perturbation of up to 2.7 % for P and up to 4.9 % for S, centred on east-

central Iceland and present, though showing some variation in amplitude, down to at least layer 6 (412-527 km depth). The roughly axially-symmetric core of this feature is around 100-130 km wide, although the symmetry of the overall anomaly changes from axial to planar with increasing depth. The presence of the anomaly in layer 7 (527-646 km) is strong evidence that it persists even at these great depths, but the divergent nature of the ray set at this depth means that this result is less reliable and any interpretation of such deep features must be treated with caution.

A secondary feature is the linear extension of the negative velocity anomaly to the south-west in layer 3 (107-204 km). Although there may be some evidence for a continuation of this feature in layer 4 (e.g., model s_10_75_400, Figure 5.18), it is not continuous with depth and appears as a branch-like horizontal feature in the vertical cross sections, best exposed in section CC' of the 75-km block-width models p_10_75_400 (Figure 5.15) and s_10_75_400 (Figure 5.21).

A low-velocity feature present in both P and S models extends northwards from northern Iceland. This feature begins in layer 2 and is more persistent with depth. When viewed in cross section (e.g. section AA' of model p_10_75_400, Figure 5.15), it can be seen to extend some 550 km in the north-south direction. The overall shape of the anomaly is therefore different in west-east and north-south profile (e.g., sections AA' and DD' of model p_10_75_400, Figure 5.15). The central, columnar anomaly does not widen significantly with depth other than in the north-south direction, particularly when considering the central (red) core of the feature, which is most significant. In layer 7, this north-south-trending anomaly develops into an arcuate feature, although at this depth it is unlikely that blocks have been sampled well enough for this feature to be significant. The blank areas of the S-wave layer sections at this depth, especially at the 50- and 75-km block sizes (Figures 5.18 and 5.19), reveal significant gaps in the ray bundle, which contribute to the dispersed anomaly pattern which is common to all models in this lowest layer. The reason for including this layer in the inversion is to demonstrate the practical limit on the depth to which the results should be interpreted.

The strong velocity anomalies which saturate the velocity scale in the "special first layer" indicate strong heterogeneity in the crust. In nearly all the plots presented here, e.g. Figures 5.12 and 5.18, for both P and S, certain stations

consistently have strong anomalies in the special first layer, in particular stations HOT27 and HVE (Figures 3.1 and 3.4). Consistently, station HOT27 shows a strong low-velocity perturbation, which changes to high beneath HVE and, in S models such as s_10_75_400 (Figure 5.18), back to low for station HOT28 to the south. This was also noticed at a seismic station located near to HOT27 by workers in a previous study (I. Bjarnason, *pers. comm.*)

5.2.7   Thick-layered models with horizontal smoothing

Figure 5.24 to Figure 5.35 show these thick-layered models with horizontal smoothing applied using an offset-and-average method (Evans & Achauer, 1993). The original assemblage of blocks was offset by half a block in each direction along each axis. Inversions were performed for each assemblage and the resulting "pseudo-model", consisting of 4 small blocks for each original large one, has velocity perturbations which are the average of the 4 values corresponding to each small block.
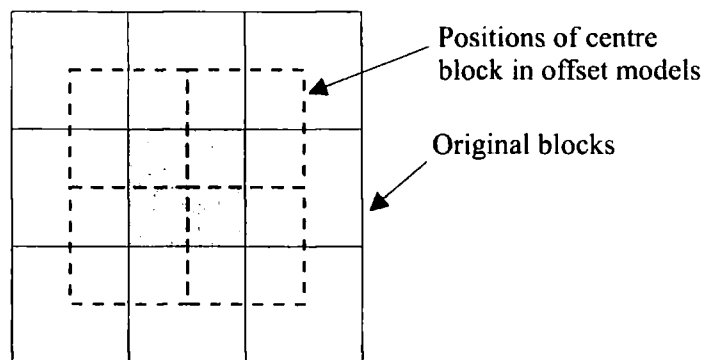
Figure 5.23 Offset-and-averaging procedure. An original model (centre block shaded) was offset by half a block width in each direction. The dashed squares represent the positions of the centre square in each of the offset models.
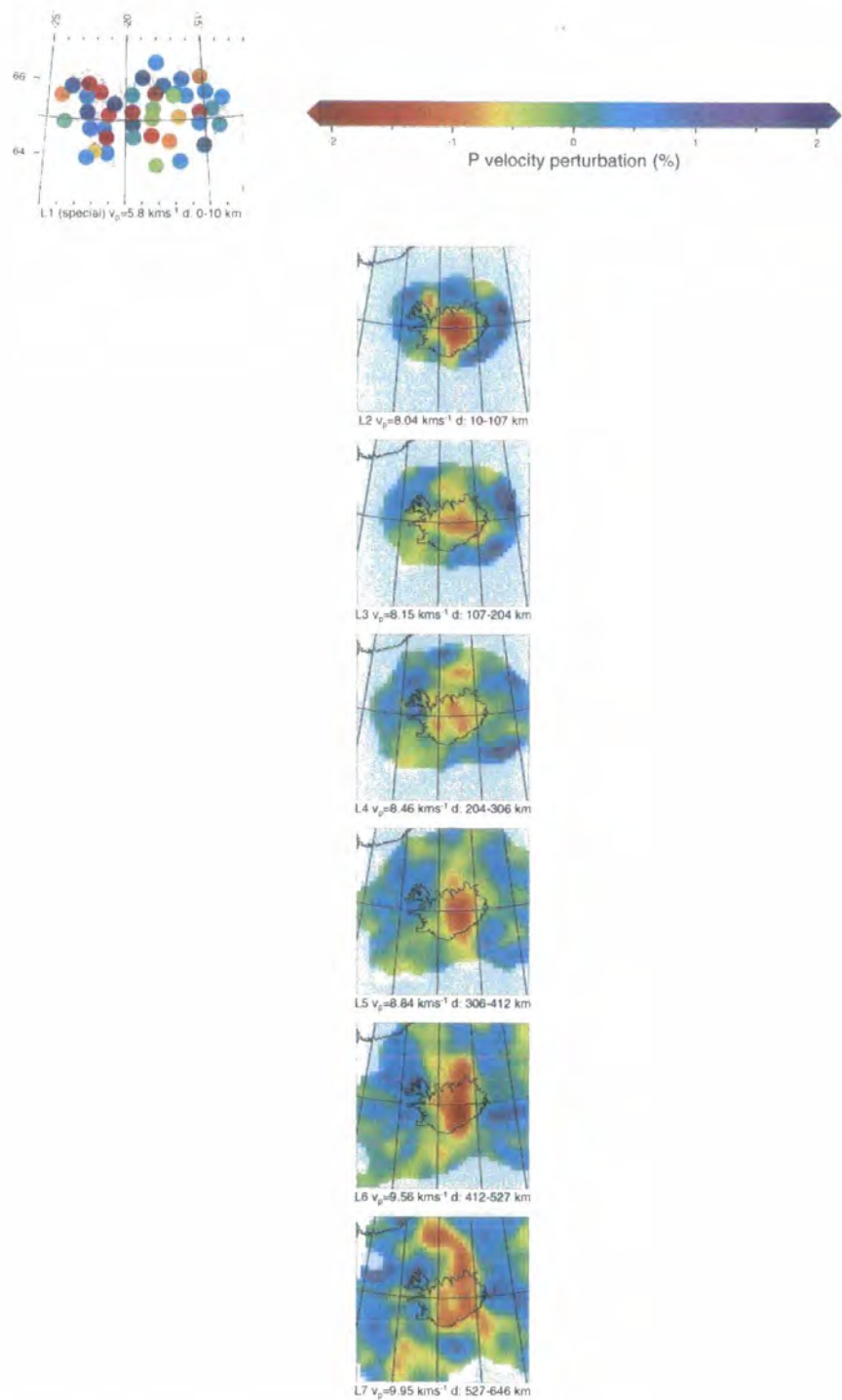
Figure 5.24 As for Figure 5.11 except for model p_10_100_400_av.
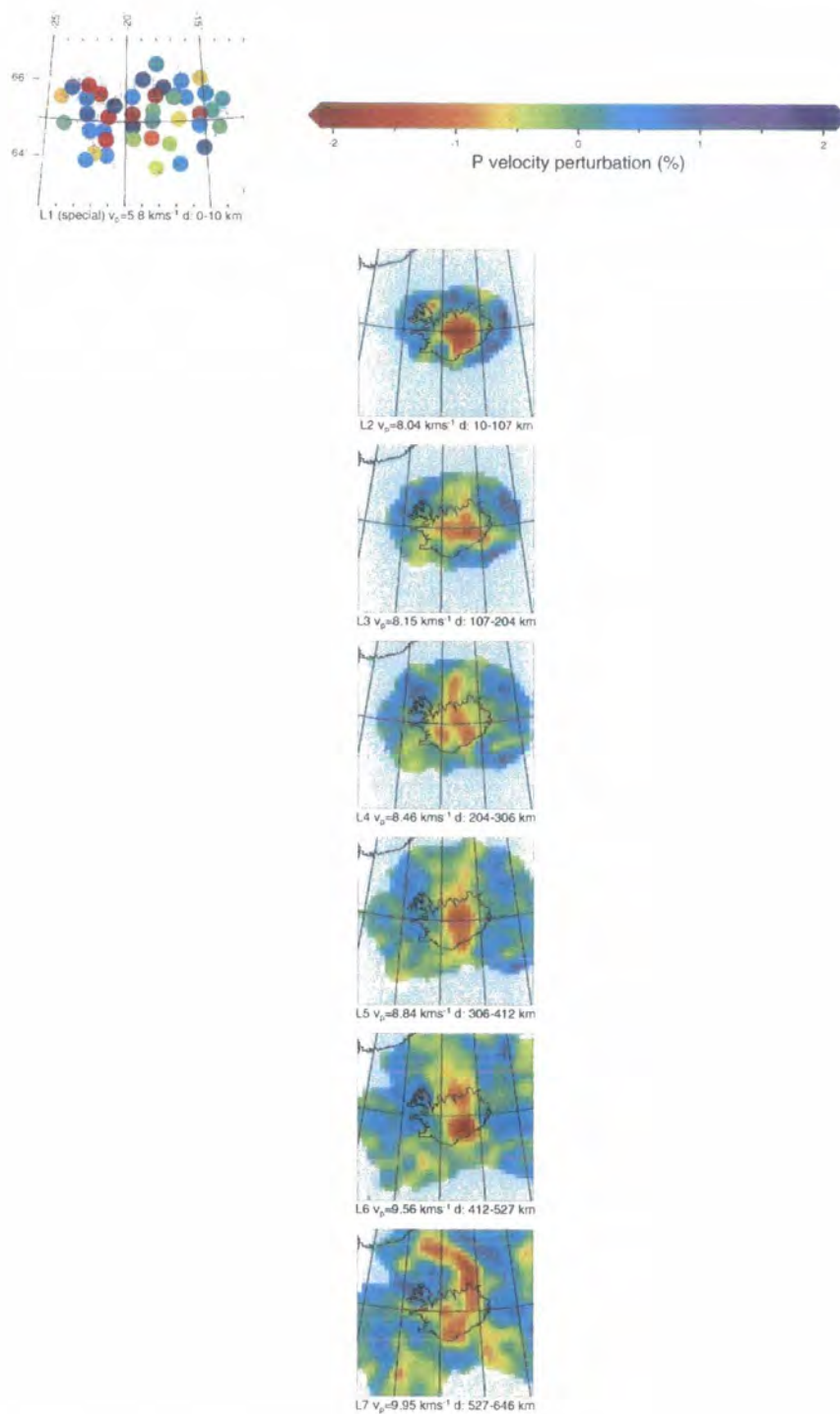
Figure 5.25 As for Figure 5.11 except for model p_10_75_400_av.

L1 (special) v_p=5.8 kms⁻¹ d: 0-10 km

P velocity perturbation (%)

L2 v_p=8.04 kms⁻¹ d: 10-107 km

L3 v_p=8.15 kms⁻¹ d: 107-204 km

L4 v_p=8.46 kms⁻¹ d: 204-306 km

L5 v_p=8.84 kms⁻¹ d: 306-412 km

L6 v_p=9.56 kms⁻¹ d: 412-527 km

L7 v_p=9.95 kms⁻¹ d: 527-646 km
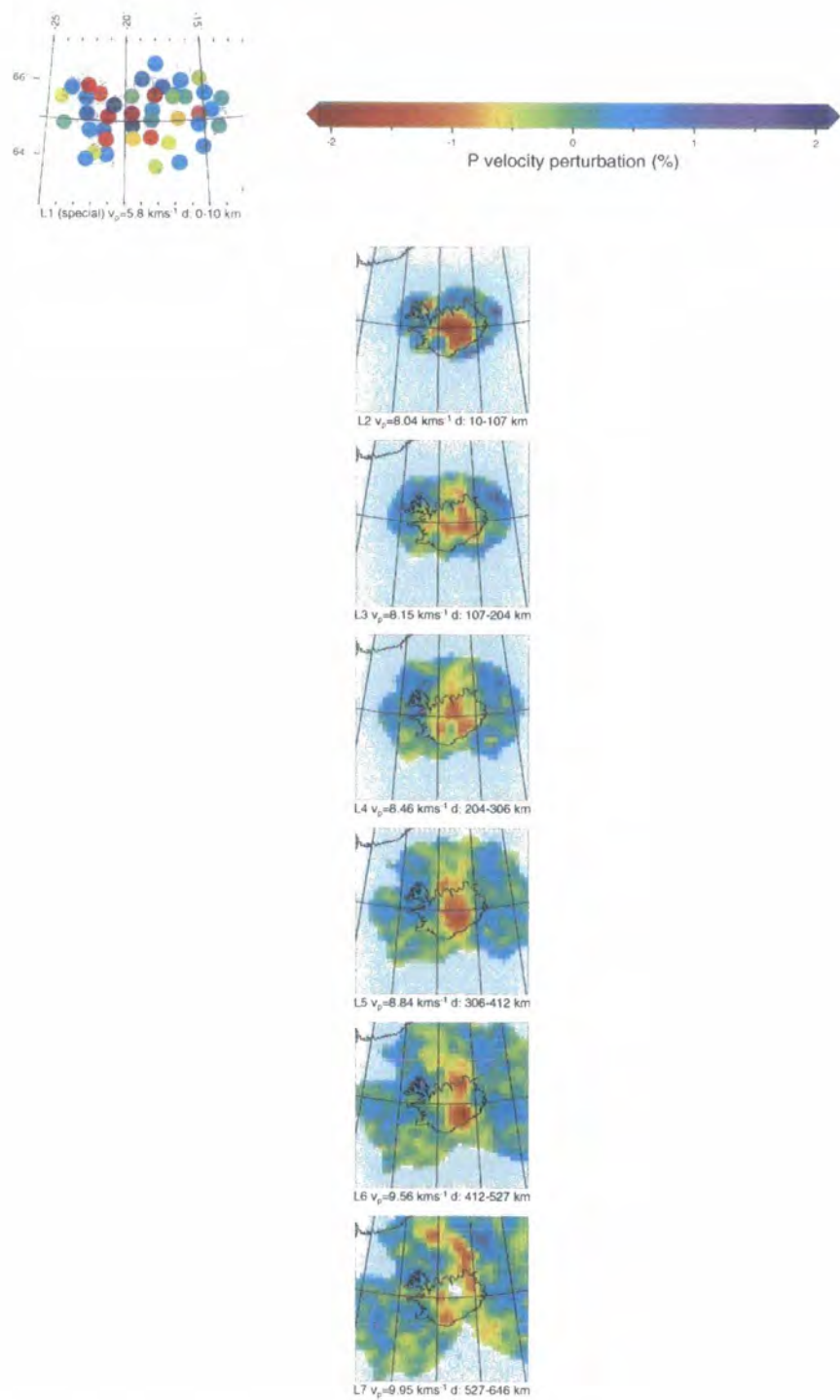
Figure 5.26 As for Figure 5.11 except for model p_10_50_400_av.
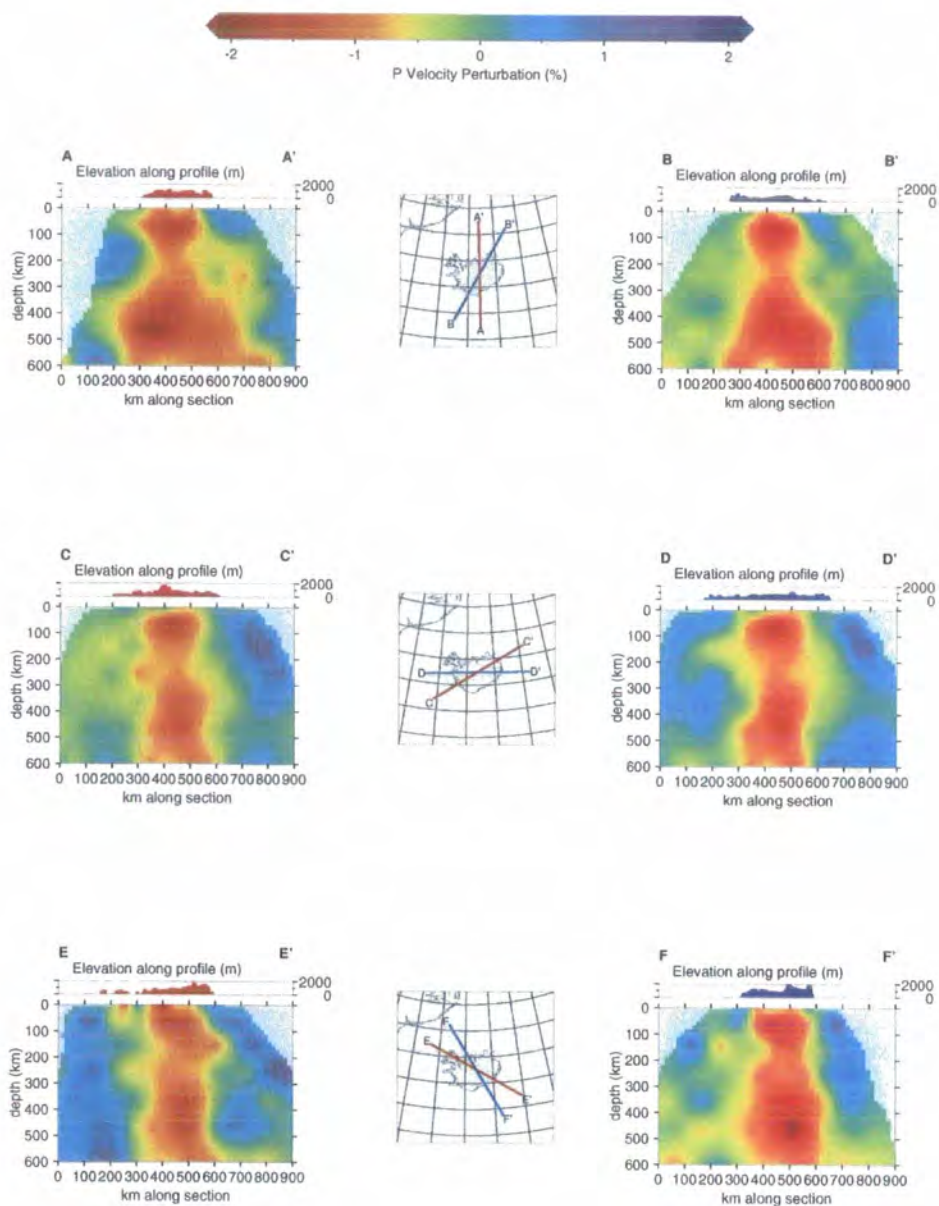
Figure 5.27 As for Figure 5.14 except for model p_10_100_400_av.
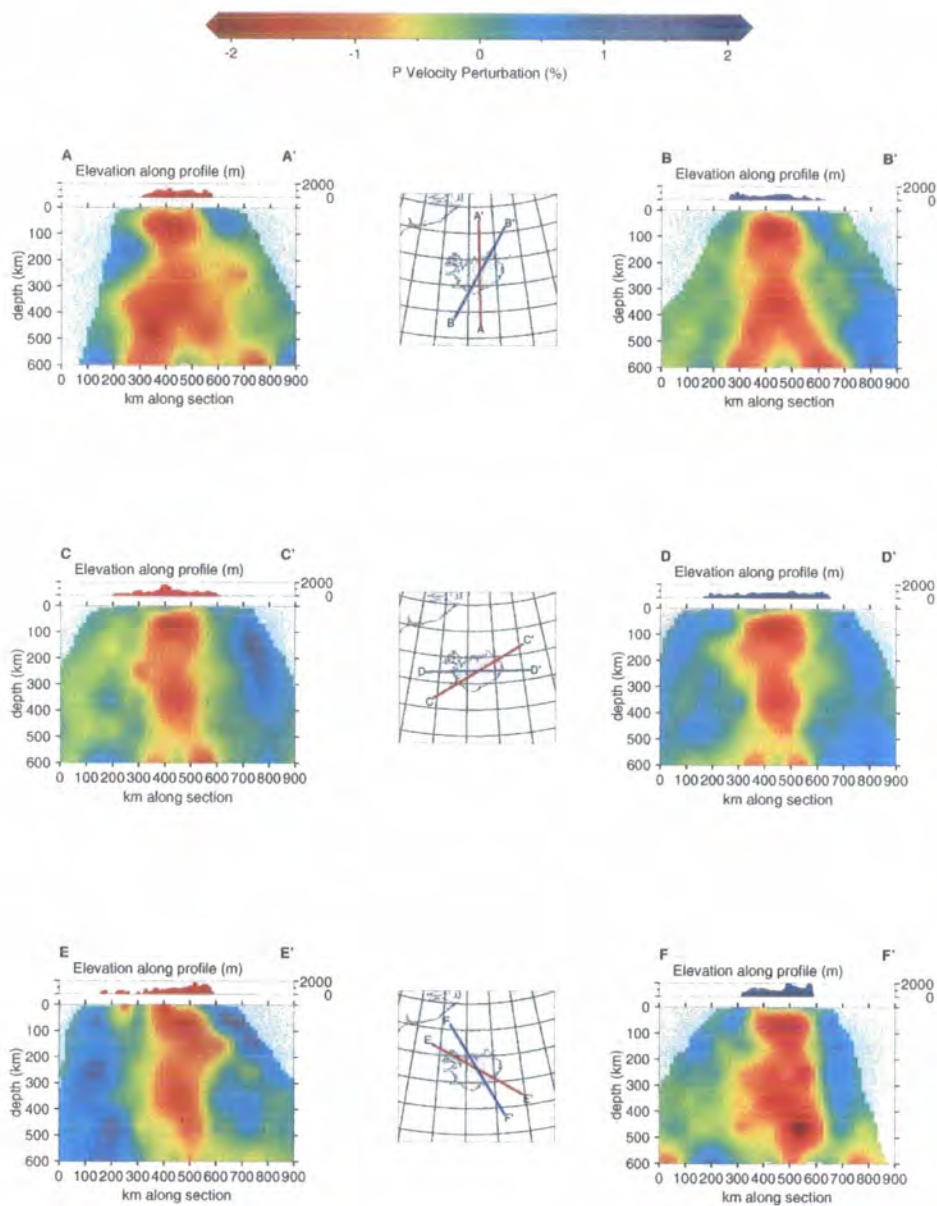
Figure 5.28 As for Figure 5.14 except for model p_10_75_400_av.
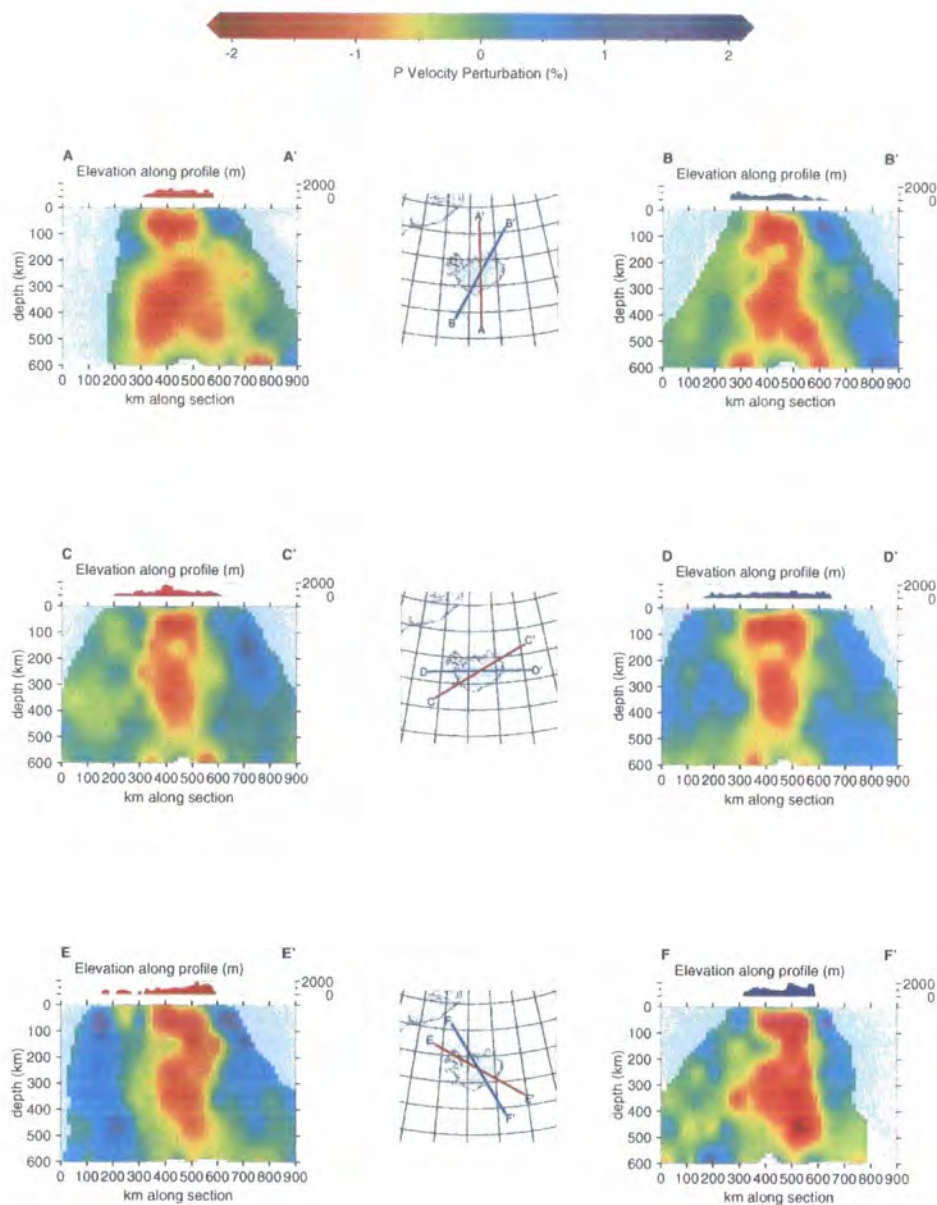
Figure 5.29 As for Figure 5.14 except for model p_10_50_400_av.
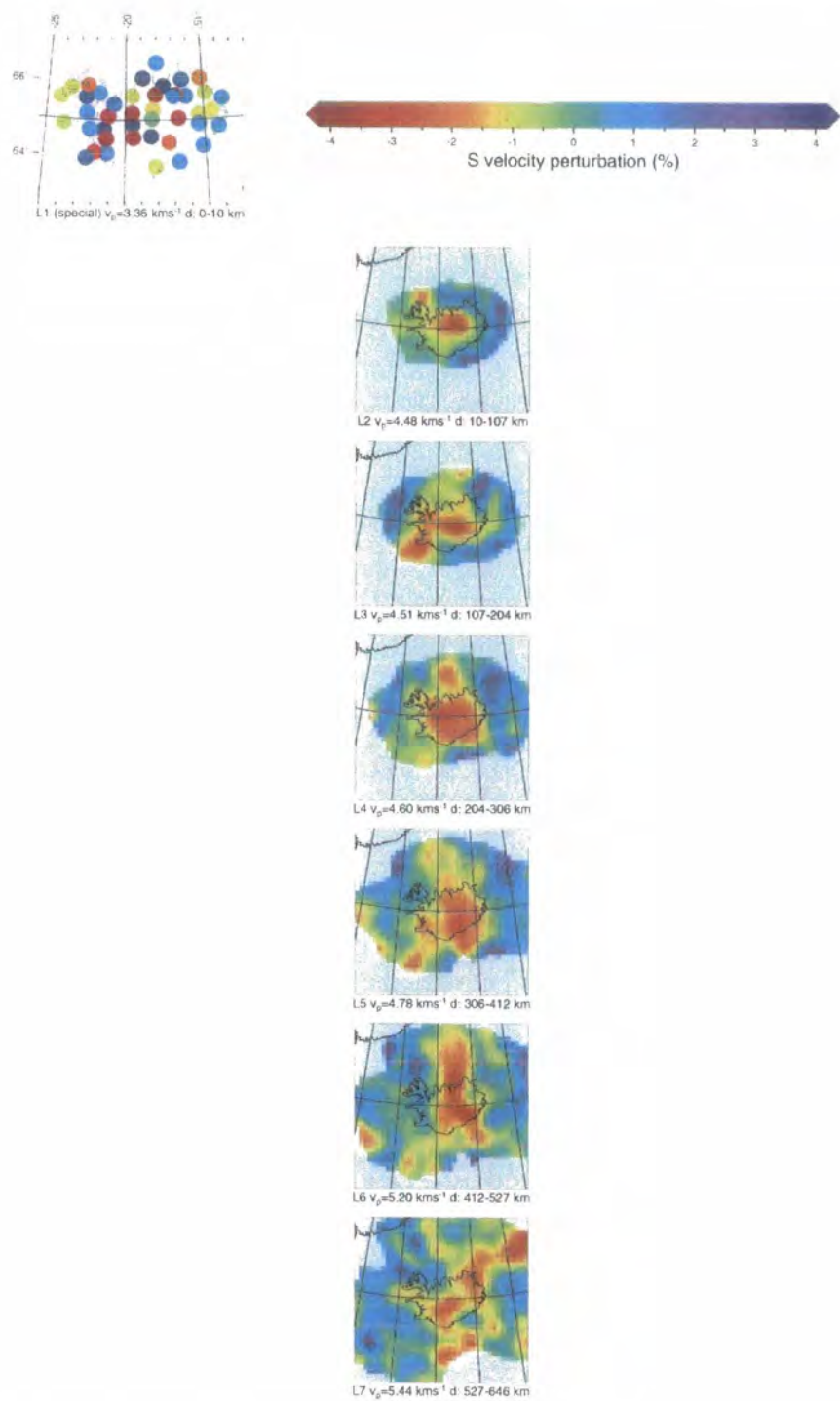
Figure 5.30 As for Figure 5.11 except for model s_10_100_400_av.
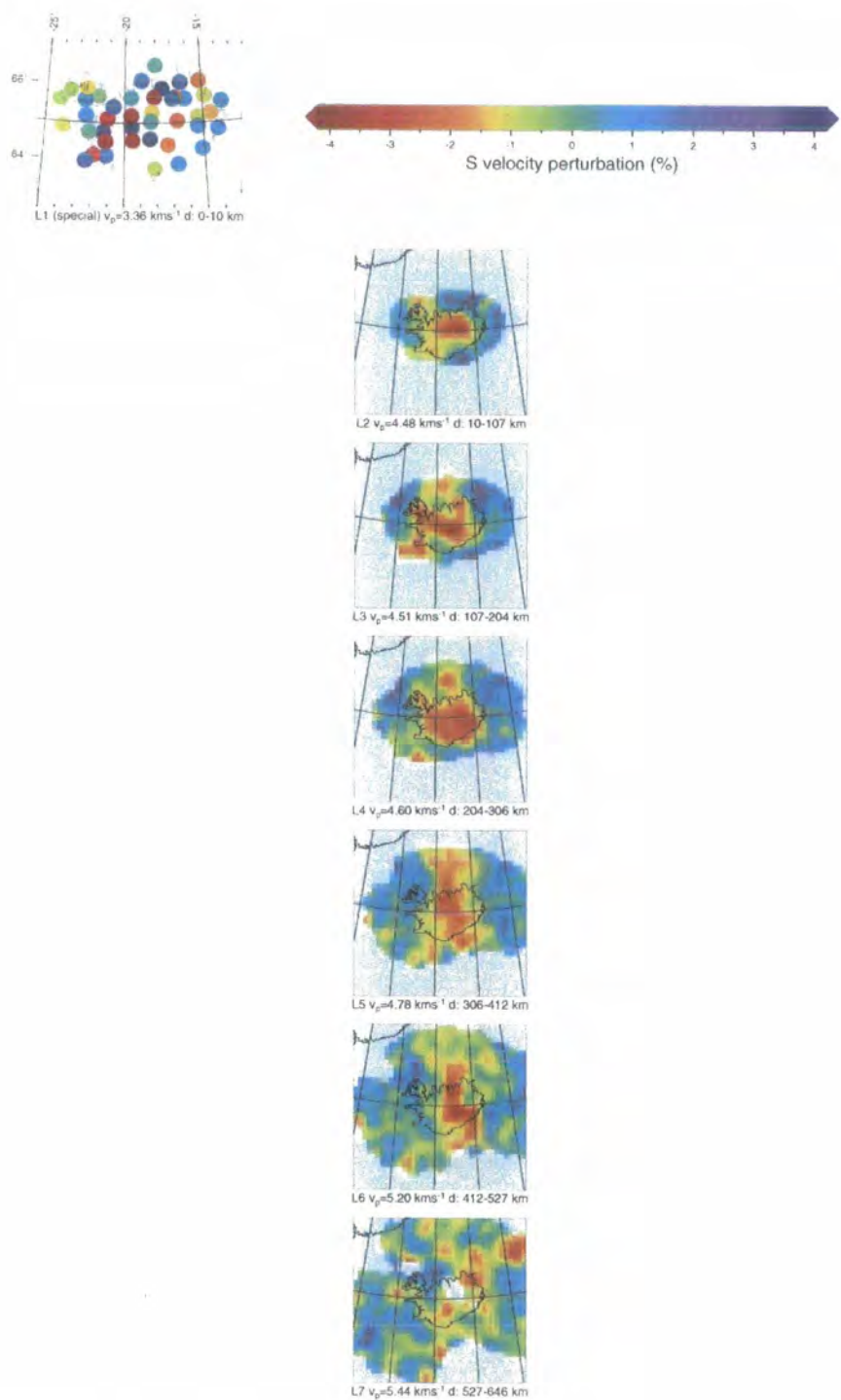
Figure 5.31 As for Figure 5.11 except for model s_10_75_400_av.
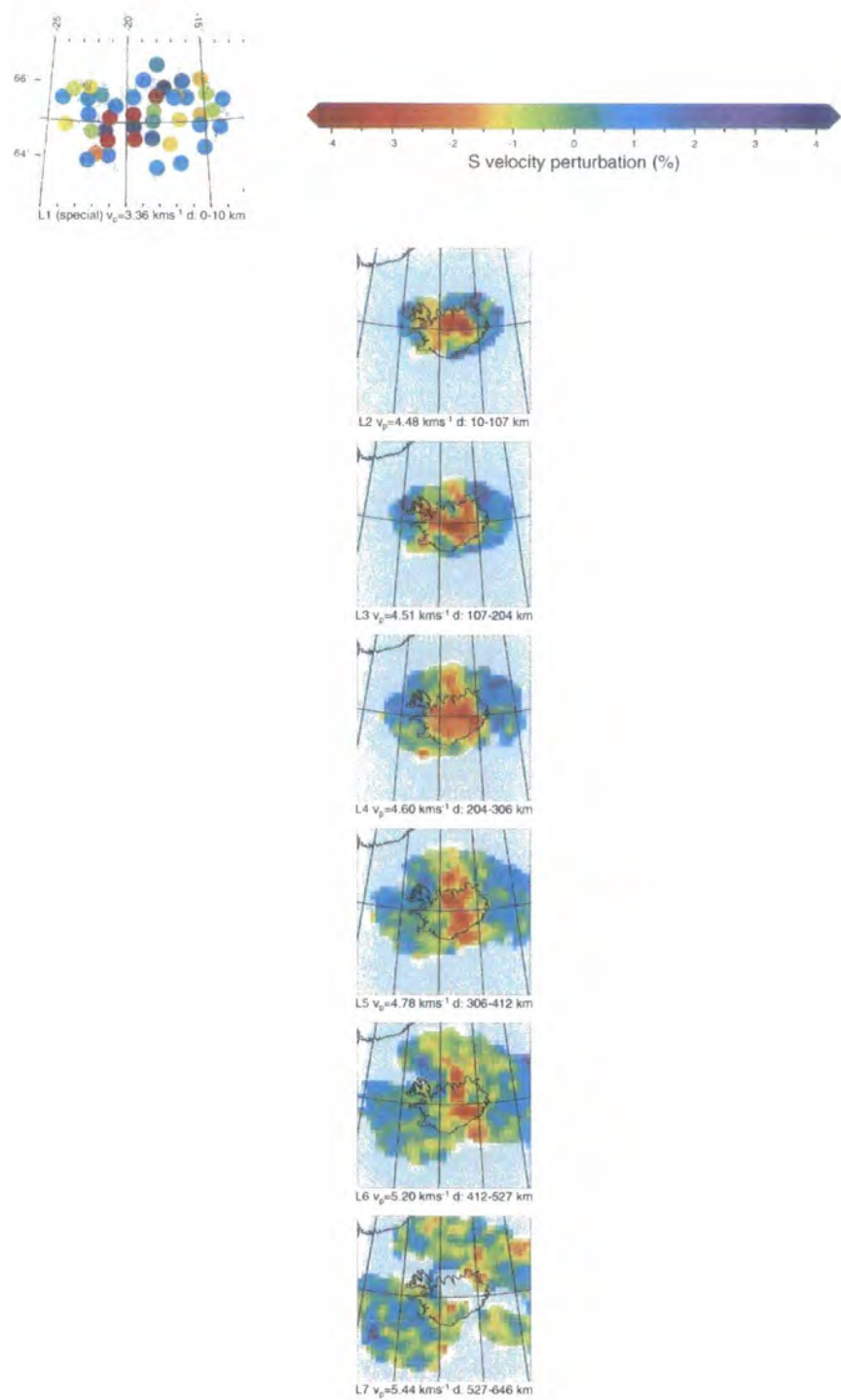
Figure 5.32 As for Figure 5.11 except for model s_10_50_400_av.
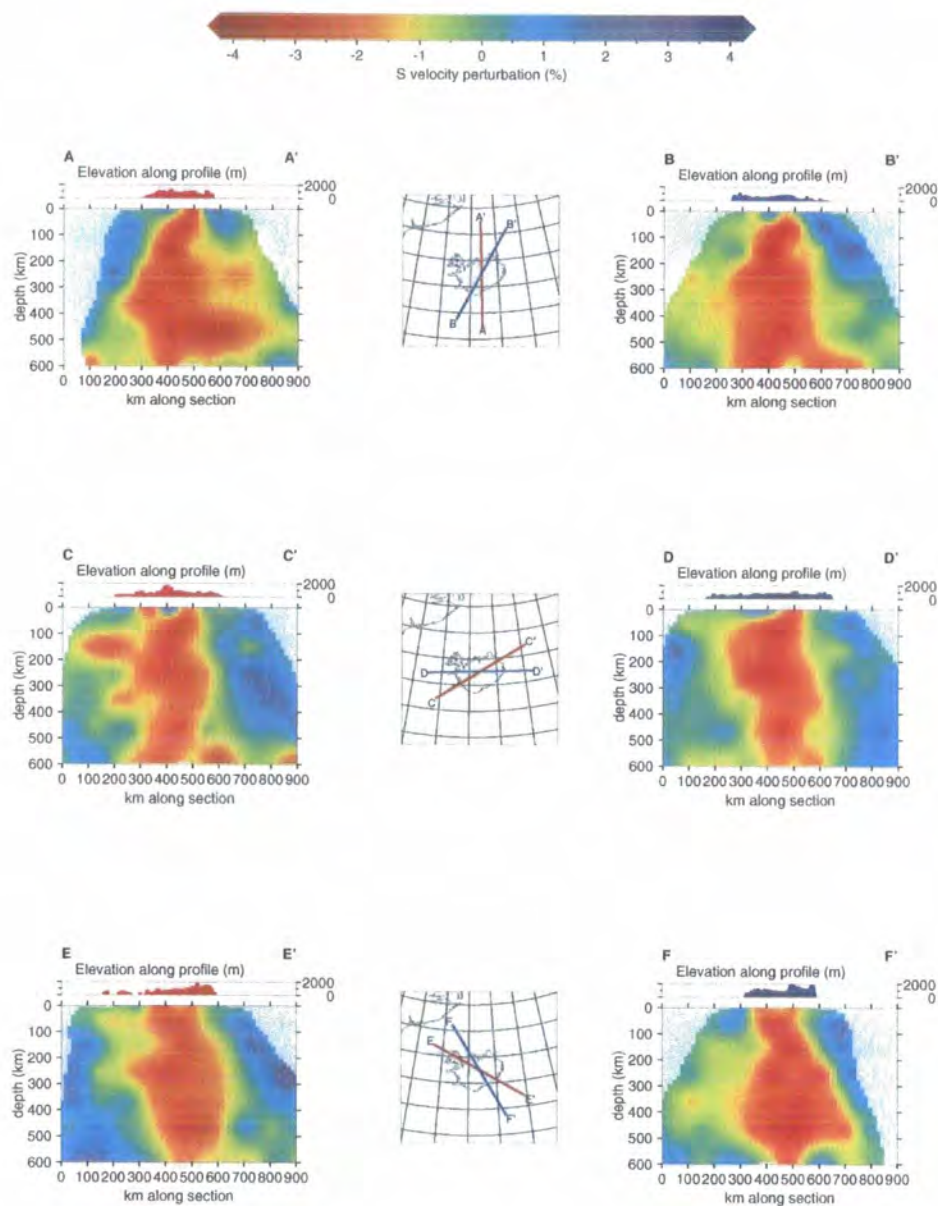
Figure 5.33 As for Figure 5.14 except for model s_10_100_400_av.
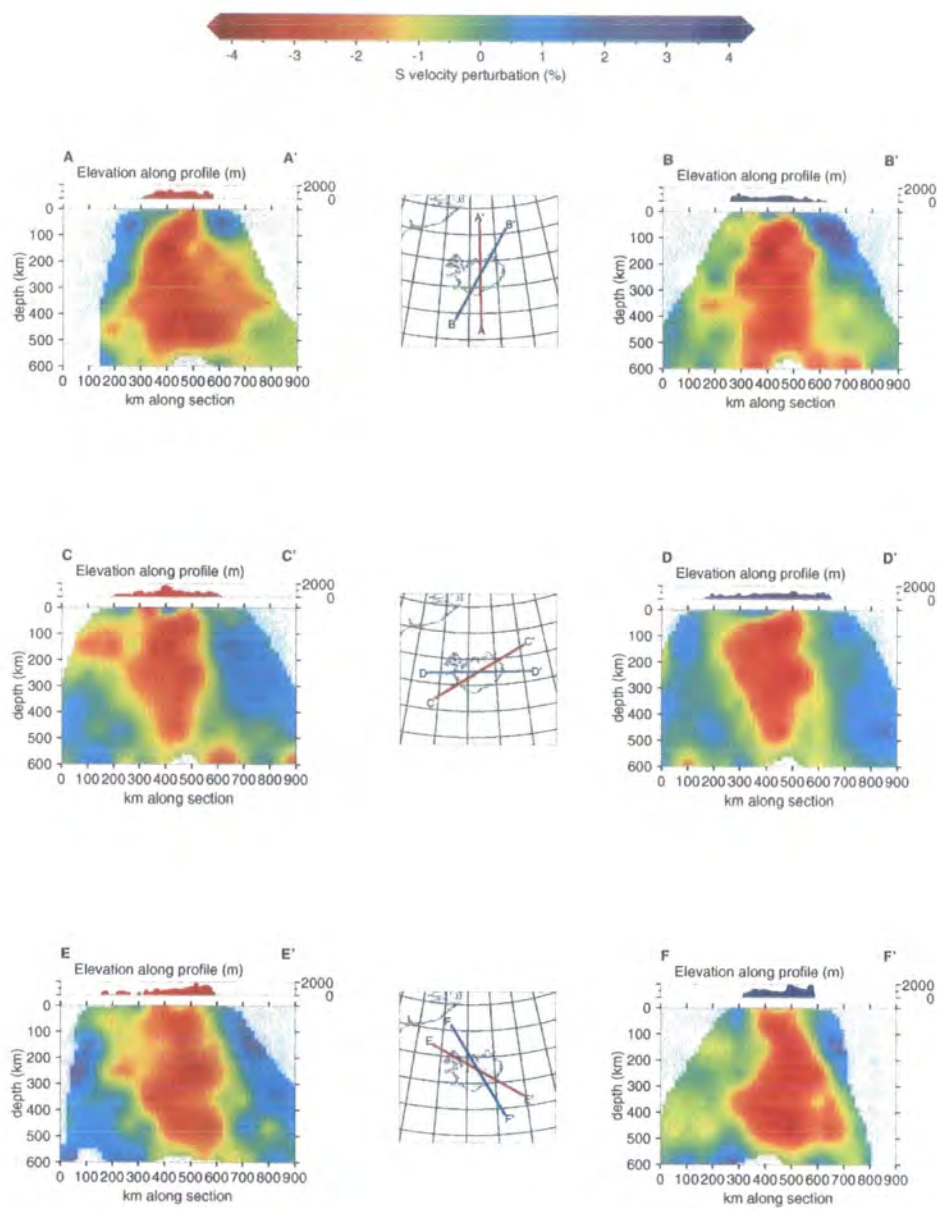
Figure 5.34 As for Figure 5.14 except for model s_10_75_400_av.
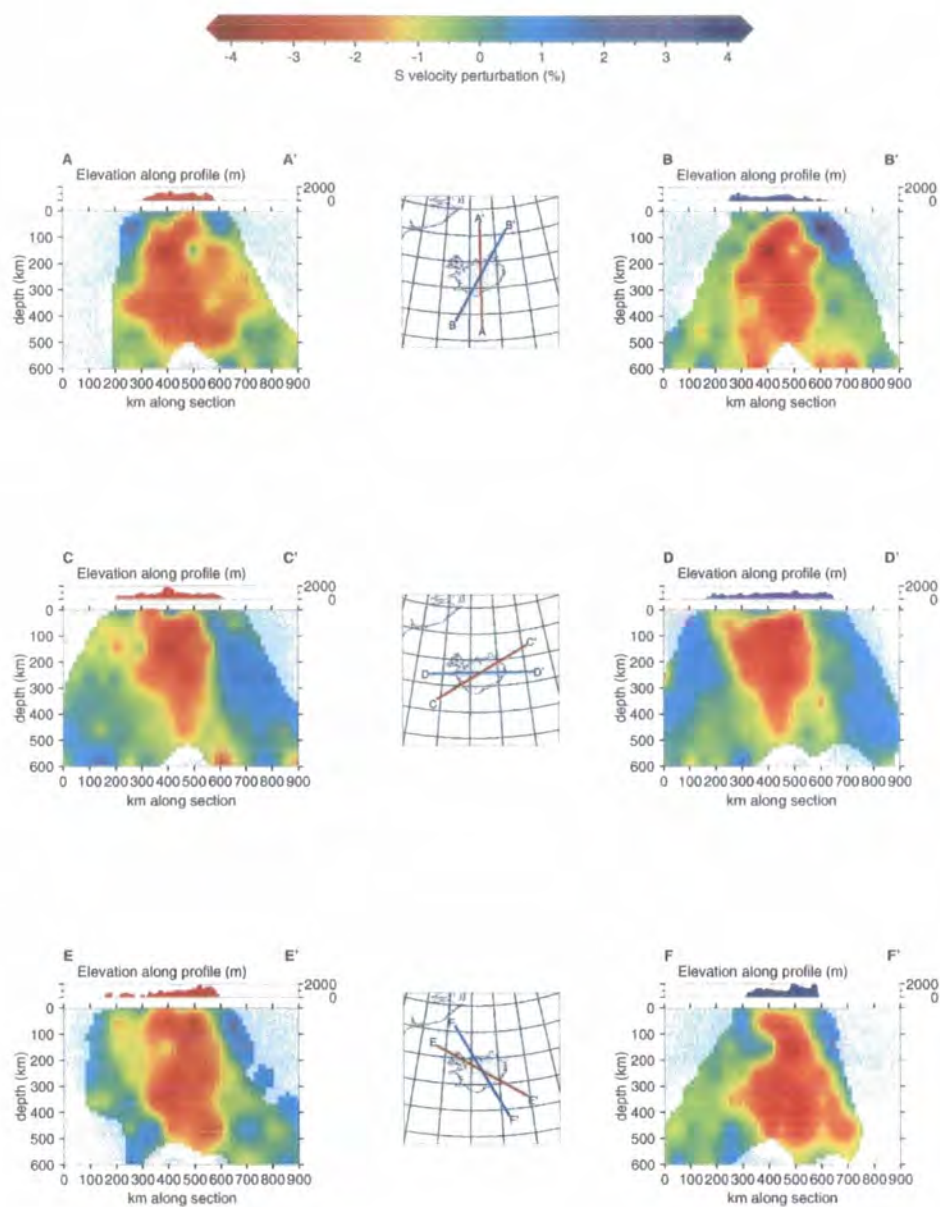
Figure 5.35 As for Figure 5.14 except for model s_10_50_400_av.

An example of how such averaging mitigates the "disappearing anomaly" effect (Ellsworth, 1977) is seen by comparing Figures 5.11 and 5.24. The offset-and-

averaged model p_10_100_400_av shows a northerly extension to the central Iceland anomaly in layer 3 (107-204), which is not seen in model p_10_100_400, suggesting that this particular anomaly had previously been concealed by being divided over and "absorbed" by the surrounding, relatively large (100-km) blocks. Also, the central anomaly in layer 2 has increased in amplitude as a result of this process. The high-amplitude, central anomaly in layer 4 is weakened, while the opposite occurs in layer 5 and layer 6. Averaging has the greatest effect on models with blocks 100-km wide, suggesting that this is too coarse a parameterisation for this experiment.

Comparison of the 75-km block-width models p_10_75_400 and p_10_75_400_av in horizontal map section (Figures 5.12 and 5.25) reveals relatively little change in magnitude or shape of the central anomaly. Peripheral features such as the narrow, linear features to the south-west and north in layers 3 and 4 change slightly in appearance, with some increase in the magnitude of the high-velocity features to the east in layer 3. The model with 50 km blocks is also stable with respect to averaging.

In the S models s_10_100_400 and s_10_100_400_av (Figure 5.17 and Figure 5.30), the central anomaly has been strengthened by averaging and, in layer 3, peripheral features such as the lows to the north and east have increased in spatial extent. The overall distribution of low-velocity features in Layer 4 is relatively unchanged, although the eastward and south-western extensions of the anomaly appears to have weakened. In layer 5, the western portion of the central anomaly is weakened by smoothing, leaving a north-south trending feature which is even more developed in layer 6. This persists to layer 7, although averaging produces a noisier result there, suggesting that the structure at this depth is poorly constrained.

Compared in vertical cross-section (Figures 5.20 - 5.22 and Figures 5.33 - 5.35), the main effect of averaging seems to has been to homogenise some of the detail, smoothing out some of the spatially small, strong anomalies and producing a central anomaly which is more uniform. This effect is strongest in the 100-km block model.

A common feature of the west-east vertical sections CC' and DD' is a narrowing of the central, columnar, low-velocity feature with depth (e.g. Figure

5.34). This is not the case for sections AA' and FF', which sample the northward elongation of the feature at depth.

5.2.8 Layer-thinned models (vertical "smoothing")

Results for the half- and one-third-thickness "layer-thinned" models are presented in Figures 5.36 - 5.47 and Figures 5.48 - 5.59 respectively. The horizontal map views show that the overall results are similar to the thick-layered models. The vertical sections, however, reveal strong amplitude fluctuations between vertically adjacent layers which appear as horizontal streaks. Comparison of equivalent models, e.g. Figures 5.15 and 5.40 reveals, nevertheless, that the basic shape of the anomaly is generally consistent. Consistency between models of different layer thickness is best for those with block widths of 50 and 75 km and worst for those with 100-km wide blocks.
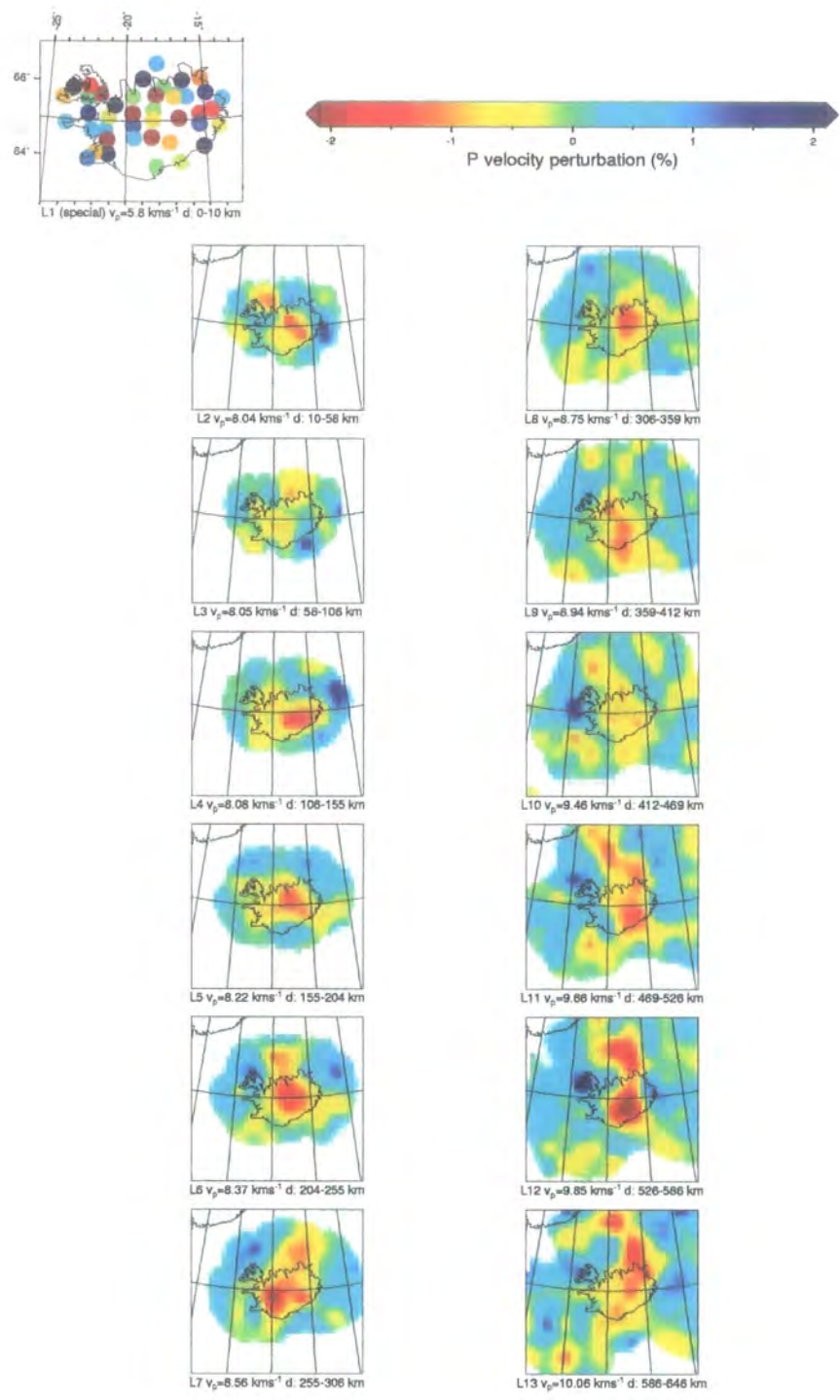
Figure 5.36 As for Figure 5.11 except for model p_10_100_225
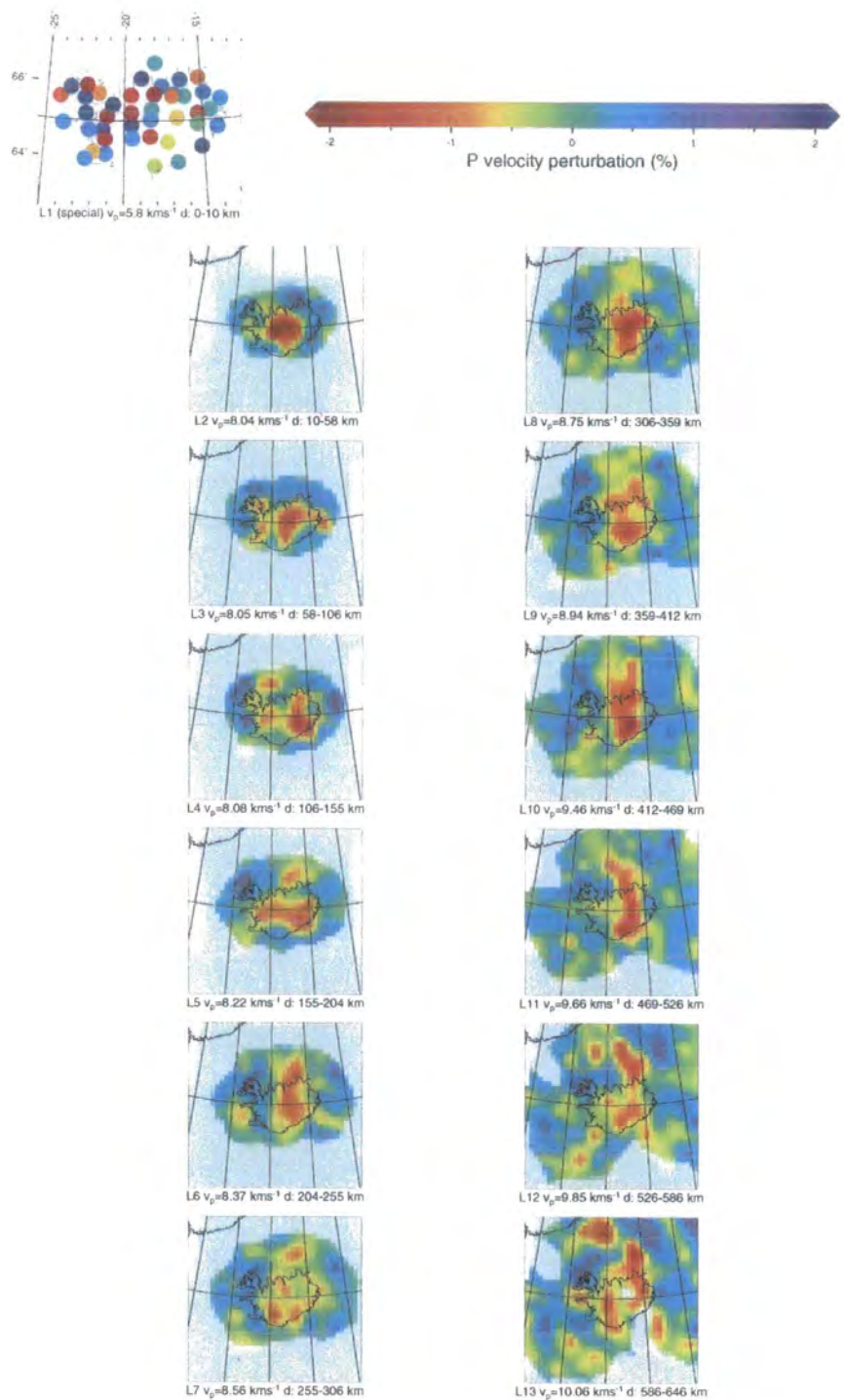
Figure 5.37 As for Figure 5.11 except for model p_10_75_225.
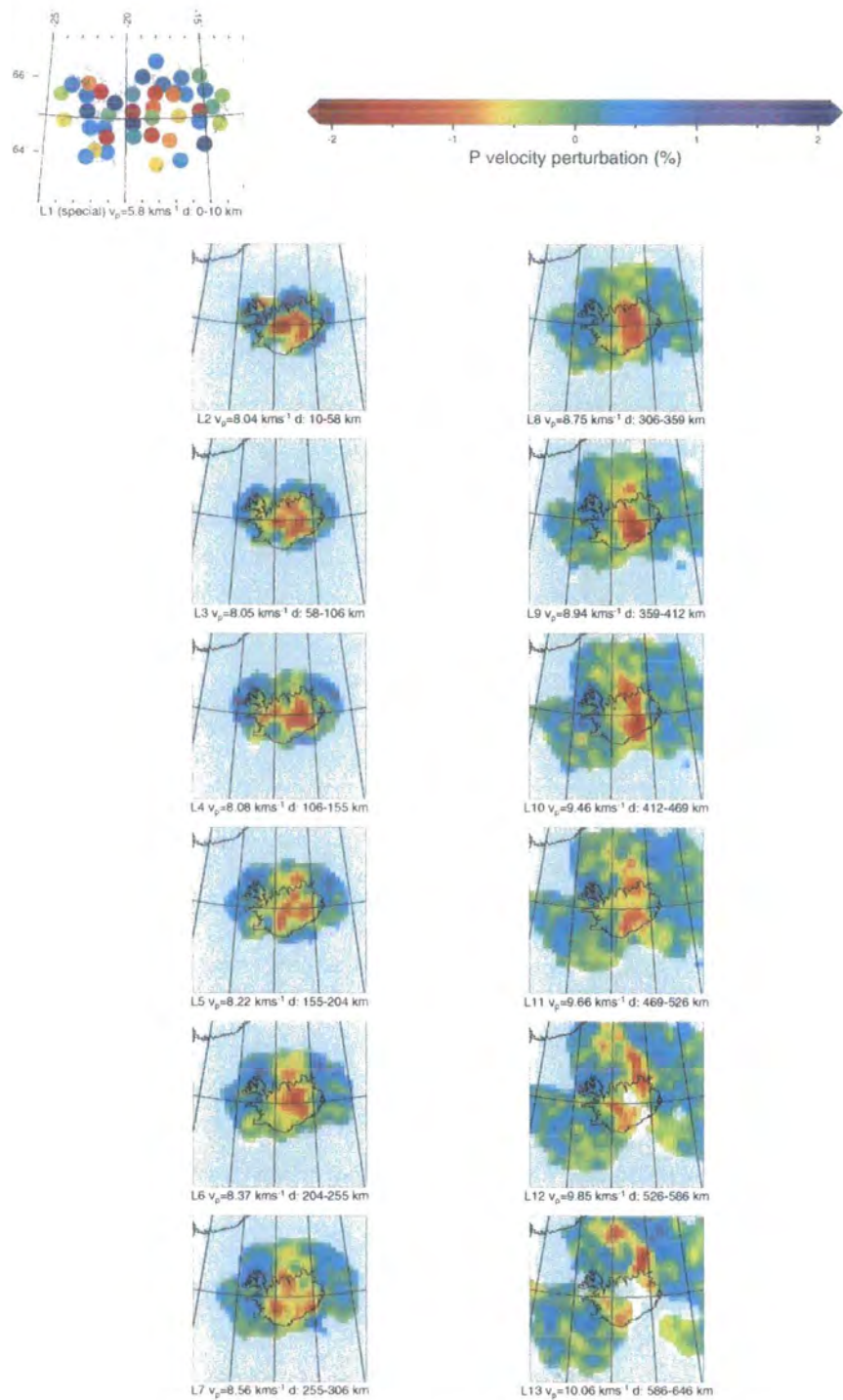
Figure 5.38 As for Figure 5.11 except for model p_10_50_225.
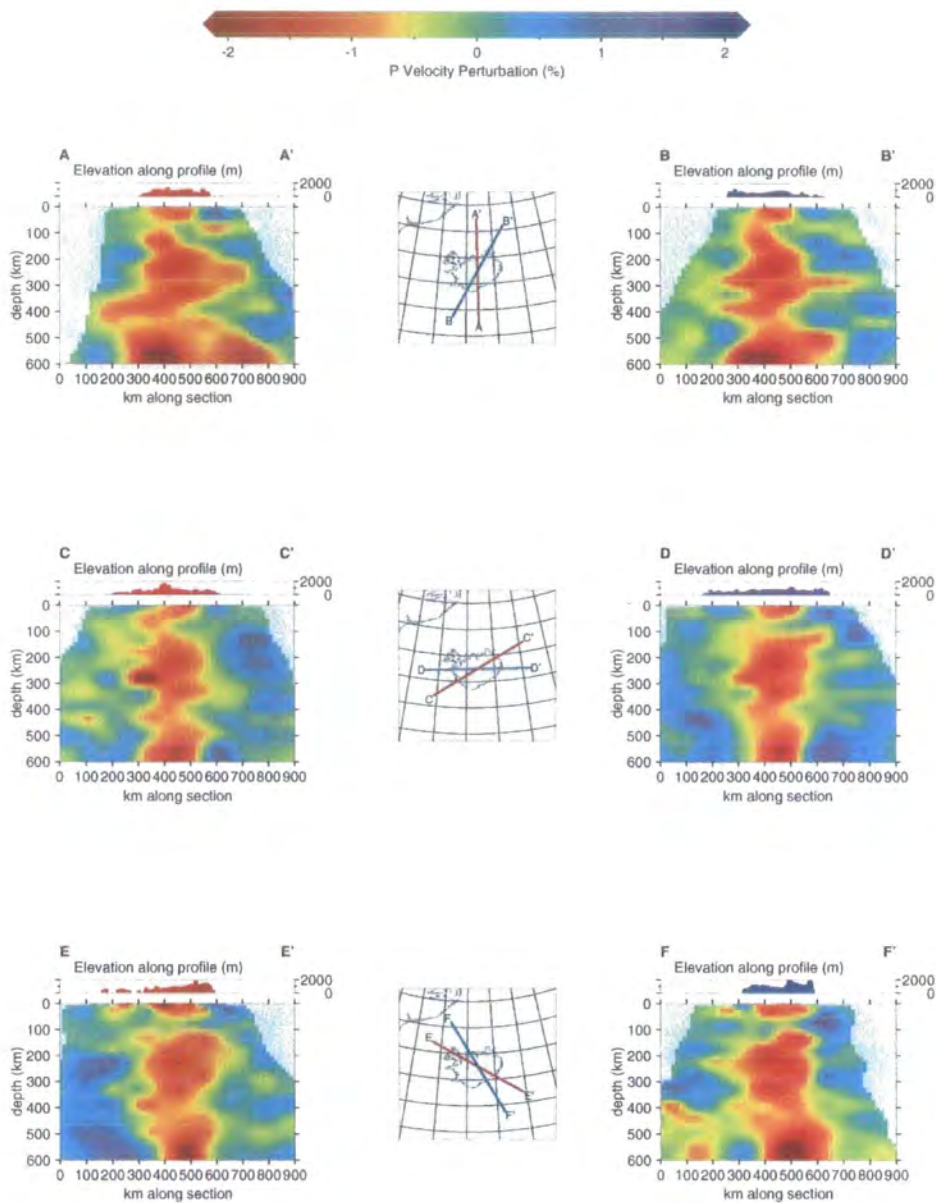
Figure 5.39 As for Figure 5.14 except for model p_10_100_225.
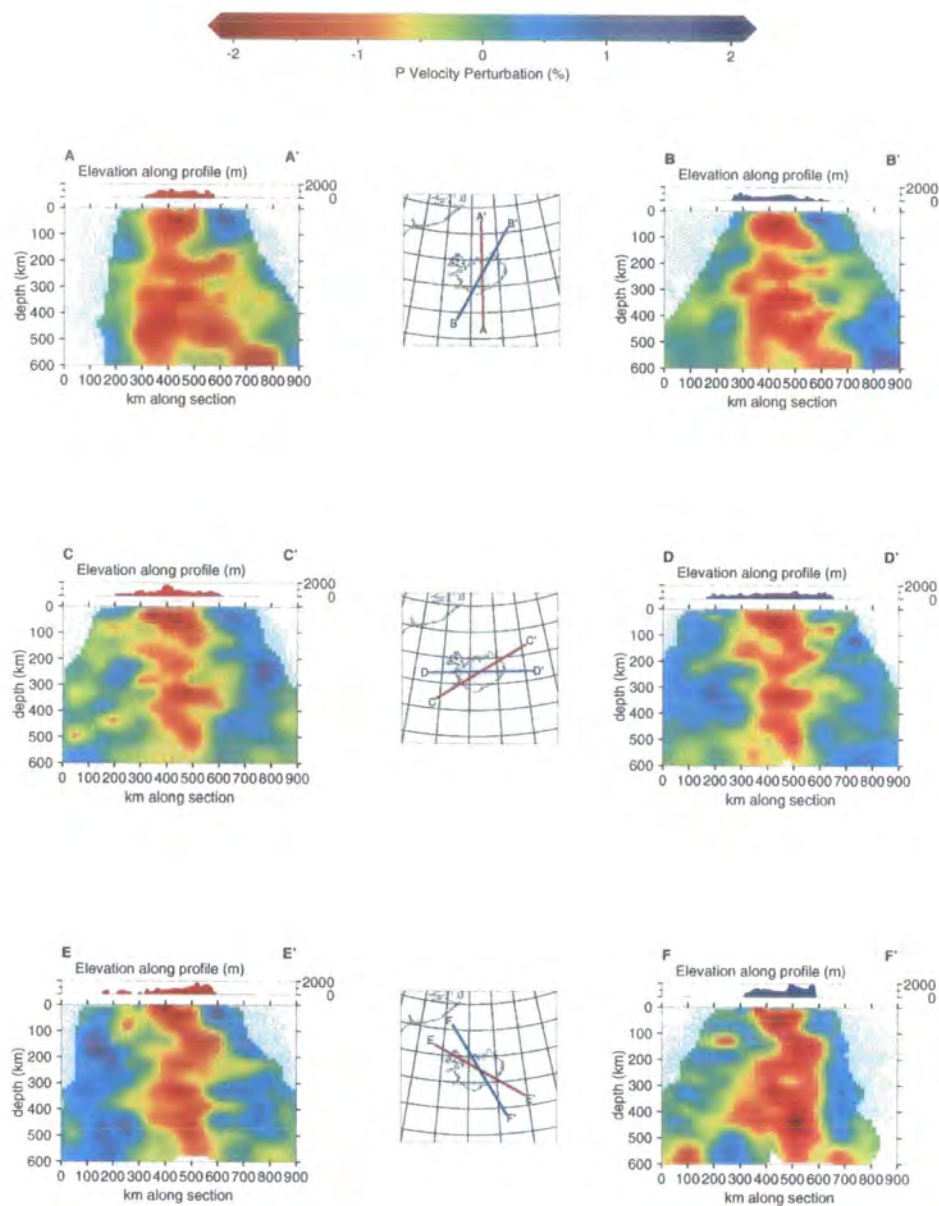
Figure 5.40 As for Figure 5.14 except for model p_10_75_225.
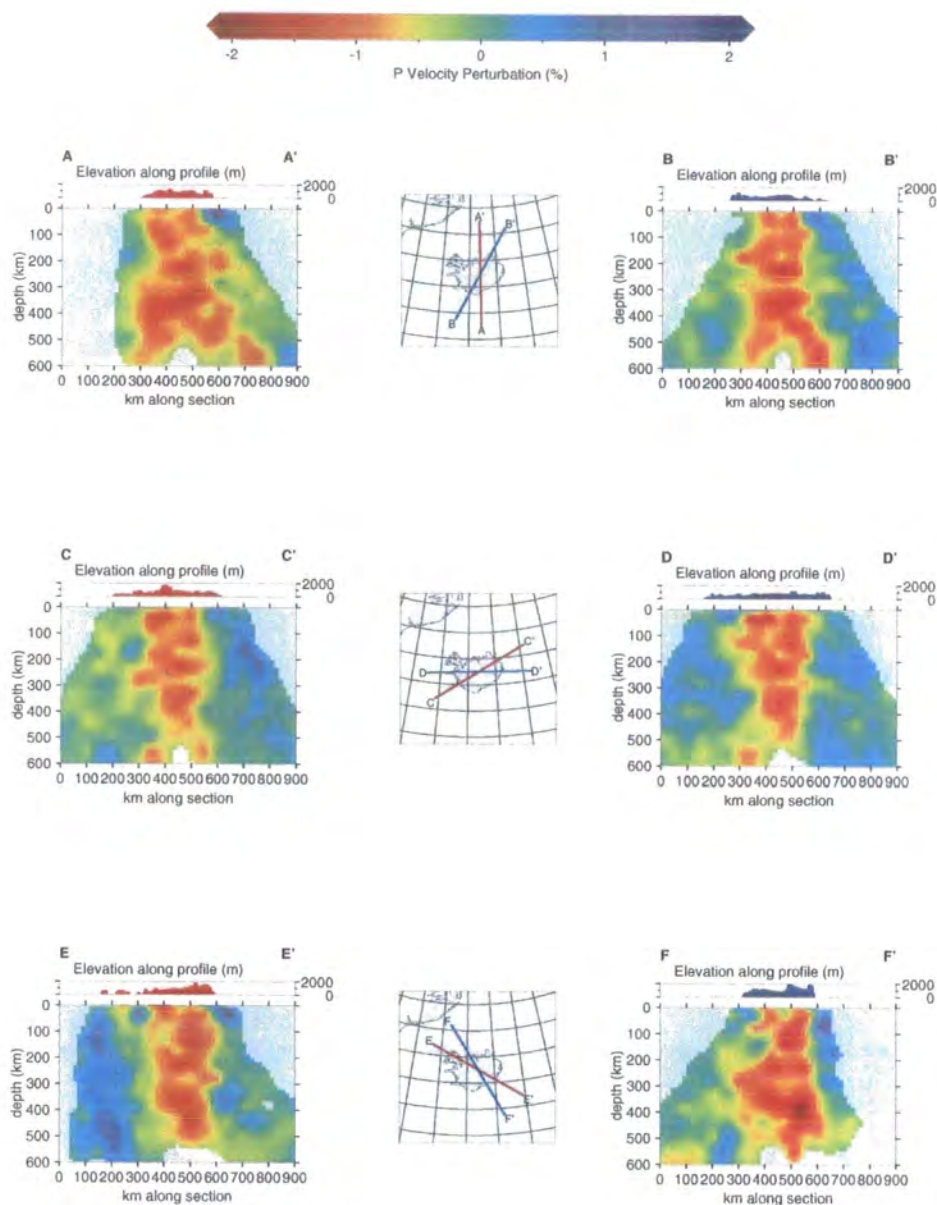
Figure 5.41 As for Figure 5.14 except for model p_10_50_225.
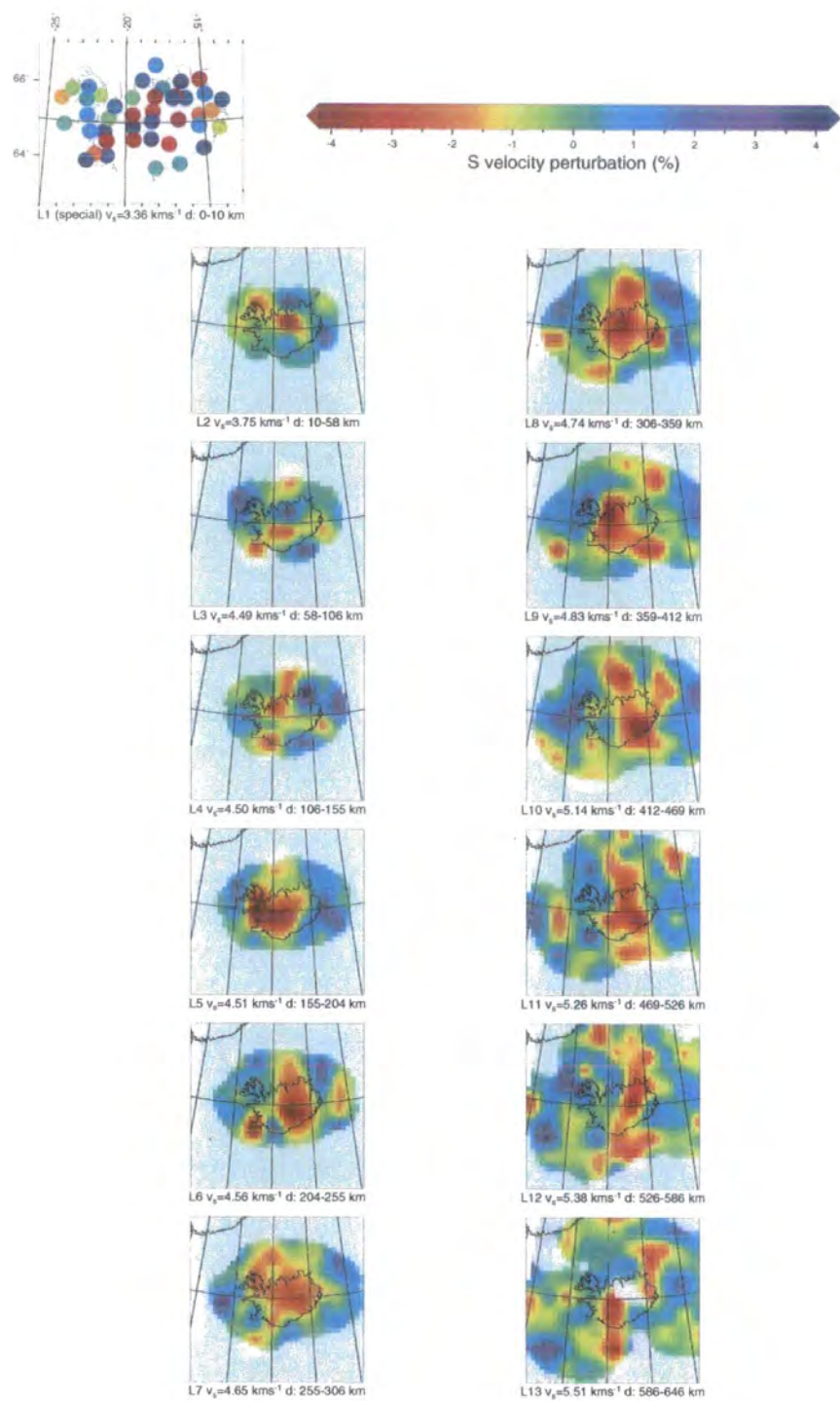
Figure 5.42 As for Figure 5.11 except for model s_10_100_225.
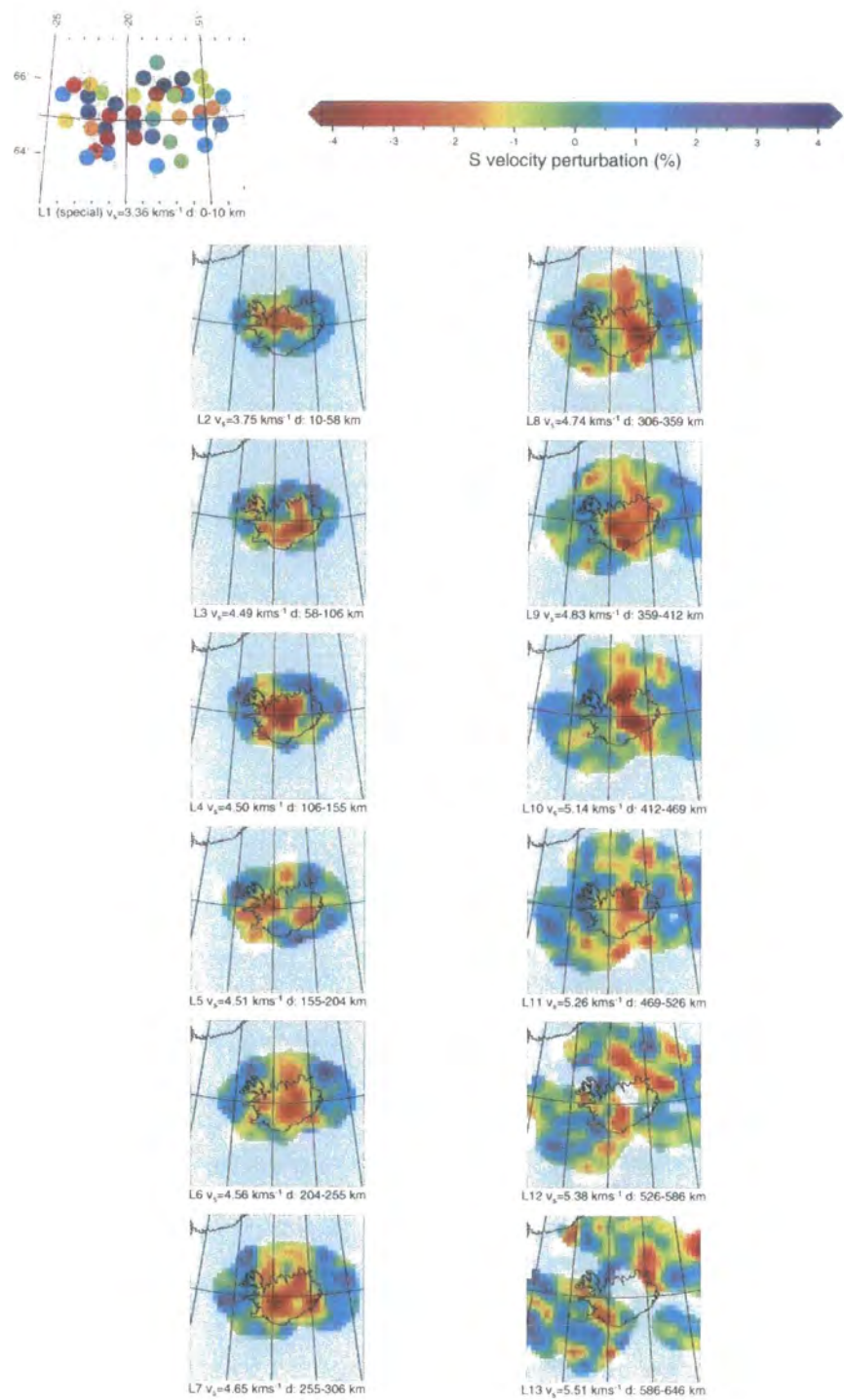
Figure 5.43 As for Figure 5.11 except for model s_10_75_225.
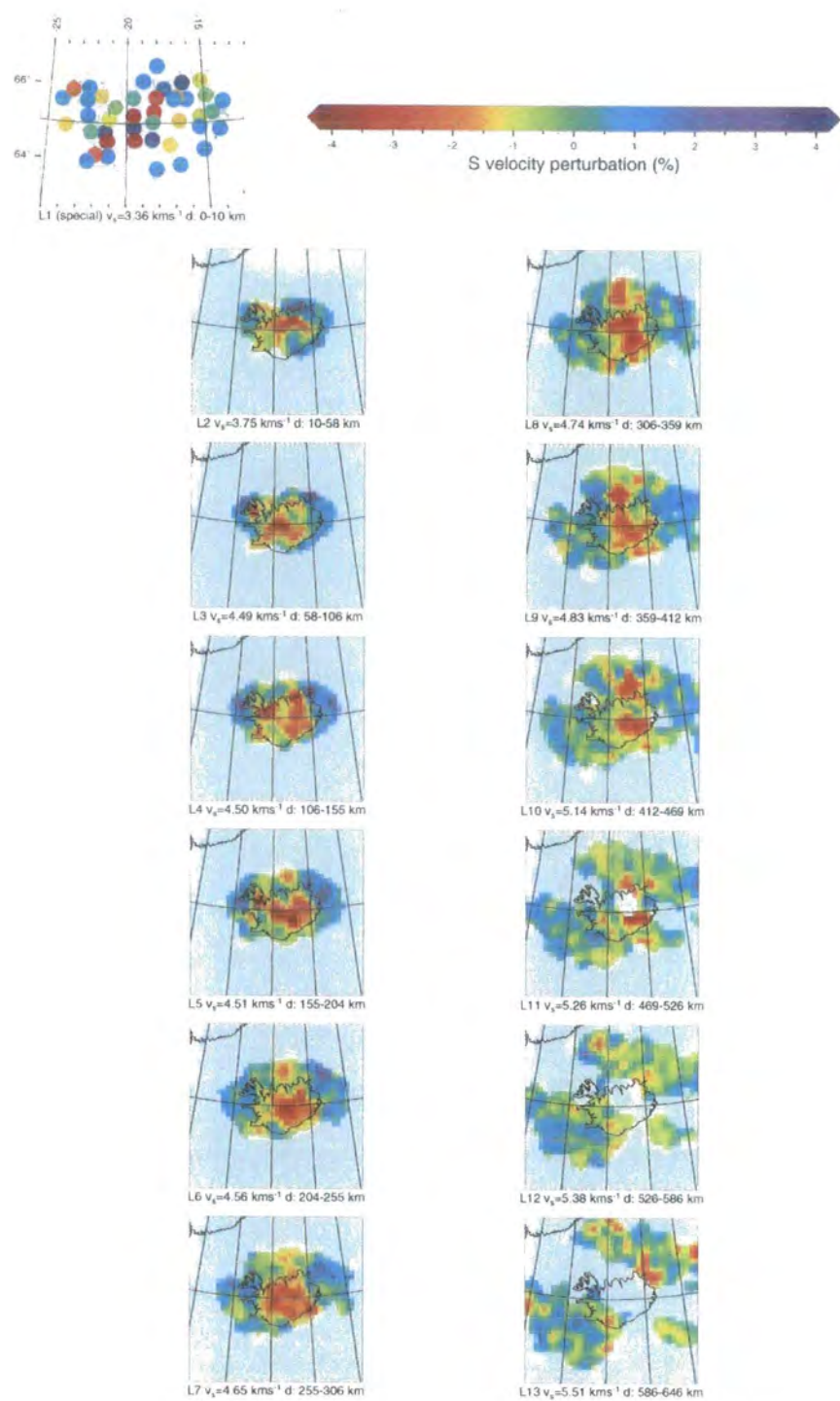
Figure 5.44 As for Figure 5.11 except for model s_10_50_225.
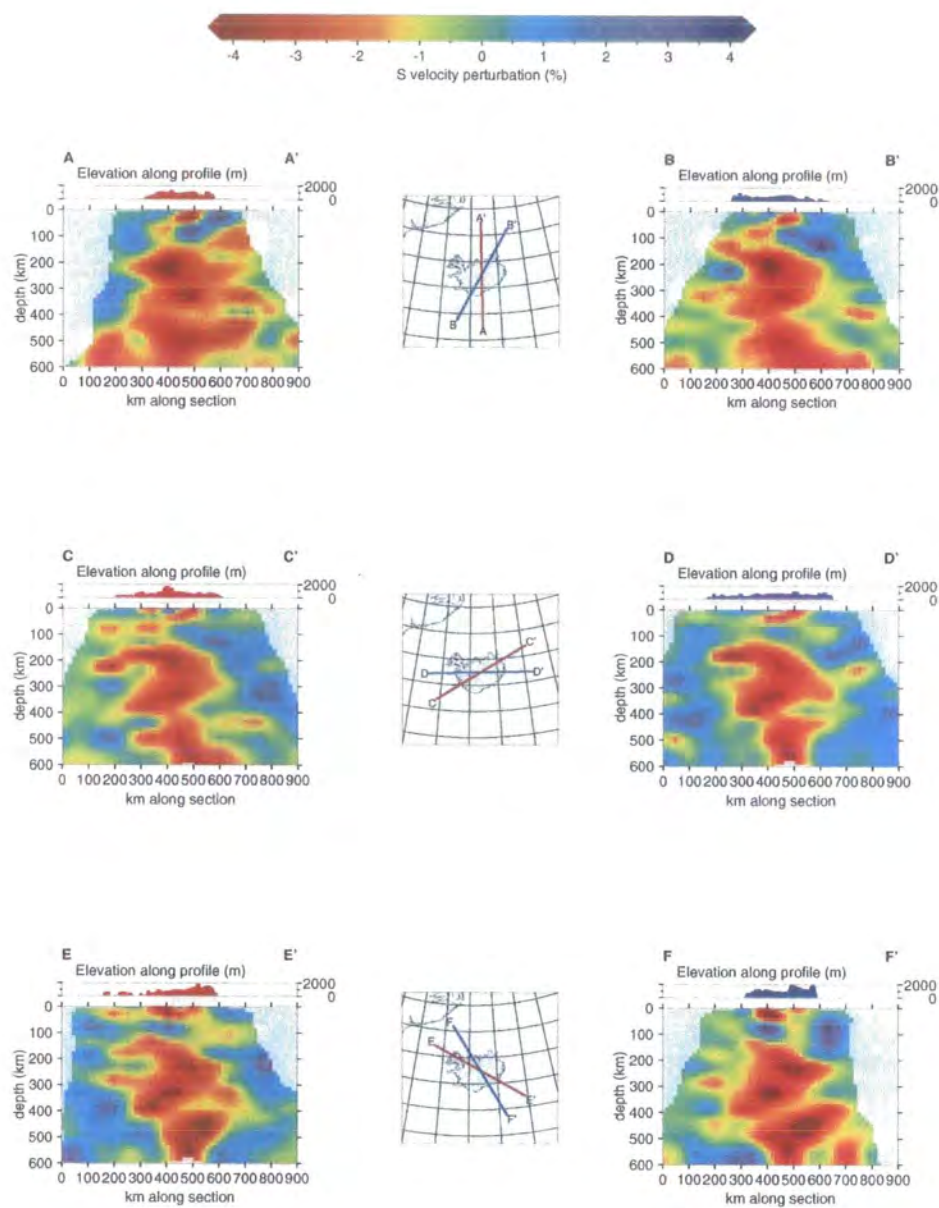
Figure 5.45 As for Figure 5.14 except for model s_10_100_225.
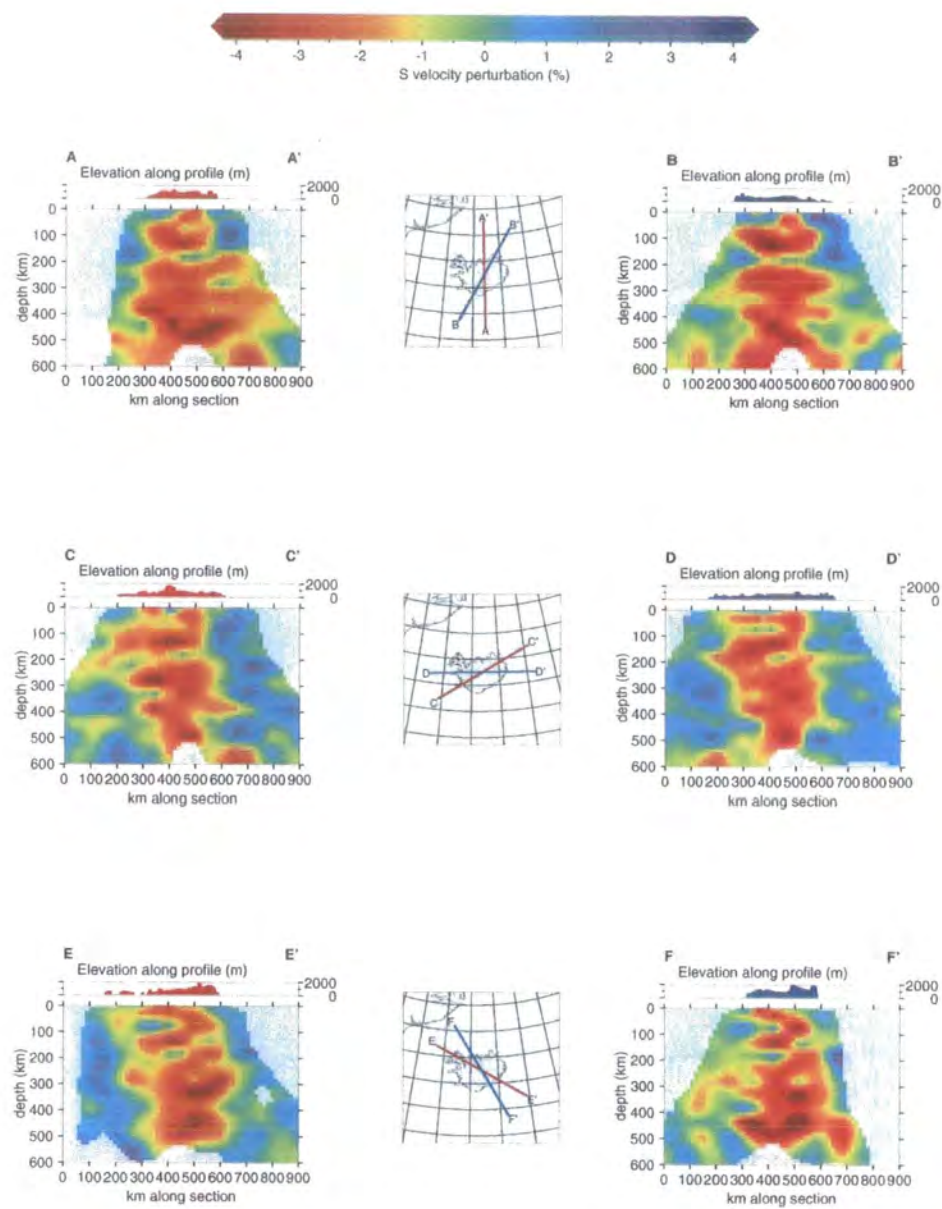
Figure 5.46 As for Figure 5.14 except for model s_10_75_225.
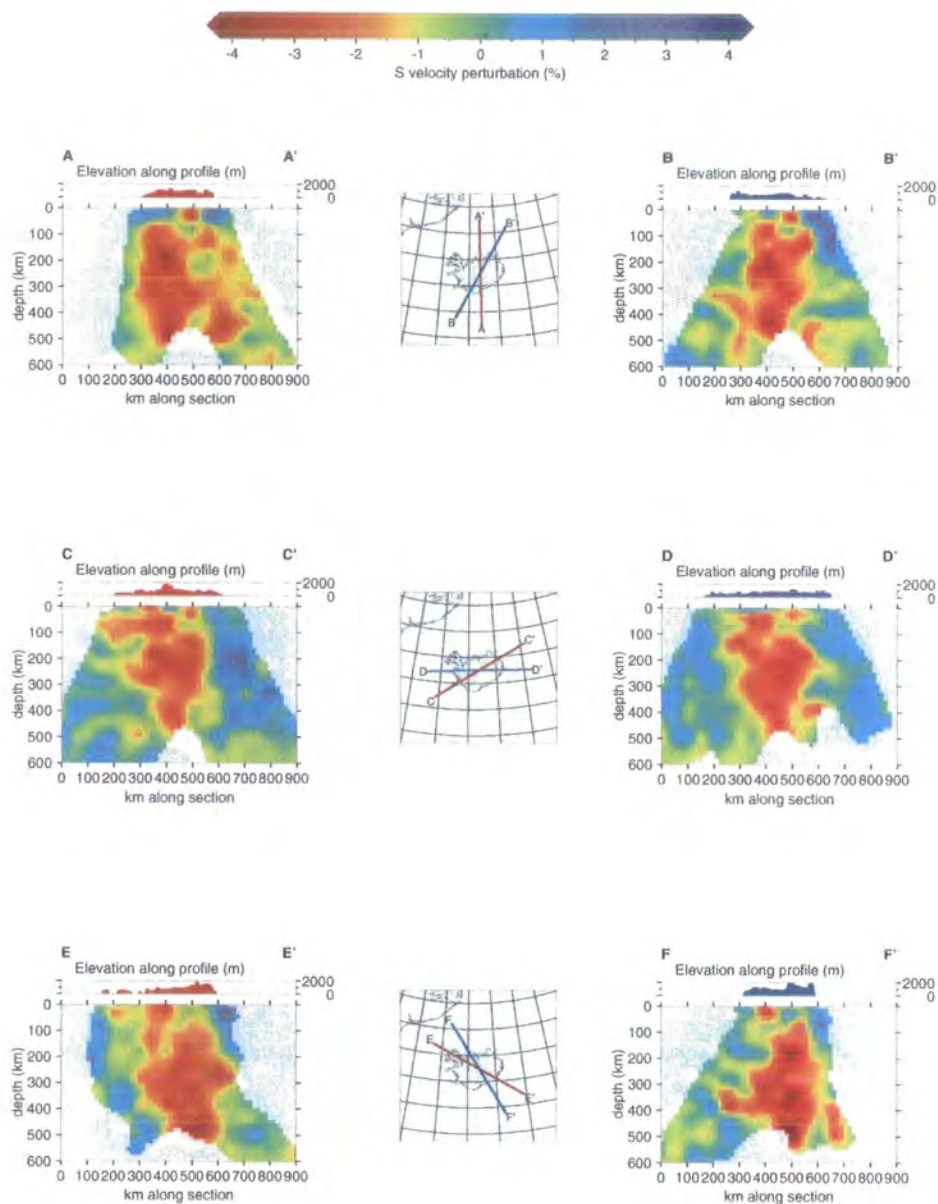
Figure 5.47 As for Figure 5.14 except for model s_10_50_225.
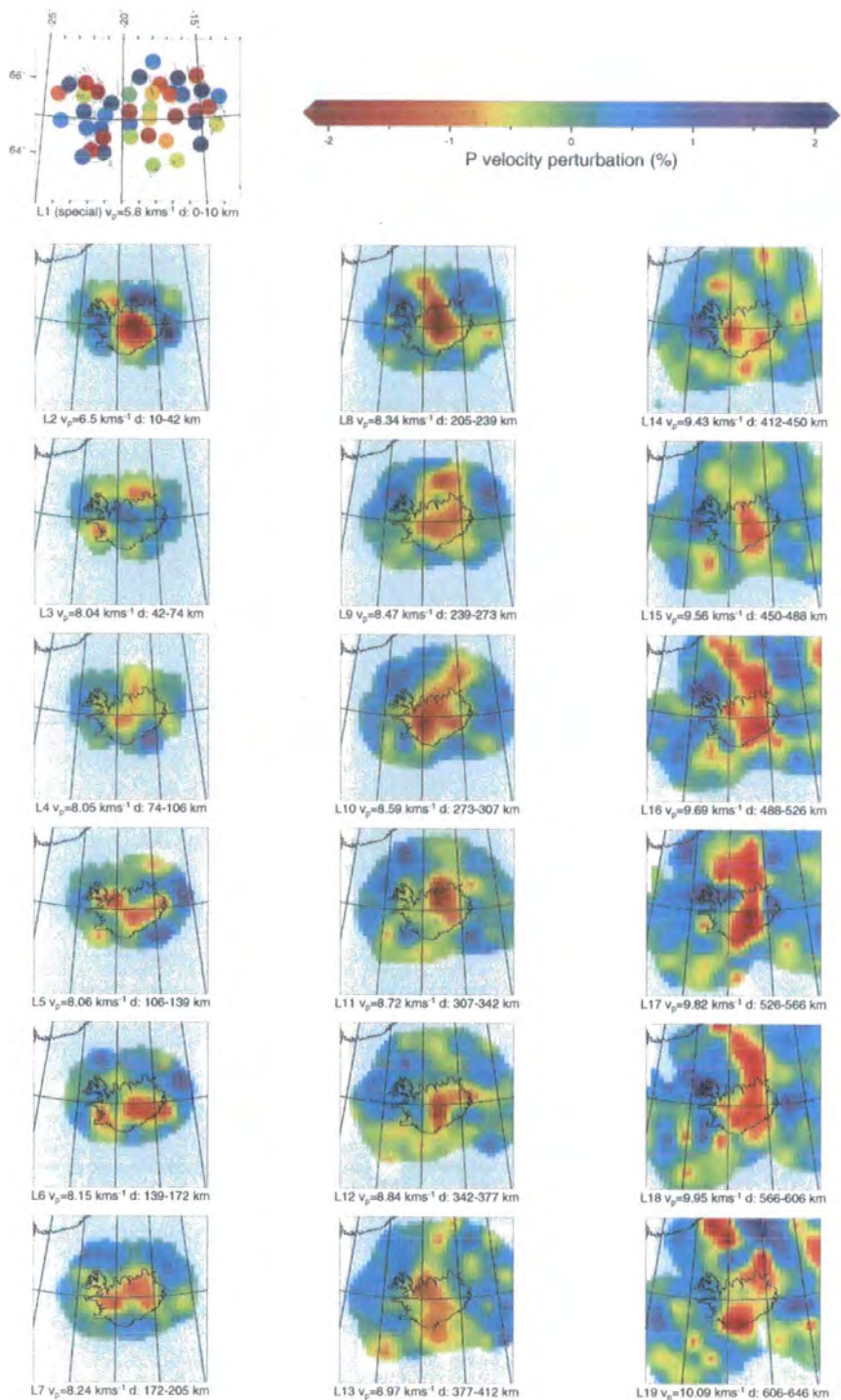
Figure 5.48 As for Figure 5.11 except for model p_10_100_161.
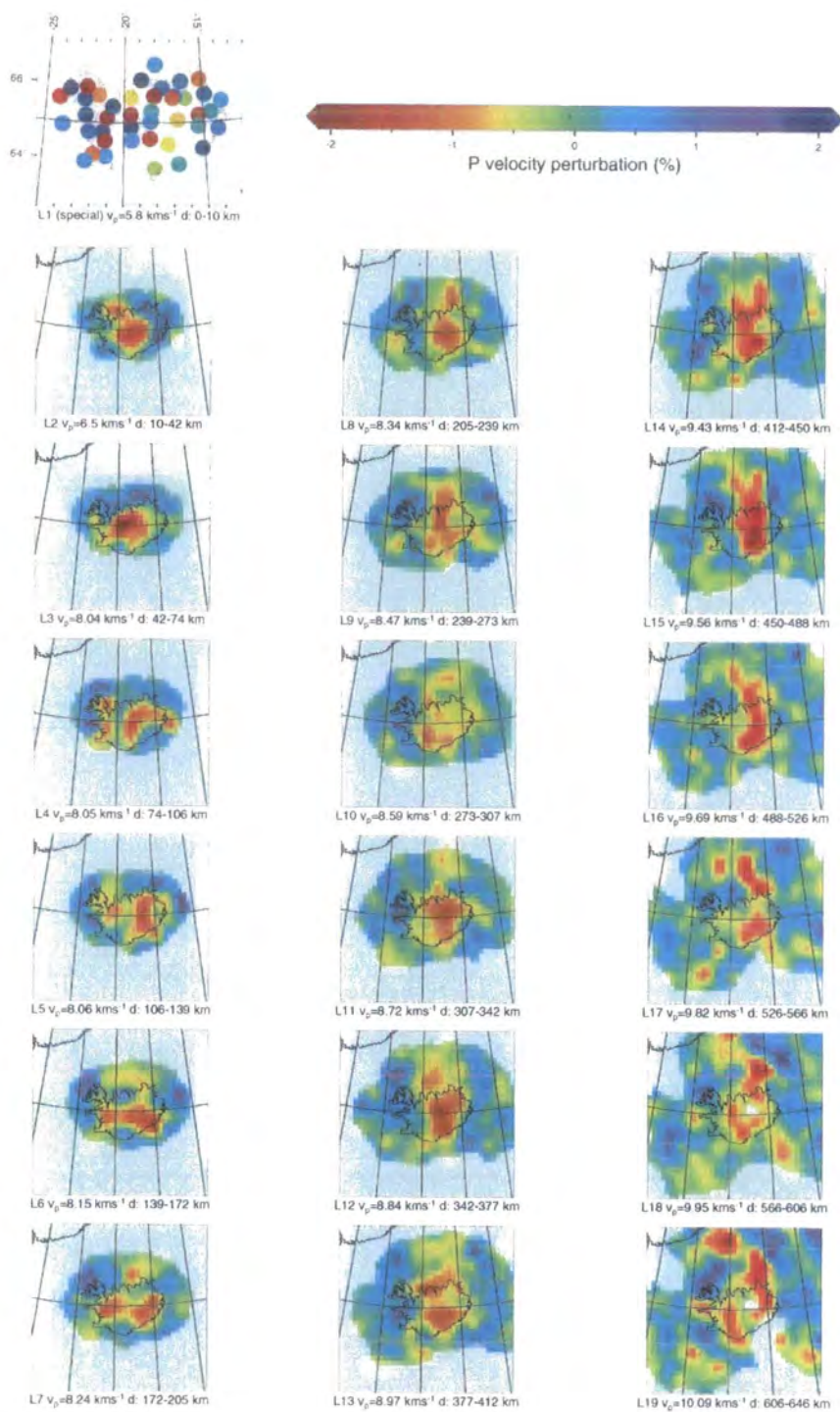
Figure 5.49 As for Figure 5.11 except for model p_10_75_161.
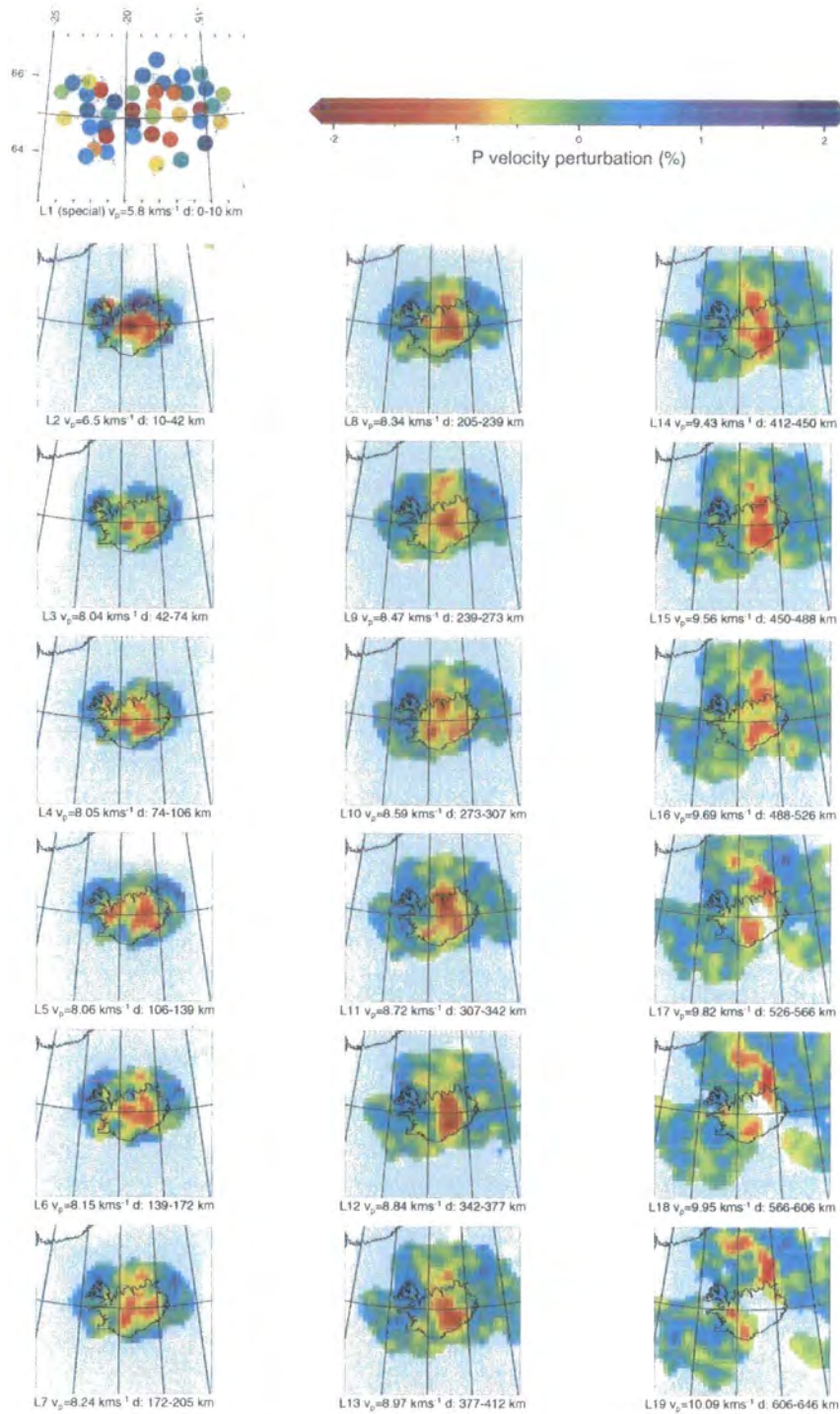
Figure 5.50 As for Figure 5.11 except for model p_10_50_161.
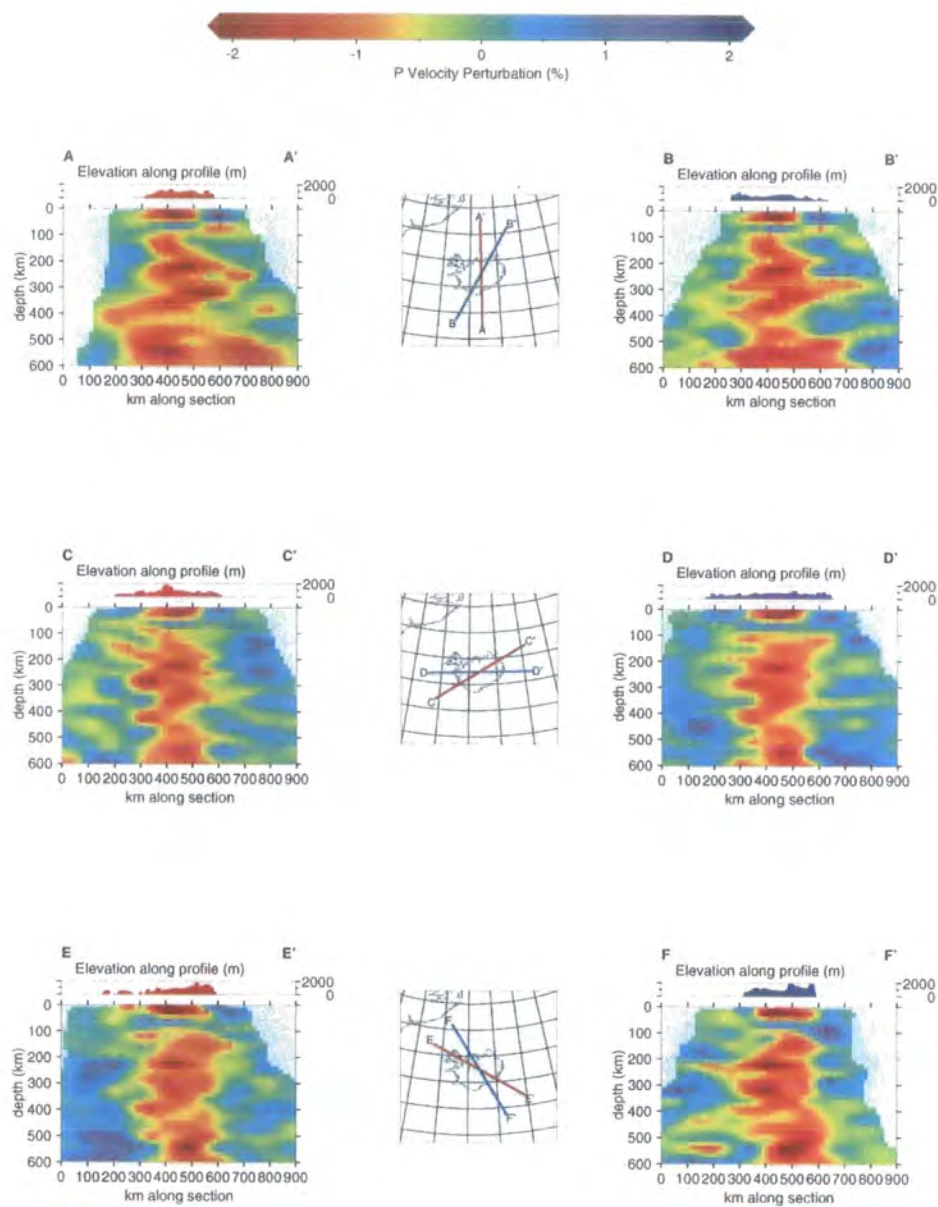
Figure 5.51 As for Figure 5.14 except for model p_10_100_161.
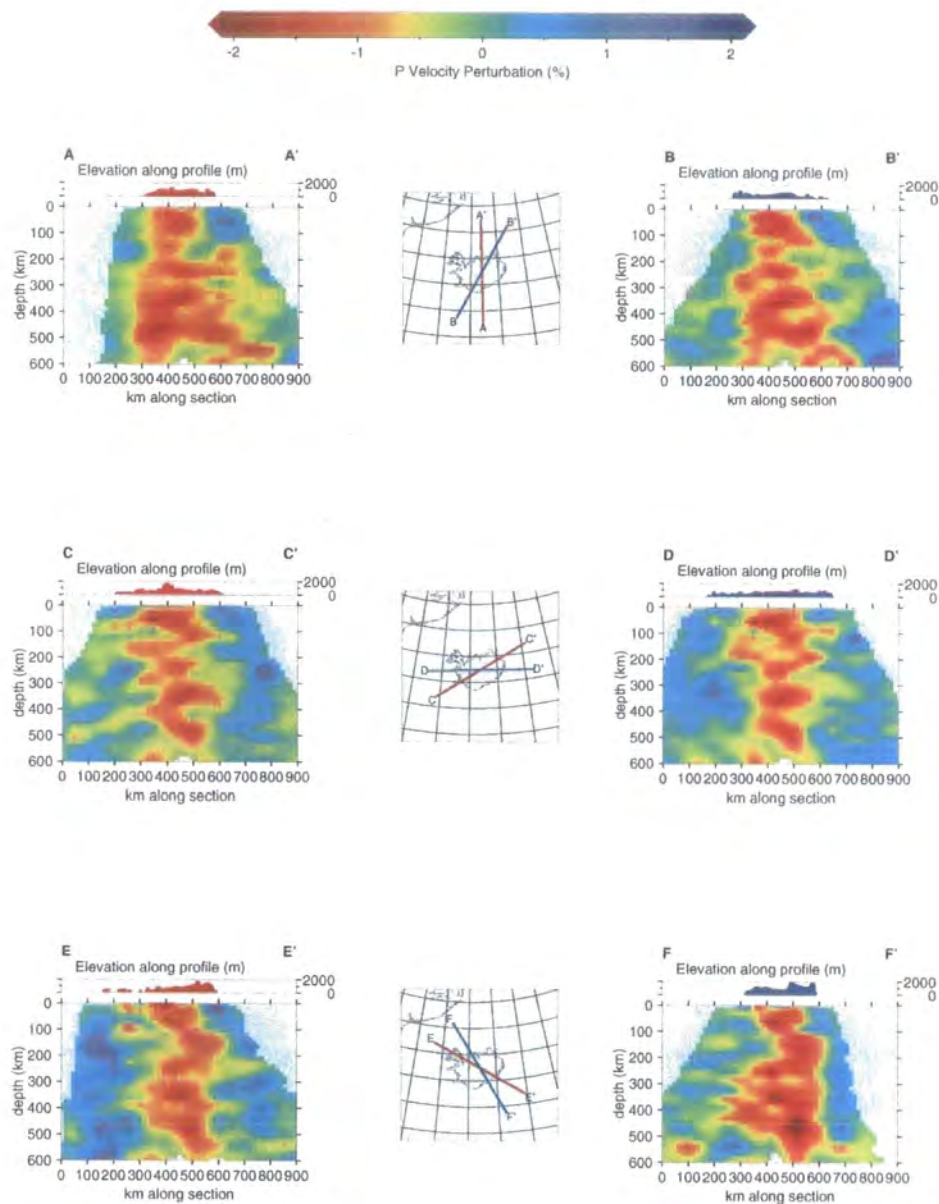
Figure 5.52 As for Figure 5.14 except for model p_10_75_161.
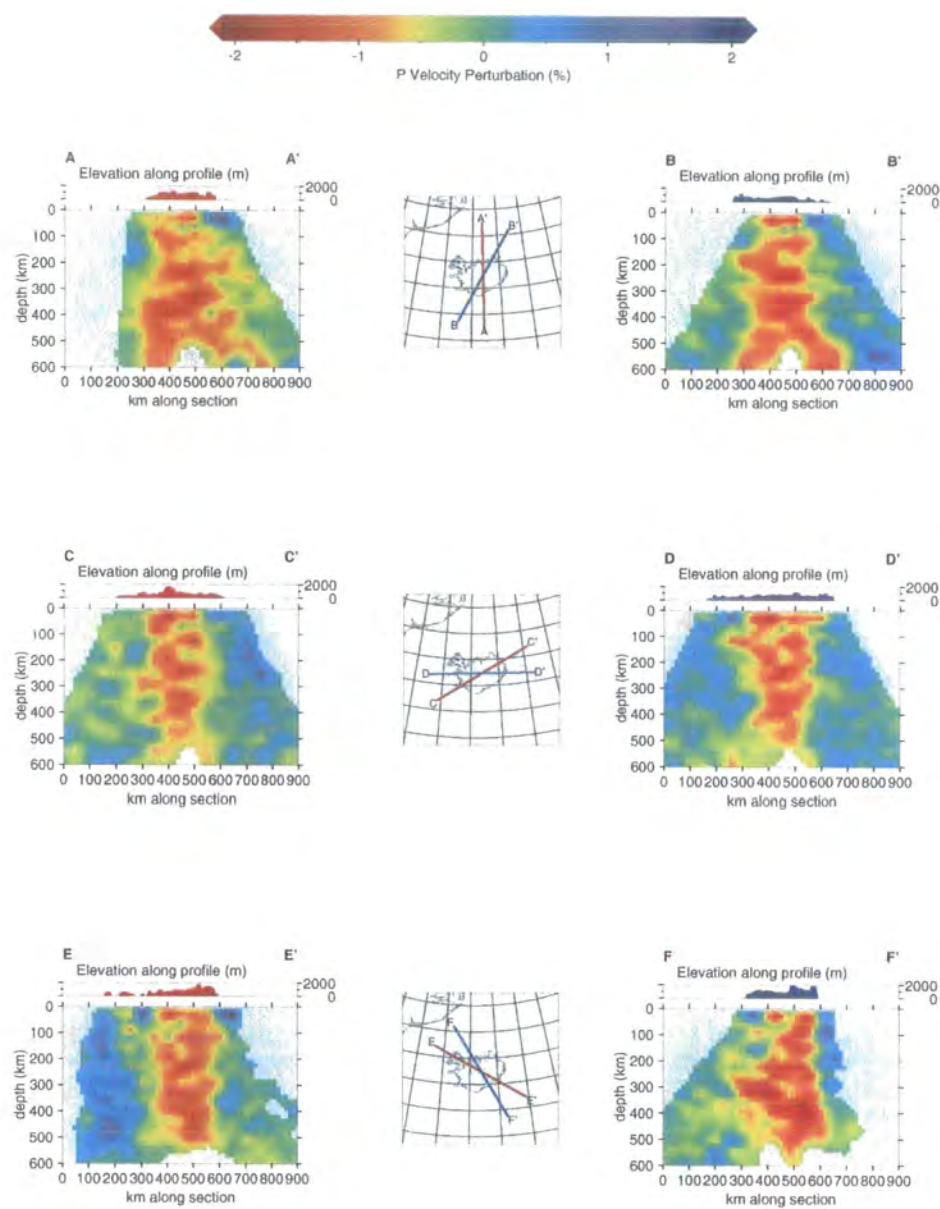
Figure 5.53 As for Figure 5.14 except for model p_10_50_161.
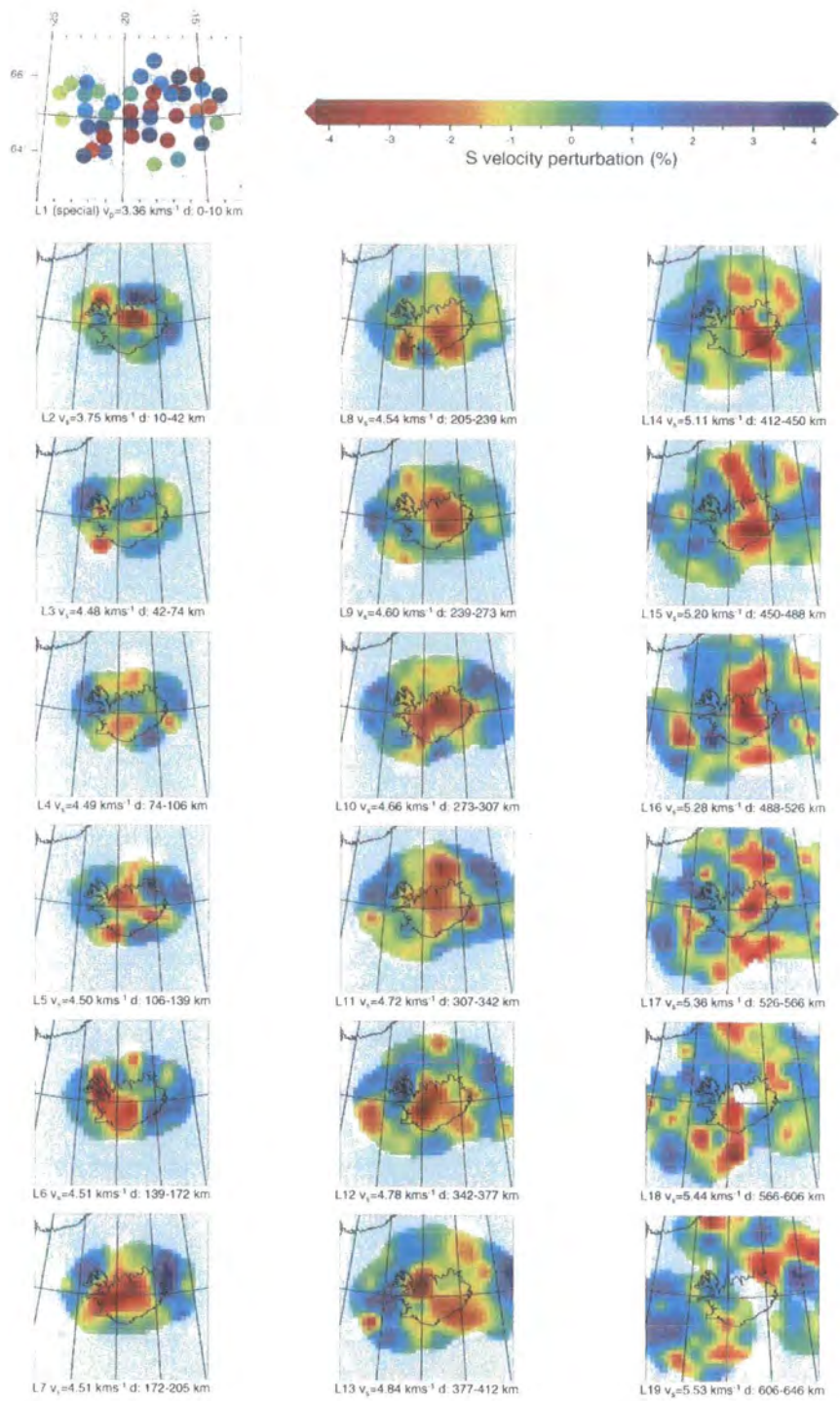
Figure 5.54 As for Figure 5.11 except for model s_10_100_161.
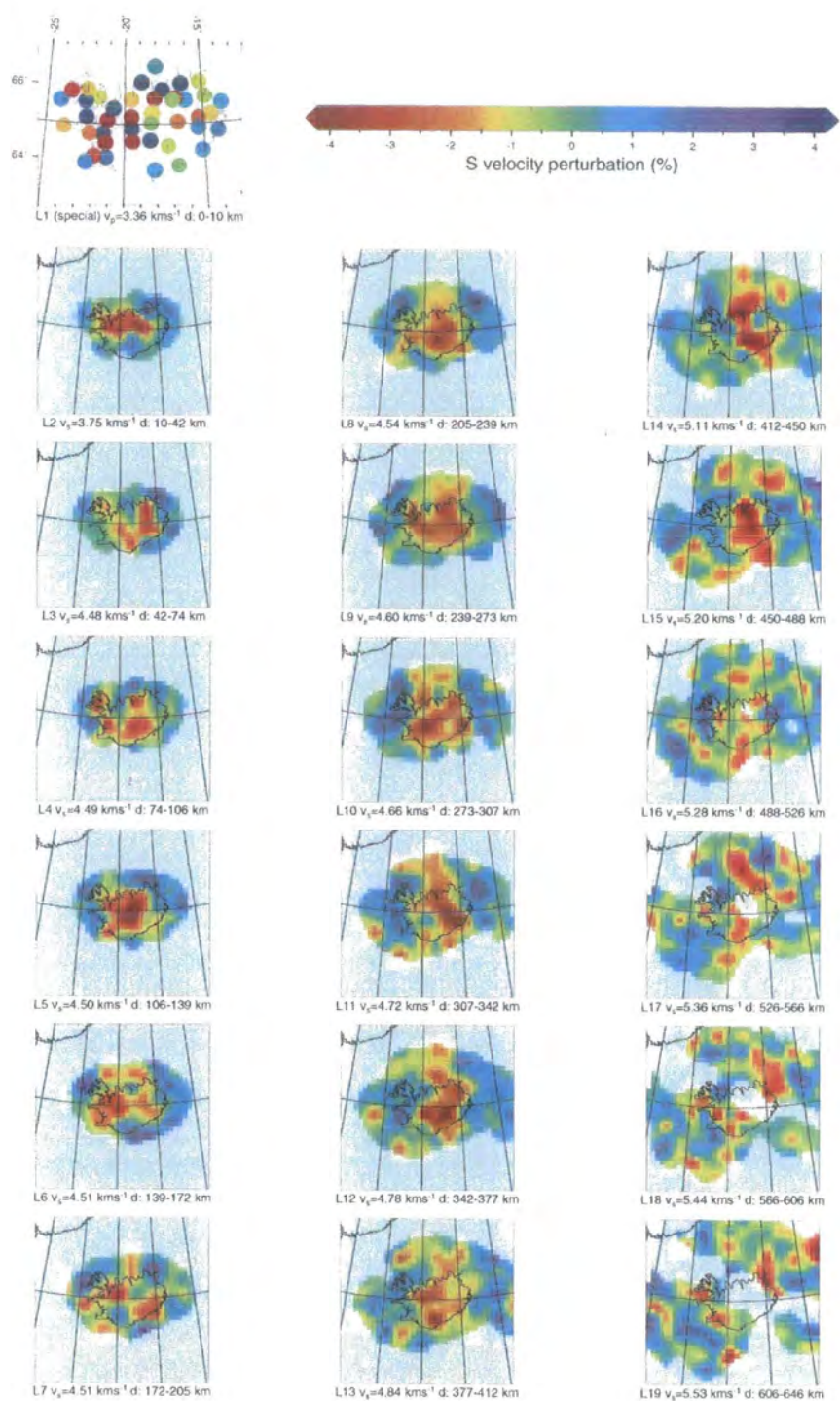
Figure 5.55 As for Figure 5.11 except for model s_10_75_161.
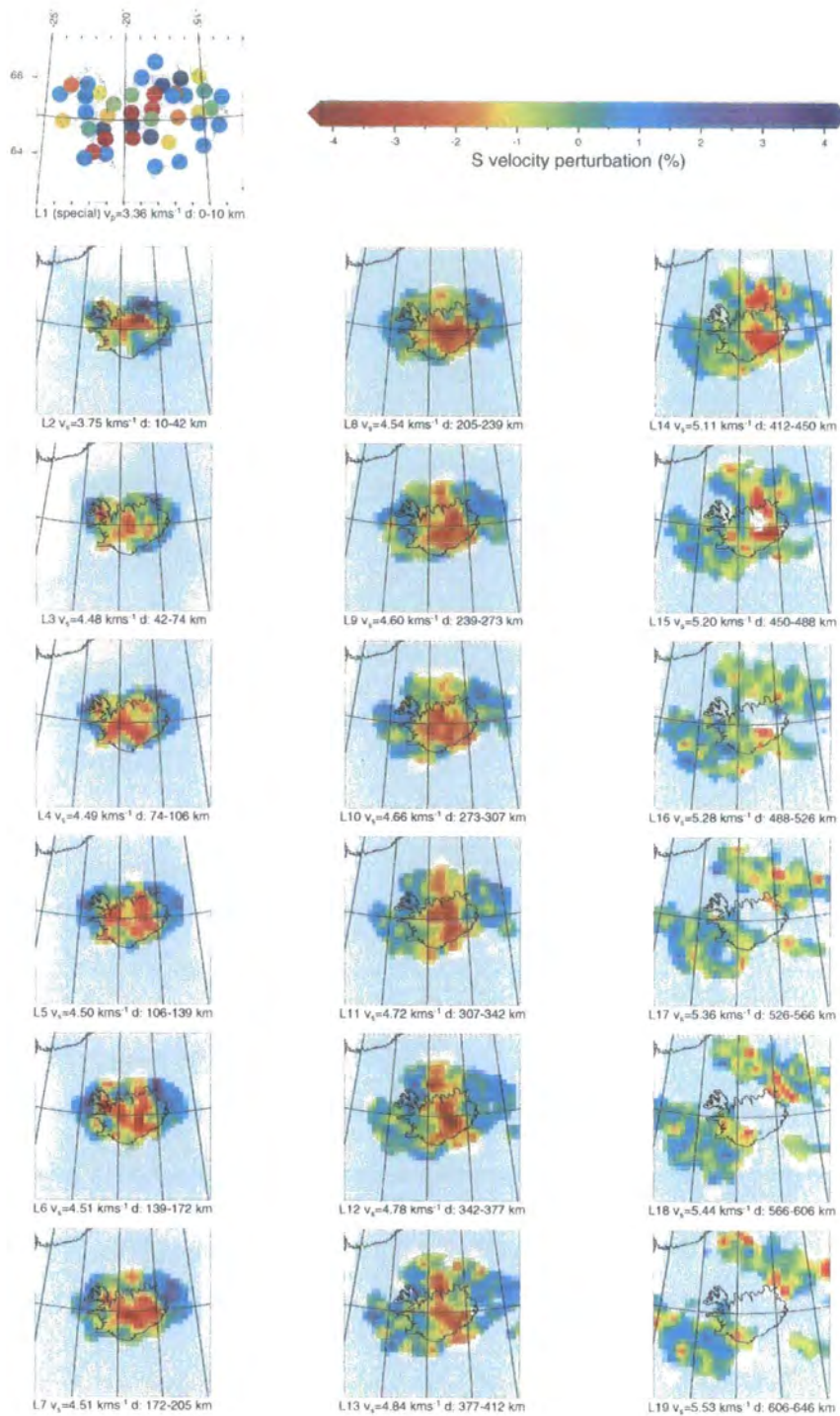
Figure 5.56 As for Figure 5.11 except for model s_10_50_161.
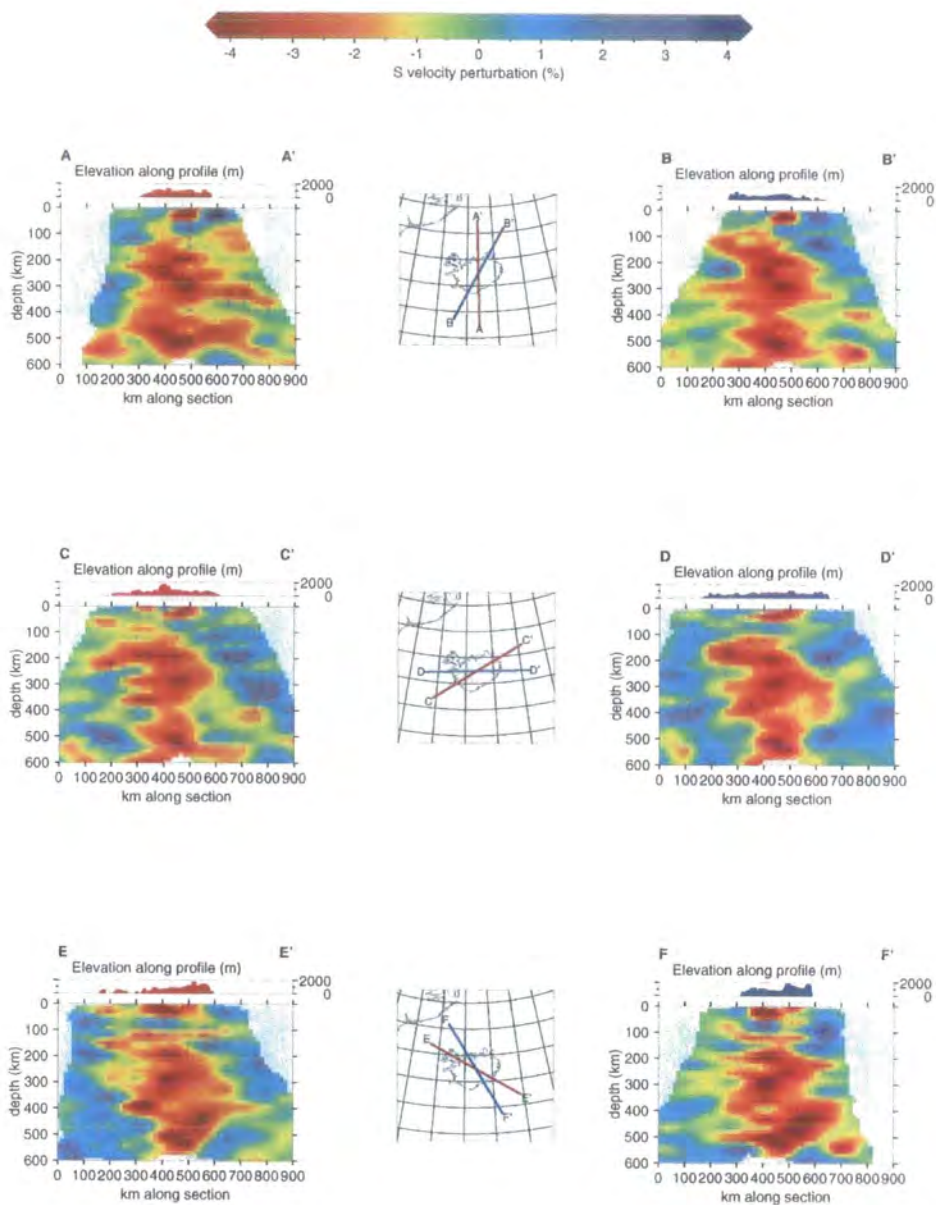
Figure 5.57 As for Figure 5.14 except for model s_10_100_161.
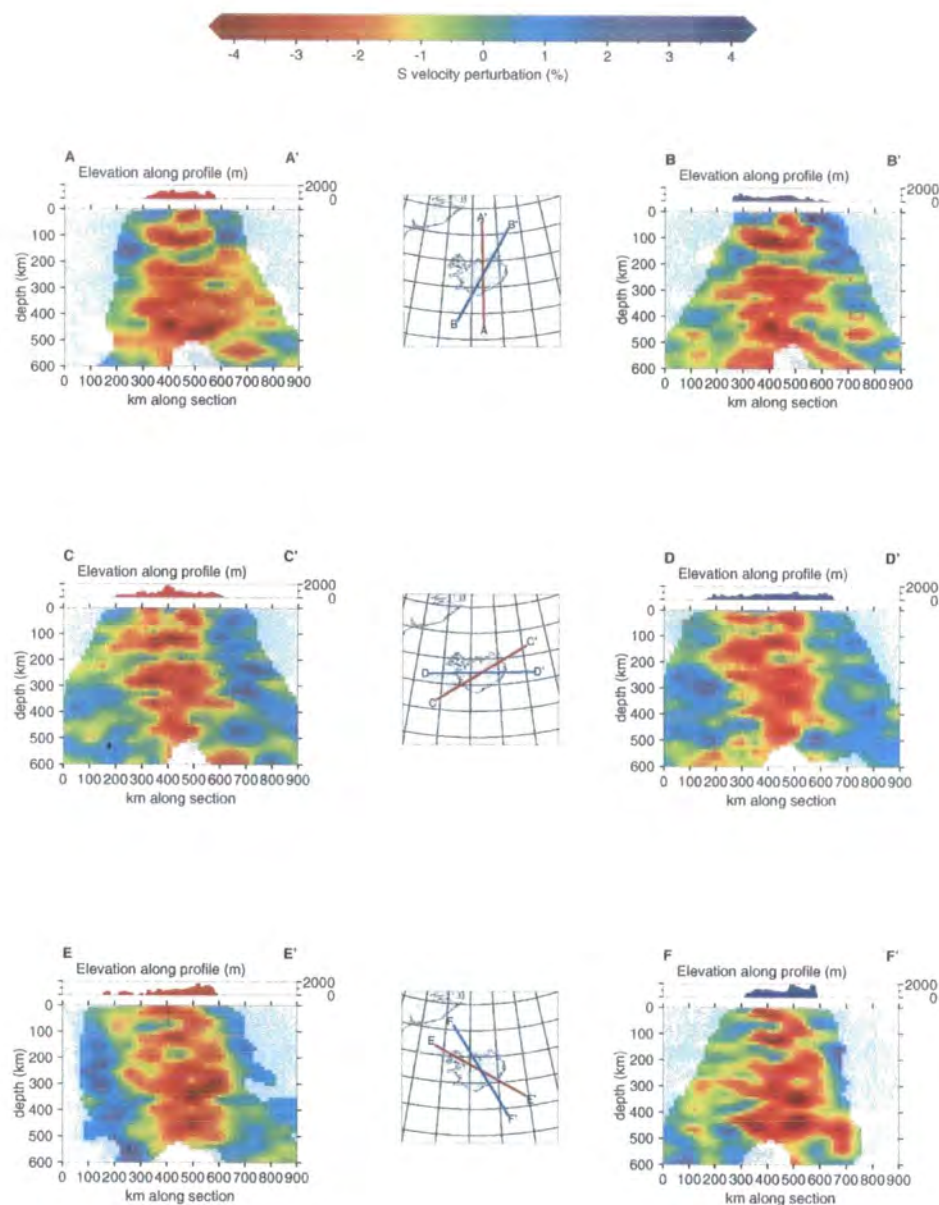
Figure 5.58 As for Figure 5.14 except for model s_10_75_161.
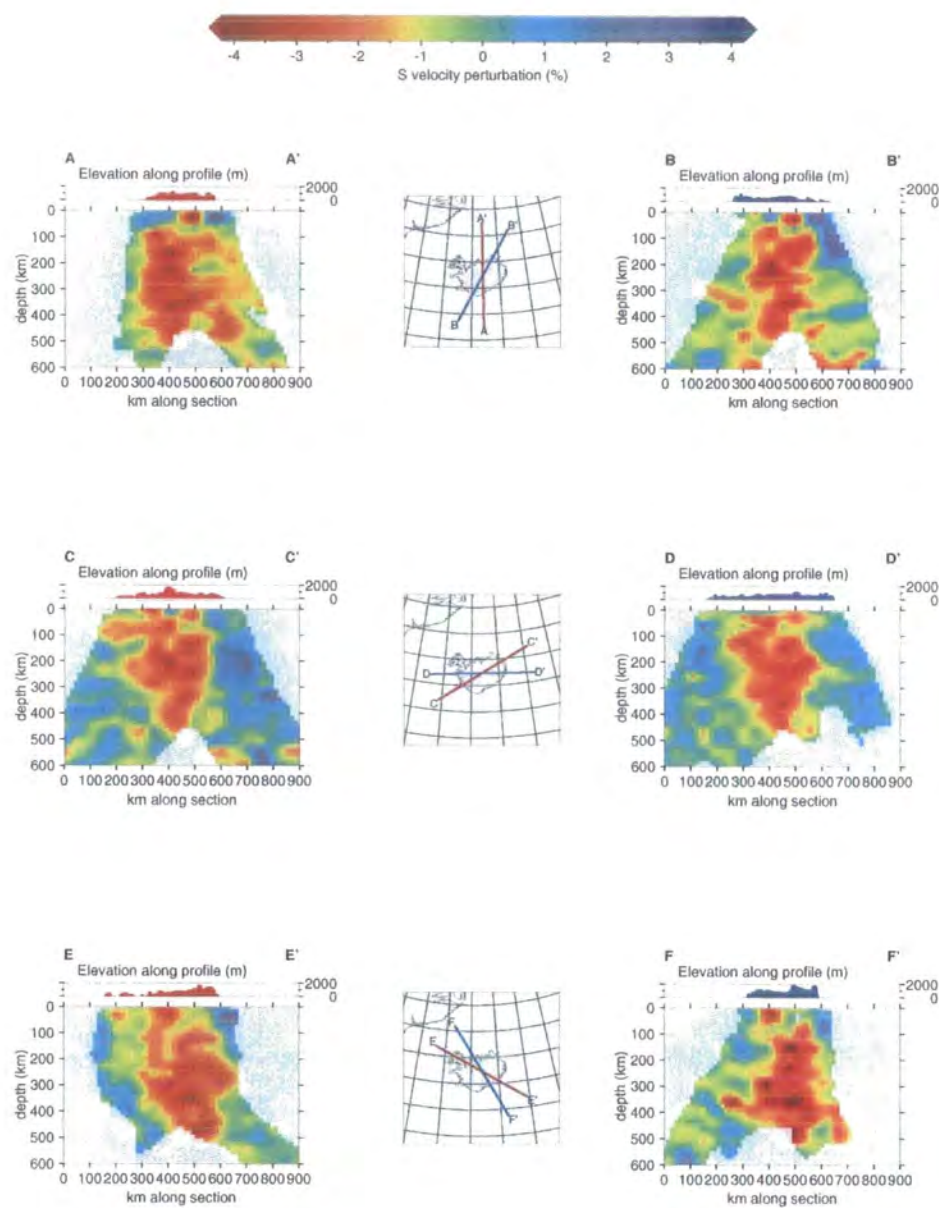
Figure 5.59 As for Figure 5.14 except for model s_10_50_161.

5.2.9   Horizontally-smoothed thin-layered models

It is apparent from Figures 5.36 - 5.59 that thinning the layers in the model makes the result noisier. It is intuitive that increasing the damping would counteract this, but it was found to have surprisingly little effect on the inter-layer anomaly amplitude fluctuations in the thinned models. The problem is remedied to some extent with the application of the offset-and-averaging procedure, as shown in Figures 5.60 - 5.81, at least in the case of the 50- and 75-km block width models. It was not possible to apply the offset-and-averaging procedure to model p_10_50_161 because of difficulties running the inversion with the very large number of blocks involved.
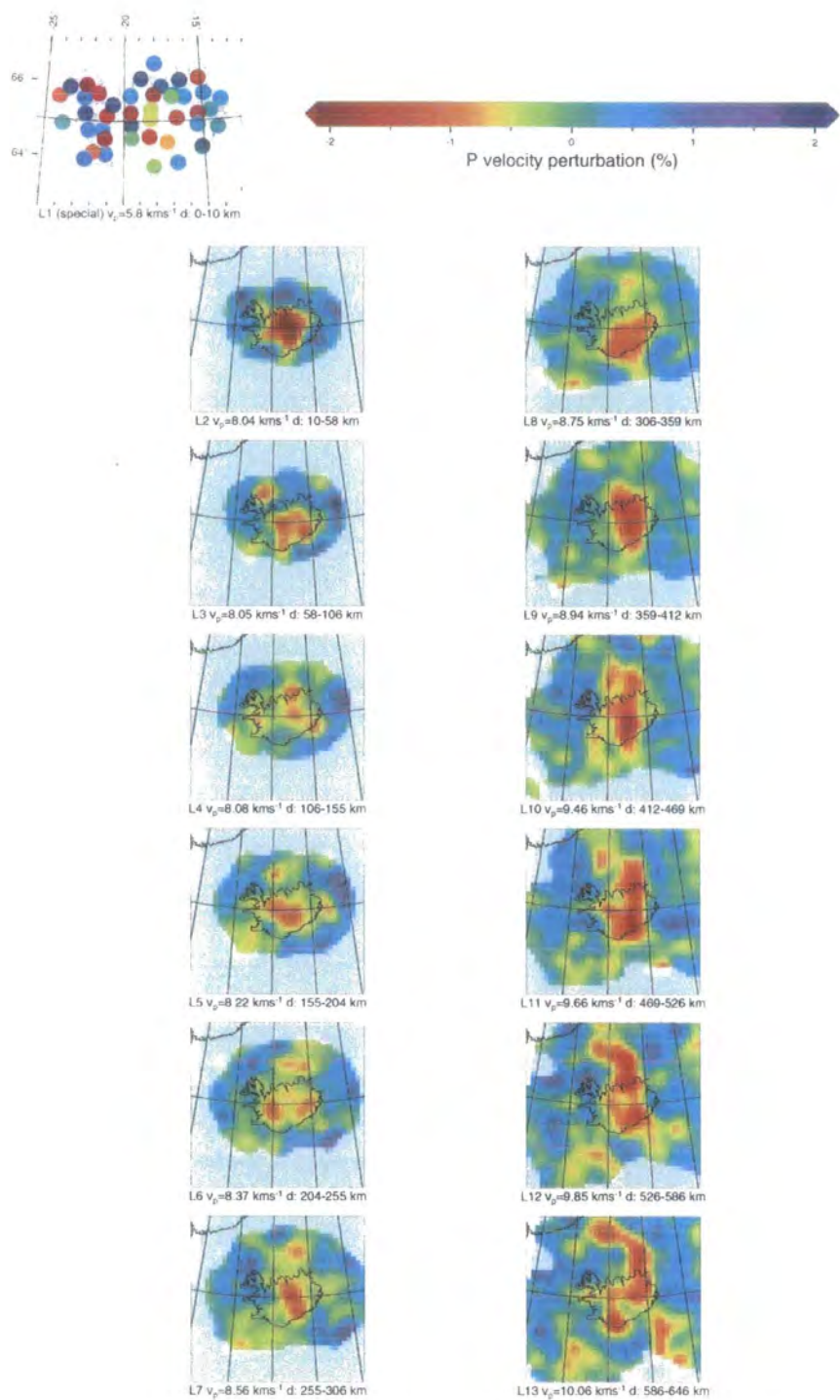
Figure 5.60 As for Figure 5.11 except for model p_10_100_225_av.
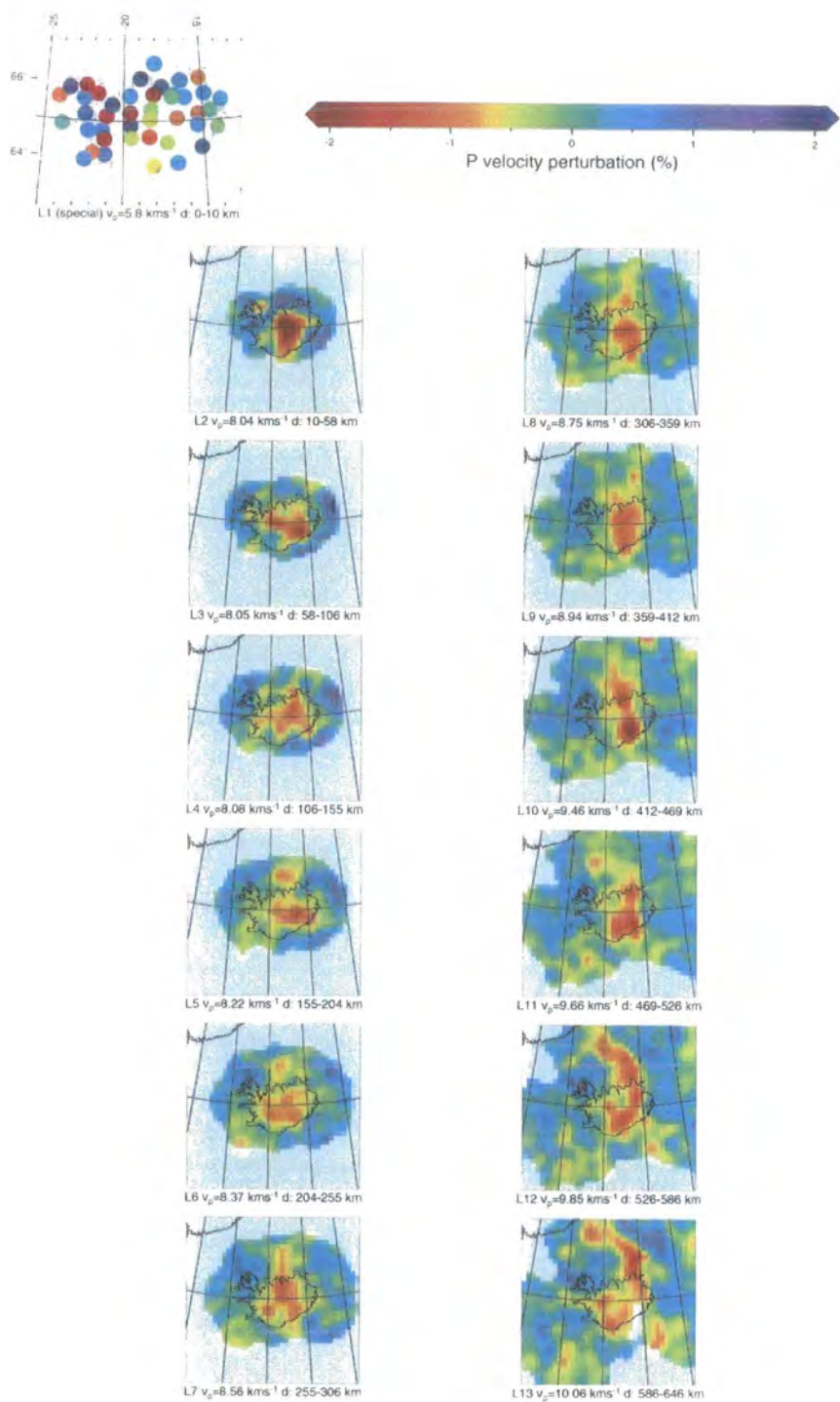
Figure 5.61 As for Figure 5.11 except for model p_10_75_225_av.
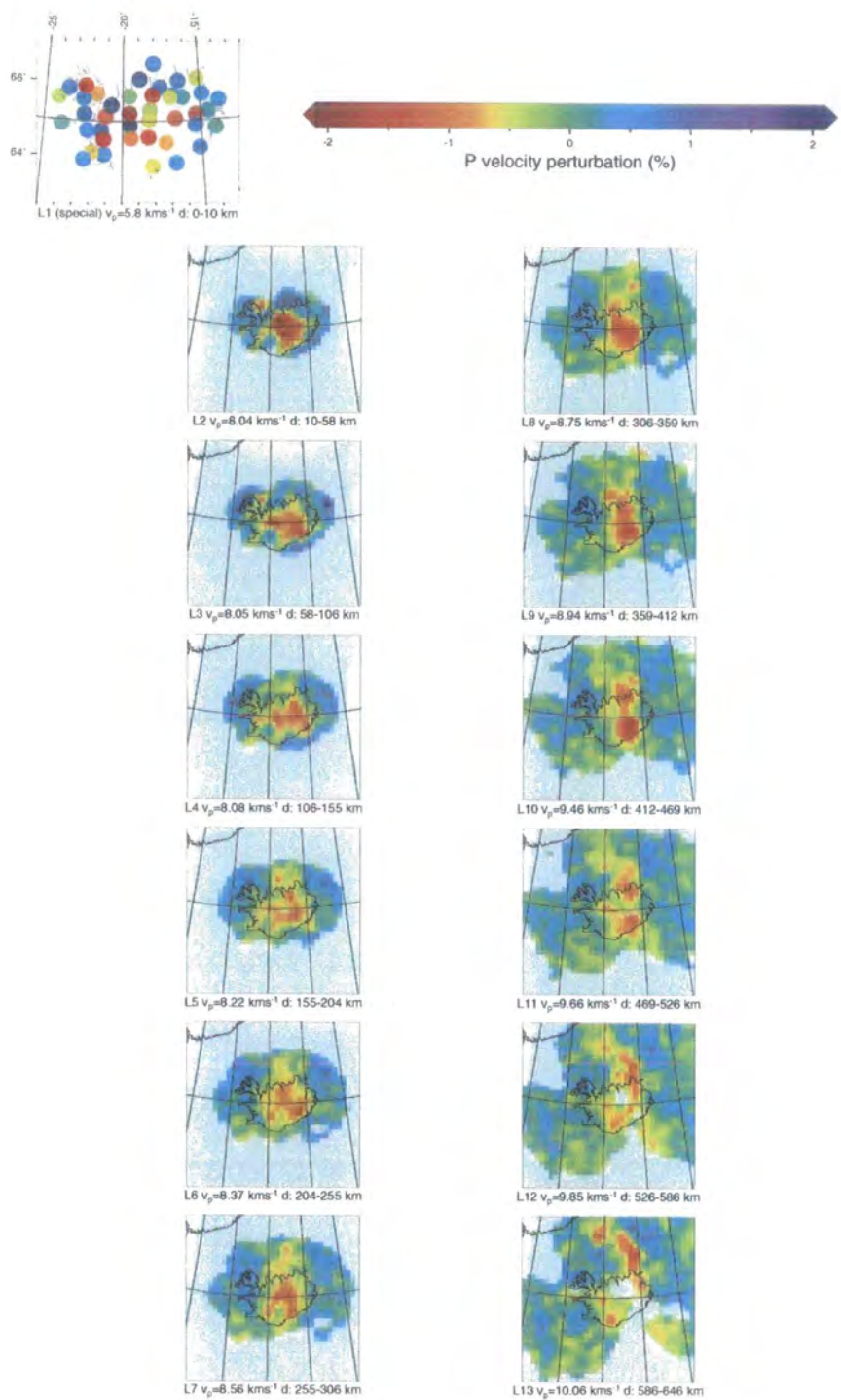
Figure 5.62 As for Figure 5.11 except for model p_10_50_225_av.
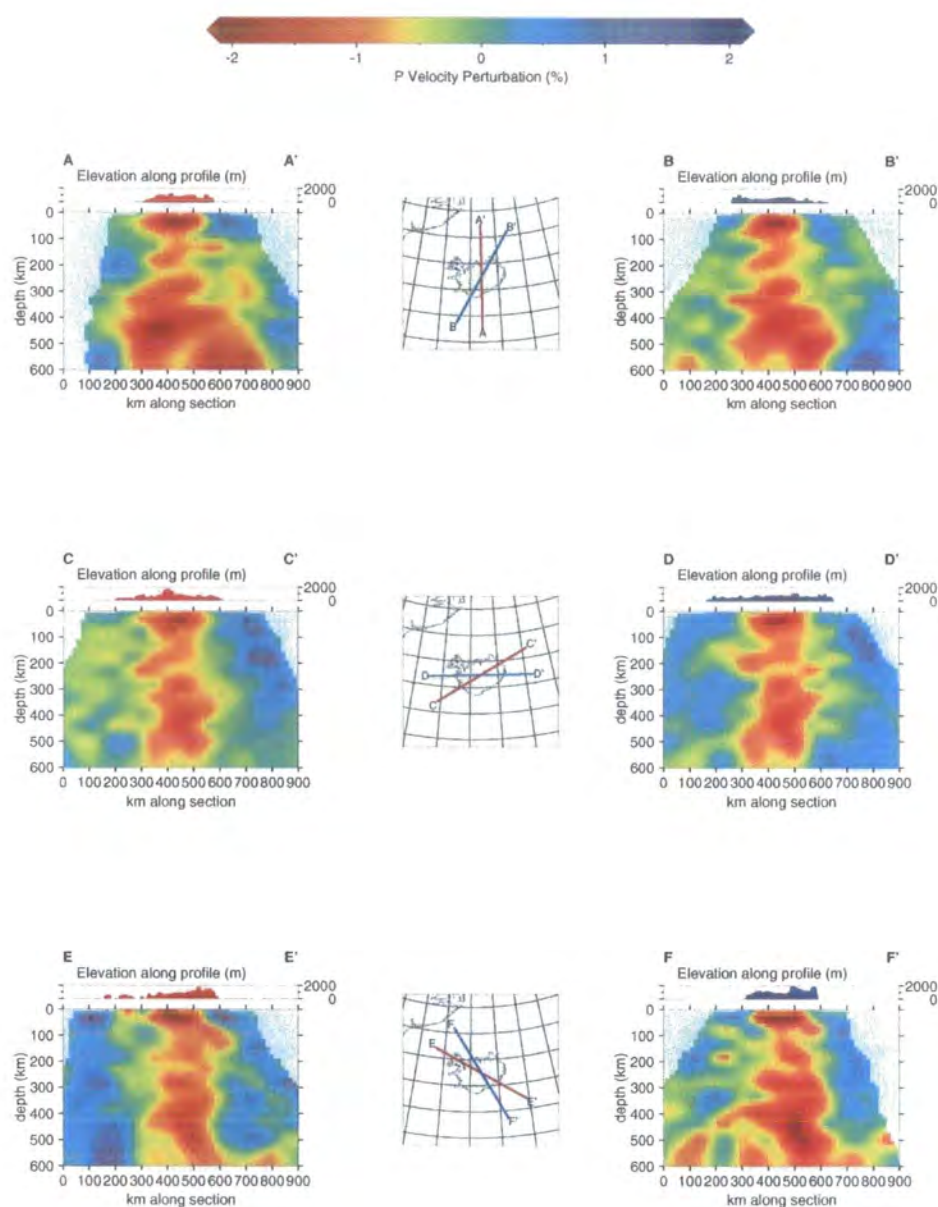
Figure 5.63 As for Figure 5.14 except for model p_10_100_225_av.
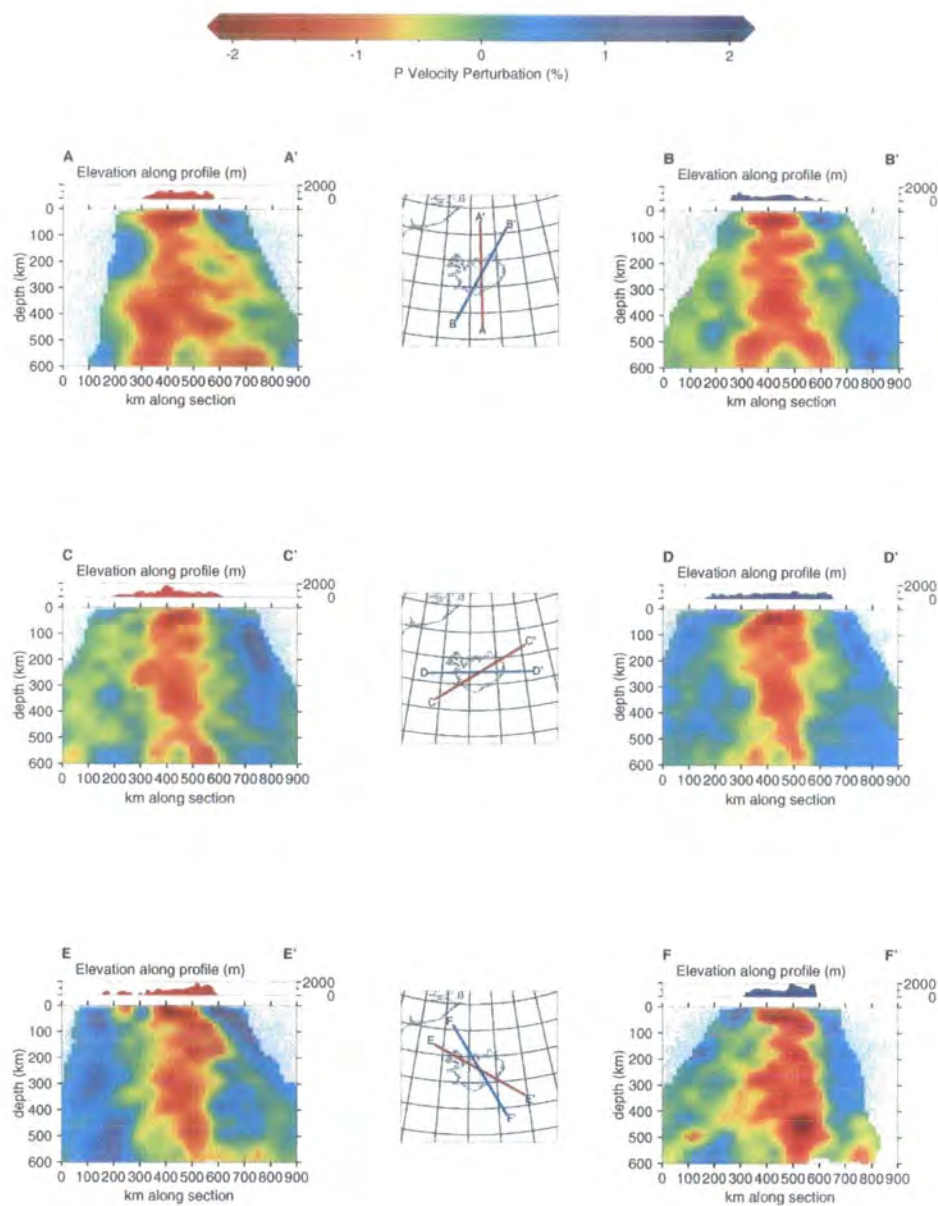
Figure 5.64 As for Figure 5.14 except for model p_10_75_225_av.
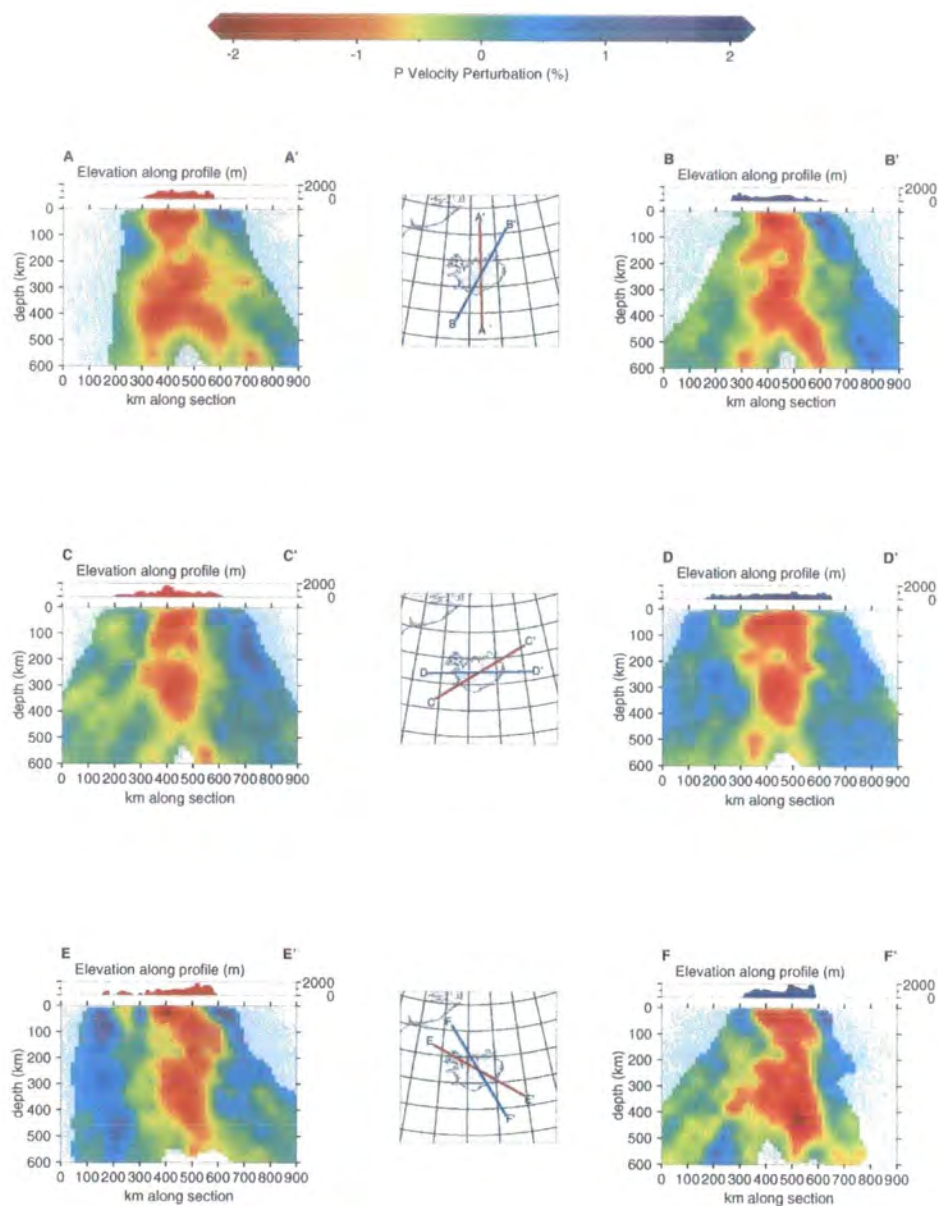
Figure 5.65 As for Figure 5.14 except for model p_10_50_225_av.
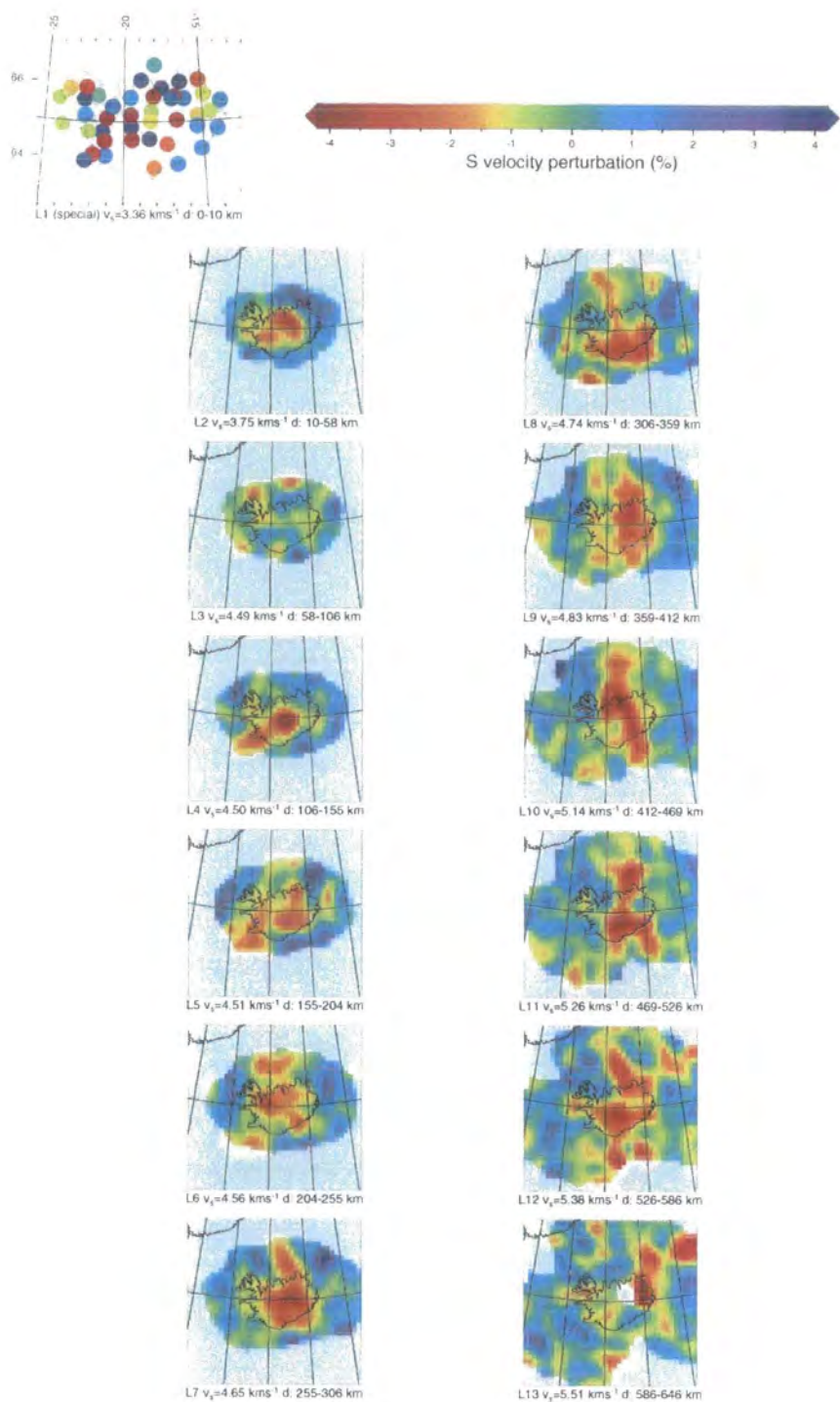
Figure 5.66 As for Figure 5.11 except for model s_10_100_225_av.
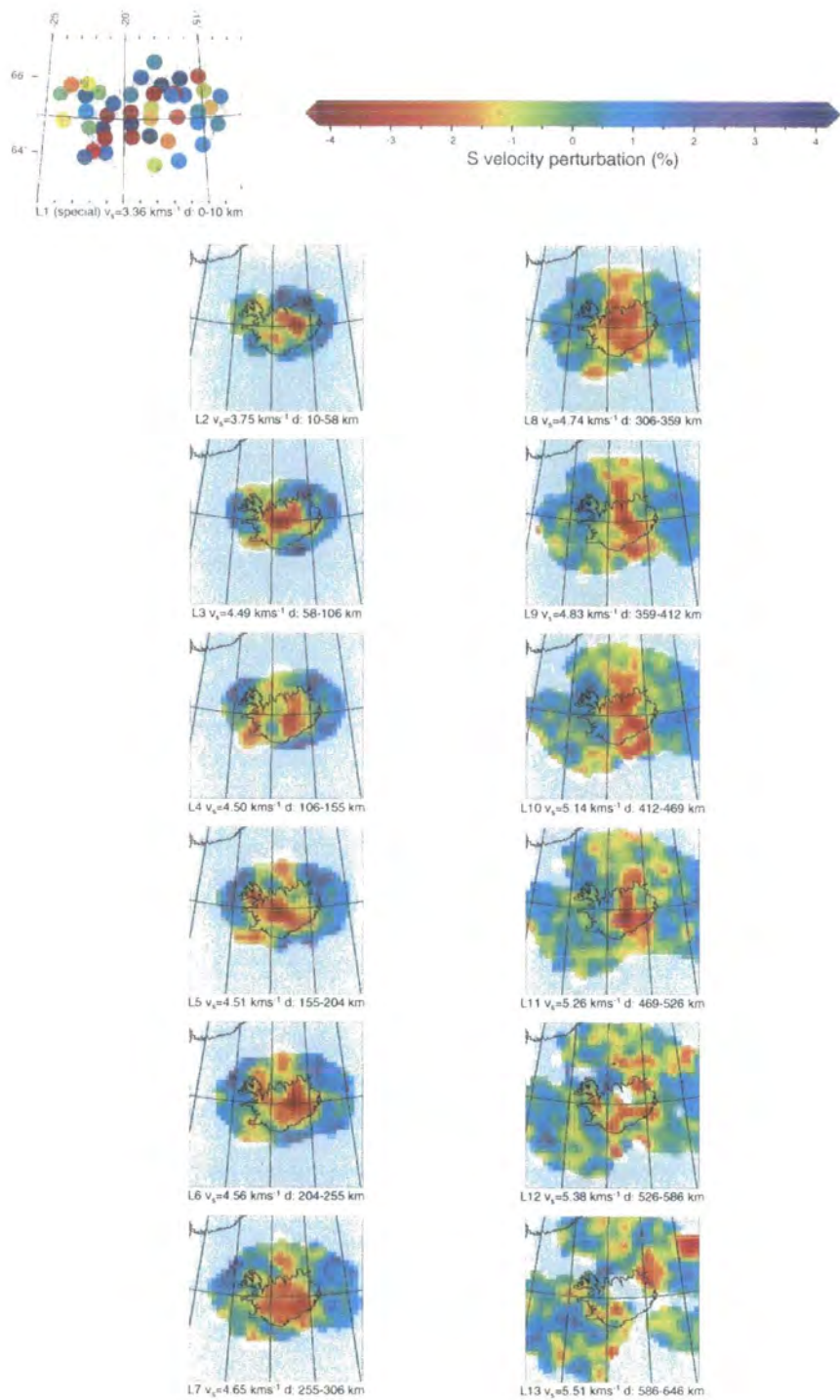
Figure 5.67 As for Figure 5.11 except for model s_10_75_225_av.
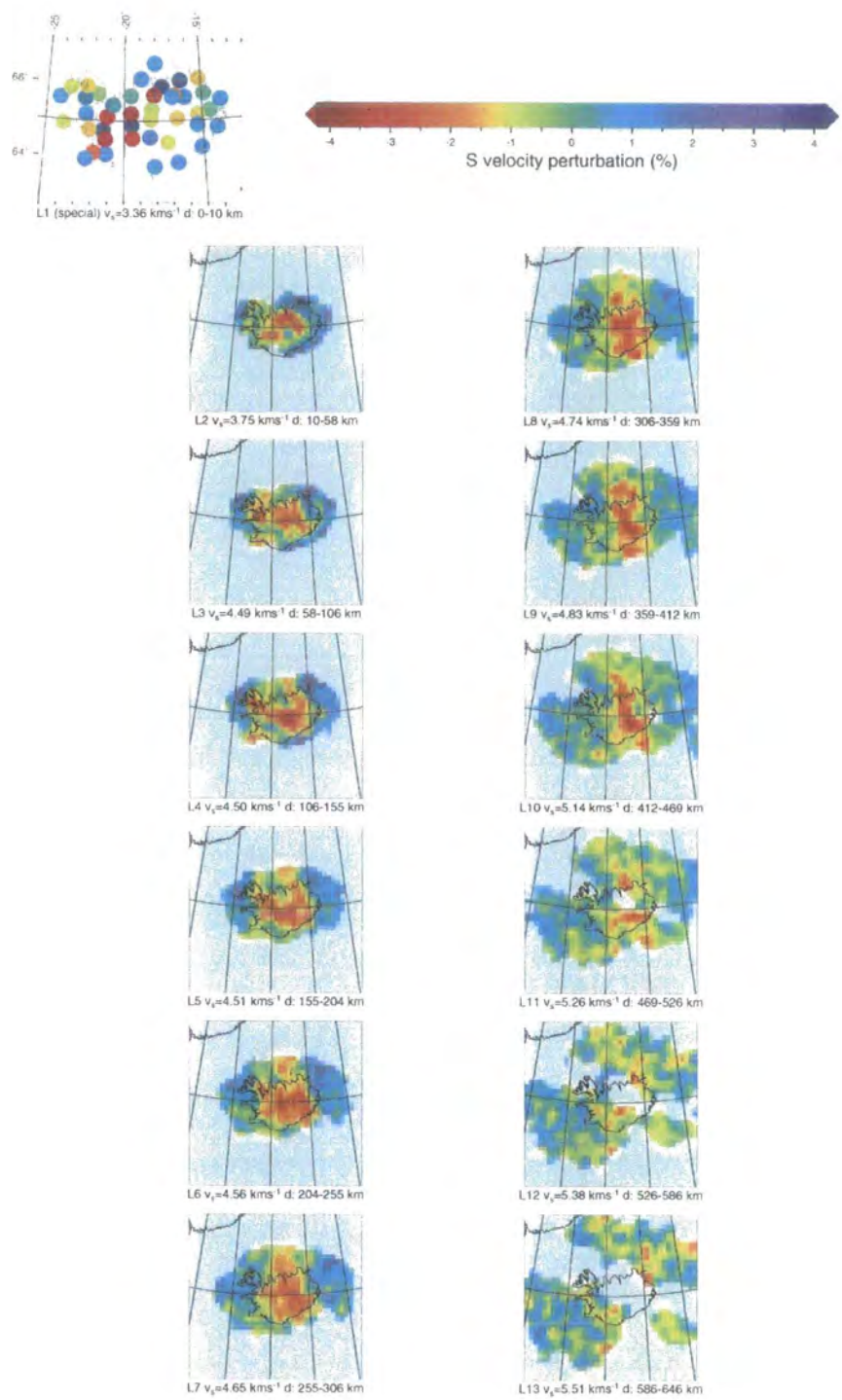
Figure 5.68 As for Figure 5.11 except for model s_10_50_225_av.
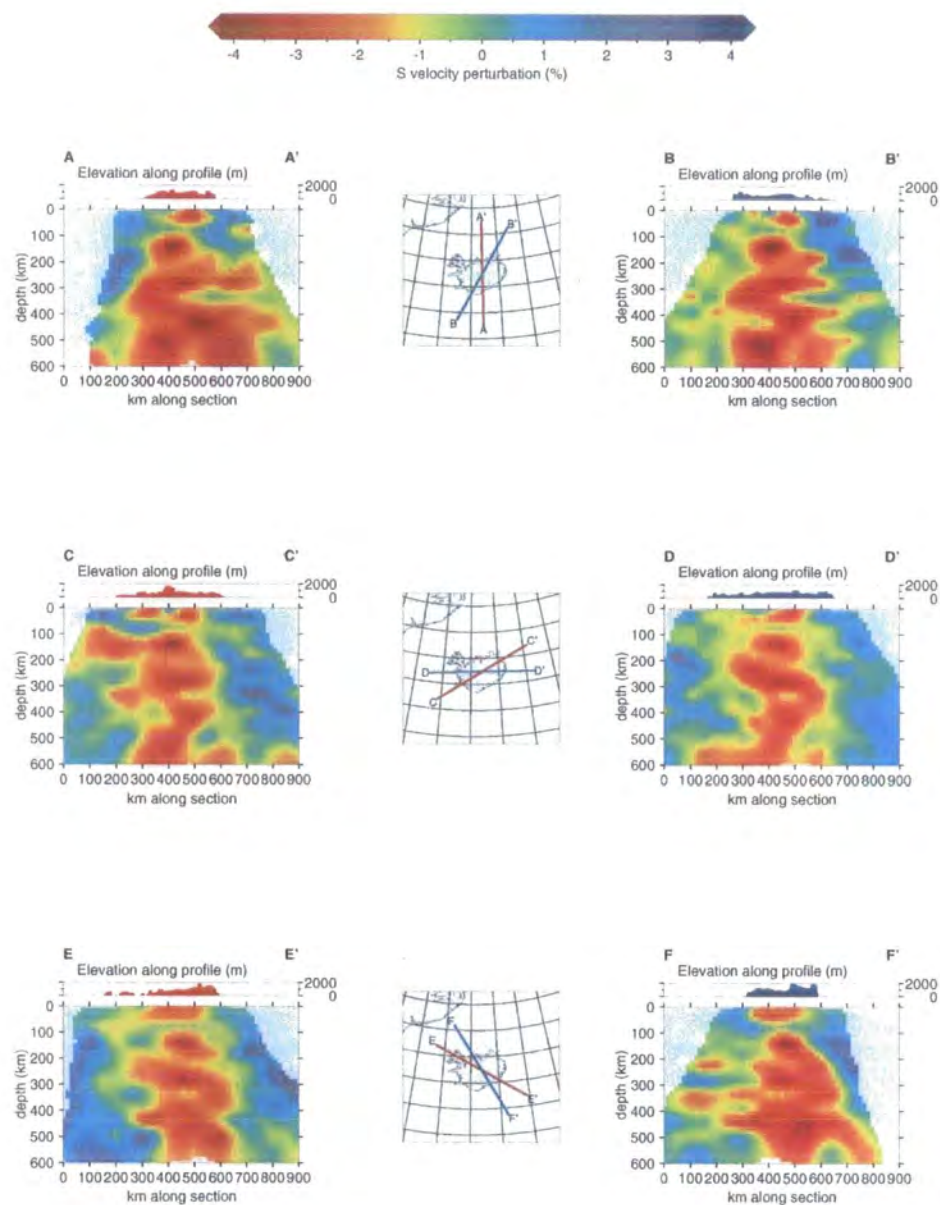
Figure 5.69 As for Figure 5.14 except for model s_10_100_225_av.
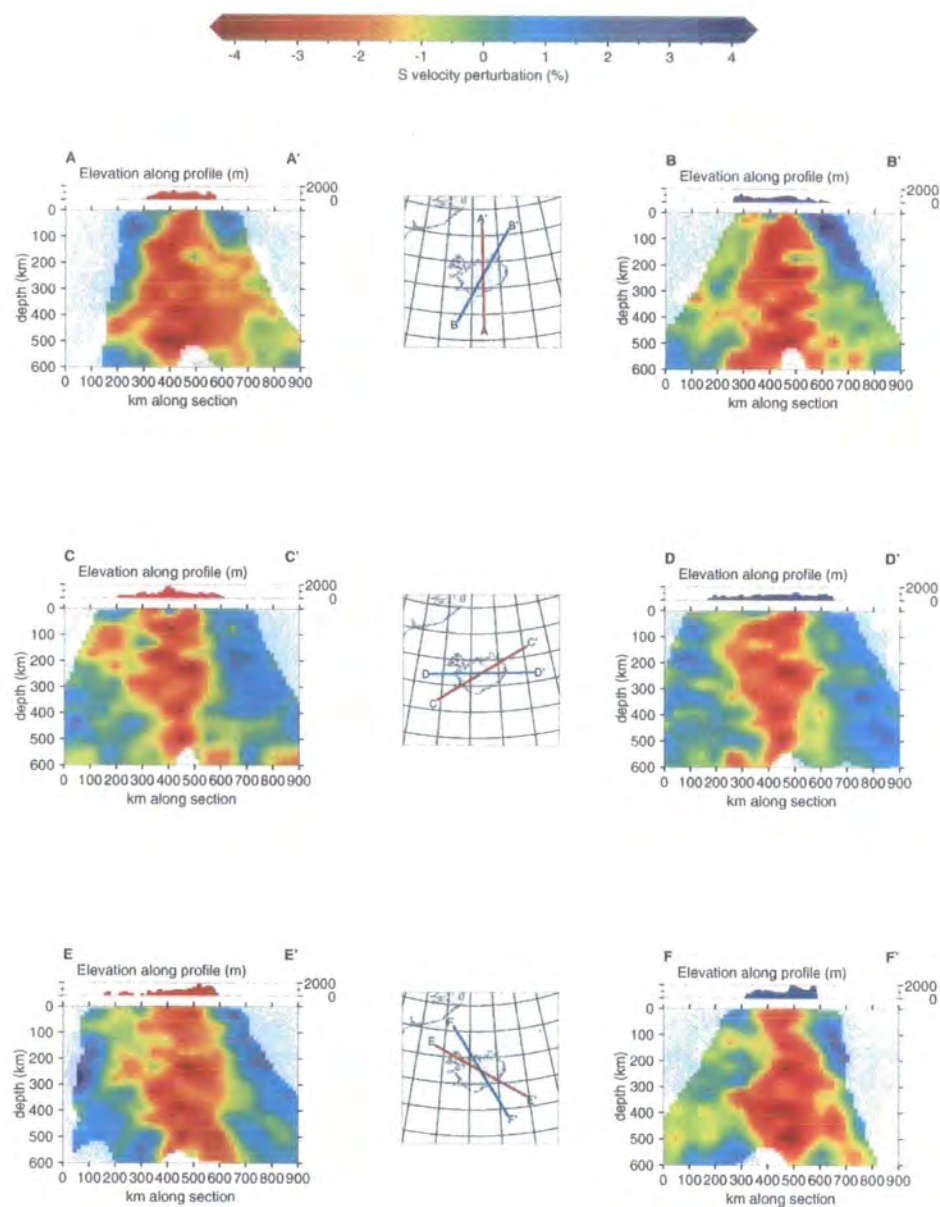
Figure 5.70 As for Figure 5.14 except for model s_10_75_225_av.
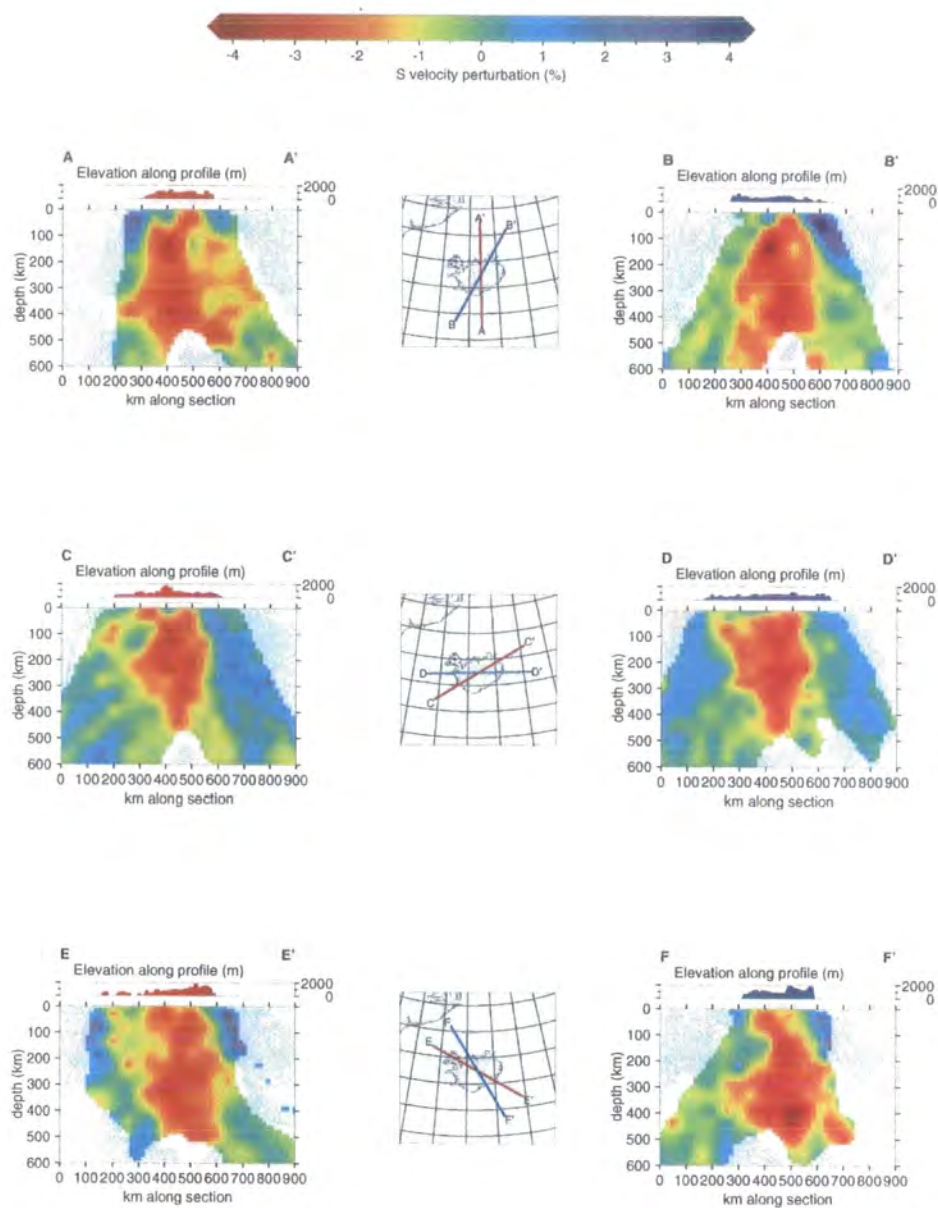
Figure 5.71 As for Figure 5.14 except for model s_10_50_225_av.
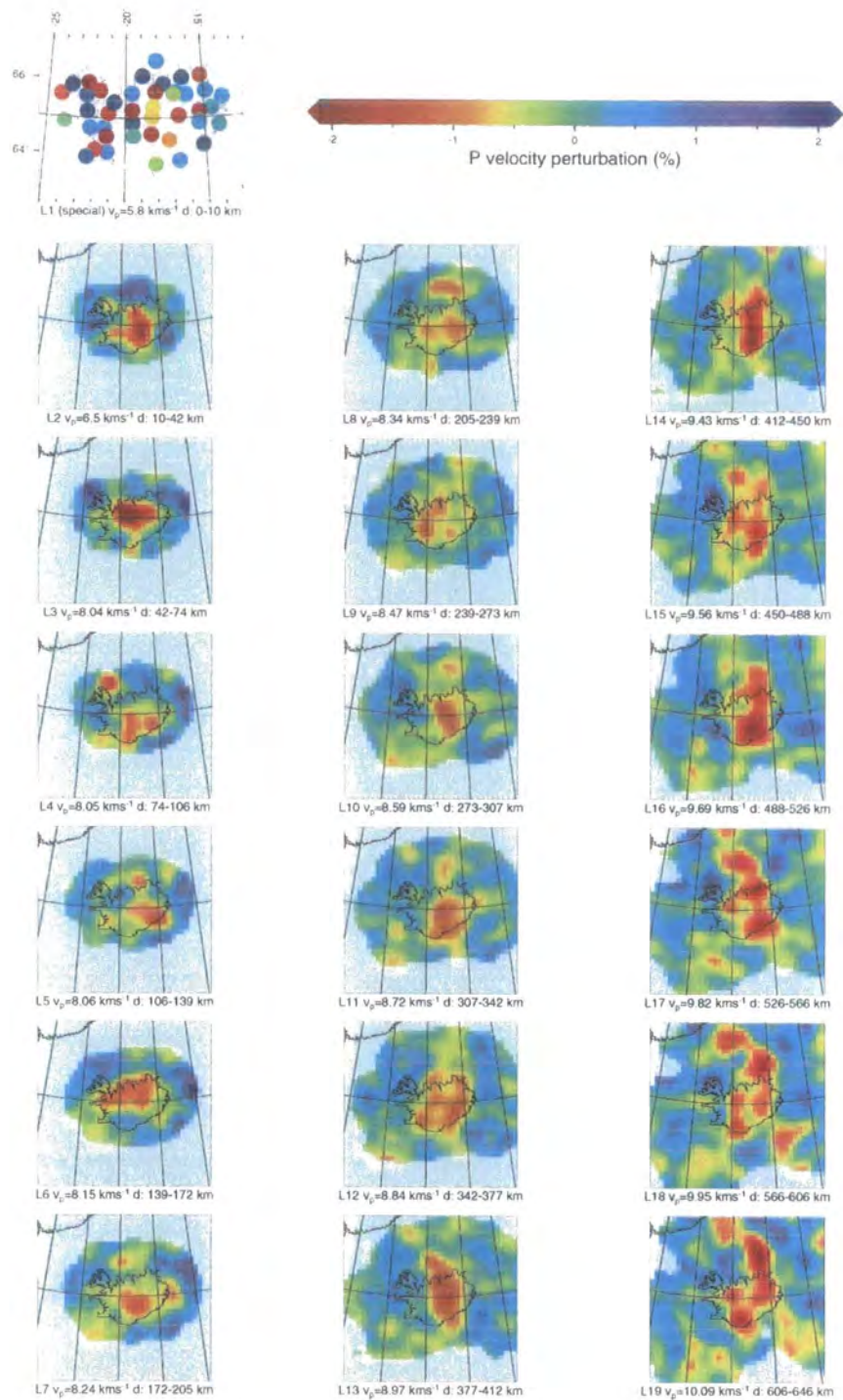
Figure 5.72 As for Figure 5.11 except for model p_10_100_161_av.
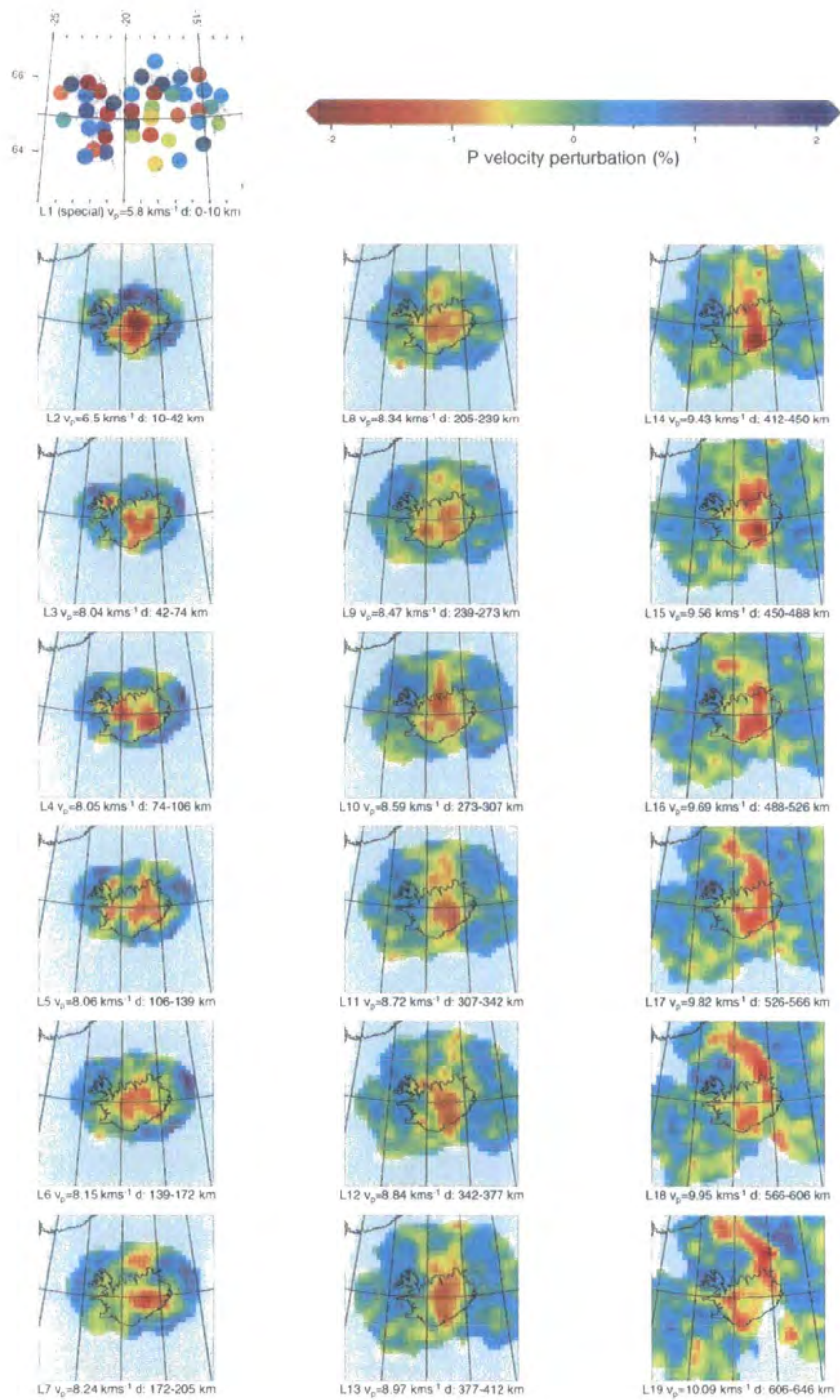
Figure 5.73 As for Figure 5.11 except for model p_10_75_161_av.
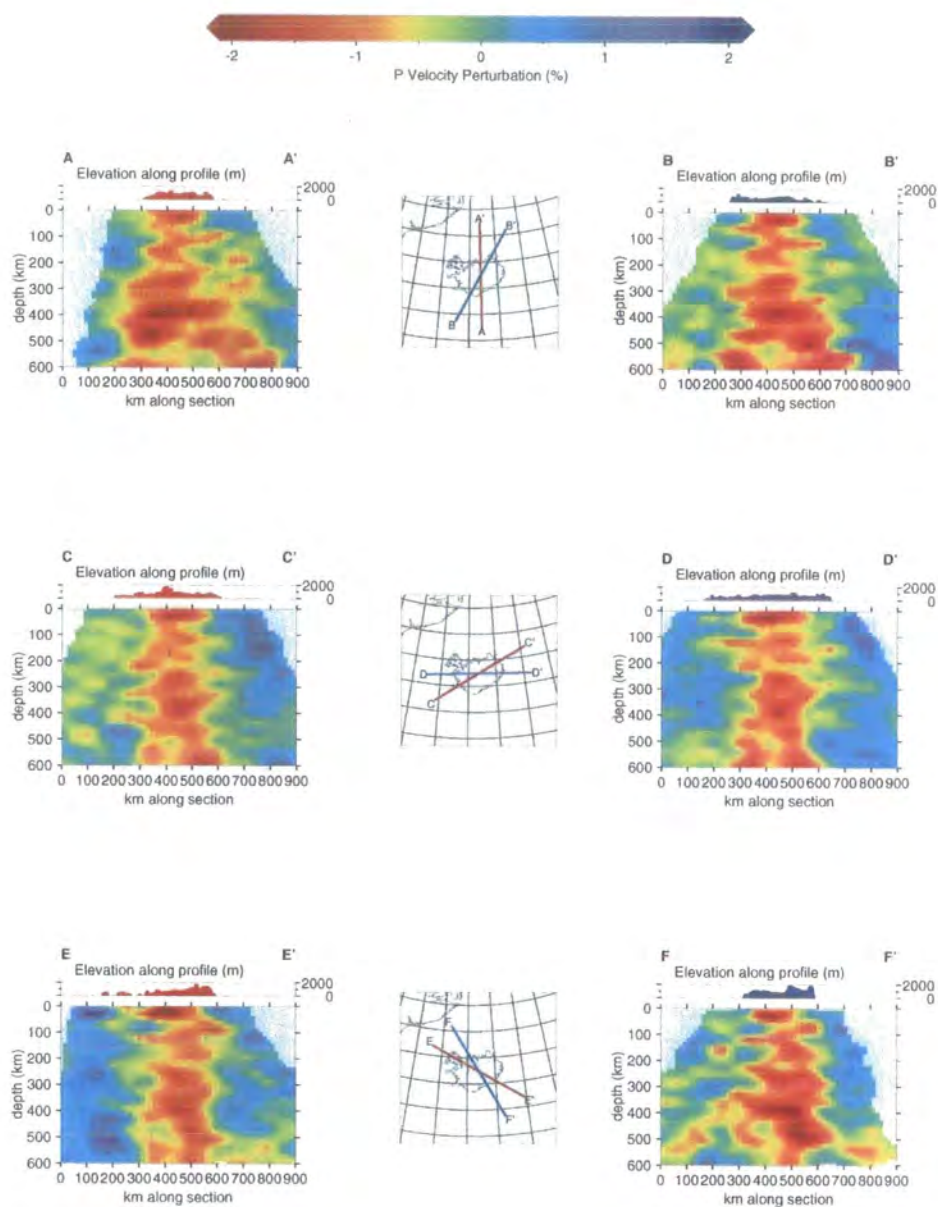
Figure 5.74 As for Figure 5.14 except for model p_10_100_161_av.
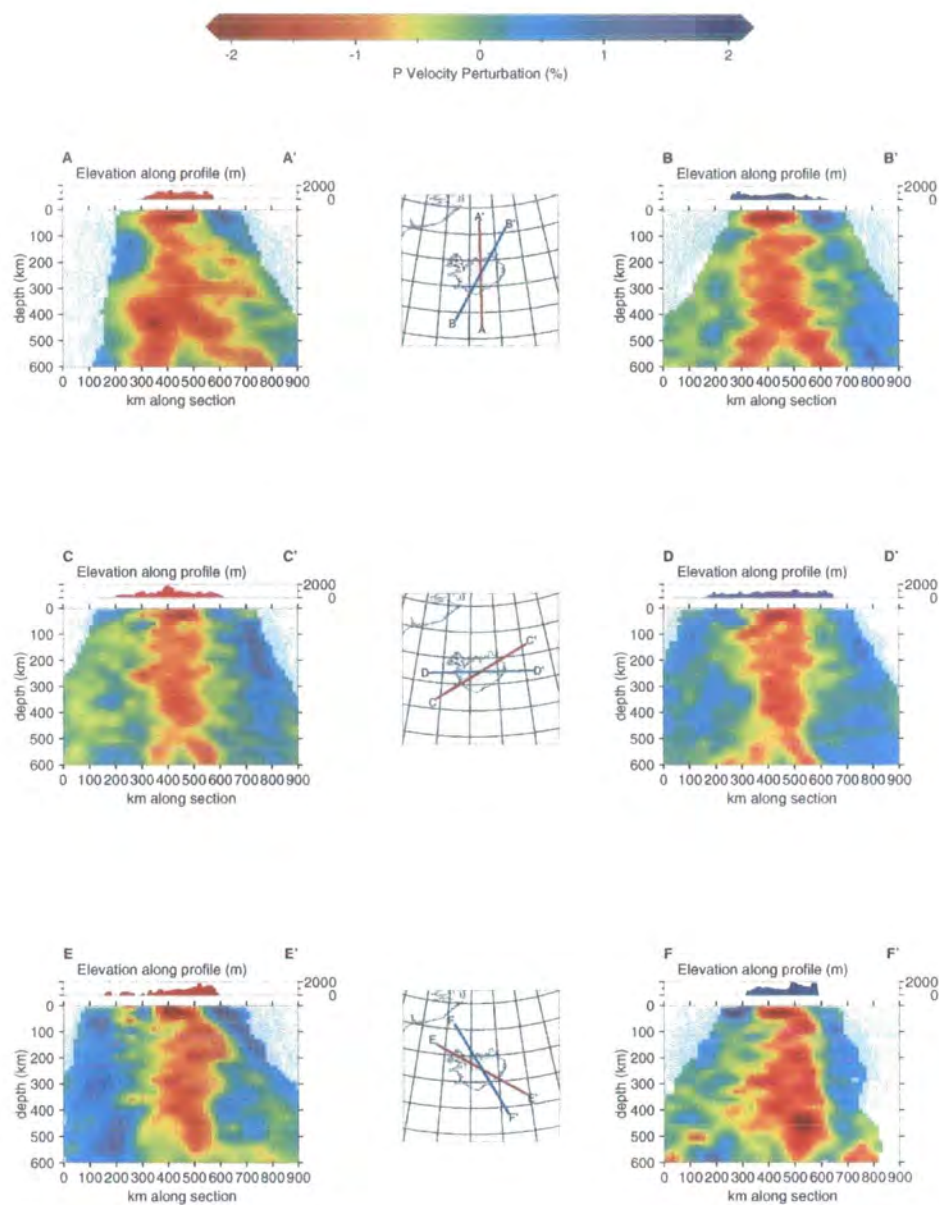
Figure 5.75 As for Figure 5.14 except for model p_10_75_161_av.
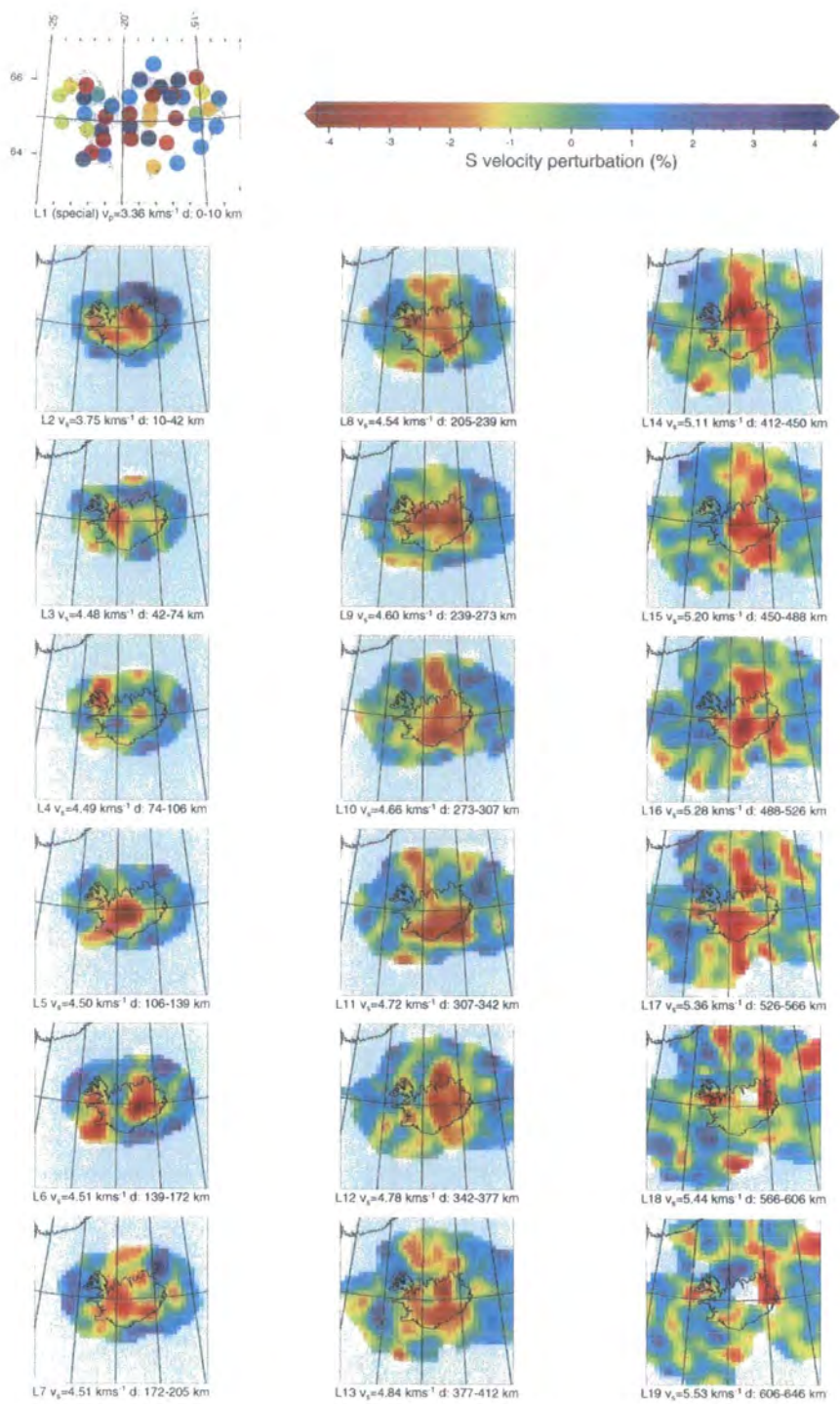
Figure 5.76 As for Figure 5.11 except for model s_10_100_161_av.
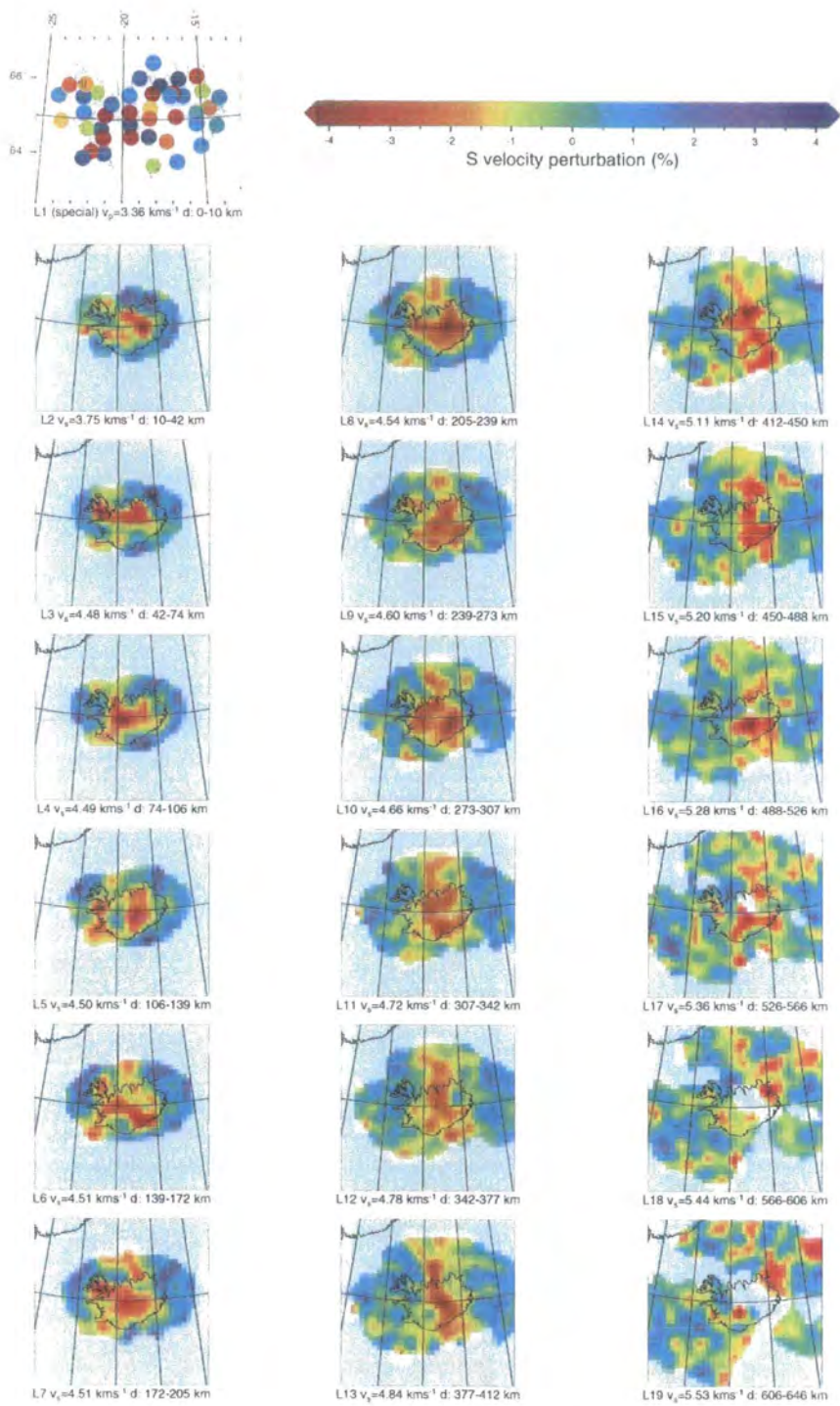
Figure 5.77 As for Figure 5.11 except for model s_10_75_161_av.
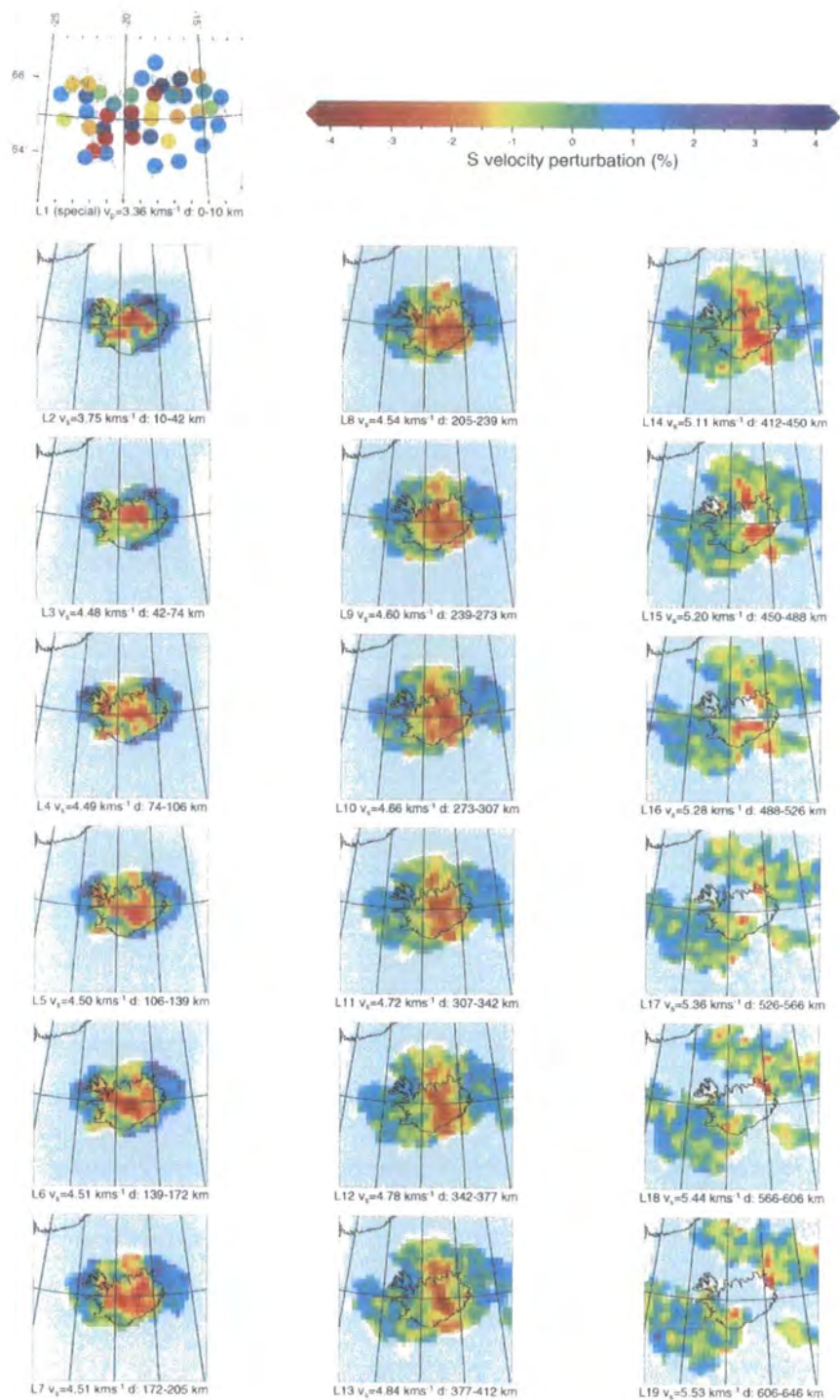
Figure 5.78 As for Figure 5.11 except for model s_10_50_161_av.
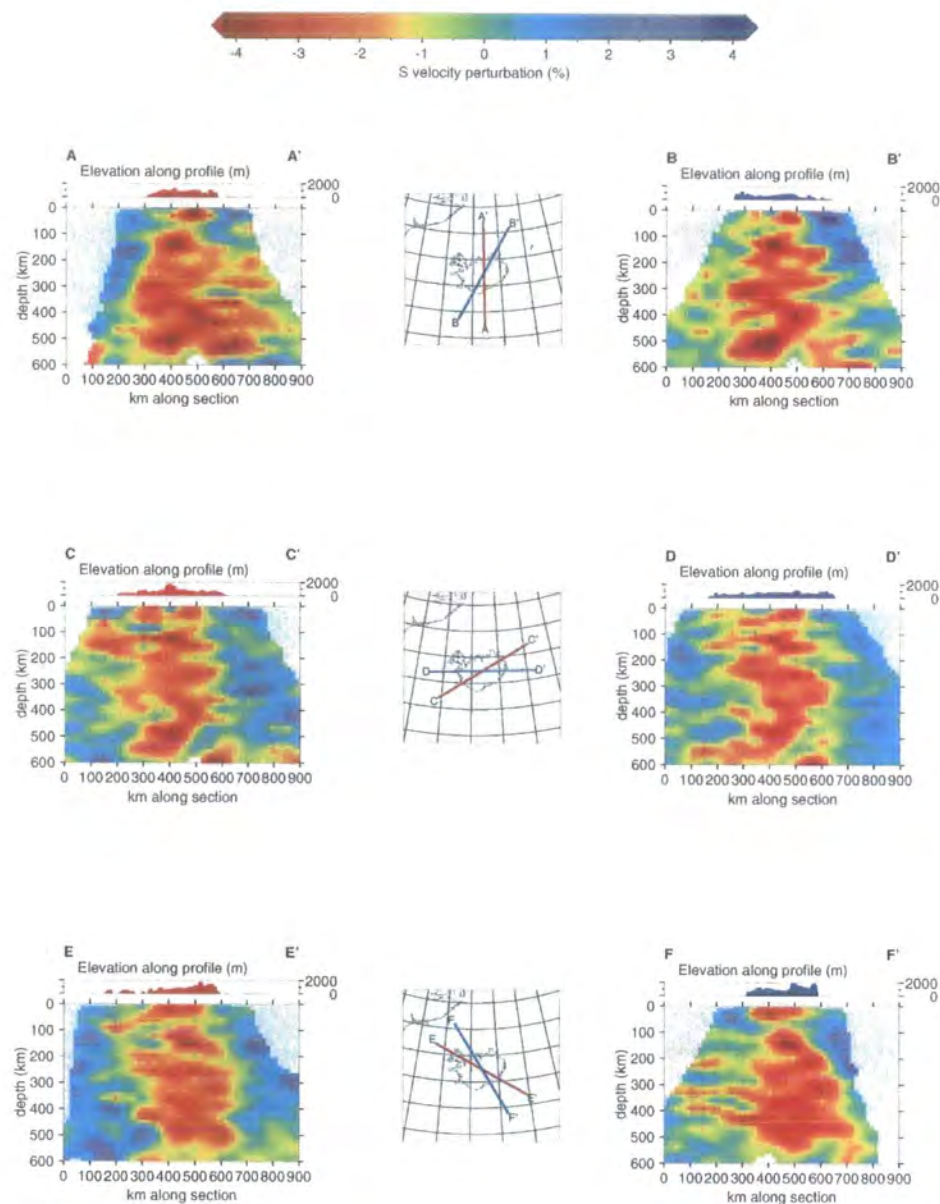
Figure 5.79 As for Figure 5.14 except for model s_10_100_161_av.
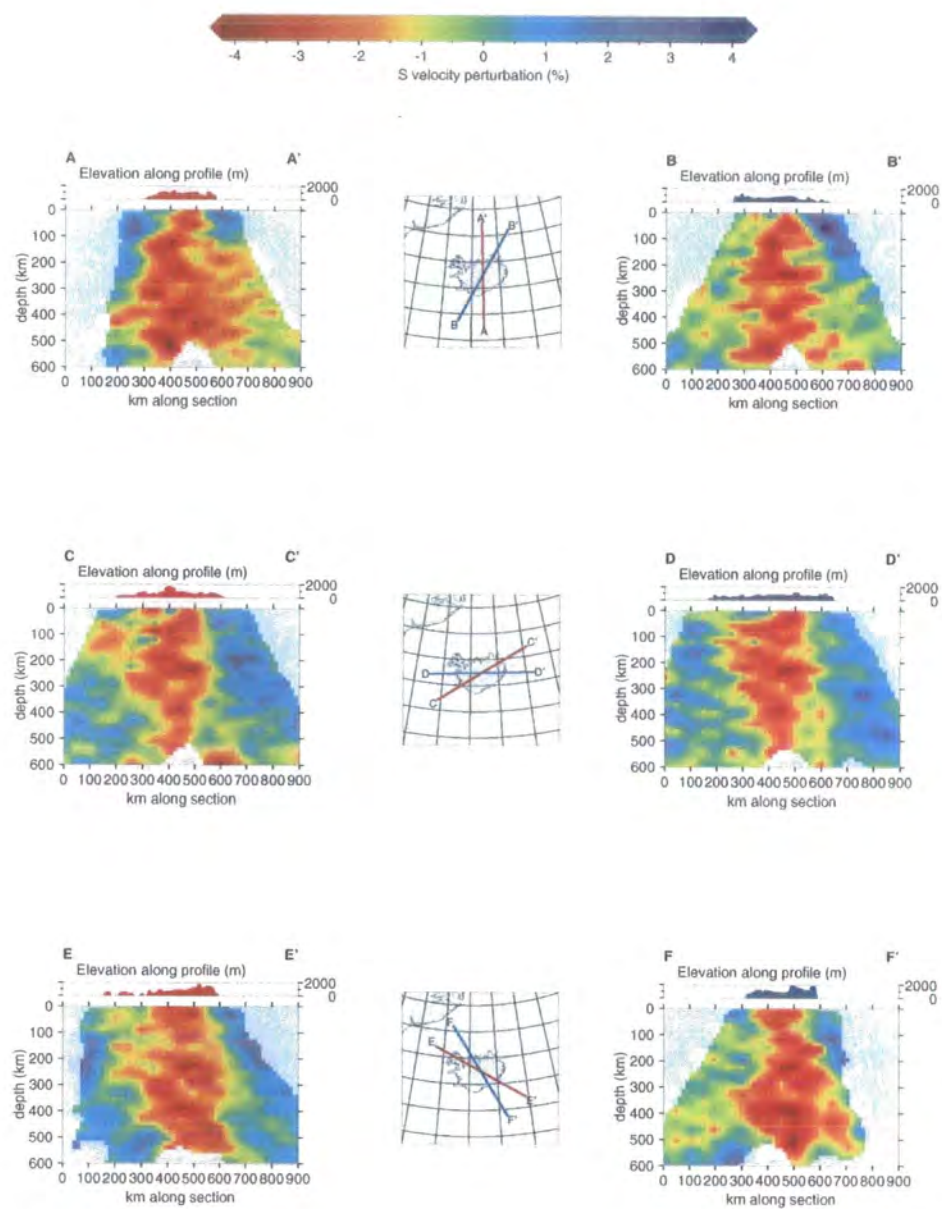
Figure 5.80 As for Figure 5.14 except for model s_10_75_161_av.
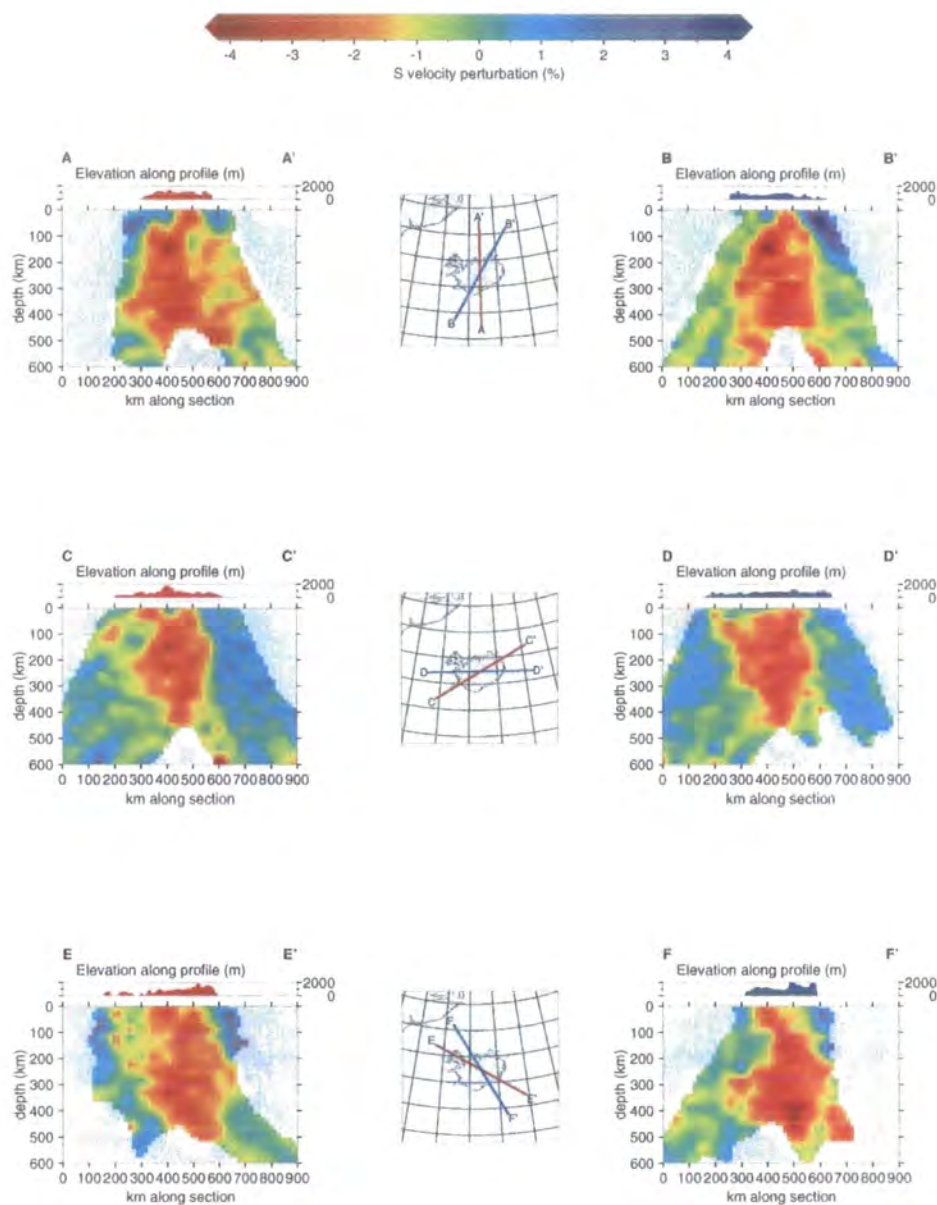
Figure 5.81 As for Figure 5.14 except for model s_10_50_161_av.

The fluctuation in anomaly amplitude with depth is most prominent in the cases of models where the horizontal block dimensions exceed their vertical

dimensions. For example, the offset-and-averaged model p_10_100_161_av (Figure 5.74), which has blocks 100 km wide and ~30 km thick is very noisy in vertical section. In contrast, the offset-and-averaged model s_10_50_161_av (Figure 5.81), with blocks 50 km wide and ~30 km thick, is relatively smooth in vertical section.

5.2.10 Model quality measures

Not all regions in the target volume are sampled equally and thus the reliability of the resulting velocity perturbations is variable. In order for a particular block to be modelled adequately, it is necessary that it is sampled by a minimum number of rays, well-distributed in azimuth and slowness space. In practice, limitations are placed on such a teleseismic experiment by the natural distribution of seismic sources around the globe, noise conditions and the time period during which data were gathered. The inversion program keeps track of how many rays sample each block and it is useful to examine this distribution of rays within the model. Figures 5.82 - 5.85 show the "hitcount", or number of hits per block for models p_10_75_400 and s_10_75_400.

The central regions of the model have good ray coverage from many directions, with good cross-sampling of rays, whereas those in the peripheral areas are poorer not only in number of rays but in azimuthal distribution. For example, there is a rich supply of rays from the northeast, which result in a high hit count for blocks in the northeast of the models, even for deeper layers. However, although blocks in this region are well-sampled in terms of the number of rays, only rays from this one direction are present in the ray bundle. It is not geometrically possible for rays from any other direction to sample these blocks since there are no seismic stations out at sea. Thus the results for the lower layers of the model are produced from intrinsically less well sampled blocks than the upper layers, where rays from many different directions sample the blocks.
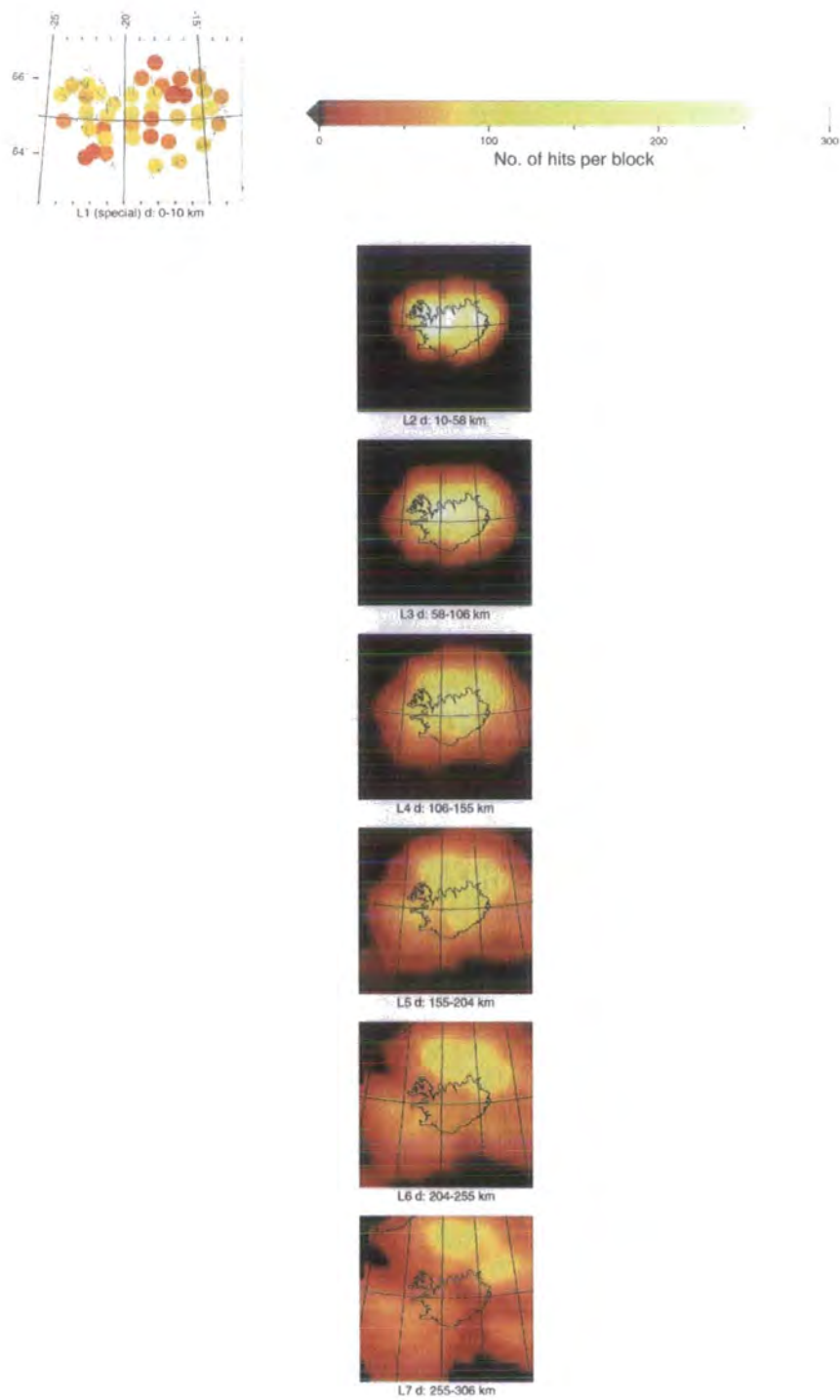
Figure 5.82 Horizontal sections showing the hitcount for model p_10_75_400.
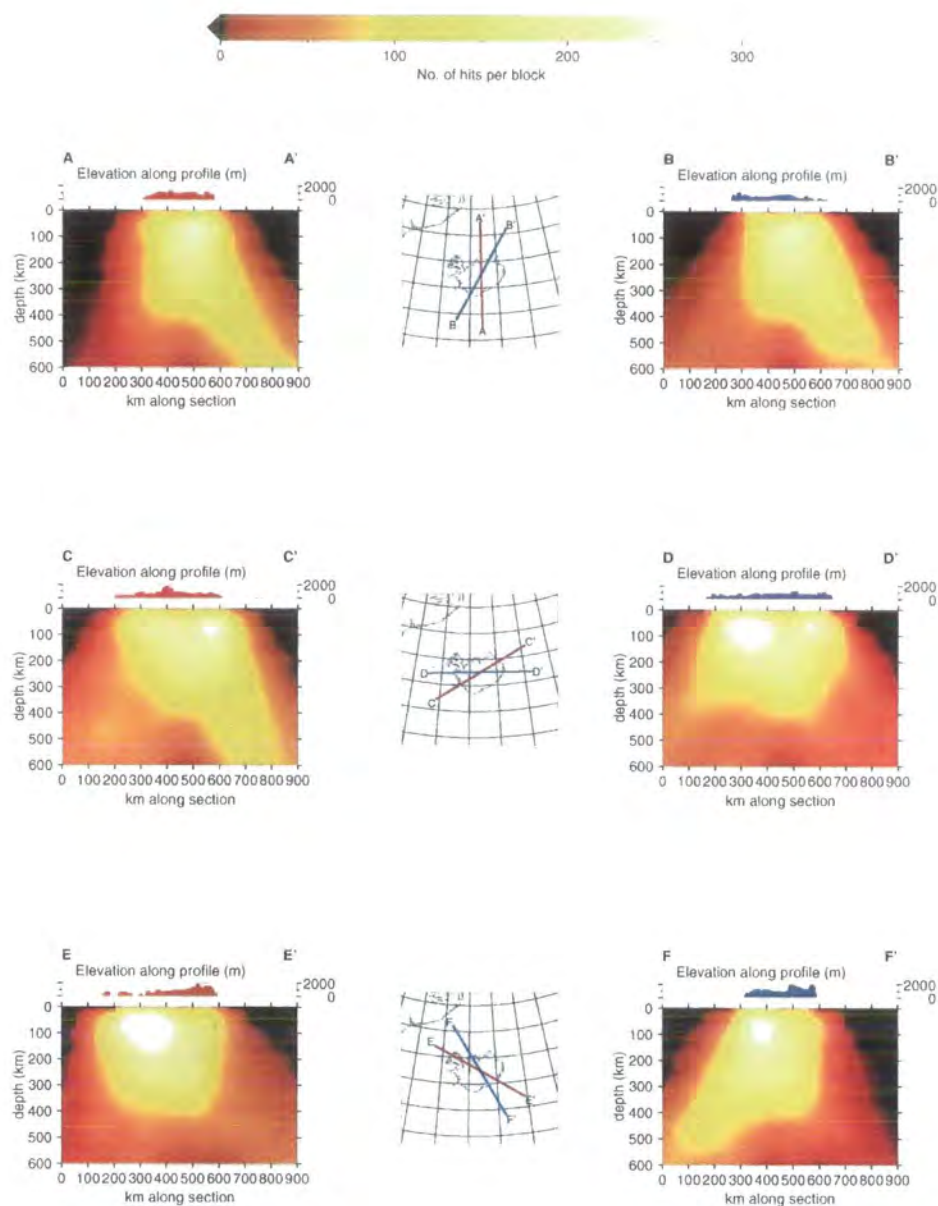
Figure 5.83 Vertical sections showing the hitcount for model p_10_75_400.
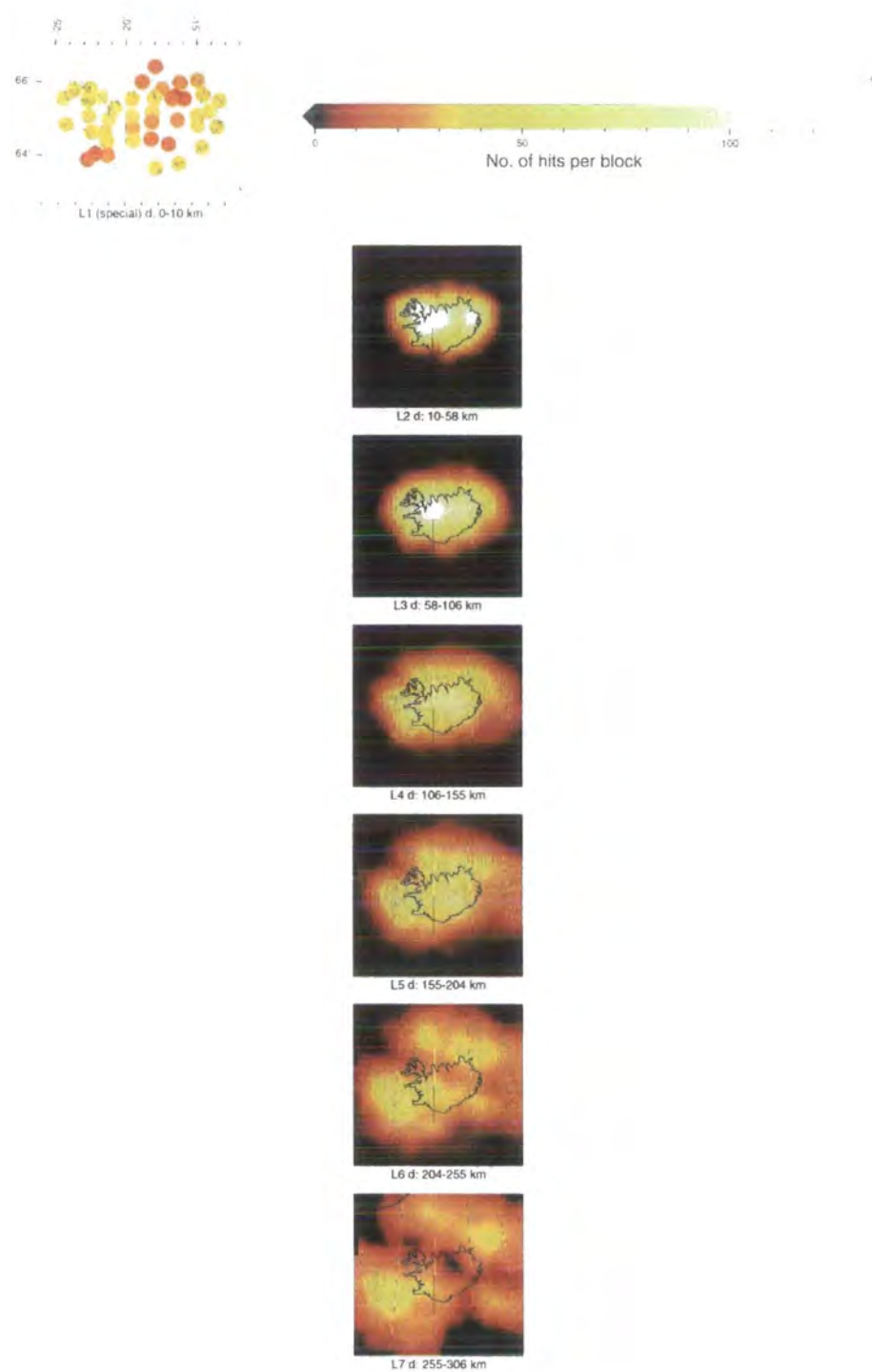
Figure 5.84 As for Figure 5.82 except for model s_10_75_400.
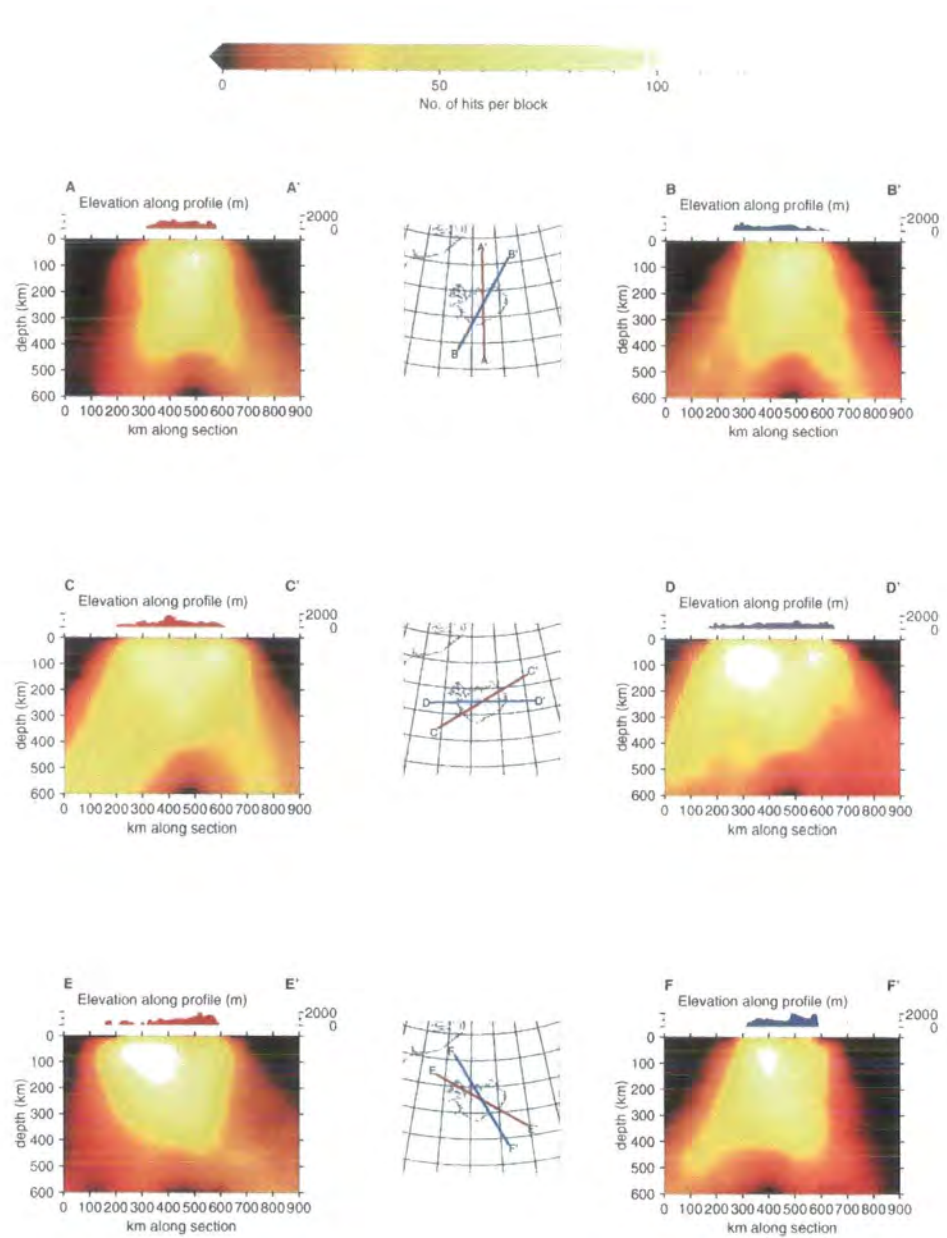
Figure 5.85 As for Figure 5.83 except for model s_10_75_400.

Figures 5.86 - 5.89 show the diagonal of the resolution matrix ($_{diag}$R) for models p_10_75_400 and s_10_75_400. In both these models, $_{Diag}$R forms a similar pattern and is highest (0.8 or greater) in a central region, which has the shape of an inverted cone, in the upper 300-400 km. The central region of low velocity can therefore be regarded as reliably resolved down to 350-400 km. This *includes* the north-south elongation of the anomaly, evidence for which is first seen in layer 3 (107-204 km), well within the "reliable" volume. The region directly beneath central Iceland below 500 km depth exhibits very low resolution, as expected from the ray distribution. The regions either side of this show $_{Diag}$R values around 0.75-0.8 in sections BB' and CC', and it is tempting to regard these as reliable also. However, it is clear from consideration of the ray geometry that these regions have only been "monochromatically" sampled by rays from a limited range of directions.

The magnitude of $_{Diag}$R alone is not enough to determine how reliable a feature is. The volume metric method is required for this, since it examines the shape of individual columns of **R** and in effect shows the "impulse response" of the model to a given velocity perturbation. This must be incorporated into any interpretation by decreasing the significance placed on features that are heavily smeared, even though they may have high values of $_{Diag}$R. In particular, the northward and south-westerly extensions to the central anomaly below around 150-200 km are probably not as reliably resolved as the central low-velocity feature itself.
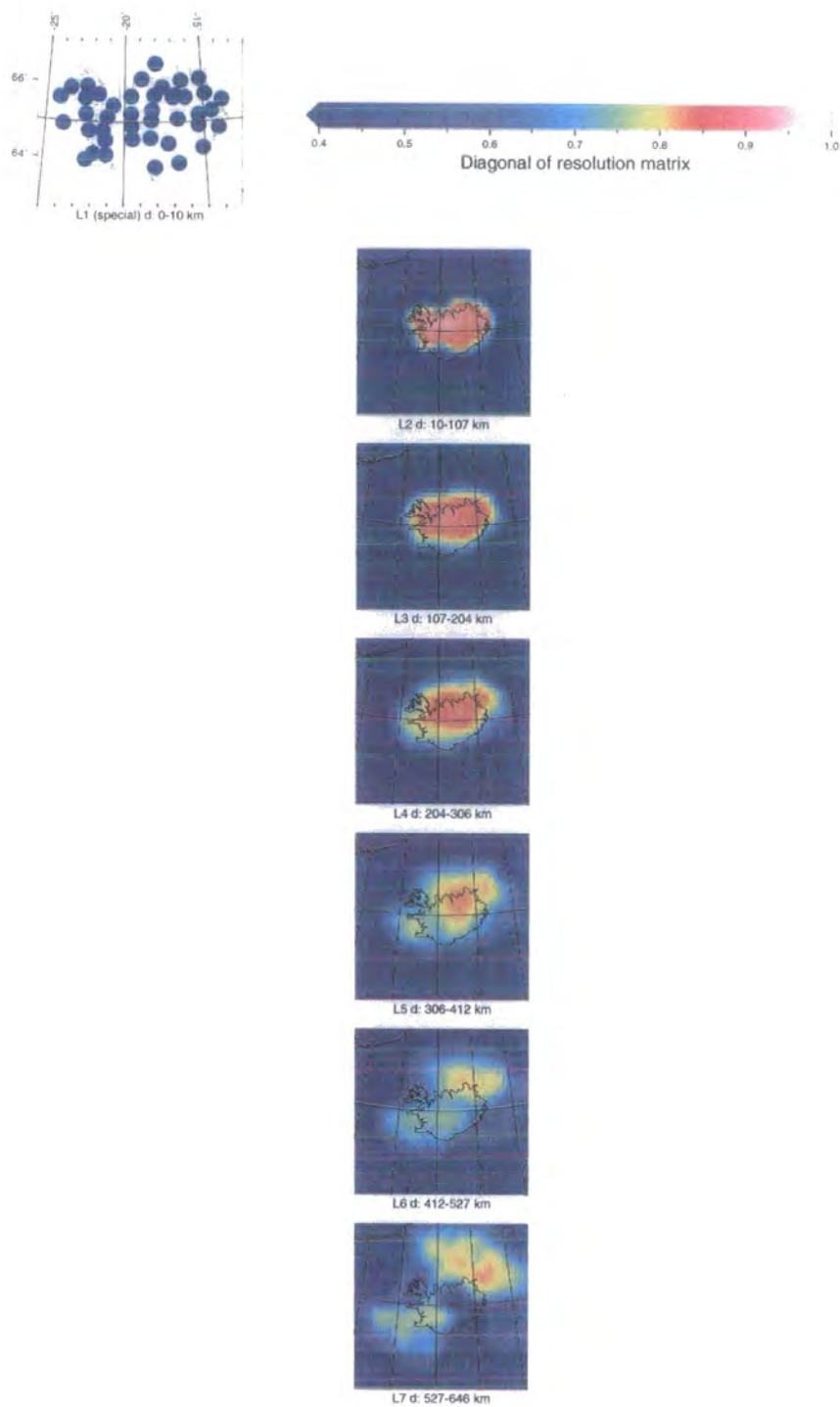
Figure 5.86 Horizontal sections showing diagonal of resolution matrix for model p_10_75_400.
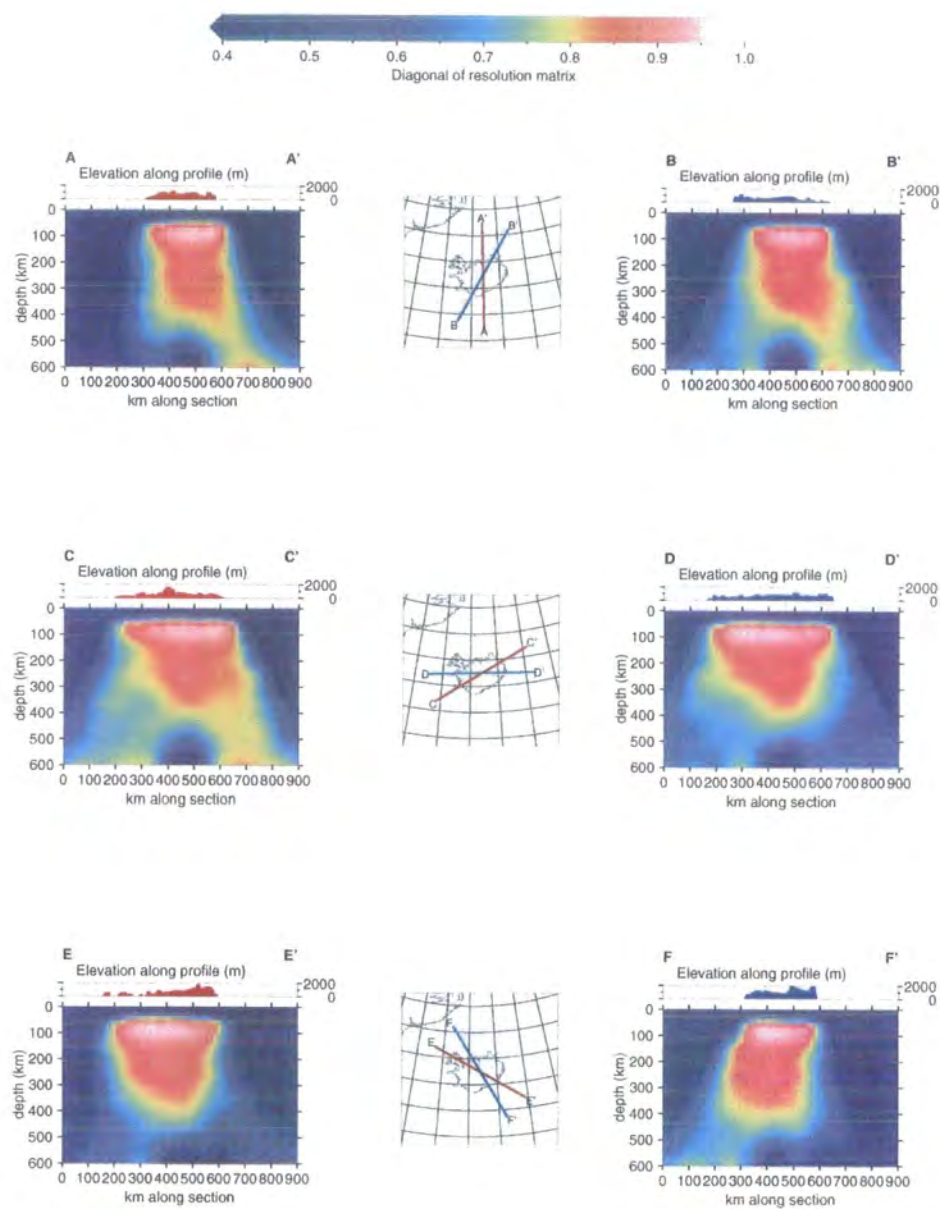
Figure 5.87 Vertical sections showing diagonal of resolution matrix for model p_10_75_400.
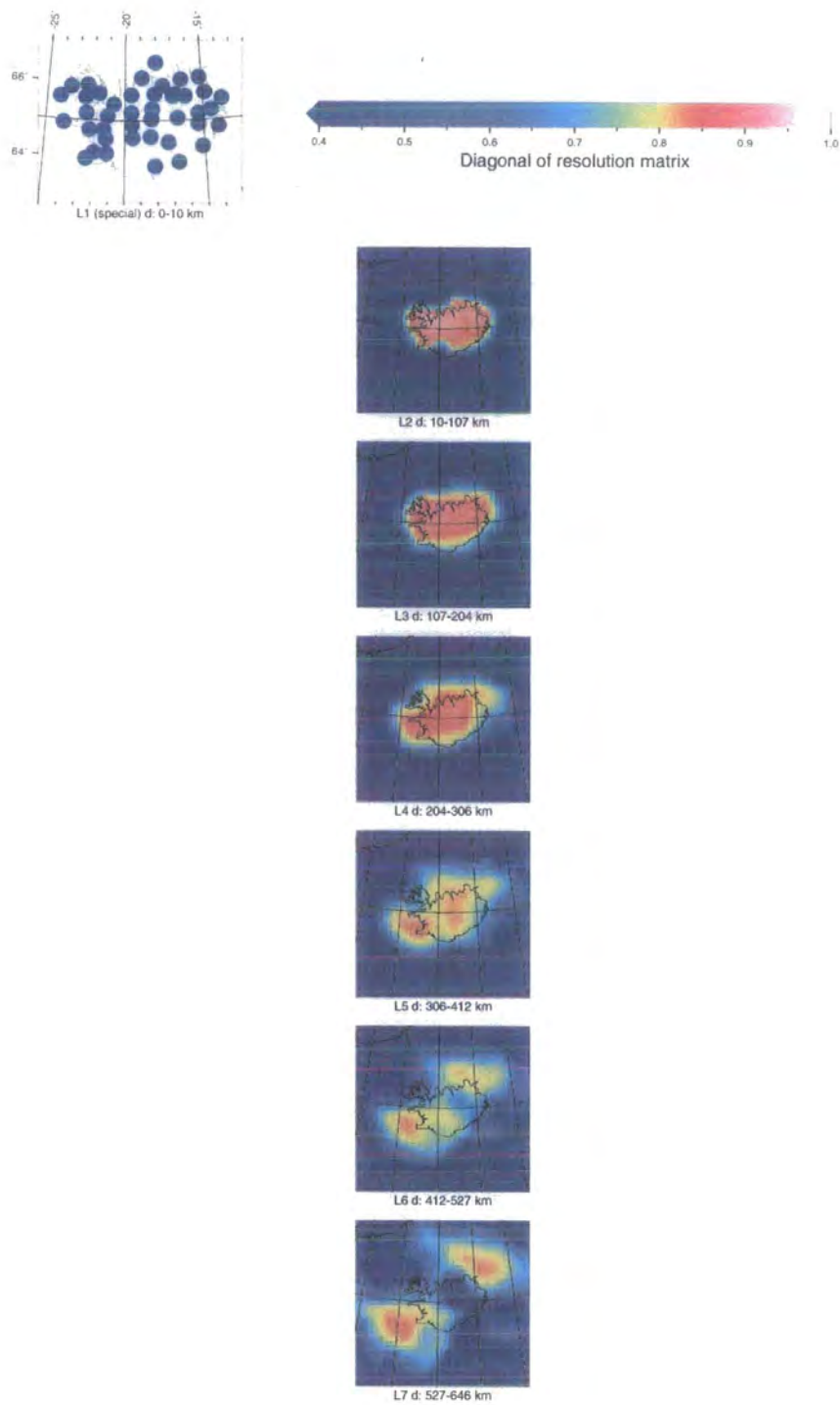
Figure 5.88 As for Figure 5.86 except for model s_10_75_400.
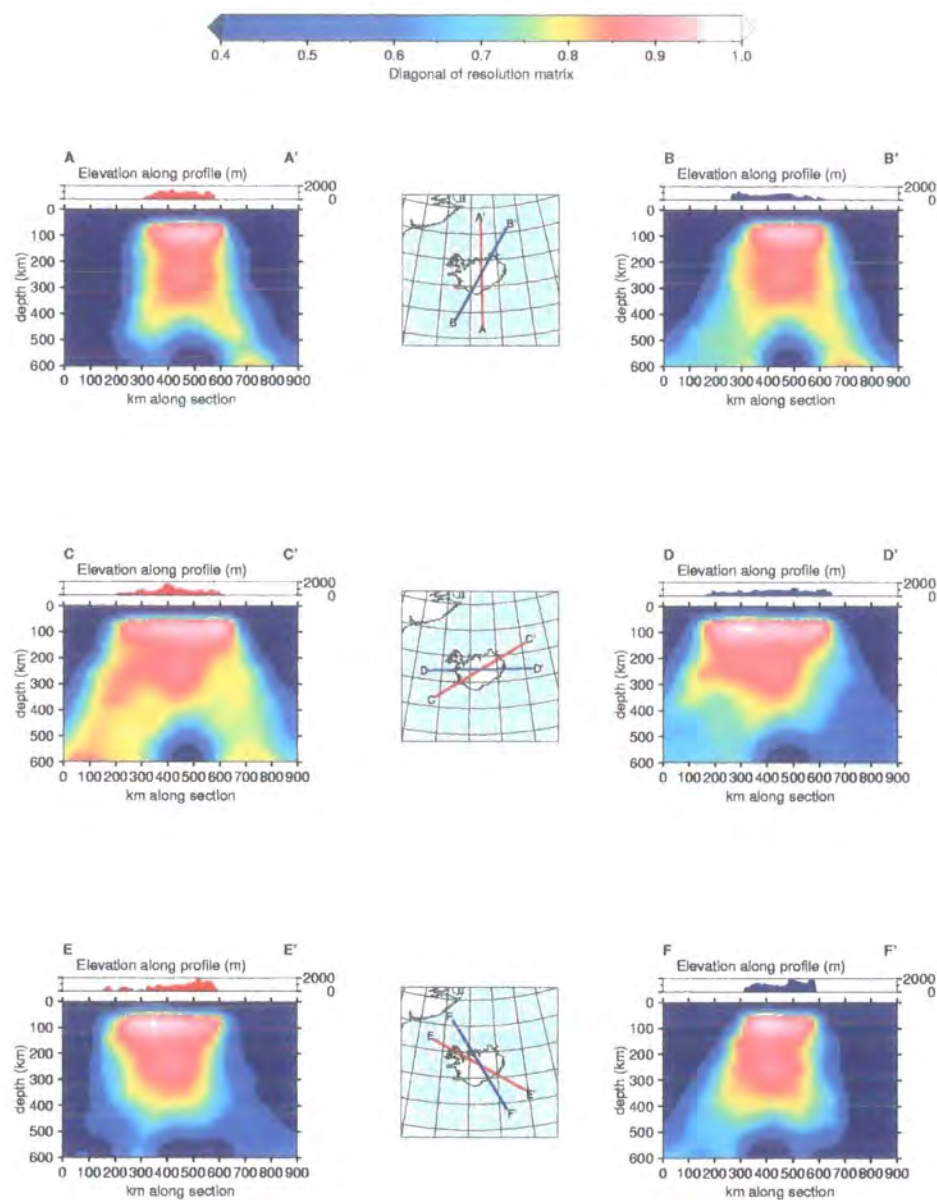
Figure 5.89 As for Figure 5.87 except for model s_10_75_400.

The effect of layer-thinning can be seen in Figures 5.90 - 5.97 which show hitcount and resolution for the 1/2-thickness-layer models p_10_75_225 and

s_10_75_225. The effect of thinning the layers is to decrease the number of hits in each block, as the (predominantly sub-vertical) ray bundle is then divided over more blocks. The diagonals of the resolution matrix are reduced because a given ray spends less time in a thinner block and thus the degree to which that block is sampled is reduced. However, although the diagonals of the resolution matrix for individual blocks are reduced, the equivalent value of $_{Diag}\mathbf{R}$ for a particular volume in space, whether divided into one, two or three vertical "compartments" remains similar for blocks in well-resolved parts of the models, as is shown below using the volume metric method (Evans & Achauer, 1993).

Representative blocks were chosen for volume metric computation (Figures 5.98 and 5.99). Here, five blocks are investigated from each of the models p_10_75_225 and s_10_75_225, both having 75-km blocks but representing the P- and S-wave 1/2-thickness models respectively.
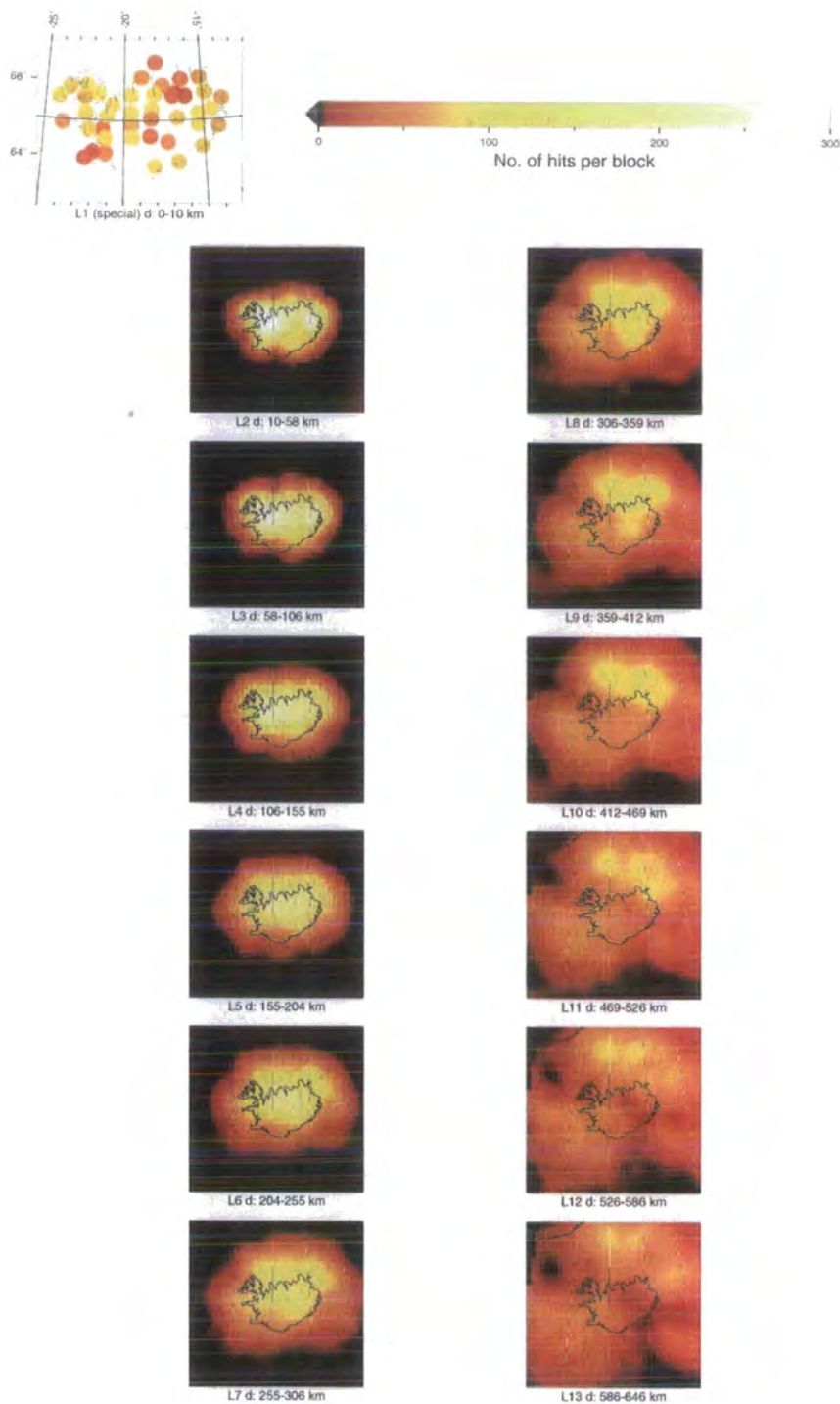
Figure 5.90 As for Figure 5.82 except for model p_10_75_225.
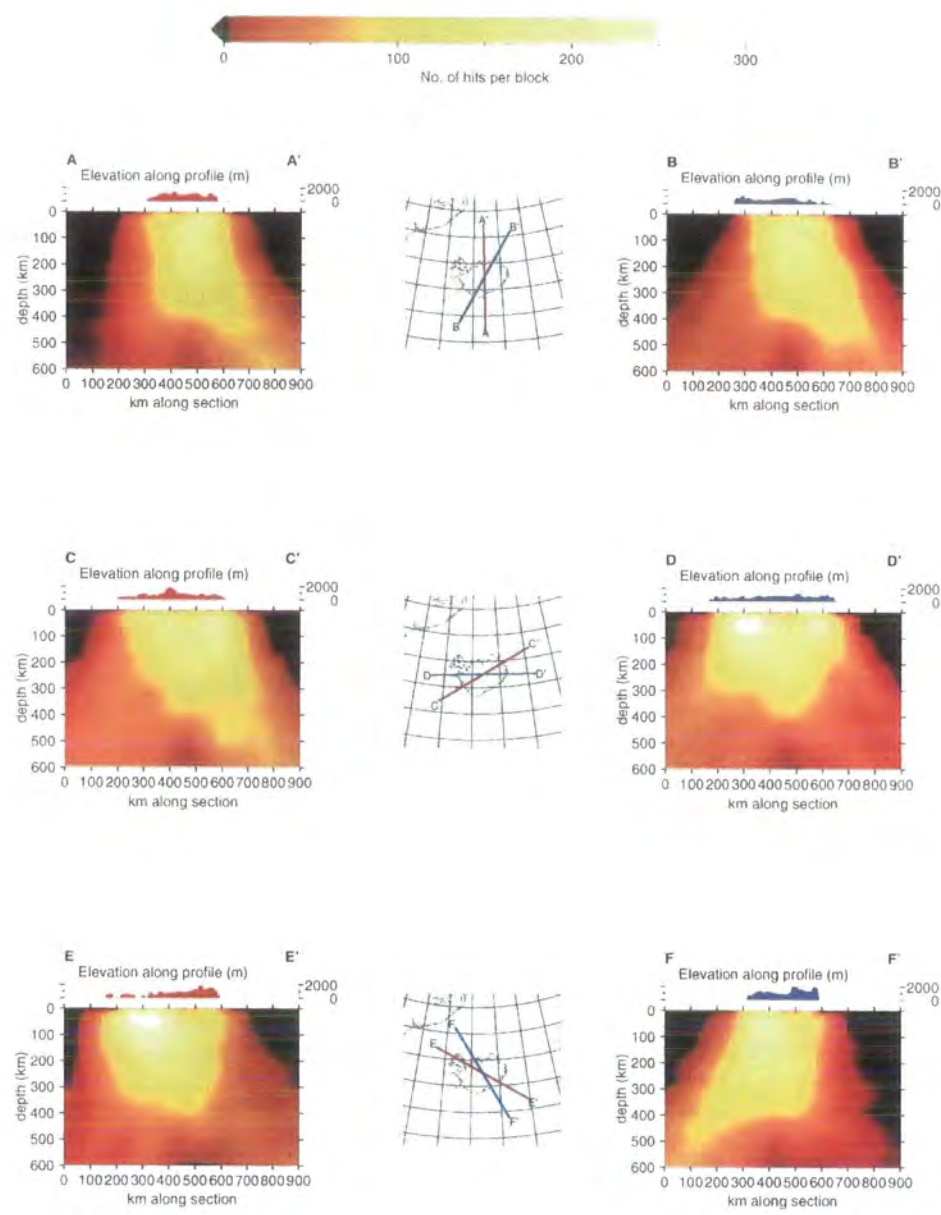
Figure 5.91 As for Figure 5.83 except for model p_10_75_225.
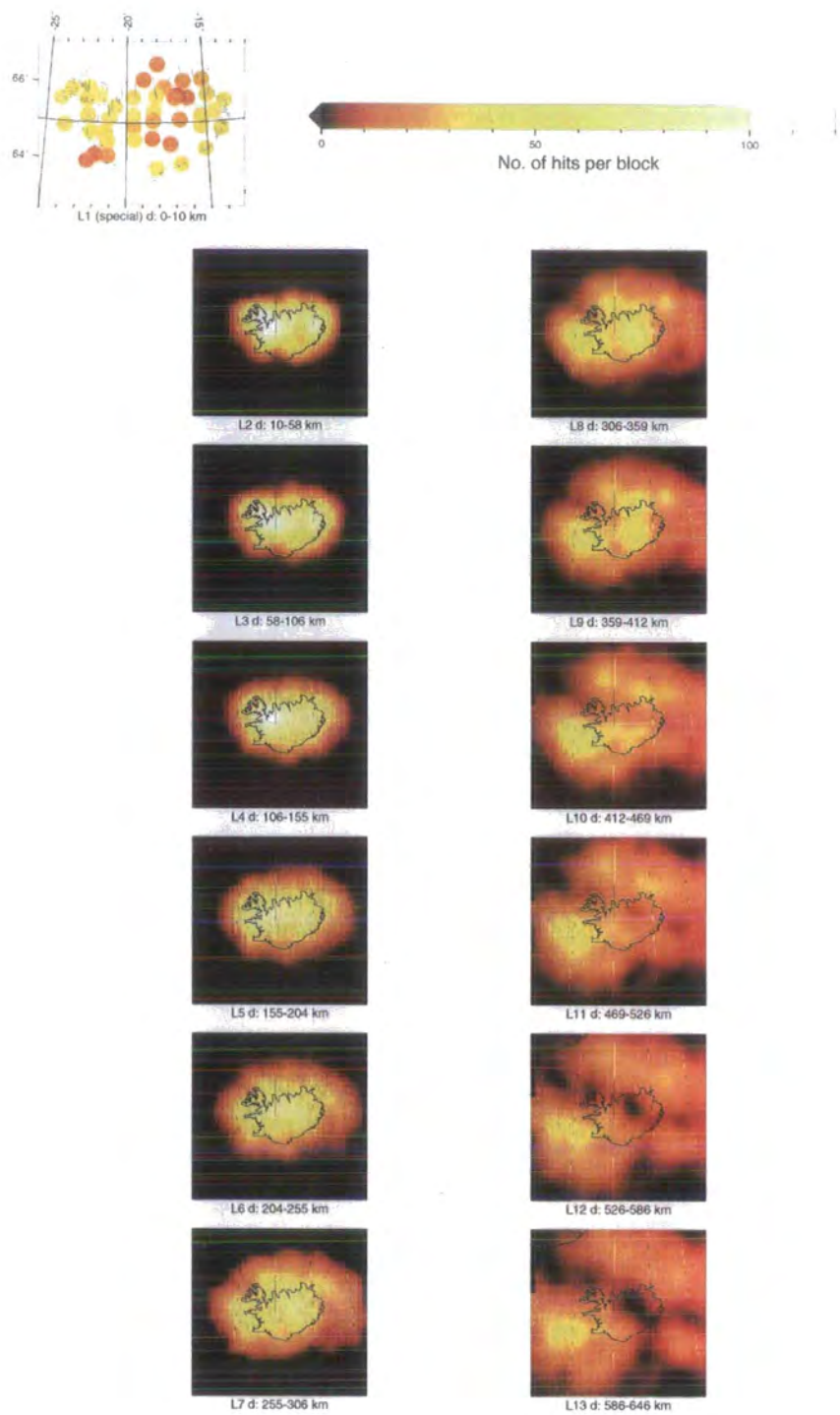
Figure 5.92 As for Figure 5.82 except for model s_10_75_225.
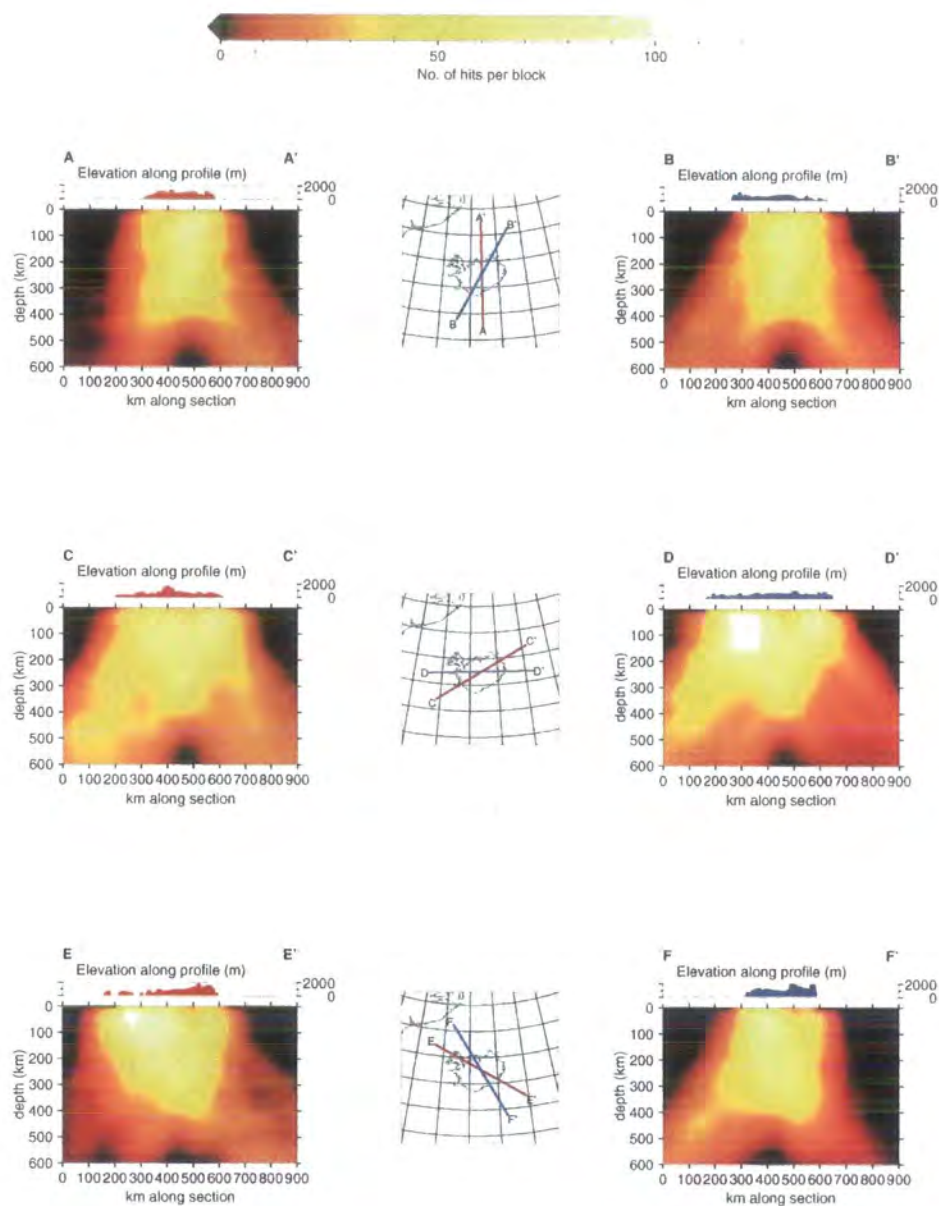
Figure 5.93 As for Figure 5.83 except for model s_10_75_225.

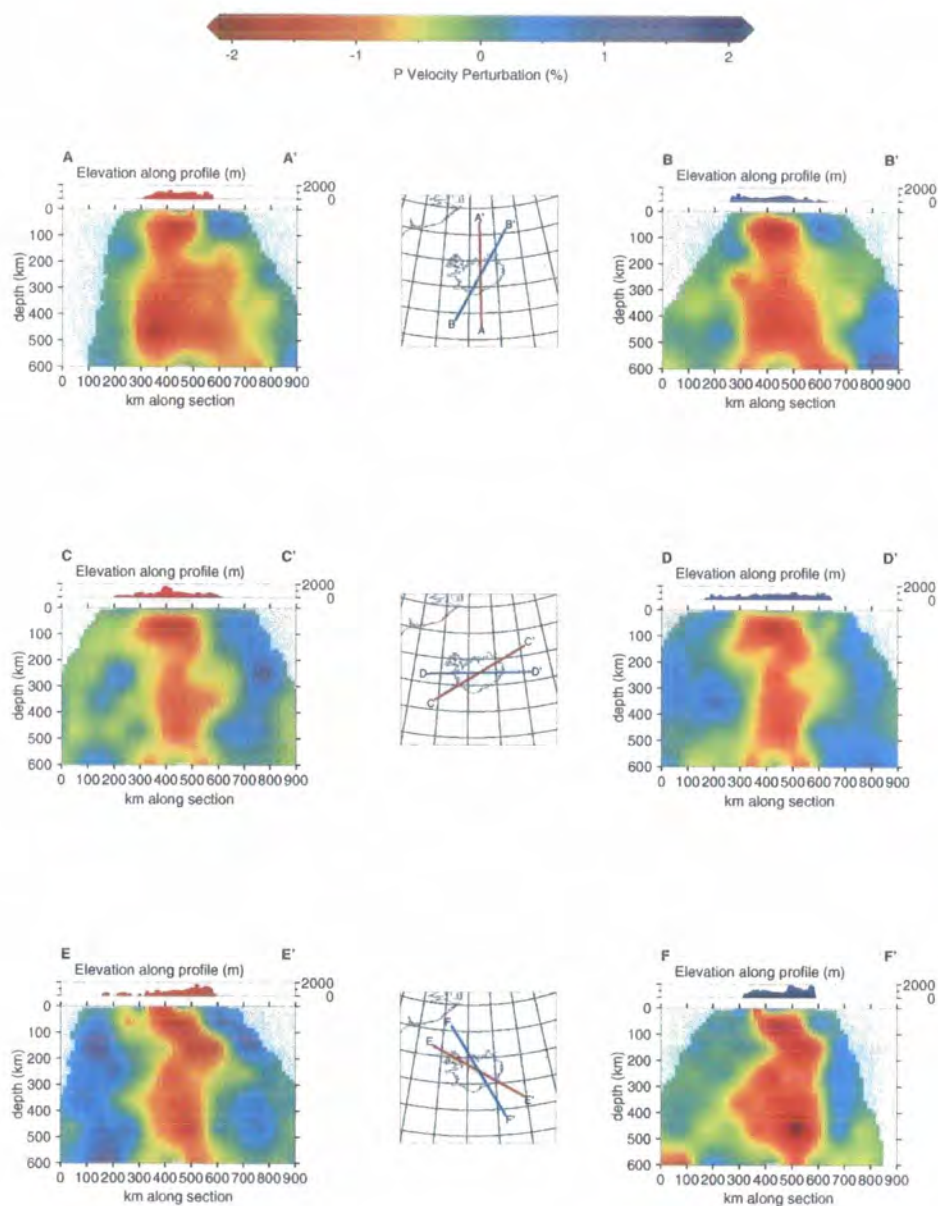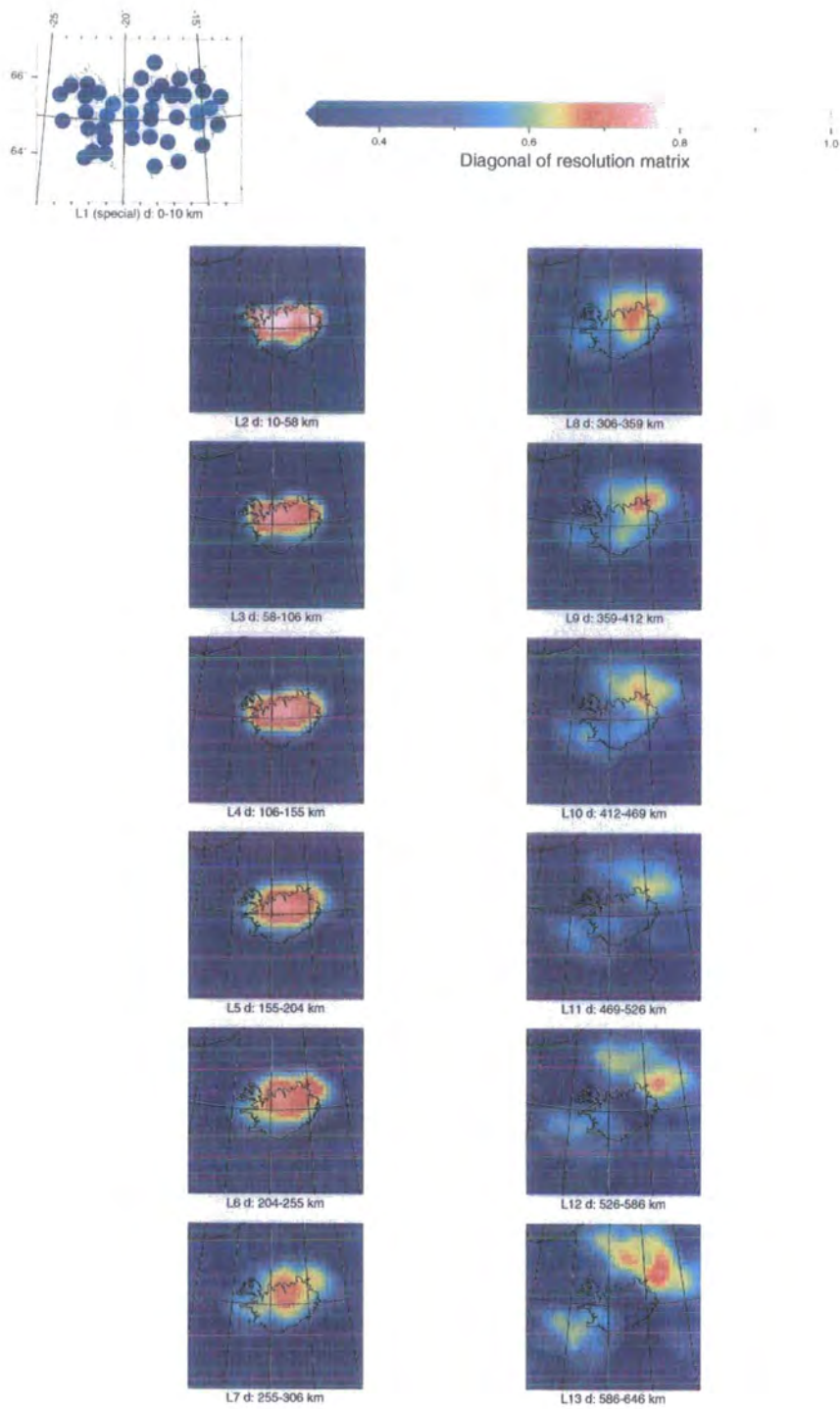Figure 5.94 As for Figure 5.86 except for model p_10_75_225.
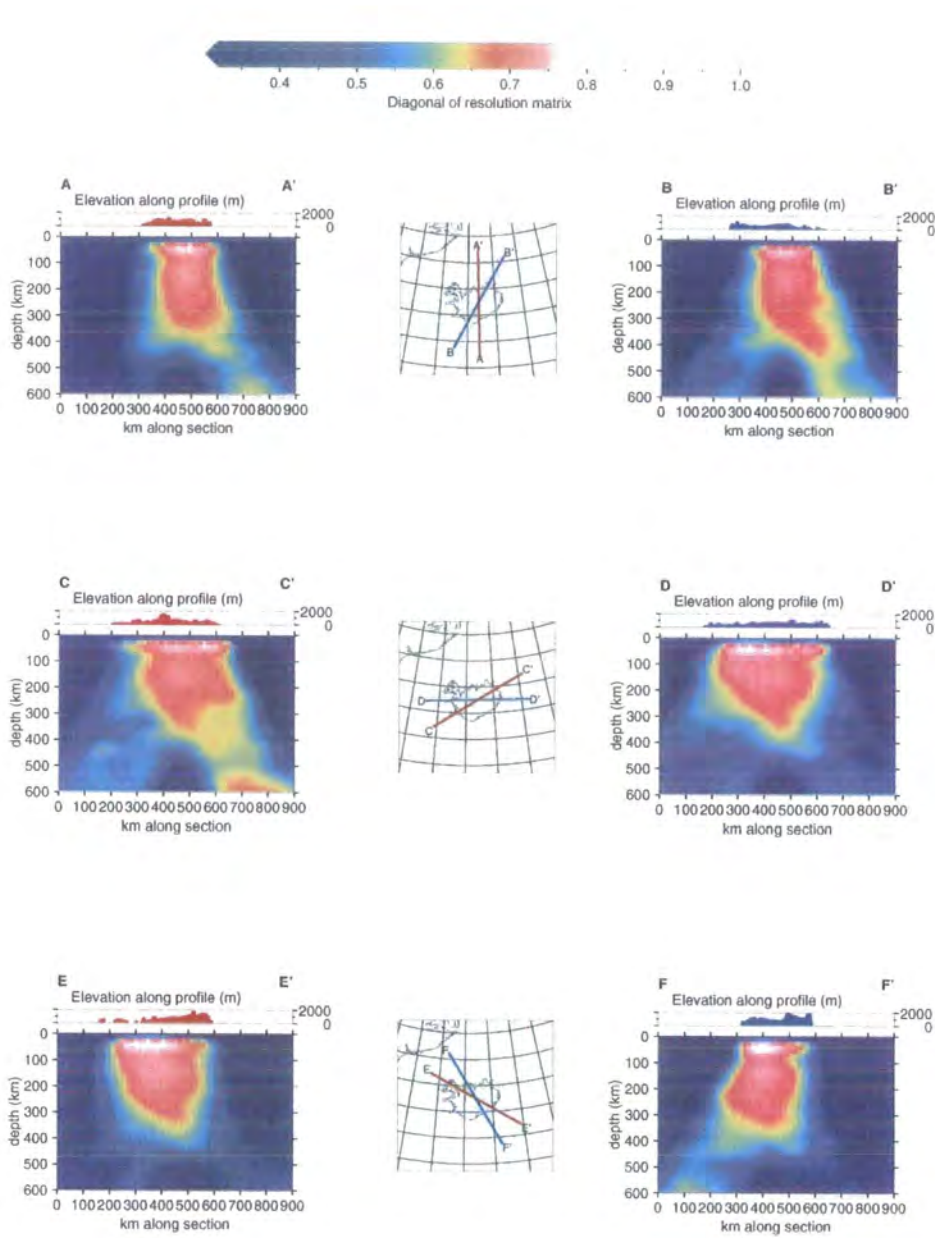
Figure 5.95 As for Figure 5.87 except for model p_10_75_225.
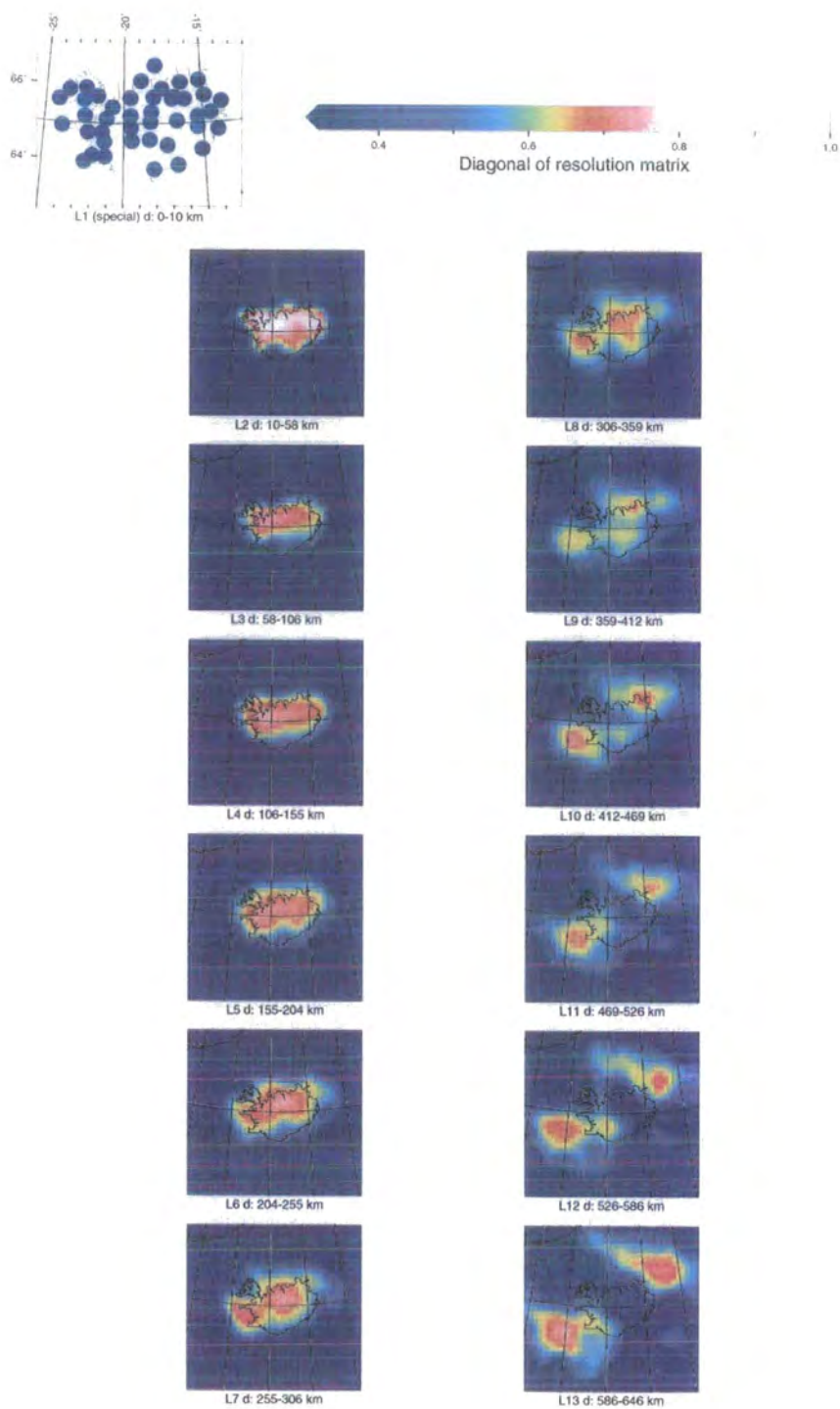
Figure 5.96 As for Figure 5.86 except for model s_10_75_225.
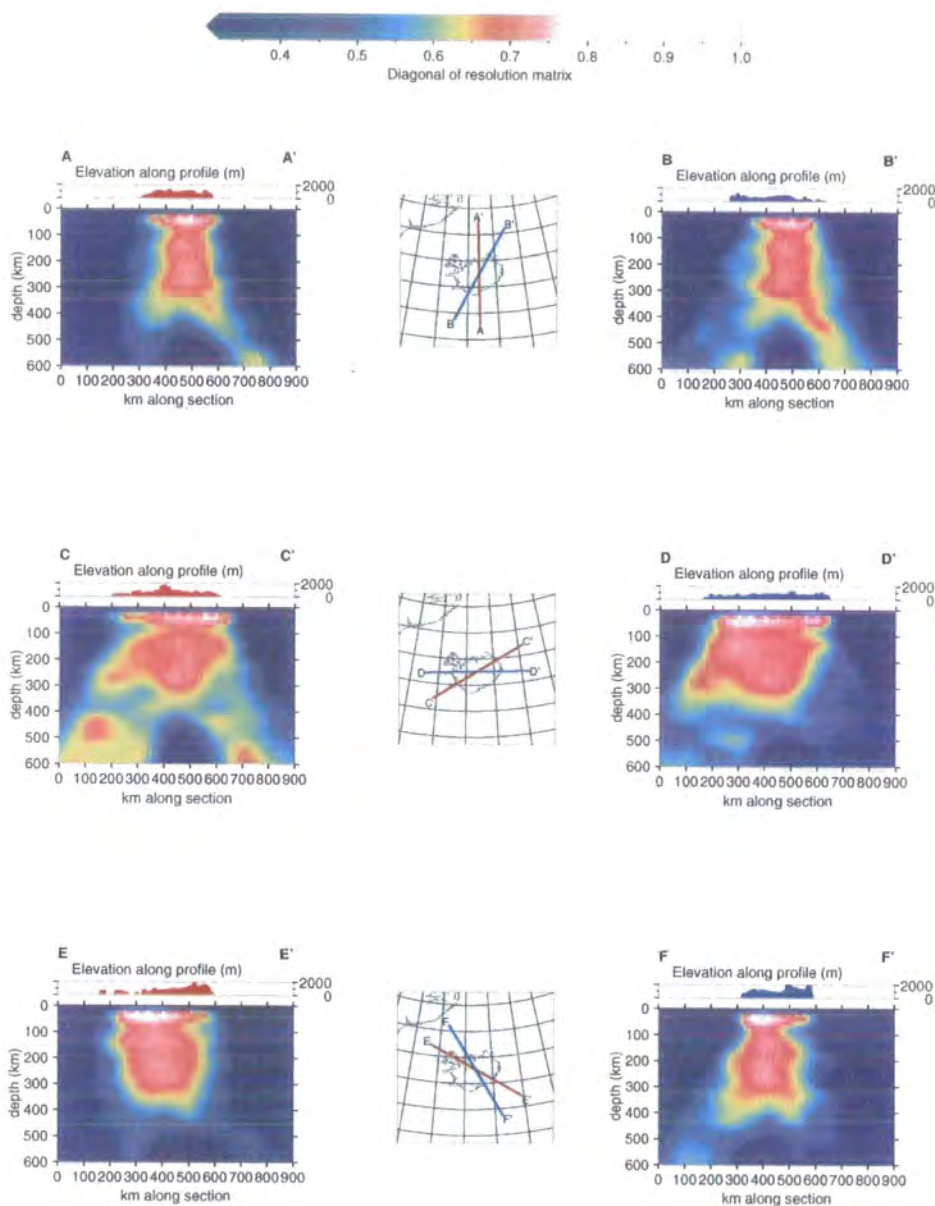
Figure 5.97 As for Figure 5.87 except for model s_10_75_225.
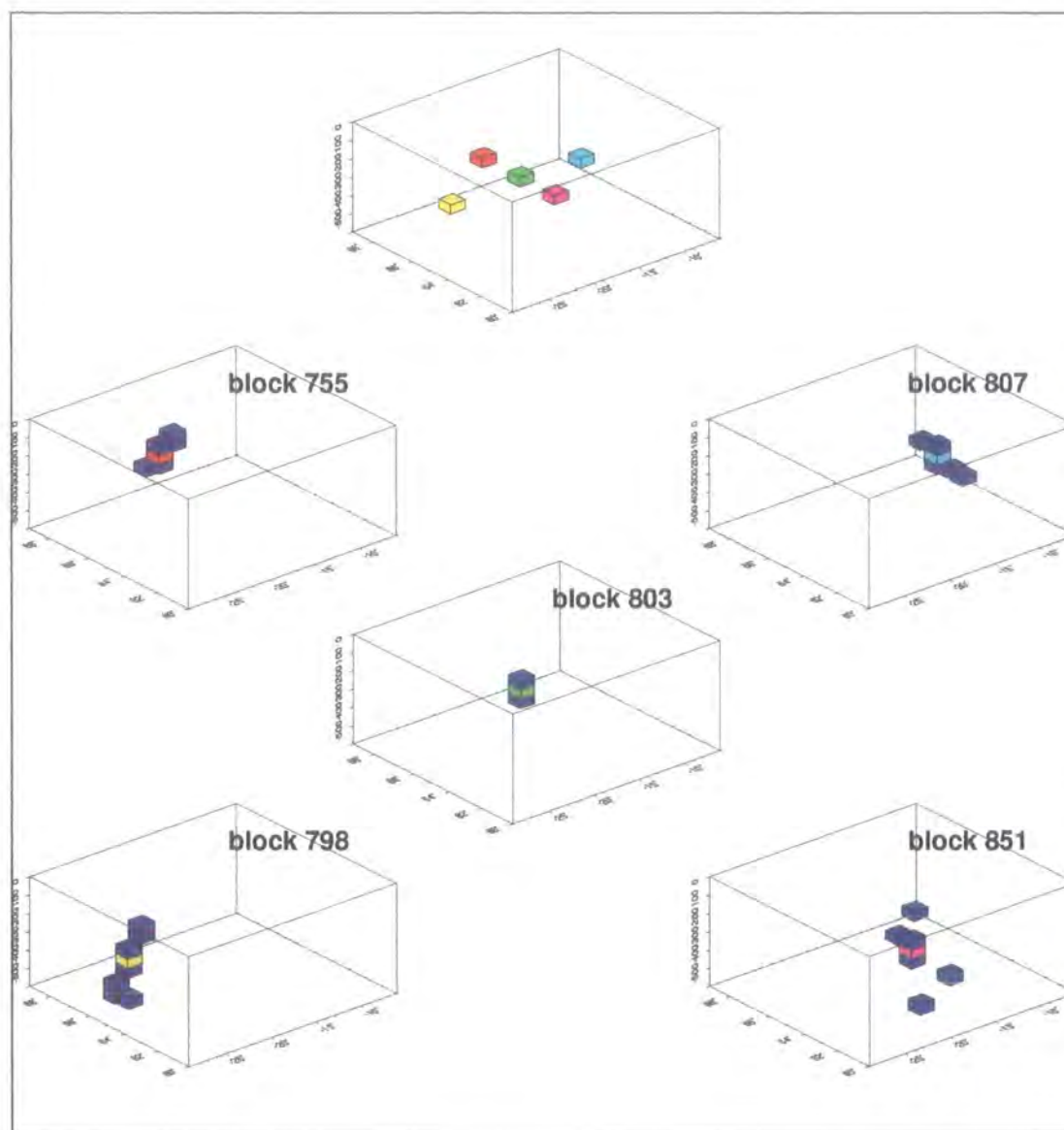
Figure 5.98 Volume metrics for an equivalent diagonal element value of 0.95 for a selection of blocks from model p_10_75_225. Top panel shows spatial relationship of 5 blocks in layer 7. Each three-dimensional box represents the entire model volume, viewed from above and from the south-west, The numbered block is shown in the colour corresponding to its position (from top panel), while other blocks which contribute to the volume metric are shown in blue.
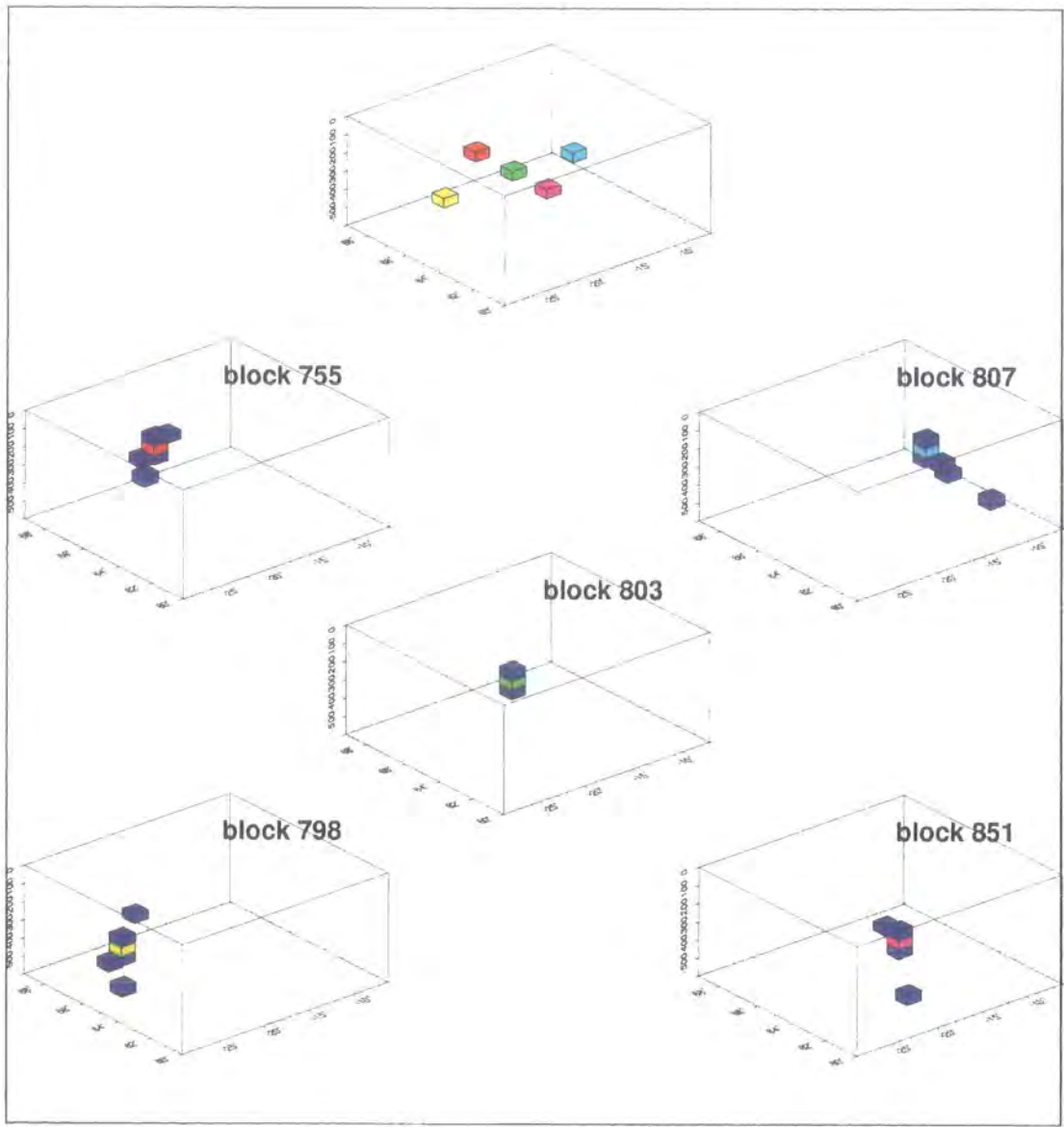
Figure 5.99 As for Figure 5.98 except for model s_10_75_225.

Figures 5.98 and 5.99 show the volume metrics for five blocks in these models at an equivalent diagonal element value of 0.95 in layer 7 (255-306 km depth). It can be seen from both of these that the blocks in the central part of the models are well-resolved in that the volume over which the anomaly has been smeared is small and constrained to a small group of vertically adjacent blocks. At the north, south, east and west edges of the models, there is some smearing in a radial direction. The volume metric plotted is that at the relatively high level of 0.95, which is an extreme test. The contributing blocks indicate that in these regions, the anomalies have been smeared along raypaths and resolution is lower in quality as well as quantity. This is as expected, since only rays from one direction are available to sample blocks in some regions. However, the important feature is that the radial smearing on the northern side of the models (block 755) is no greater than, say on the west (block 798) or east sides (block 807). If a less extreme value of $_{Diag}R$ had been used, more compact volume metrics would have resulted for all these cases, but an extreme value was chosen here to demonstrate clearly the smearing characteristics of these models. This analysis shows that the most reliable part of the model lies in an inverted cone, as illustrated by the resolution cross-sections shown in Figures 5.91 and 5.93 and that smearing is symmetric throughout the model, moderate down to depths of 300-400 km, and generally radially downwards and outwards.

5.2.11 v_P/v_S ratio perturbation

Because the ratio v_P/v_S changes significantly with depth in the IASP91 starting model (Figure 5.100), the fractional changes in v_P/v_S with respect to each layer i.e., the percentage v_P/v_S perturbation, is displayed here. Figures 5.101 and 5.102 show v_P/v_S perturbations computed from models p_10_75_400_av and s_10_75_400_av. Since the ACH method inverts for perturbations relative to initial layer velocities, and using different starting models has little effect on the final results, derived v_P/v_S ratios must be treated with caution. In addition, the errors in v_P/v_S are a function of the errors in both v_P and v_S and thus subject to greater uncertainty than either:

$$v_S^2/v_P^2\left(\sigma^2_{v_P^2/v_S^2}\right)=\sigma^2_{v_P}/v_P^2+\sigma^2_{v_S}/v_S^2 ,$$

(5.17)

where $\sigma_{v_P^2/v_S^2}$ is the error in v_P/v_S and σ_{v_P} and σ_{v_S} are the errors in v_P and v_S respectively. The *pattern* of variations in v_P/v_S throughout the model are, however, little affected by the velocity values used in the starting model.
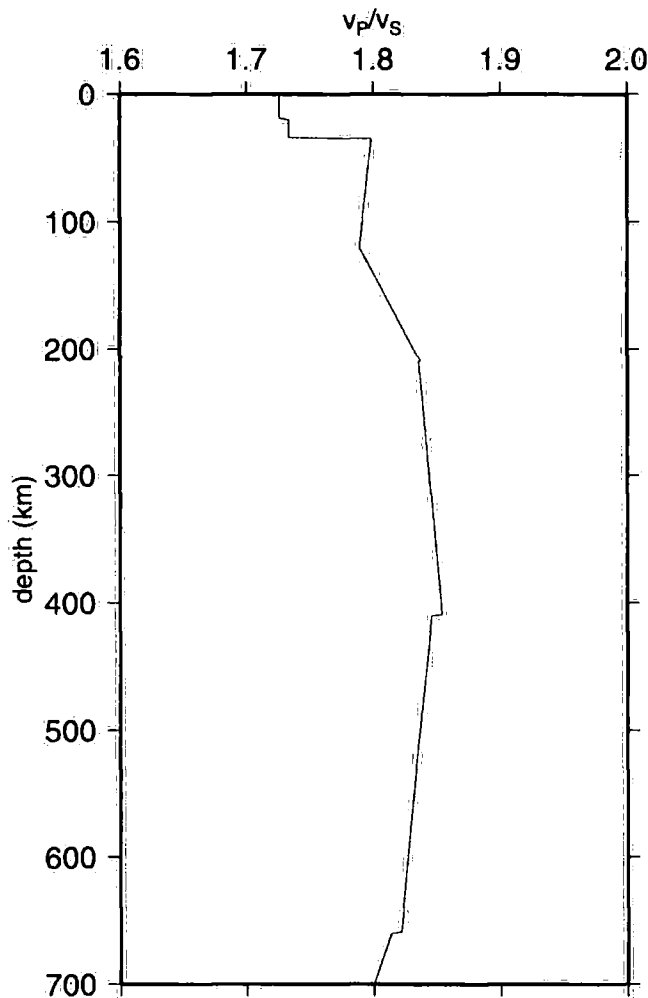
Figure 5.100 Variation of v_P/v_S with depth in the IASP91 model (Kennett & Engdahl, 1991).
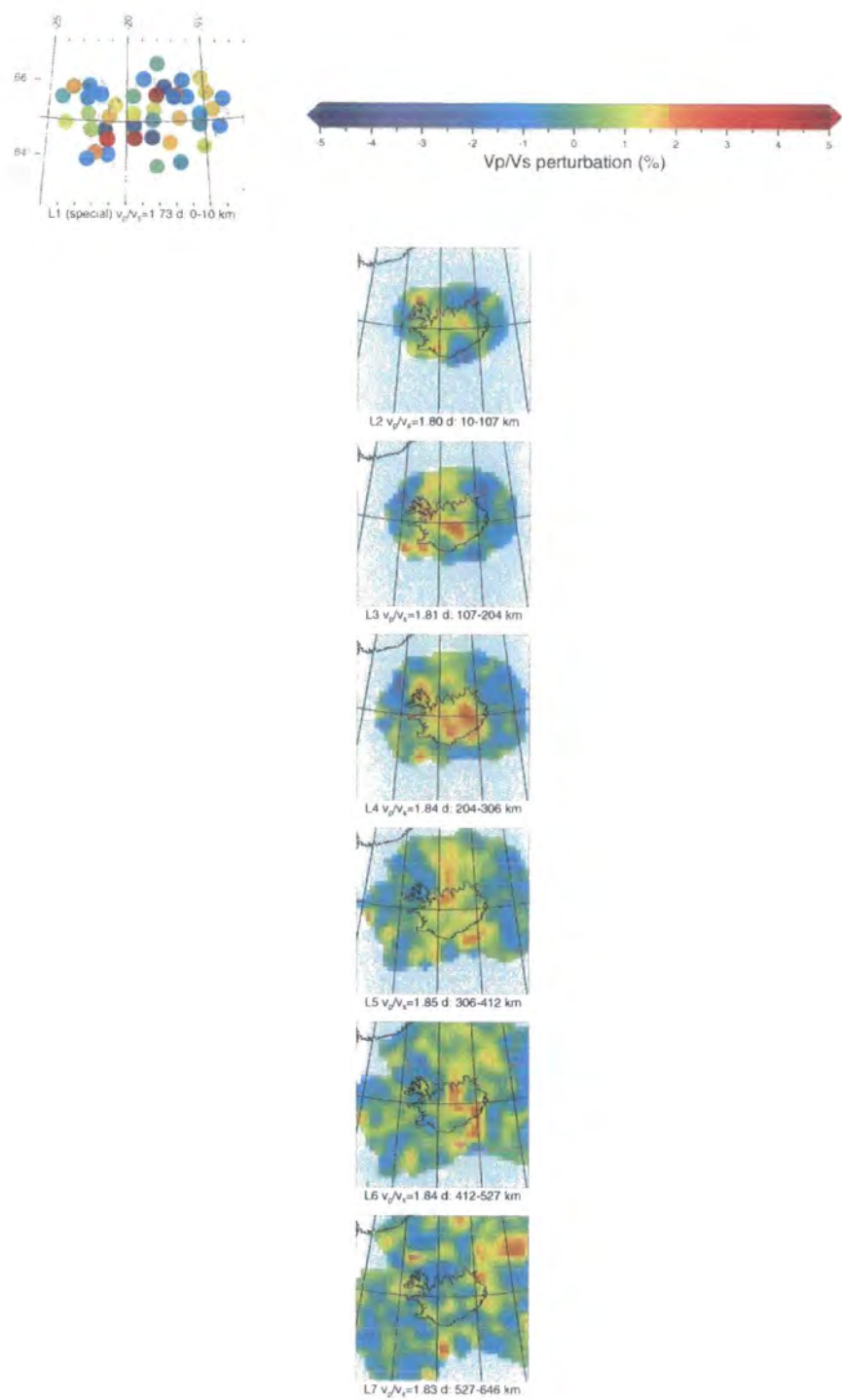
Figure 5.101 Horizontal sections of v_P/v_S perturbation calculated using models p_10_75_400 and s_10_75_400.
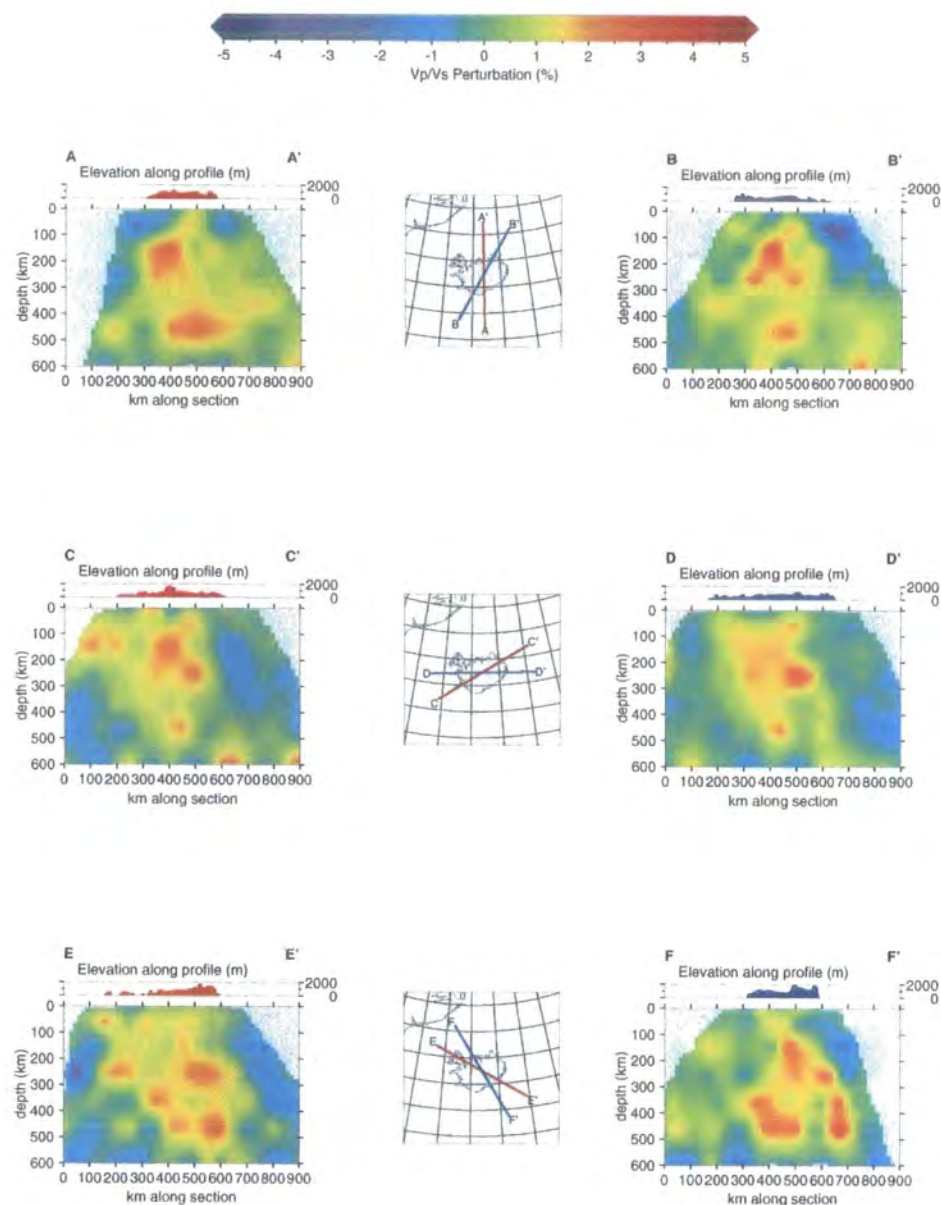
Figure 5.102 Vertical sections through v_P/v_S perturbations.

The v_P/v_S perturbation is positive and around 1% throughout most of the velocity anomaly, i.e. the anomaly magnitude is greater for shear waves than

compressional waves. In certain regions, such as beneath the Reykjanes Ridge in the depth range 100-200 km, the perturbation exceeds 2%. Beneath central Iceland in the depth range 100-300 km, the perturbation is up to 3.2%

5.3   SUMMARY OF RESULTS

• A large suite of ACH teleseismic tomography inversions were performed, using a variety of block widths and layer thicknesses. The best results are offset-and-averaged models using block widths of 75 km and layer thicknesses of 50 km (models p_10_75_225_av and s_10_75_225_av, Figures 5.61, 5.64, 5.67 and 5.70)

• The tomography has revealed that a region beneath central and east-central Iceland is characterised by P-wave velocities that are reduced by up to 2.9%, and S-wave velocities reduced by up to 4.9% relative to a parameterised IASP91 model.

• This is the main, first-order feature present in all models obtained. Volume metrics indicate that in the central part of model, smearing is of limited extent and is vertical. In peripheral areas, smearing is subvertical and oriented radially outwards. The anomaly has roughly cylindrical shape, broadening northwards to more planar symmetry in lower layers while remaining relatively narrow in its west-east dimension.

• The north-south elongation of the anomaly at depth represents a change from cylindrical to planar symmetry at around 250-300 km depth. This feature is persistent across models with different block widths and layer thicknesses, and is present in both the P- and S-wave models, which were determined independently. Analysis of the resolution and volume metrics revealed that, although there is more peripheral than central smearing, it is *no* stronger in the north-south direction than any other. This suggests that the shape of the velocity anomaly is real.

• A south-westerly trending extension of the central anomaly in the depth range 50-200 km beneath the Reykjanes Ridge, is much stronger in v_S (-2%) than v_P (-0.5%). Low velocities are present only below 160 km to the north of Iceland, beneath the Kolbeinsey Ridge. These regions are both at the periphery of the

volume of good resolution, so are less reliable than features closer to the centre of the study volume.

- v_P/v_S is 1% high throughout most of the central part of the model, and is up to 3.2% high beneath central Iceland between 100 and 200 km, and beneath east-central Iceland between 200 and 300 km depth.

Chapter 6

Interpretation and Discussion

6. INTERPRETATION & DISCUSSION

6.1   THE AZIMUTH ANOMALY STUDY

The study of azimuth anomalies for P-wave raypaths passing beneath Iceland, described in Chapter 2, places constraints on the dimensions and strength of a possible plume in the lower mantle beneath Iceland, if one exists there. Raytracing through a suite of synthetic 3-dimensional plume models revealed azimuth anomaly patterns which best match those of the NORSAR data if a low-velocity anomaly underlies Iceland region at ~1500 km depth, with a maximum velocity contrast of 1.5% and a Gaussian radius of 125 km. This result alone cannot constrain the anomaly location along the best-fitting backazimuth because bodies with various sizes and strengths at different distances all fit the observations. Also, the deepest-travelling rays in the NORSAR dataset have turning points at around 370 km above the core-mantle boundary, only just above the top of the heterogeneous D'' layer, so the possibility of some other cause for the observed anomaly cannot be ruled out. Nevertheless, a search of parameter space using a suite of models with reasonable velocity contrasts indicated that the causal feature would need to be both wider and deeper if further away from Iceland. As such, they would be evident in global seismic tomographic images.

An attempt was made to extend the study to investigate whether similar features were observable in rays arriving at a Scottish network. No suitable array exists in Scotland and so the arrival azimuths were calculated from bulletin data reported from various sources. These are less reliable than observations made by one person using a consistently processed set of seismograms, as in the case of the NORSAR data. The azimuth anomalies in the Scottish data have a very poor signal-to-noise ratio and do not present clear evidence of a plume-like velocity anomaly to the north. The geometrical quality of the experiment would have been further improved by additional data recorded in Greenland. Unfortunately, no suitable data are currently available.

6.2   THE PREFERRED ACH RESULT

The initial models used for the ACH inversion represent a wide range of spatial parameterisations of the Earth. Despite some variations, the persistence of the

broad features imaged across this range of models is convincing evidence of real, physical features in the mantle beneath Iceland. Details of the inversion results are dependent on the parameterisation used and for this reason several different models are presented in Chapter 5. The preferred model should be a compromise which shows a level of detail which is reasonably reliable but does not show excessive "checkerboard" noise.

The selection of initial models was made in the light of the results of many test inversions using a suite of models with a range of block structures and damping parameters. The optimal combination of block structure and damping parameter was selected for each of the three block sizes used. Models with blocks 100 km wide appear to be too coarsely parameterised and yield unreasonable results when the layers are thinned, when the blocks become significantly wider than they are tall. The offset-and-averaging procedure causes large changes to these models, especially when viewed in vertical section, suggesting that anomalies are divided over neighbouring blocks, not imaged reliably, and real detail is lost.

S-wave models with 50-km wide blocks exhibit unusual behaviour in that the residual variance remains unexpectedly high and strong checkerboard noise is present in layer-thinned models (e.g. model s_10_50_161, Figure 5.56). This may be because this block size is smaller than the dominant wavelength (50-75 km) of teleseismic S-waves in Iceland. Checkerboard noise is present to a lesser extent in the 50-km block width P-wave models. In summary, models with 75-km wide blocks represent the best compromise between excessive smoothing and excessive checkerboard noise in the model.

The overall shape and magnitude of the main low-velocity feature in the offset-and-averaged models p_10_75_400_av (thick-layered, Figure 5.28), p_10_75_225_av (1/2-thickness layers, Figure 5.64) and p_10_75_161_av (1/3-thickness layers, Figure 5.75) remains remarkably stable throughout the layer-thinning process. It is evident from the vertical sections of layer-thinned models, however, that although the repeatability of features between models of successively thinner layers is, on the whole, good, the 1/3-thickness suffer excessively from checkerboard noise and exhibit physically unreasonable, oscillatory anomaly patterns. The preferred models are therefore the offset-and-averaged results of a

configuration with blocks 75 km wide and layers ~50 km thick, models p_10_75_225_av (Figures 5.61 and 5.64) and s_10_75_225_av (Figures 5.67 and 5.70).

6.3   THE MAIN RESULTS AND THEIR RELIABILITY

The ACH results described here reveal a velocity anomaly in both v_P and v_S beneath Iceland which persists throughout all resolvable depths in the mantle. Second-order features are also resolved. A central, roughly cylindrical, low-velocity anomaly is imaged in the shallowest ~250 km, and below this it changes shape to adopt a north-south-striking tabular form. Low-velocity anomalies in both v_P and, more strongly, in v_S extend beneath the Reykjanes ridge to the southwest in the depth range 50-200 km. Beneath the Kolbeinsey ridge to the north, low v_P and v_S anomalies are imaged below 160 km. The anomaly in v_S is, in most respects, similar in shape to that in v_P, but stronger, with v_P/v_S at least 1% high throughout most of the resolved volume, and as high as 3.2% in places.

The best-resolved region of the target volume is a region shaped like an inverted cone shape with its base at ~40 km depth, roughly underlying the Icelandic coastline, and its apex beneath the centre of the seismic network at around 400 km depth. Blocks within this conical region have $_{Diag}R$ values of 0.65 or greater in the 1/2-thickness P model, or 0.8 in the thick-layered model. S models exhibit similar values and distribution, which suggests that it is the distribution, rather than the absolute values, of $_{Diag}R$ that are important in determining reliability. Peripheral regions begin to lose the quality of resolution that central regions have because much less crossing of rays occurs towards the edges of the ray bundle. Gaps in the station distribution also serve to degrade resolution in places, for example in southwest Iceland. Northern Iceland is well resolved, in comparison, especially since the station on the island of Grímsey extends the network offshore by ~50 km, and improves the ray coverage and resolution envelope there.

Resolution is low in the top 30-40 km of the study volume, where rays travel subvertically towards receiver stations and do not cross one another. The 10-km thick "special" first layer is treated in a different way from other layers to accommodate this, since the distribution of rays leaves large, unsampled gaps between stations and would not support a grid of regular blocks. Instead, a block is assigned to each

station. The variation in velocity perturbations in this top layer is much greater than in lower layers, and reveals high-amplitude, short-wavelength fluctuations of the order of ±5.5% in v_P and ±8.5% for v_S. The Icelandic crust is known to contain lava flows, igneous intrusions, fissure swarms, faults, magma chambers, hydrothermal systems, and hyaloclastite deposits, and to vary in thickness laterally. These all contribute to a crust with a very complex velocity structure on the scale of a few hundred metres to several km. This is small compared with the horizontal resolution of the ACH models which is on the scale of the station spacing, i.e. 50-75 km.

In the depth range 30-250 km the central, low-velocity anomaly forms a vertical, approximately cylindrical feature with a Gaussian radius of 100-130 km. The anomaly in v_P is particularly strong (up to -2.7%) in layer 2, but this may be an artifact due in part to the lower resolution towards the top of this layer and also to contamination from the heterogeneous crust. This is evident when comparing the layer-thinning sequence of models with 100, 50 and 33 km layer thicknesses (models p_10_75_400_av, Figure 5.28, p_10_75_225_av, Figure 5.64, and p_10_75_161_av, Figure 5.75). The strong anomaly appears to be contained within the second layer, whatever its thickness. This behaviour is less extreme in the S-wave models but the strongest part of the anomaly is similarly located beneath east-central Iceland. This suggests that the existence and location of the anomaly is reliable, if not the exact amplitude. Most models exhibit high velocities to the northeast and east of Iceland in layer 2.

The cylindrical anomaly beneath layer 2 is fit by a Gaussian cylinder with a radius of 100-130 km and peak amplitude around 1.6% for v_P and 4.6% for v_S, although there is some variation in the amplitude with depth. It can be seen from the velocity maps and sections in Figures 5.61, 5.64, 5.67 and 5.70 that this simplified model does not hold in places and local maxima of 2.9% v_P and 4.9% v_S occur.

There is some variation in magnitude of the central anomaly with depth, even in the thick-layered models p_10_75_400_av and s_10_75_400_av (Figures 5.28 and 5.34). This is best seen by comparing vertical sections from a thick layered model with the same sections on progressively thinner-layered models. Where there is a slight vertical change in anomaly amplitude in the thick-layered model, this is often present in the thinner-layered models, but with a higher amplitude. This suggests that

a localised, real feature is being absorbed into too coarse a block model in the thick-layered model.

North-south elongation of the central, low-velocity anomaly begins at around 250-300 km depth which is still within the envelope of good resolution. It persists from there to the lowest layer where it develops into an arcuate feature bending to the northwest in the P-wave model (Figure 5.61), while the S-wave anomaly breaks up into checkerboard noise. Some semblance of the arcuate feature is nonetheless still evident. I make no attempt to interpret anomalies deeper than 500 km, as the resolution below this depth is low in both magnitude and "quality" - rays are unevenly distributed and the "hitcount" is low. It is clear from the horizontal map views of sections through $_{Diag}R$ (Figures 5.94 and 5.96), that the volume of good resolution in the upper layers is elongated east-west. This is primarily due to the distribution of seismic stations, the lateral extent of which is dictated by the shape of the Iceland. However, the high-hitcount envelope also extends to the southwest and northeast in the deeper layers, i.e., the greatest concentration of rays are from these directions. The volume metric analysis (Figures 5.98 and 5.99) shows that damping smears velocity anomalies no more in the north-south direction than in any other, implying that the elongation is adequately resolved.

The low-velocity anomaly extends beneath the Reykjanes ridge in the depth range 50-200 km and, in this region, is much stronger in v_S (-2.4%) than v_P (-0.5%). This feature is not as reliable as the central, low-velocity anomaly as it is at the edge of the envelope of "good" resolution, but it is a persistent feature in models of different spatial parameterisation, which adds confidence. An anomaly of this kind is found beneath the Kolbeinsey Ridge to the north but only below around 160 km. Above this depth, the absence of such an anomaly is well resolved (e.g. Figure 5.61).

v_P/v_S is at its highest beneath central Iceland in the depth range 100-300 km. It is only reliable for the thick-layered model since v_P/v_S is much less well constrained than either the perturbation in v_P or v_S. This is because the uncertainty in v_P/v_S combines the uncertainties in both v_P and v_S.

6.4   SEISMIC WAVE-SPEED VARIATIONS BENEATH HOTSPOTS

Seismic wave speeds are sensitive to several physical and chemical phenomena that are expected in the mantle beneath a ridge-centred hotspot such as

Iceland. The excess temperature of the mantle beneath Iceland has been estimated at 263 K (Schilling, 1991), but the effect of temperature alone goes only some way to explain the observed wave speed reductions of over 2% in v_P and over 4% in v_S. v_P is reduced by about 0.5 % per 100 K increase in temperature, v_S by 1.2 to 1.6 times as much (Ito et al., 1996). An excess temperature of this order would account for ~50% of the observed anomaly in v_P and ~40% of that observed in v_S.

In addition to the effect of the temperature of the rock matrix, the presence of melt is known to cause a significant decrease in seismic velocity and electrical resistivity, as the rock is made mechanically softer (Mavko, 1980). Temperature dependence of velocity is affected by both anharmonicity and anelasticity (Karato, 1993) (Figure 6.1). The velocity decrease due to anharmonicity is an effect due only to the temperature of the rock. The presence of melt, however, causes an anelastic effect which is much stronger for shear waves than for compressional waves.
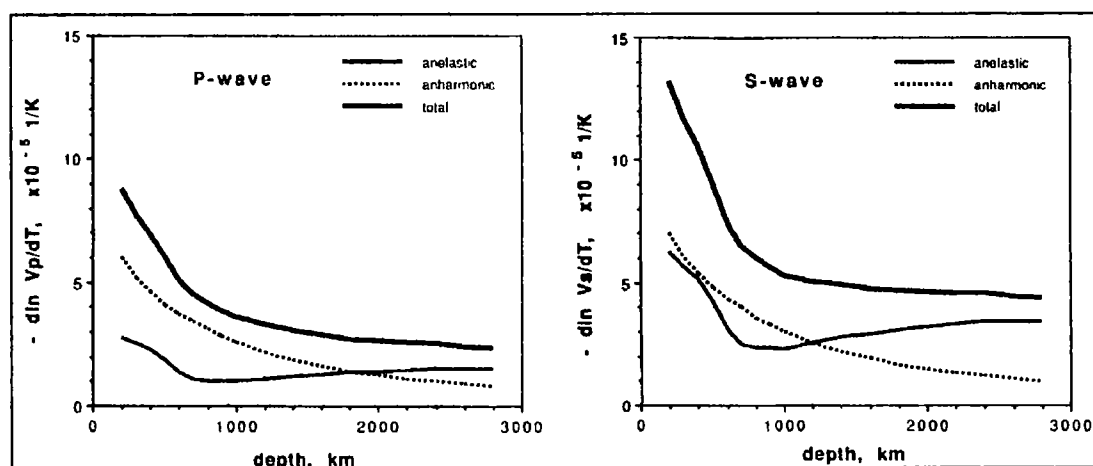
Figure 6.1 Temperature derivatives of seismic wave speeds for P and S waves in the mantle. From (Karato, 1993).

In addition to the proportion of melt present, the geometrical distribution of the melt is also important when considering the effect on waves passing through the medium. As melt is formed, it accumulates between grains of the solid matrix in inclusions ranging in shape from fibre-like tubules at grain triple-junctions to oblate, "penny-shaped" inclusions or thin films. The reduction of P-wave velocity in olivine basalt has been shown to be nearly twice as great for melt distributed as penny-shaped inclusions than for the same proportion of melt distributed only in triple-junction tubules (Faul et al., 1994). Table 6.1 shows the reduction in seismic velocity

per percent melt fraction for these two melt distribution geometries. Chemical depletion of mantle material, on the other hand, increases v_P by 0.1% for each 1% increase in compositional depletion.

Table 6.1 Reduction in wave velocity per percent melt fraction (Faul *et al.*, 1994).

Phase	Triple-junction tubules	Penny-shaped inclusions
v_P	1.0%	1.8%
v_S	2.3%	3.3%

Other factors may also affect the measured delay times, such as wavefront healing, which has been shown to decrease the size of time delays by up to 40%, e.g. Allen et al. (1999). This would have a corresponding effect on the magnitude of velocity anomalies. No analysis of shear-wave splitting has been made. This has been shown to contribute substantially to the size of S-wave delays across Iceland (Bjarnason *et al.*, 1996) and could influence the difference between the P- and S-wave models. Anisotropy from the alignment of the olivine crystallographic a [100] axis would be expected to increase the S-wave velocity parallel to the flow direction of the plume, and thus might work to reduce the observed S-wave delays.

6.5 INTERPRETATION

The results presented here are consistent with the hypothesis of a plume-like convective upwelling beneath Iceland. The maximum amplitudes of the anomaly in the relatively well-resolved centre of the target volume are approximately -1.6% for v_P and -4.6% for v_S. Values of 2% and 4% were used by Wolfe *et al.* (1997) to determine the excess temperature of the plume relative to the surrounding mantle as 300 K according to the P-wave model and 600 K according to the S-wave model. This was based on the effect of temperature alone. However, correction for anelastic effects (Karato, 1993) reduces these estimates to 200 and 300 K respectively, which is more in line with values predicted by modelling (e.g., Schilling, 1991). The fact that the v_S anomaly is much greater than the v_P anomaly is also predicted by the anelastic effect, since the presence of even a small amount of melt has a much larger effect on shear waves than compressional waves. A specific example of this is seen beneath the Reykjanes ridge at 50-200 km depth, where the v_S anomaly (-2.4%)

greatly exceeds the v_P anomaly (-0.5%). This is interpreted as evidence of melt, and implies the transport of material from the main plume outwards beneath the ridge. That the Kolbeinsey ridge only reliably shows low velocities below ~160 km suggests that the Tjörnes fracture zone acts as a barrier to lateral flow of material in that direction.

The variation in strength of the low-velocity anomaly with depth is a significant feature, particularly in terms of the variation in v_P/v_S. If this variation is real, it represents an interesting second-order feature of the velocity field which is consistent with models of a plume whose excess temperature at a given point varies with time. A time-variant, pulsating convective nature has been proposed to explain surface features such as the V-shaped, outward-propagating ridges along the Reykjanes ridge (e.g., White *et al.*, 1995). These features appear to represent variations in magma supply rate on a time scale of 10 Ma, however. Assuming an ascent rate of 20 cm/a in the plume, material would rise 500 km in 2.5 Ma. The variations imaged here, therefore, cannot directly explain the V-shaped ridges on the Reykjanes ridge. Radiogenic Pb isotope concentration maxima are known to correlate with lava production rates between during the period 15 - 3 Ma (Hanan & Schilling, 1997). The fact that v_P/v_S is over 1% high throughout most of the plume indicates that temperatures in the mantle must be elevated to such a degree that up to a few percent of partial melt is present.

Perhaps the most remarkable feature of the results is the north-south elongation of the central low-velocity anomaly which begins at 250-300 km depths and continues throughout all deeper layers. Numerical models of basally-heated convection predict a change in the shape of a hot upwelling from tabular to cylindrical in the middle of the convecting layer (Houseman, 1990) similar to that observed here. If the Iceland plume is a continuous convective upwelling originating in the lower mantle, then it should have achieved cylindrical form before it penetrated the upper mantle. Thus, from these results, it appears that the Iceland plume must originate not far from the bottom of our image.

These results therefore suggest that the plume beneath Iceland spans a convection cell which is restricted to the upper mantle, challenging the model of a whole-mantle plume (Bijwaard & Spakman, 1999). There are many problems with

models that involve plumes penetrating unaffected through the endothermic transition at 670 km, since this would provide a significant impediment to convection. Indeed, Bijwaard & Spakman (1999) add to their interpretation the caveat that, "with the present resolution we cannot distinguish between a continuous upwelling from the CMB to the surface, or an upwelling from the upper-to-lower mantle discontinuity, induced by an upwelling from the CMB." The latter is supported by other numerical modelling of a lower mantle with temperature- and pressure-dependent rheology (Steinbach & Yuen, 1997). This would suggest that, when plumes from the lower mantle impinge on the 670 km boundary, the development of secondary plumes in the upper mantle is induced, where vigorous but time-dependent convection occurs. It is also true that the velocity anomaly in the whole-mantle plume model (Bijwaard & Spakman, 1999) is weak (mostly less than 0.5%) in the lower mantle and weaker (0.3%) near the CMB, which is surprising in the light of the very low velocities reported in that region (Helmberger *et al.*, 1998). Only *above* the 670-km discontinuity does it attain amplitudes greater than or equal to 0.5%, suggesting that the lower-mantle part of the model may not be very significant. Recently, other large-scale tomography work has revealed a shear-wave speed anomaly of -2.5% beneath Iceland which is confined to the upper mantle (Megnin *et al.*, 1999; Ritsema *et al.*, 1999).

The zone of ultra-low velocities (-10% v_P and -30% v_S) at the CMB beneath the Iceland region (Helmberger *et al.*, 1998) and evidence of flow-like structures in the same region beneath Hawaii (Russell *et al.*, 1998) cannot be ignored, however, since these are important evidence for the root of an upwelling feature in the lower mantle. The most likely interpretation, in the light of the results of this study, is that these are systematically related to, yet not necessarily *continuous* with, upper-mantle plumes. This still leaves the question of a transport mechanism which would explain signatures of lowermost-mantle and even traces of outer-core geochemistry in surface rocks, e.g. Brandon *et al.* (1998). This might be explained by interaction between the upper- and lower-mantle convective systems whereby small amounts of lower-mantle material are entrained in the core of the upper-mantle plume, while maintaining a "sheath" of upper-mantle-type material around this, e.g. Fitton *et al.* (1997). The variation of anomaly magnitude with depth, which may indicate time-variant plume strength, a process also suggested by Pb-isotope geochemistry (Hanan

& Schilling, 1997), might also be evident in the amounts of such lower-mantle material entrained into the upper-mantle plume, although this would be difficult to distinguish from variations in overall plume flux.

6.6   SHORTCOMINGS OF THE ACH STUDY

That broadly similar images have emerged from two independently-processed datasets (P- and S-wave arrival times), strengthens confidence in the final results. However, both the methodology and the data suffer from shortcomings, which are discussed here, along with suggestions for improvements as part of future work.

The ACH method. The ACH method is a robust and reliable, if unsophisticated method of teleseismic tomography. It has been tested in many different experiments and its behaviour is well understood and documented, making it a reliable tool with which to tackle an inversion problem.

The ACH approach used here (Evans & Achauer, 1993) is a single-step, non-iterative inversion scheme, and as such makes no attempt to correct for refraction due to modelled velocity perturbations. In reality, rays are bent by the velocity perturbations that we model, with the curvature of ray path dependent on the fractional velocity anomaly. For the relatively small velocity anomalies involved here (<5%), the effect is small, but in some geometrical circumstances it could result in a ray being assigned to the wrong block in the model. This is another reason why the block size of 50 km may be too small for the experiment geometry used here. Three-dimensional raytracing through a preliminary model could be used to refine subsequent models in this respect.

The coordinate system of the ACH method is cartesian, whereas spherical geometry is more appropriate for experiments with a seismic network of several hundred km. An error in the treatment of local grid north values was discovered and corrected during the course of this study (Appendix 24), but the method still relies on a mixture of cartesian and geographical coordinates in defining the block structure, which is adequate when the depth extent is not great, but may well affect the validity of the block structure when the depth becomes a significant fraction of the Earth's radius. The target volume in this case extends to 646 km, or $0.1R_E$, so the effect is small, but the ACH programs would benefit from being re-written in spherical coordinates at some stage.

Data. The data used here represent a large proportion of the clearest seismic events recorded during the experiment, but the resulting ray set is limited by the natural distribution of seismic sources, and by the high level of microseismic noise and attenuation in Iceland. However, the dataset is the largest to date which has been used to image the Icelandic mantle (Table 6.2), and has the best distribution in azimuth and angles of approach.

The arrival times were measured by hand, which is labour-intensive and prone to systematic and random errors. Systematic errors are minimised if, as was the case here, all picks are made by the same analyst, but there were still many outliers which had to be eliminated at the data quality control stage (Section 4.3). Low signal-to-noise ratios, caused by microseismic noise and attenuation, prevented many seismograms from being used. Pick errors were estimated to be around 1 sample (0.05 s for P picks and 0.1 s for S picks). These might be improved by numerical cross-correlation (VanDecar & Crosson, 1990). Numerical cross-correlation is not straightforward, however. It is prone to cycle-skipping and other systematic errors which require that each individual pick is reviewed manually, increasing the time needed to compile a dataset of several thousand picks. In order to avoid cycle-skipping, a manual estimate pick has first to be made, then a suitable cross-correlation time window chosen, followed by a manual check to make sure that the output value is reasonable. However with careful use, it can improve pick accuracies by 10-15 %, so development of a suitable method may well prove useful in refining the current dataset, picks from which could be used as starting values.

Teleseismic tomography relies on the natural distribution of seismic sources to provide sampling of the target volume from all directions. In reality, certain directions have fewer natural sources than others, with the result that the dataset is rich in data from some directions, such as the northeast and southwest, and poor from other directions such as the southeast. In the search for data from event-poor regions, it was often the case that poor quality events only were found. However, a detailed search of such regions for the best data would improve the ray distribution of the current dataset. Also, the current dataset could be improved by adding more picks from core phases, which approach the target volume at near-vertical angles and

would fill gaps left in the present ray distribution which, as it stands, is dominated by rays at epicentral distances of 30-90°.

No synthetic modelling of anomalies was attempted. However, this is a valuable method by which an inversion model can be evaluated. Future modelling of this kind is recommended.

Starting model. *A priori* seismic structure of Iceland has been largely ignored in this study, mainly because it is the perturbations relative to a standard Earth model that are of first-order importance. The ACH method as it stands does not enable heterogeneous initial models to be specified. This would be a major improvement which would allow account to be made of variations in the Icelandic crust, the thickness of which has been shown to vary from 25 km in the northwest to nearly 40 km beneath southern central Iceland (e.g., Darbyshire *et al.*, 1998; Allen *et al.*, 1999; Du & Foulger, 1999). Assuming crustal and mantle velocities of, say, 7.2 and 7.8 km s^{-1} respectively, this could cause a relative difference in travel time across Iceland of up to 0.16 s. Crustal models derived from refraction profiles or receiver function analysis could be used to apply time corrections to measured time delays, in effect stripping away the influence of the crust.

6.7 COMPARISON WITH PREVIOUS STUDIES

Two previous studies have mapped the mantle beneath Iceland using regional teleseismic velocity tomography (Tryggvason *et al.*, 1983; Wolfe *et al.*, 1997) (Table 6.2).

Table 6.2 Comparison of datasets

	Tryggvason *et al.* (1983)	**Wolfe *et al.* (1997)**	**My Study**
No. of stations	39	16	42
Data type	Analogue, short-period instruments, paper record seismograms, vertical component only	Broadband, digital instruments, 3-component	Broadband, digital instruments, 3-component
P-wave models			
No. of events	61	86	113 (160 phases)
No. of arrival times	714	601	3159
S-wave models			
No. of events	N/A	78	66 (73 phases)
No. of arrival times	N/A	560	1338

The first study used only P-wave arrival times, which were measured from paper records made by short-period (4 Hz) analogue instruments. 39 stations were used, but the distribution was poor, since the study made use of seismic stations installed to monitor local seismicity. These were grouped in clusters in the southwest, south and northeast of Iceland, leaving large gaps in areas such as the Western Fjords in the northwest, and Vatnajökull glacier in the southeast. The velocity anomalies imaged are shown in Figure 6.2.
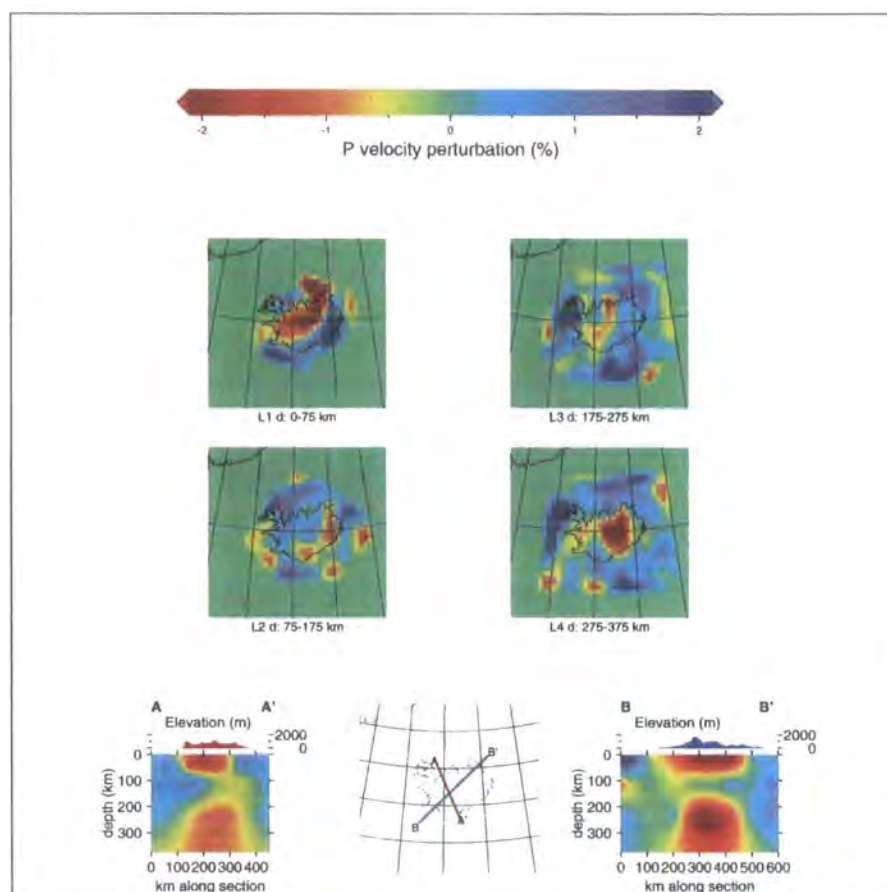
Figure 6.2 P-wave velocity anomalies of Tryggvason *et al.* (1983), redrawn using the same plotting conventions and colour scale as figures for P-wave models in Chapter 5.

The study imaged a significant low-velocity anomaly, centred on Iceland, which varied considerably in amplitude between the top layer (0-75 km, up to -3.9%) and layer 3 (175-275 km, up to -1.1%). The anomaly strength increased again in the bottom layer (275-375 km, up to -3.4%). The anomaly in the top layer was roughly parallel to the active rift zone, while in lower layers, the low-velocity feature shifts significantly southeastward, with high velocities (up to 1.2%) present beneath the

first-layer low-velocities in west-central Iceland, showing as a significant gap in the low-velocity column in the vertical sections. One of the main differences between my results and those of Tryggvason *et al.* (1983) is the prominent correlation of the anomaly in the first layer with the neovolcanic zone and its continuation north of Iceland below the Kolbeinsey ridge. An equivalent anomaly beneath the Kolbeinsey Ridge is absent in my results to a high degree of confidence. Also, the anomalies of Tryggvason *et al.* (1983) are relatively weak and narrow in the depth range 75-275 km, compared with anomalies of significant size and amplitude in layers 4, 5 and 6 of model p_10_75_225_av (Figure 5.61). The v_P/v_S perturbation at these depths indicate that the v_P anomaly is much weaker than v_S, however. In the deepest layer of Tryggvason *et al.* (1983), the anomaly is strong (-3.4%) and centred on east-central Iceland, but does not show the north-south elongation which initiates at this depth the model from my study. Strong, low-velocities are found to the north at this depth in the model of Tryggvason *et al.* (1983), leaving a roughly circular central anomaly. The south-westerly extension of the low-velocity anomaly is shared by both models, though stronger in the model of Tryggvason *et al.* (1983).

The overall impression is that, in the results of Tryggvason *et al.* (1983), most of the signal has been forced into layers 1 and 4, while leaving layers 2 and 3 with relatively small anomalies, and strong, high-velocity "side-lobes". Tryggvason *et al.* (1983) also used a version of the ACH method, but with a relatively coarse parameterisation comprising 4 layers with thicknesses of 75 or 100 km, and blocks of around 100 km width.

The P- and S-wave models of Wolfe *et al.* (1997) are shown in Figure 6.3. Wolfe *et al.* (1997) used a sparse network of 16 broadband, digital seismometers that covered Iceland more uniformly than that of Tryggvason *et al.* (1983), but with a much lower station density than the present study, which used a total of 42 broadband stations. Arrival times for P and S waves were measured by numerical cross-correlation at similar frequency bands to this study, but fewer earthquakes and picks were used (Table 6.2).

The P- and S-wave models of Wolfe *et al.* (1997) (Figure 6.3) are similar to each other in general form but the anomaly in v_S (-4%) is stronger than in v_P (-2%).
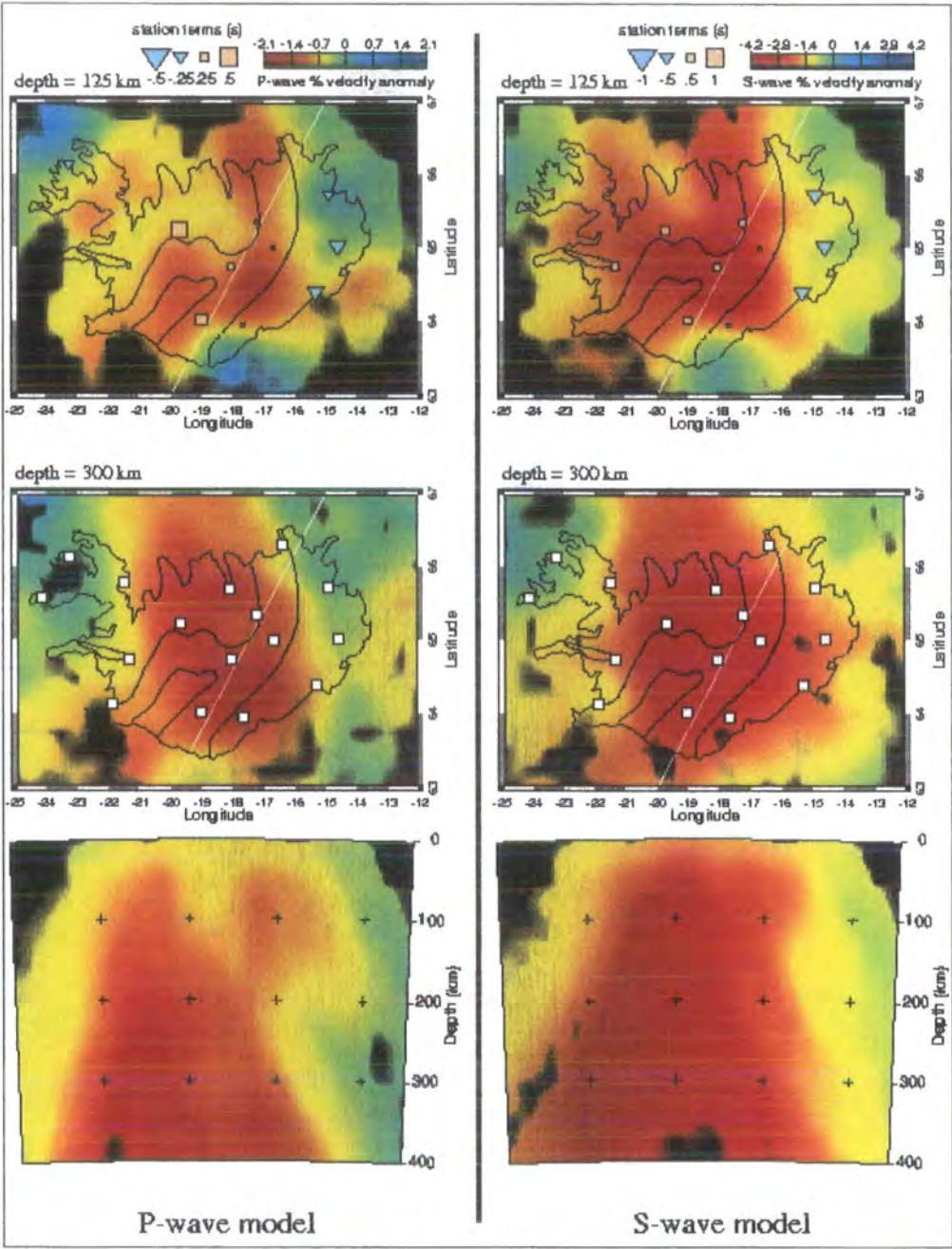
Figure 6.3 P- and S-wave models of Wolfe *et al.* (1997).

Their results are similar to mine in that the feature is persistent through all depths in both models. In horizontal cross-section at 300 km, the P- and S-wave models are fit by a radial velocity function of Gaussian radius 150-200 km. Both P and S models show a progressive widening of the anomaly with depth. At 125 km depth, the anomalies underlie the neovolcanic zone. Low velocities are also imaged

below the Western Fjörds, especially in v_S. Comparing the results at this depth with an equivalent depth range in the model of Tryggvason *et al.* (1983) (Figure 6.2) reveals significant differences, since the rift-parallel features in that model are much shallower, being in the depth-range 0-75 km.

The inversion method used for the study of Wolfe *et al.* (1997) was non-linear and inverted for three-dimensional velocity structure, earthquake relocations and station terms together, using a method which minimised spatial gradients and roughness. This may explain the relatively smooth nature of the velocity anomalies. The spacing of velocity nodes in their model was 25 km in depth, 0.5° in longitude (~25 km at the latitude of Iceland) and 0.25° in latitude (~25 km), which is a remarkably dense network of nodes considering the 100-150 km station spacing and relatively low ray density compared with the that of the present study. Wolfe *et al.* (1997) report that resolution tests indicate that the structures imaged are well resolved. Questions have been raised about the surprising uniformity of the plume of Wolfe *et al.* (1997), particularly in view of the fact that the anomaly is conical, widens with depth, and appears to mimic the ray bundle. Independent resolution tests (Keller *et al.*, 1997) suggest the data used could equally well be explained by a body that extends no deeper than 200 km and that the deeper parts of the body could be simply vertical smearing.

Interestingly, the model of Wolfe *et al.* (1997) also displays some broadening of the P- and S-wave anomalies in the north-south direction in the horizontal section at 300 km depth. This is seen, for example in the -1% v_P or -2% v_S "contours" towards the edge of the horizontal sections in Figure 6.3. However, without additional sections, it is not possible to say whether or not the tabular structure I image below 250 km is also imaged in the results of Wolfe *et al.* (1997).

6.8   DISCUSSION IN REGIONAL CONTEXT

This study provides evidence to support the hypothesis of a plume beneath Iceland, which satisfies the requirements of many geochemical models which require a source for Icelandic basalts distinct from that of MORB. The plume is imaged here down to over 400 km depth and is consistent with a thin, hot plume model (e.g., Allen *et al.*, 1999). There is no apparent evidence for upward broadening of the

plume head as suggested by theoretical models (e.g., White & McKenzie, 1989) and global tomography (Bijwaard & Spakman, 1999; Ritsema *et al.*, 1999). Global tomography suggests a plume head of 1200 km diameter above 400 km depth. However, the geometry of those experiments does not allow resolution of features on a scale smaller than ~500 km (J. Ritsema, *pers. comm.*). Low velocities are, however, generally confined to the volume vertically beneath Iceland in my model, and this is consistent with many other geophysical data, such as the gravity and geoid anomalies, which suggest that the plume centre underlies east-central Iceland. A more extensive network, for example using sea-floor sensors around Iceland, would be necessary to investigate the volume beyond the limits of the current ray bundle.

I find little evidence for rift-parallel low-velocities in the top 100 km compared with the models of Wolfe *et al.* (1997) and Tryggvason *et al.* (1983). Elongation of the low-velocity anomalies beneath the Reykjanes ridge between 50 and 200 km depth is imaged, however, and this is evidence for the channelling of melt along that part of the plate boundary. This is consistent with geochemical profiles of the Reykjanes ridge which suggest the mixing of "normal" asthenospheric and plume material in decreasing proportions outward along the ridge. Indeed, dehydration of the mantle due to this process has been proposed to reconcile the over-thick crust predicted by the thin, hot plume model with observed values along the Reykjanes ridge (Wolfe *et al.*, 1997; Ito *et al.*, 1999).

6.9   DISCUSSION IN GLOBAL CONTEXT

There is currently a resurgence of interest in mapping the depth extent and structure of currently active plumes, and understanding their role in plate tectonics. This is a result of the fast development of suitable geophysical tools. Over the last few years there has been rapid progress in the development of seismic instrumentation, and an upsurge in the availability of large quantities of broadband instruments, both permanent installations and for temporary deployments. The massive increase in available computing power has also facilitated a surge in the development of computer methods such as teleseismic waveform tomography. The experiment described in this thesis represents what is probably one of the first of a new era of advanced plume studies.

Because of this, comparable studies of other plumes are few, and deployed inferior instrumentation and data processing techniques. It is nonetheless interesting to compare the results. The Yellowstone hotspot was studied by Iyer *et al.* (1981) who deployed stations in an array over 800 km broad, centred on the Yellowstone caldera. A low-velocity body with P-wave anomaly up to -4% was detected beneath Yellowstone, but its base was clearly imaged at 150 - 200 km depth. It appears from this that the seismic signature of the Yellowstone "plume" extends to just below the lithosphere but no deeper. The Hawaii hotspot was studied by Ellsworth & Koyanagi (1977) whose data were limited to recordings from land stations on Hawaii, whose maximum aperture, being only 150 km, greatly restricts the depth extent to which structural imaging is possible. Little lateral inhomogeneity was detected in the upper 75 km, and very small low-velocity anomalies from 75 to 160 km. The Hawaii case thus appears to be the reverse of Yellowstone, though it must be taken into account that the island of Hawaii is so small that possibly only the tip of the plume was studied. Both the Yellowstone and the Hawaii studies reveal very different results from those described in this thesis, for the Iceland plume, which has a strong low-velocity signature from the surface down to at least 400 km depth, and whose morphological variations suggest an origin in the mantle transition zone.

Global tomography images seismic anomalies on a much larger scale than local experiments, and resolution is generally no better than on a scale of 500 km, and often only 1,000 km. Global tomography results are emerging from the early era, however, when agreement between models tended to be poor, and now there is considerable agreement between models derived independently and using different techniques (e.g. Megnin *et al.*, 1999; Ritsema *et al.*, 1999). The results of global tomography strongly support the conclusions of this thesis, i.e., a model of an Iceland plume confined to the upper mantle, with much weaker seismic anomalies beneath, in the lower mantle. In other parts of the world, however, there is much stronger evidence for whole-mantle structures. For example, Ritsema *et al.* (1999) detect a major, low-velocity body arising from the base of the lower mantle beneath the south Atlantic and rising to the northeast to reach the surface beneath the east African rift.

The present global picture of plumes is thus one that suggests tremendous variability. Examples may be quoted of plumes that appear to arise from the CMB

(e.g., the south Atlantic-east Africa plume), the mantle transition zone (e.g., Iceland), the topmost asthenosphere (e.g., Yellowstone) and to have very little seismic anomaly at all in the upper 150 km (e.g., Hawaii). As yet there are insufficient case histories to support a generic model to explain this variability, and the next one or two decades may well produce some very exciting results in this field.

6.10 CONCLUSIONS

1. Teleseismic P-wave azimuthal anomalies detected at an array in Norway can be modelled as the effect of a plume in the lower mantle beneath Iceland. A Gaussian velocity anomaly of 125 km radius at ~1500 km depth with an amplitude of 1.5% is a candidate model that fits the observations.

2. Iceland is underlain by a coherent low-velocity body in which seismic wave speeds are reduced by up to 2.9% in v_P and 4.9% in v_S. The low-velocity body persists throughout the whole of the well-resolved depth range, from around 30 km to at least 400 km.

3. The low-velocity body can be approximated by a Gaussian, cylindrical velocity function of radius 100-130 km in the upper 300 km of the model. This is interpreted as a mantle plume with an excess temperature of the order of 200-300 K.

4. There is a change from axisymmetric to north-south-orientated planar symmetry at around 250-300 km depth. This tabular root is present in both P- and S-wave models and persists from 250-300 km to the bottom of the well-resolved volume at ~400 km, and below. This change in morphology is expected towards the base of a basally-heated convection cell and implies that the Iceland plume arises from the mantle transition zone.

5. Beneath the Reykjanes ridge, in the depth range 50-200 km, v_S is reduced by up to 2% in places where v_P is only 0.5% low. This is interpreted as the presence of, and possible channelling of, melt beneath the ridge axis. The Kolbeinsey ridge shows low velocities only below 160 km. This is interpreted as the Tjörnes fracture zone acting as a barrier to lateral flow of melt away from the plume in this direction.

6. The v_P/v_S ratio is over 1% high throughout most of the plume, with the strongest anomalies of up to 3.2% occurring beneath central Iceland from 100 to 200 km and beneath east-central Iceland from 200 to 300 km. This implies that small but variable amounts of partial melt (up to a few percent) are present throughout the plume.

6.11 SUGGESTED FUTURE WORK

- The teleseismic dataset should be extended to include more core phases and events from regions with few seismic sources.

- Data from sea-floor sensors should be acquired and added to the dataset. This could be achieved by a long-term ocean-bottom seismometer deployment.

- Apply numerical cross-correlation to refine the pick qualities.

- Correct the arrival times to account for crustal thickness and velocity structure across Iceland obtained from receiver function and surface wave work currently in progress.

- Investigate the effect of anisotropy on the velocity models and v_P/v_S estimates.

- Investigate wavefront healing, and apply corrections to the velocity amplitudes as appropriate.

- Refine the ACH program code, or apply another tomography method which enables

    a) Operation in spherical geometry,

    b) the use of laterally heterogeneous starting models, and

    c) iteration and raytracing through a preliminary model, to account for ray refraction.

- Synthetic modelling of velocity anomalies, in particular to explore more fully the effect of smearing and the reliability of the results of the present work.

BIBLIOGRAPHY

Achauer, U., J.R.R. Ritter, P.K.H. Maguire, R.P. Meyer, P. Davis, P. Slack, W.V. Green & A. Glahn (1994). New ideas on the Kenya rift based on the inversion of the combined dataset of the 1985 and 1989/90 seismic tomography experiments. *Tectonophysics* **236**, 305-329.

Aki, K. (1993). Overview, in *Seismic tomography: theory and practice*. H.M. Iyer and K. Hirahara (eds). Chapman & Hall, London.

Aki, K., A. Christoffersson & E.S. Husebye (1976). Three-dimensional seismic structure of the lithosphere under Montana LASA. *Bull. Seismol. Soc. Am.* **66**, 501-524.

Aki, K., A. Christoffersson & E.S. Husebye (1977). Determination of the three-dimensional seismic structure of the lithosphere. *J. Geophys. Res.* **82**, 277-296.

Allen, R.M., G. Nolet, W.J. Morgan, K. Vogfjörd, B.H. Bergsson, P. Erlendsson, G.R. Foulger, S. Jakobsdóttir, B.R. Julian, M. Pritchard, S. Ragnarsson & R. Stefánsson (1999). The thin hot plume beneath Iceland. *Geophys. J. Int.* **137**, 51-63.

Anderson, D.L. (1998). The scales of mantle convection. *Tectonophysics* **284**, 1-17.

Anderson, D.L., T. Tanimoto & Y.S. Zhang (1992). Plate-tectonics and hotspots: the third dimension. *Science* **256**, 1645-1651.

Angenheister, G., H. Gebrande, H. Miller, P. Goldflam, W. Weigel, W.R. Jacoby, G. Pálmason, S. Björnsson, P. Einarsson, N.I. Pavlenkova, S.M. Zverev, I.V. Litvinenko, B. Loncarevic & S.C. Solomon (1980). Reykjanes Ridge Iceland Seismic Experiment (RRISP 77). *J. of Geophys.* **47**, 228-238.

Beblo, M. & A. Björnsson (1980). A model of electrical resistivity beneath northeast Iceland, correlation with temperature. *J. Geophys.* **47**, 184-190.

Beblo, M., A. Bjornsson, K. Arnason, B. Stein & P. Wolfgram (1983). Electrical-conductivity beneath Iceland - constraints imposed by magnetotelluric results on temperature, partial melt, crust-structure and mantle structure. *J. Geophys.* **53**, 16-23.

Berteussen, K.A. (1975). Array analysis of lateral inhomogeneities in the deep mantle. *Earth Planet. Sci. Lett.* **28**, 212-216.

Bijwaard, H. & W. Spakman (1999). Tomographic evidence for a narrow whole mantle plume below Iceland. *Earth. Planet. Sci. Lett.* **166**, 121-126.

Bijwaard, H., W. Spakman & E.R. Engdahl (1998). Closing the gap between regional and global travel time tomography. *J. Geophys. Res.* **103**, 30055-30078.

Birt, C.S., P.K.H. Maguire, M.A. Khan, H. Thybo, G.R. Keller & J. Patel (1997). The influence of pre-existing structures on the evolution of the southern Kenya Rift Valley - evidence from seismic and gravity studies. *Tectonophysics* **278**, 211-242.

Bjarnason, I.T., W. Menke, O.G. Flovenz & D. Caress (1993). Tomographic image of the mid-Atlantic plate boundary in southwestern Iceland. *J. Geophys. Res.* **98**, 6607-6622.

Bjarnason, I.T., C.J. Wolfe, S.C. Solomon & G. Gudmundson (1996). Initial results from the ICEMELT experiment: Body-wave delay times and shear-wave splitting across Iceland. *Geophys. Res. Lett.* **23**, 459-462.

Boehler, R. (1993). Temperatures in the Earth's core from melting-point measurements of iron at high static pressures. *Nature* **363**, 534-536.

Brandon, A.D., R.J. Walker, J.W. Morgan, M.D. Norman & H.M. Prichard (1998). Coupled Os-186 and Os-187 evidence for core-mantle interaction. *Science* **280**, 1570-1573.

Brandsdóttir, B., W. Menke, P. Einarsson, R.S. White & R.K. Staples (1997). Faroe-Iceland Ridge Experiment .2. Crustal structure of the Krafla central volcano. *J. Geophys. Res.* **102**, 7867-7886.

Brandsdóttir, B. & W.H. Menke (1992). Thin low-velocity zone within the Krafla caldera, NE-Iceland attributed to a small magma chamber. *Geophys. Res. Lett.* **19**, 2381-2384.

Buland, R. & C.H. Chapman (1983). The computation of seismic travel times. *Bull. Seismol. Soc. Am.* **73**, 1271-1302.

Bungum, H., E.S. Husebye & F. Ringdal (1971). The NORSAR array and preliminary results of data analysis. *Geophys. J. R. Astron. Soc.* **25**, 115-126.

Courtney, R.C. & R.S. White (1986). Anomalous heat flow and geoid across the Cape Verde Rise: evidence for dynamic support from a thermal plume in the mantle. *Geophys. J. R. Astron. Soc.* **87**, 815-867.

Crotwell, H.P., T.J. Owens & J. Ritsema (1999). The Tau-P toolkit: flexible travel-time and raypath utilities. *Seismological Research Letters* **70**, 154-160.

Crough, S.T. (1983). Hotspot swells. *Ann. Rev. Earth Planet. Sci.* **11**, 163-193.

Darbyshire, F.A., I.T. Bjarnason, R.S. White & O.G. Flovenz (1998). Crustal structure above the Iceland mantle plume imaged by the ICEMELT refraction profile. *Geophys. J. Int.* **135**, 1131-1149.

Darbyshire, F.A., K.F. Priestley, R.S. White, G. Gudmundsson, S. Jakobsdóttir & R. Stefánsson (1997). The crustal structure of northeastern Iceland: Constraints from broadband teleseismic body waves. *EOS Trans. Amer. Geophys. U.* **78 (Fall Meeting Supplement)**, F500.

DeMets, C., R.G. Gordon, D.F. Argus & S. Stein (1994). Effect of recent revisions to the geomagnetic reversal time- scale on estimates of current plate motions. *Geophys. Res. Lett.* **21**, 2191-2194.

Du, Z.J. & G.R. Foulger (1999). The crustal structure beneath the northwest fjords, Iceland, from receiver functions and surface waves. *Geophys. J. Int.* **139**, 419-432.

Ellsworth, W.L. (1977). Three-dimensional structure of the crust and upper mantle beneath the island of Hawaii. Ph.D. Thesis, Mass. Inst. of Technology, 327pp.

Ellsworth, W.L. & R.Y. Koyanagi (1977). Three-dimensional crust and mantle structure of Kilauea volcano, Hawaii. *J. Geophys. Res.* **82**, 5379-5394.

Evans, J.R. & U. Achauer (1993). Teleseismic velocity tomography using the ACH method: Theory and application to continental-scale studies., in *Seismic tomography: theory and practice*. H.M. Iyer and K. Hirahara (eds). Chapman & Hall, London. 319-360.

Eysteinsson, H. & J.F. Hermance (1985). Magnetotelluric measurements across the eastern neovolcanic zone In south iceland. *J. Geophys. Res.* **90**, 10093-10103.

Farnetani, C.G. (1997). Excess temperature of mantle plumes: The role of chemical stratification across D". *Geophys. Res. Lett.* **24**, 1583-1586.

Faul, U.H., D.R. Toomey & H.S. Waff (1994). Intergranular basaltic melt is distributed in thin, elongated inclusions. *Geophys. Res. Lett.* **21**, 29-32.

Field, P.R. (1994). Crustal structure of the spreading plate boundary in Iceland and the north Atlantic from gravity data, Ph.D. Thesis, University of Durham.

Fitton, J.G., A.D. Saunders, M.J. Norry, B.S. Hardarson & R.N. Taylor (1997). Thermal and chemical structure of the Iceland plume. *Earth. Planet. Sci. Lett.* **153**, 197-208.

Gebrande, H., H. Miller & P. Einarsson (1980). Seismic structure of Iceland along RRISP-profile I. *J. Geophys. Res.* **47**, 239-249.

Granet, M., G. Stoll, J. Dorel, U. Achauer, G. Poupinet & K. Fuchs (1995). Massif-Central (France) - New constraints on the geodynamical evolution from teleseismic tomography. *Geophys. J. Int.* **121**, 33-48.

Granet, M., M. Wilson & U. Achauer (1995). Imaging a mantle plume beneath the French Massif Central. *Earth. Planet. Sci. Lett.* **136**, 281-296.

Gripp, A.E. & R.G. Gordon (1990). Current plate velocities relative to the hotspots incorporating the nuvel-1 global plate motion model. *Geophys. Res. Lett.* **17**, 1109-1112.

Hanan, B.B. & J.G. Schilling (1997). The dynamic evolution of the Iceland mantle plume: the lead isotope perspective. *Earth. Planet. Sci. Lett.* **151**, 43-60.

Hardarson, B.S., J.G. Fitton, R.M. Ellam & M.S. Pringle (1997). Rift relocation - a geochemical and geochronological investigation of a palaeo-rift in northwest Iceland. *Earth. Planet. Sci. Lett.* **153**, 181-196.

Hards, V.L., P.D. Kempton & R.N. Thompson (1995). The heterogeneous Iceland plume: new insights from the alkaline basalts of the Snaefell volcanic centre. *J. Geol. Soc. Lond.* **152**, 1003-1009.

Hart, S.R., J.-G. Schilling & J.L. Powell (1973). Basalts from Iceland and along the Reykjanes ridge: Sr isotope geochemistry. *Nature* **246**, 104-107.

Harvey, D. & D. Quinlan (1996). Datascope Seismic Application Package (DSAP), Joint Seismic Processing Center, University of Colorado.

Helgason, J. (1984). Frequent shifts of the volcanic zone in Iceland. *Geology* **12**, 212-216.

Helgason, J. (1985). Shifts of the plate boundary in Iceland - some aspects of tertiary volcanism. *J. Geophys. Res.* **90**, 84-92.

Helmberger, D.V., L. Wen & X. Ding (1998). Seismic evidence that the source of the Iceland hotspot lies at the core-mantle boundary. *Nature* **396**, 251-255.

Hermance, J.F. (1981). Crustal Genesis In Iceland - Geophysical constraints on crustal thickening with age. *Geophys. Res. Lett.* **8**, 203-206.

Hersir, G.P., A. Björnsson & L. Pedersen (1984). Magnetotelluric survey across the active spreading zone in southwest Iceland. *J. Volc. Geotherm. Res.* **20**, 253-265.

Houseman, G.A. (1990). The thermal structure of mantle plumes - axisymmetric or triple- junction. *Geophys. J. Int.* **102**, 15-24.

Husebye, E.S., A. Christoffersson & K. Aki (1976). Preliminary results on the 3-dimensional seismic structure of the lithosphere under the USGS Central California Seismic Array. *Geophys. J. R. Astron. Soc.* **46**, 319-340.

Ito, G., J. Lin & C.W. Gable (1996). Dynamics of mantle flow and melting at a ridge-centered hotspot: Iceland and the Mid-Atlantic Ridge. *Earth. Planet. Sci. Lett.* **144**, 53-74.

Ito, G., J. Lin & C.W. Gable (1997). Interaction of mantle plumes and migrating mid-ocean ridges: Implications for the Galapagos plume-ridge system. *J. Geophys. Res.* **102**, 15403-15417.

Ito, G., Y. Shen, G. Hirth & C.J. Wolfe (1999). Mantle flow, melting, and dehydration of the Iceland mantle plume. *Earth. Planet. Sci. Lett.* **165**, 81-96.

Iyer, H.M., J.R. Evans, G. Zandt, R.M. Stewart, J.M. Coakley & J.N. Roloff (1981). A deep low-velocity body under the Yellowstone Caldera, Wyoming - delineation using teleseismic P-wave residuals and tectonic interpretation - summary. *Geological Society Of America Bulletin* **92**, 792-798.

Ji, Y. & H.C. Nataf (1998). Detection of mantle plumes in the lower mantle by diffraction tomography: Hawaii. *Earth. Planet. Sci. Lett.* **159**, 99-115.

Julian, B.R., G.R. Foulger, M.J. Pritchard & J.R. Evans (1999). A geometrical error in some versions of the ACH method of teleseismic tomography. *Bull. Seismol. Soc. Am. (submitted)*.

Julian, B.R. & D. Gubbins (1977). Three-dimensional seismic ray tracing. *J. Geophys.* **43**, 95-113.

Karato, S. (1993). Importance of anelasticity in the interpretation of seismic tomography. *Geophys. Res. Lett.* **20**, 1623-1626.

Kaspar, T. & J.R.R. Ritter (1997). On the use of later teleseismic arrivals in ACH-tomography with an application in SE-Kenya. *Geophys. Res. Lett.* **24**, 1827-1830.

Keller, W., D.L. Anderson & R.W. Clayton (1997). Resolution of the seismic structure in the mantle beneath Iceland. *EOS Trans. Amer. Geophys. U.* **78** (**Fall Meeting Supplement**), F500.

Kendall, J.M. & P.G. Silver (1996). Constraints from seismic anisotropy on the nature of the lowermost mantle. *Nature* **381**, 409-412.

Kennett, B.L.N. & E.R. Engdahl (1991). Travel times for global earthquake location and phase identification. *Geophys. J. Int.* **105**, 429-466.

Kent, R.W. (1995). Magnesian Basalts From the Hebrides, Scotland - Chemical-Composition and Relationship to the Iceland Plume. *J. Geol. Soc.* **152**, 979-983.

Lay, T., Q. Williams & E.J. Garnero (1998). The core-mantle boundary layer and deep Earth dynamics. *Nature* **392**, 461-468.

Long, R.E. & M.G. Mitchell (1970). Teleseismic P-wave delay time in Iceland. *Geophys. J. R. Astron. Soc.* **20**, 41-48.

Masson, F. & J. Trampert (1997). On ACH, or how reliable is regional teleseismic delay time tomography? *Phys. Earth Planet. Inter.* **102**, 21-32.

Mavko, G.M. (1980). Velocity and attenuation in partially molten rocks. *J. Geophys. Res.* **85**, 5173-5189.

McNutt, M.K., D.W. Caress, J. Reynolds, K.A. Jordahl & R.A. Duncan (1997). Failure of plume theory to explain midplate volcanism in the southern Austral islands. *Nature* **389**, 479-482.

Megnin, C., B. Romanowicz & L. Breger (1999). The 3D shear velocity structure of the mantle from the inversion of waveform data. *EOS Trans. Amer. Geophys. U.* **(Fall Meeting Supplement).**

Menke, W., B. Brandsdottir, P. Einarsson & I.T. Bjarnason (1996). Reinterpretation of the RRISP-77 Iceland shear-wave profiles. *Geophys. J. Int.* **126**, 166-172.

Menke, W., B. Brandsdottir, S. Jakobsdottir & R. Stefánsson (1994). Seismic anisotropy in the crust at the mid-Atlantic plate boundary in south-west Iceland. *Geophys. J. Int.* **119**, 783-790.

Menke, W. & V. Levin (1994). Cold crust in a hot spot. *Geophys. Res. Lett.* **21**, 1967-1970.

Menke, W. & D. Sparks (1995). Crustal accretion model for Iceland predicts cold crust. *Geophys. Res. Lett.* **22**, 1673-1676.

Morgan, W.J. (1971). Convection plumes in the lower mantle. *Nature* **230**, 42-43.

Morgan, W.J. (1972). Deep mantle convection plumes and plate motions. *Am. Assoc. Petr. Geol. Bull.* **56**, 203-213.

Morgan, W.J. (1981). Hotspot tracks and the opening of the Atlantic and Indian oceans, in *The Sea*. C. Emiliani (eds). Wiley Interscience, New York. 443-487.

Nataf, H.C. & J. Vandecar (1993). Seismological detection of a mantle plume. *Nature* **364**, 115-120.

Nunns, A.G. (1983). Plate tectonic evolution of the Greenland-Scotland ridge and surrounding regions, in *Structure and development of the Greenland-Scotland ridge*. M.H.P. Bott et al. (eds). Plenum Press, New York and London. 11-30.

Pálmason, G. (1973). Kinematics and heat flow in a volcanic rift zone, with application to Iceland. *Geophys. J. R. Astron. Soc.* **33**, 451-481.

Pálmason, G. & K. Saemundsson (1974). Iceland in relation to the mid-Atlantic ridge. *Ann. Rev. Earth Planet. Sci.* **2**, 25-50.

Ribe, N.M., U.R. Christensen & J. Theissing (1995). The dynamics of plume-ridge interaction, 1: Ridge-centered plumes. *Earth Planet. Sci. Lett.* **134**, 155-168.

Ritsema, J., H.J. vanHeijst & J.H. Woodhouse (1999). Complex shear wave velocity structure imaged beneath Africa and Iceland. *Science* **286**, 1925-1928.

Rögnvaldsson, S. (1997). The transfer function of the SIL seismic data acquisition system. http://www.vedur.is/~sr/text/resp-html/resp-html.html .

Russell, S.A., T. Lay & E. Garnero (1998). Seismic evidence for small-scale dynamics in the lowermost mantle at the root of the Hawaiian hotspot. *Nature* **396**, 255-258.

Saemundsson, K. (1979). Outline of the geology of Iceland. *Jökull* **29**, 7-28.

Saunders, A.D., M. Storey, R.W. Kent & M.J. Norry (1992). Consequences of plume-lithosphere interactions. *Geol. Soc. Spec. Pub.* **68**, 41-60.

Schilling, J.G. (1973). Iceland mantle plume: geochemical study of Reykjanes ridge. *Nature* **242**, 565-571.

Schilling, J.G. (1991). Fluxes and excess temperatures of mantle plumes inferred from their interaction with migrating midocean ridges. *Nature* **352**, 397-403.

Shen, Y., S.C. Solomon, I.T. Bjarnason & C.J. Wolfe (1998). Seismic evidence for a lower-mantle origin of the Iceland plume. *Nature* **395**, 62-65.

Sheppard, R.M. (1973). NORSAR array mislocations, in *Seismic Discrimination* (Semiannual technical summary). Lincoln Laboratory, Lexington. 12-13.

Sigvaldason, G.E., S. Steinthorsson, N. Oskarsson & P. Imsland (1974). Compositional variation in recent Icelandic tholeiites and the Kverkfjöll hotspot. *Nature* **251**, 579-582.

Slack, P.D., P.M. Davis, W.S. Baldridge, K.H. Olsen, A. Glahn, U. Achauer & W. Spence (1996). The upper mantle structure of the central Rio Grande rift region from teleseismic P and S wave travel time delays and attenuation. *J. Geophys. Res.* **101**, 16003-16023.

Sleep, N.H. (1984). Tapping of magmas from ubiquitous mantle heterogeneities: an alternative to mantle plumes? *J. Geophys. Res.* **89**, 9980-9990.

Sleep, N.H. (1990). Hotspots and mantle plumes: Some phenomenology. *J. Geophys. Res.* **95**, 6715-6736.

Sleep, N.H. (1992). Hotspot Volcanism and Mantle Plumes. *Ann. Rev. Earth. Planet. Sci.* **20**, 19-43.

Smallwood, J.R., R.S. White & R.K. Staples (1998). Deep crustal reflectors under Reydarfjordur, eastern Iceland: crustal accretion above the Iceland mantle plume. *Geophys. J. Int.* **134**, 277-290.

Staples, R.K., R.S. White, B. Brandsdottir, W. Menke, P.K.H. Maguire & J.H. McBride (1997). Faroe-Iceland Ridge Experiment .1. Crustal structure of northeastern Iceland. *J. Geophys. Res.* **102**, 7849-7866.

Steck, L.K. & W.A. Prothero (1991). A 3-D raytracer for teleseismic body wave arrival times. *Bull. Seismol. Soc. Am.* **81**, 1332-1339.

Stefánsson, R., R. Bödvarsson, R. Slunga, P. Einarsson, S. Jakobsdóttir, H. Bungum, S. Gregersen, J. Havskov, J. Hjelme & H. Korhonen (1993). Earthquake prediction research in the south Iceland seismic zone and the SIL project. *Bull. Seismol. Soc. Am.* **83**, 696-716.

Steinbach, V. & D.A. Yuen (1997). Dynamical effects of a temperature- and pressure-dependent lower-mantle rheology on the interaction of upwellings with the transition zone. *Phys. Earth Planet. Inter.* **103**, 85-100.

Thompson, P.E. & P.J. Tackley (1998). Generation of mega-plumes from the core-mantle boundary in a compressible mantle with temperature-dependent viscosity. *Geophys. Res. Lett.* **25**, 1999-2002.

Thorbergsson, G., I.T. Magnusson & G. Palmason (1990). Gravity data and gravity map of Iceland. National Energy Authority, Reykjavík, OS-90001/JHD-01.

Tilmann, F.J., D. McKenzie & K.F. Priestley (1998). P and S wave scattering from mantle plumes. *J. Geophys. Res.* **103**, 21145-21163.

Tryggvason, E. (1964). Arrival times of P-waves and upper mantle structure. *Bull. Seismol. Soc. Am.* **54**, 727-736.

Tryggvason, K. (1981). 3-D mapping of the Iceland hotspot. Ph.D. Thesis, University of Oslo.

Tryggvason, K., E.S. Husebye & R. Stefánsson (1983). Seismic image of the hypothesized Icelandic hot spot. *Tectonophysics* **100**, 94-118.

van der Hilst, R.D., S. Widiyantoro & E.R. Engdahl (1997). Evidence for deep mantle circulation from global tomography. *Nature* **386**, 578-584.

VanDecar, J.C. & R.S. Crosson (1990). Determination of teleseismic relative phase arrival times using multi-channel cross-correlation and least squares. *Bull. Seismol. Soc. Am.* **80**, 150-169.

Vandecar, J.C., D.E. James & M. Assumpcao (1995). Seismic evidence for a fossil mantle plume beneath South-America and implications for plate driving forces. *Nature* **378**, 25-31.

Vogt, P.R. (1983). The Iceland mantle plume: Status of the hypothesis after a decade of new work, in *Structure and Development of the Greenland-Scotland Ridge.* M.H.P. Bott, S. Saxov, M. Talwani and T. J. (eds). Plenum Publishing Corporation, New York. 191-213.

Ward, R.W. & C.-Y. Young (1980). Mapping seismic attentuation within geothermal systems using teleseisms with application to the Geysers - Clear Lake region. *J. Geophys. Res.* **85**, 5227-5236.

Watson, S. & D.P. McKenzie (1991). Melt generation by plumes: A study of Hawaiian volcanism. *J. Petrol.* **12**, 501-537.

Watts, A.B. (1976). Gravity and bathymetry in the central Pacific Ocean. *J. Geophys. Res* **81**, 1533-1553.

Welke, H., G. Moorbath, L. Cumming & H. Sigurdsson (1968). Lead isotope studies on igneous rocks from Iceland. *Earth Planet. Sci. Lett.* **4**, 221-231.

Wen, L.X. & D.V. Helmberger (1998). Ultra-low velocity zones near the core-mantle boundary from broadband PKP precursors. *Science* **279**, 1701-1703.

White, R. & D. McKenzie (1989). Magmatism at rift zones - the generation of volcanic continental margins and flood basalts. *J. Geophys. Res.* **94**, 7685-7729.

White, R.S., J.W. Bown & J.R. Smallwood (1995). The temperature of the Iceland plume and origin of outward- propagating V-shaped ridges. *J. Geol. Soc.* **152**, 1039-1045.

Williams, Q. & R. Jeanloz (1990). Melting relations in the iron-sulfur system at ultra-high pressures - implications for the thermal state of the Earth. *J. Geophys. Res.* **95**, 19299-19310.

Williams, Q., J. Revenaugh & E. Garnero (1998). A correlation between ultra-low basal velocities in the mantle and hot spots. *Science* **281**, 546-549.

Wilson, J.T. (1963). A possible origin of the Hawaiian islands. *Can. J. Phys.* **41**, 863-870.

Wilson, J.T. (1965). Evidence from oceanic islands suggesting movement within the Earth. *Philos. Trans. R. Soc. London* **A25**, 145-165.

Wolfe, C.J., I.T. Bjarnason, J.C. VanDecar & S.C. Solomon (1997). Seismic structure of the Iceland mantle plume. *Nature* **385**, 245-247.

Wysession, M.E. (1996). Continents of the core. *Nature* **381**, 373.

Young, C.-Y. & R.W. Ward (1980). Three-dimensional 1/Q model of the Coso Hot Springs known geothermal resource area. *J. Geophys. Res.* **85**, 2459-2470.

Zandt, G. (1978). Study of three-dimensional heterogeneity beneath seismic arrays in central California and Yellowstone, Wyoming, Massachusetts Institute of Technology.

Zhang, Y.-S. & T. Tanimoto (1991). *Ridges and hotspots: perspectives from global tomography.* Caltech Plume Symposium, Los Angeles.

Zverev, S.M., I.P. Kosminskaya, G.A. Krasilstchikova & G.G. Mikhota (1976). The crustal structure of Iceland and the Iceland-Faroe-Shetland region. *Soc. Sci. Isl.* **Greinar V**, 73-93.

Appendices

APPENDICES

Appendix 1.   SIL SEISMIC STATIONS USED IN THIS STUDY.

Station	Name	Latitude (° N)	Longitude (° E)	Elevation (m)	Comments	Sensor type
ASB	Asbjarnastaðir	64.749	-21.326	110		STS-2
GIL	Gilhagi	66.077	-16.351	141		CMG-3T
GRA	Granastaðir	65.918	-17.578	25		CMG-3T
GRI	Grímsey	66.542	-18.010	36		CMG-3T
GRS	Grímsstadir	65.638	-16.124	390		CMG-3T
HVE	Hveravellir	64.871	-19.559	641		CMG-3T
KRA*	Krafla	65.695	-16.778	437	* removed 1/11/96	CMG-3T
KRO	Krokur	64.098	-21.120	139		CMG-3T
REN*	Reynihlið	65.647	-16.915	344	* installed 15/11/96	CMG-3T
SIG	Siglufjörður	66.132	-18.915	16		CMG-3T
SKR	Skrokkalda	64.560	-18.386	812		CMG-3ESP
VOG	Vogar					

Appendix 2.   EXTRACT OF FILE televents.lib

The earthquake catalogue file `televents.lib` is produced at Veðurstofa Íslands and stored in the directory `/eq/YYYY/teleseism/` for the year `YYYY`. It lists major teleseisms saved and their location in the directory structure. A small sample of the file is reproduced here:

```
TELESEISMIC EVENTS 1996 (from August 14th)

sav : automatically saved
crt : not saved because of criteria
old : not saved because too old
man : manually saved
-----------------------------------------------------------------------------------------------
yyyymoda hhmmss.s latitude longitude depth  M  mL  epicd rem    path         prefix   d Region
-----------------------------------------------------------------------------------------------
19960815 073350.3 -13.2556  166.5339  33.0 6.0 Ms  126.6 sav /1996/aug/15/07:49:00 07:49:00 0 VANUATU ISLANDS
19960819 041915.6  51.4311 -178.4464  33.0 5.7 Mb   61.1 sav /1996/aug/19/04:29:00 04:29:10 0 ANDREANOF ISL, ALEUTEAN IS.
19960819 062411.1 -41.4896   80.2335  10.0 5.9 Ms  129.6 crt                      x        x 9 MID-INDIAN RIDGE
19960820 001102.3  77.9402    7.5805  21.2 5.5 Mb   13.5 sav /1996/aug/20/00:14:00 00:14:00 0 SVALBARD REGION
19960822 053541.8  -7.0634  123.2153 589.8 5.5 Mb  114.6 crt                      x        x 9 BANDA SEA
19960822 014455    53.14    -35.31    10.0 4.7 Mb   12.7 man /1996/aug/22/01:47:00 01:47:50 0 NORTH ATLANTIC OCEAN
19960823 215605.1  -4.2036 -104.3136  10.0 5.5 Ms   90.4 sav /1996/aug/23/22:08:00 22:08:50 0 CENTRAL EAST PACIFIC RISE
19960827 105050.0 -36.8726   78.0973  10.0 5.9 Ms  124.8 crt                      x        x 9 MID-INDIAN RIDGE
19960828 160145.6 -10.5377  161.2646  33.0 5.5 Mb  124.0 crt                      x        x 9 SOLOMON ISLANDS
19960828 063050     1.04    -28.18    10.0 4.9 Mb   62.8 man /1996/aug/28/06:40:00 06:40:00 0 CENTRAL MID-ATLANTIC RIDGE
19960829 062207    73.52      5.68    10.0 4.6 Mb   10.5 man /1996/aug/29/06:24:00 06:24:00 0 GREENLAND SEA
19960831 204722.9  51.4122 -178.2263  62.6 5.8 Mb   61.1 sav /1996/aug/31/20:57:00 20:57:20 0 ANDREANOF ISL. ALEUTEAN IS.
19960901 064541.3 -11.8277  166.5654 186.3 5.5 Mb  125.2 crt                      x        x 9 SANTA CRUZ ISLANDS
19960902 204153.2  12.5500  143.7100  33.0 5.7 Ms   99.7 sav /1996/sep/02/20:55:00 20:55:20 0 SOUTH OF MARIANA ISLANDS
```

Appendix 3.   HOTSPOT NETWORK STATIONS

Station	Name	Lat (°N)	Lon (°E)	Elev (m)	N_{mag} (°)	Comments	Sensor type	Power source
HOT01	Reykir	64.494	-21.168	205	340	Sensor on concrete floor of unused barn at abandoned farm. Possibly gravel between floor and bedrock.	CMG-3ESP	Mains
HOT02	Ásbrún	64.746	-22.232	40	339	Sensor in shallow hole, on bedrock, behind a farmhouse. DAS in basement/garage.	CMG-3ESP	Mains
HOT03	Ingjaldshóll	64.908	-23.853	35	338	Sensor & DAS in mortuary near to church on hill.	CMG-40T	Mains
HOT04	Ormsstaðir	65.181	-22.423	40	339	Sensor & DAS in old milk dairy.	CMG-3ESP	Mains
HOT05	Brú	65.110	-21.096	35	340	Sensor & DAS in basement of apartment block. Possible sources of noise nearby (road, generator, gas station, river).	CMG3-ESP	Mains
HOT06	Hólmavík	65.705	-21.678	25	339	Sensor & DAS in basement of house. Base of cement on bedrock.	CMG-3ESP	Mains
HOT07	Eyri	65.598	-22.510	40	338	Sensor on bedrock in unfinished basement of summerhouse.	CMG-3ESP	Mains
HOT08	Ólafsviti	65.610	-24.161	8	337	Sensor on cement floor in lighthouse, directly on top of bedrock.	CMG-3ESP	Mains
HOT09	Þingeyri	65.874	-23.486	50	338	Sensor on bedrock in unfinished basement of family house.	CMG-3ESP	Mains
HOT10	Reykjanesskóli	65.927	-22.428	7	338	Sensor on bedrock in small concrete shed, in hole in concrete floor.	CMG-3ESP	Mains
HOT 11	Bóðvarshólar	65.423	-20.722	108	340	Sensor on concrete floor of abandoned mink house, now used as workshop. Floor is concreted onto fractured basalt.	CMG-3T	Mains
HOT 12	Hávík	65.671	-19.600	38	340	Sensor on concrete floor of garage of summerhouse. Rock beneath was dynamited to build garage; layer of gravel is beneath the cement.	CMG-3T	Mains
HOT 13	Súlur	65.686	-18.100	24	341	Sensor on isolated cement pillar constructed for WWSSN seismometer station, in basement of police station.	CMG-3T	Mains
HOT 14	Hólsgerði	65.303	-18.257	245	341	Sensor on cement floor of basement of deserted farmhouse. House built on massive landslide of huge boulders. No bedrock in this valley.	CMG-3ESP	Mains
HOT 15	Finnafjörður	66.121	-15.172	20	343	Sensor on concrete floor of family house, on spot where concrete was poured directly on bedrock or v. large boulder. Little bedrock in this area.	CMG-3ESP	Mains

HOT 16	Borgarfjorður-eystri	65.541	-13.754	5	344	Sensor on concrete floor in wooden shack at harbour. Floor was poured directly onto bedrock without gravel layer in between.	CMG-3ESP	Mains
HOT 17	Setberg	65.255	-14.504	80	343	Sensor on bedrock exposed in basement of family house.	CMG-3ESP	Mains
HOT 18	Grund	65.166	-15.309	342	343	Sensor on concrete floor in basement of uninhabited farmhouse. No bedrock in valley.	CMG-3ESP	Mains
HOT 19	Fell	64.812	-14.100	50	344	Sensor in pit cemented onto bedrock, behind abandoned mink shed.	CMG-3ESP	Mains
HOT 20	Hagi	64.288	-15.139	15	344	Sensor on exposed bedrock in basement of farmhouse.	CMG-3ESP	Mains
HOT 21	Fagurhólsmýri	63.877	-16.641	20	343	Sensor on bedrock in corrugated iron lean-to built up against a basalt cliff. DAS in disused store nearby.	CMG-3ESP	Mains
HOT 22	Hunkubakkar	63.770	-18.131	65	342	Sensor on bedrock in large barn in farmyard.	CMG-3ESP	Mains
HOT23	Grímsfjall	64.407	-17.266	1730	342	Sensor standing on cement pad poured onto tuff just outside mountain refuge hut. 8 solar panels installed, 6 connected. DAS inside hut.	CMG-3ESP	Solar panels, 12V batteries
HOT 24	Snæfell	64.887	-15.354	600	343	Sensor on bedrock in pit dug down to bedrock in outcrop by river. DAS in mountain refuge hut nearby. 6 solar panels installed.	CMG-3ESP	Solar panels, 12V batteries
HOT 25	Askja	65.054	-16.652	920	343	Sensor on cement pad on hard tuff 50 m from Dyngja hut. Softer tuff cut away to harder tuff below.	CMG-40T	Solar panels, 12V batteries
HOT 26	Laugafell	65.029	-18.332	740	342	Sensor on concrete pad poured onto tuff layer about 1 m deep behind new house at Laugafell. DAS in attic.	CMG-3ESP	Solar panels, 12V batteries
HOT 27	Blöndulón	65.200	-19.590	450	341	Sensor on lowest floor of concrete building containing control equipment for emergency overspill dam of Blöndulón. Building was cemented to massive bedrock for dam engineering purposes.	CMG-3ESP	Mains
HOT 28	Leppistungur	64.532	-19.484	600	341	Sensor in pit dug down to bedrock behind refuge hut. 6 solar panels installed.	CMG-40T	Solar panels, 12V batteries
HOT 29	Vatnsdalsgerði	65.728	-14.838	60	341	Sensor on concrete floor of turf potato store. Floor was poured onto bedrock in corner where sensor is placed.	CMG-40T	Mains
HOT 30	Veðurstofa	64.130	-21.900	50	340	Sensor in seismometer vault in basement of Veðurstofa Íslands building.	CMG-3ESP	Mains

Appendix 4. EQUIPMENT LIST FOR HOTSPOT STATIONS

"Standard" Station	Tiles
Seismometer (Guralp CMG-3ESP, CMG-3T or CMG-40T)	Plastic sheet
Seismometer cable (coloured, 5 m)	Small bucket
DAS 24-bit data logger (REFTEK Data Acquisition System)	Insulation jacket
DAS power cable (grey, 2 m)	Breakout box enclosure
DAS cable (grey twin, 5 m)	Battery clamps
Power supply	Drain pipe
60 Amp hr lead-acid battery	Insulating tape
Power board	Mains plug
2 battery cables (grey, 1 m)	
Disk	**Additional equipment for "highland" station:**
SCSI cable (black, 0.5 m)	6 30 Watt solar panels & associated cables
Disk power cable (grey, 0.5 m)	Bank of 8 150 Amp hr lead-acid batteries
GPS clock	Wooden crate for batteries
GPS cable (grey, 6 m)	Insulation for batteries
Breakout box with 3mm Allen wrench	
Large bucket	

Appendix 5.   STATION SETUP INSTRUCTIONS

1. Vault	
a)	Dig pit on a slope about 0.75 m deep to bedrock.
b)	Pour cement pad, smooth it, draw magnetic north line and affix tile.
c)	Install drain pipe downhill to surface.
d)	Install vault wall (large bucket). Run blue seismometer cable out (through hole in wall of bucket). Fill around outside of wall with dirt.

2. Power	
a)	Connect power supply to "BATTERY" terminal strip on power board. Both black & white wires to board's white wire. Both red wires to board's red wire.
b)	Connect battery to same terminal on power board, in parallel with power supply. Black wire to board's white wire. Red wire to board's red wire.
c)	Connect DAS power cable (2m grey) to "STATION" strip on power board. Black wire to board's brown wire. Red wire to board's orange wire.
d)	Attach 5 m double grey cable to "STATION" strip o power board. Black wire to board's brown wire. White wire to board's orange wire.
e)	Plug power supply into mains.

3. Seismometer	
a)	Position seismometer on tile with brass pointer oriented to magnetic north.
b)	Unlock seismometer feet by turning brass screws anticlockwise. Level the seismometer. Lock the adjustable feet. Check north orientation again.
c)	Connect single cable (blue, yellow or grey) to seismometer. Fasten cable so a pull won't move seismometer. Recheck seismometer level.
d)	Unlock masses. Replace O-rings and plugs.
e)	Plug other end of single (blue) cable into "SENSOR" port on breakout box.
f)	Plug double grey cable into "RECORDER" port on breakout box.
g)	Plug double grey cable into "POWER" port on breakout box.
h)	Connect breakout box "CONTROL" port to Guralp control box using control box cable.
i)	Centre seismometers for each channel using knob and switch on control box. Set left-hand knob in turn to V, N/S and E/W and flick "MASS CNTR" switch.
j)	Disconnect control box from breakout box. Close "CONTROL" port on breakout box with spare connector on double grey cable.
k)	Fasten insulation to small bucket, invert and place over sensor.
l)	Close vault.
m)	Shelter breakout box in plastic enclosure with drainage.

4. DAS	
a)	Using grey cable, connect power from DAS (either power port) to disk.
b)	Using black SCSI cable, make data connection between DAS and disk (either SCSI port).
c)	Situate GPS clock/antenna for clear view of sky and connect to "COMM" port on DAS using grey GPS cable.
d)	Connect single grey cable that was attached to power board to free power port on DAS.
e)	Attach black connector on double grey cable into "CH. 4-6" socket on DAS.

5. Loading parameters into DAS and acquisition startup
a) Load parameters from, or check pre-set parameters in EHT terminal against, those on printed sheet.
b) Plug in EHT to DAS and perform the following operations:
COMMNCTNS/SEND PRMS/YES
UTILITIES/NEXT MENU/FRMT SCSI/DISK/YES
NEXT MENU/CLEAR RAM/YES
PREV MENU/SYS RESET/YES
TIME   check time is correct
MONITOR/2/{4|5|6} stomp test
COMMNCTNS/START ACQ/0/0/YES

Appendix 6.   STANDARD EHT PARAMETERS FOR HOTSPOT PROJECT

Station						
Experiment name	HOTSPOT					
Station number	number from coloured map					
Station name	farm or place name					
Operation mode	CP & SC					
Channel	1	2	3	4	5	6
Channel name	Deactivated			Z	N	E
Azimuth				0	0	90
Inclination				90	0	0
Preamp				1	1	1
Sensor model				3ESP or 40T or 3T (see top of seismometer)		
Sensor serial no.				Serial number from top of seismometer		
Data Stream	1	2	3			
Stream name	**20sps**	**1sps**	**trg100sps**			
Channel #s	4,5 & 6	4,5 & 6	4,5 & 6			
Sample rate	20	1	100			
Data form	CO	CO	CO			
Trigger type	CON	CON	EVT			
Trigger parameters						
Trigger channel(s)			4			
Pre-trigger length			5			
Record length	1200	28800	30			
Sta lngth			0.2			
Lta lngth			30			
Mean removal			10			
Trigger rate			8			
Lta hold			Active			
Calibration						
Start time	1996<ret>next day ending in 0 or 5 <ret> 07<ret>30<ret>00<ret>					
Rep interval	5 days					
# of calibrations	0 (means infinite)					
Record length	5					
Step function						
Step	On					
Interval	90					
Step size	91					
Amplitude	0.1					
Out	COIL					

Appendix 7.   CLOCK CORRECTIONS
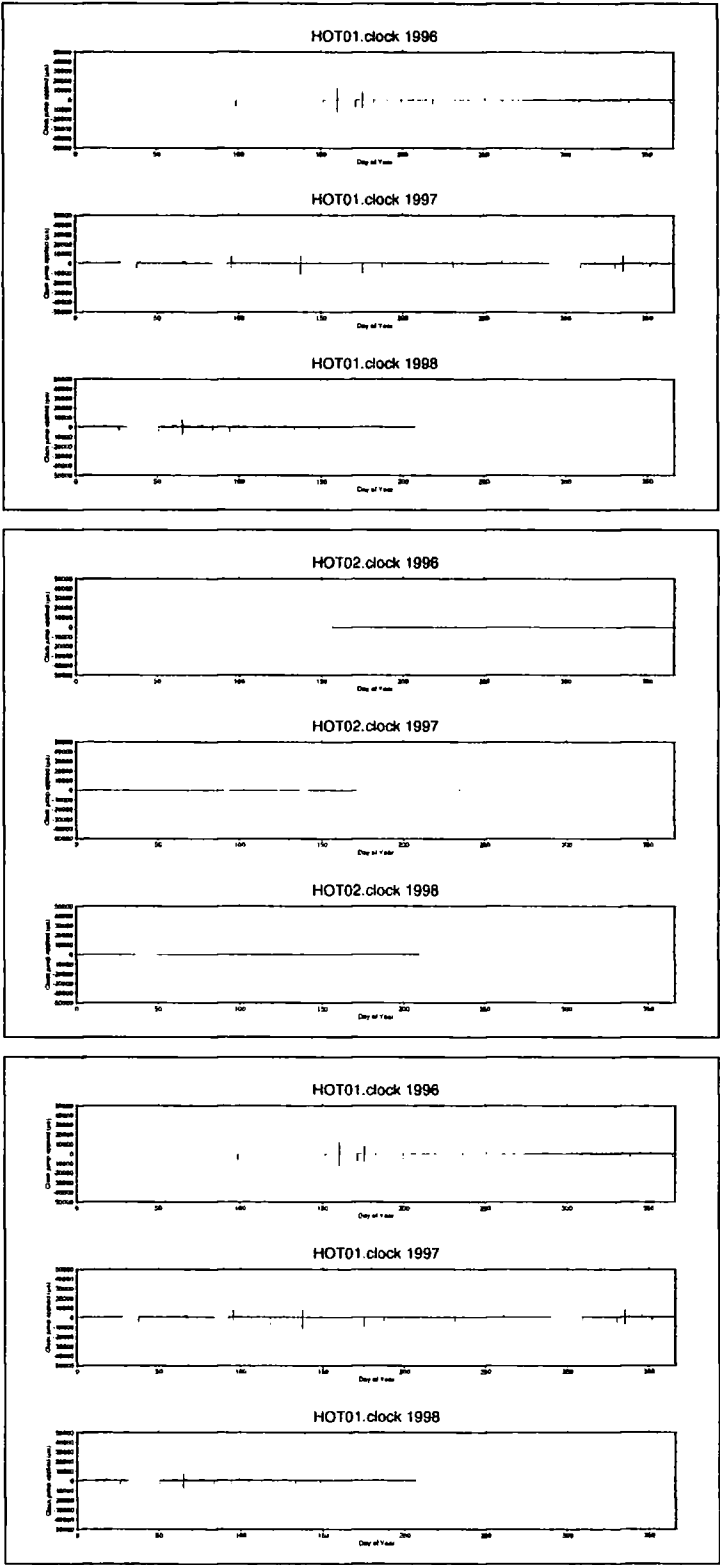
Clock corrections for stations HOT01, HOT02 & HOT03. Graphs show the "time jerk" applied to the internal clock of the DAS computer to re-synchronise it with that of the GPS system.
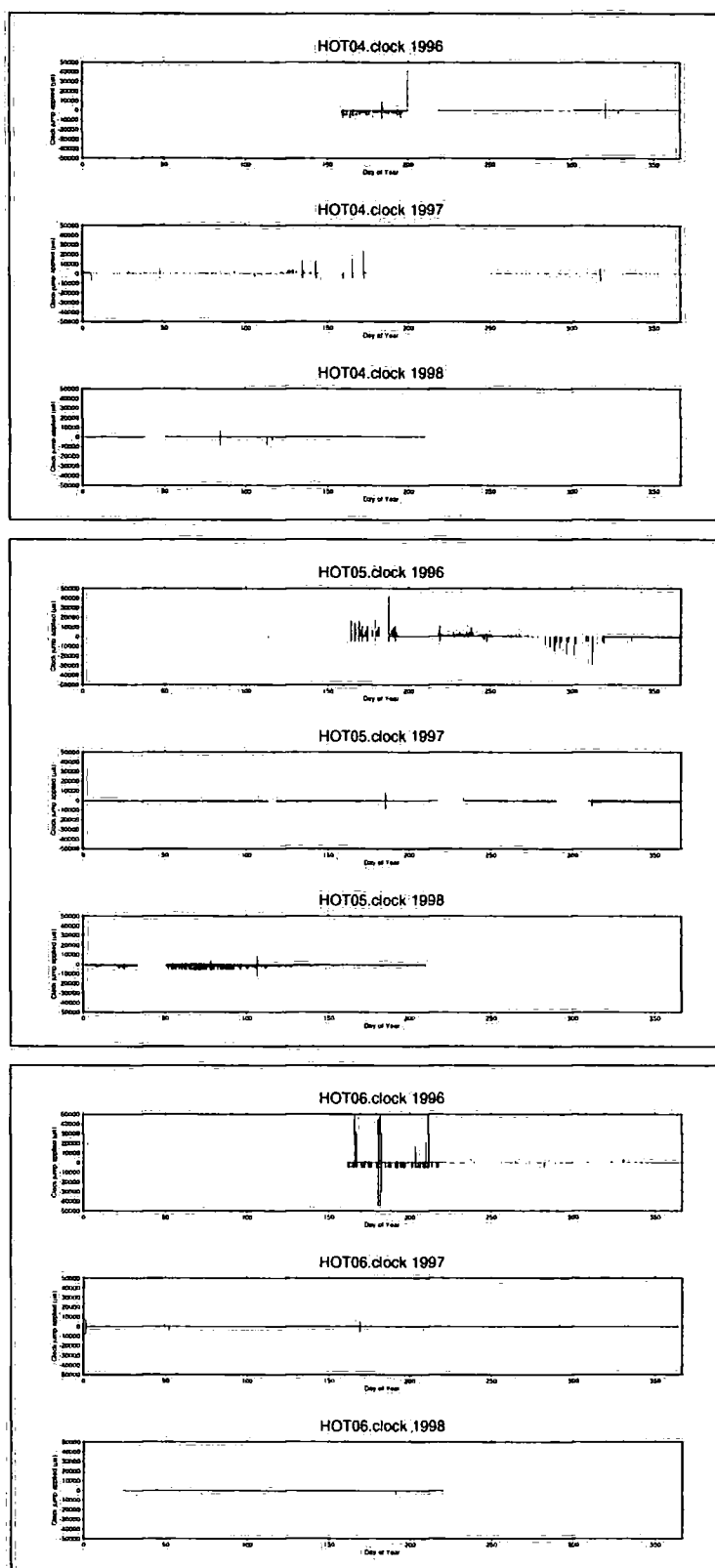
Clock corrections for stations HOT04, HOT05 & HOT06
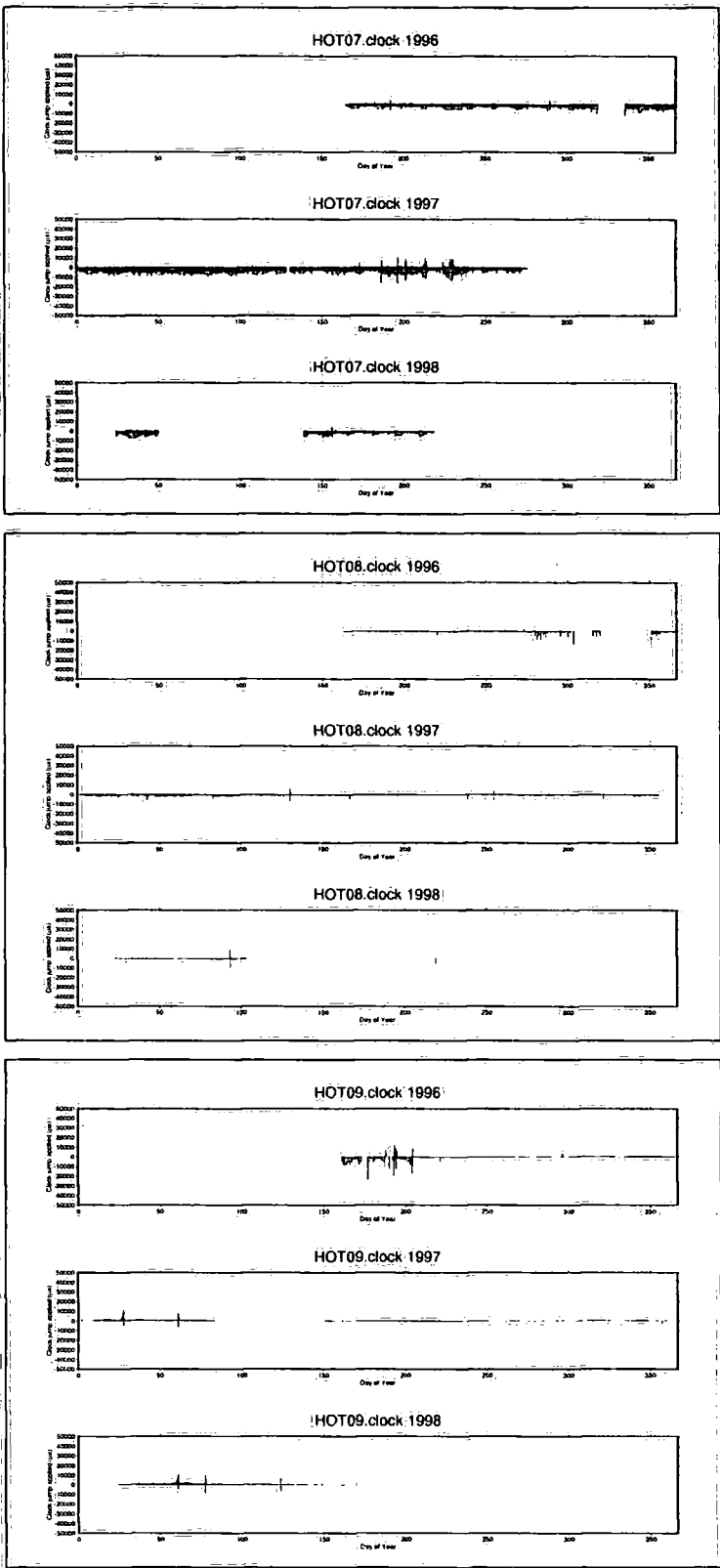
Clock corrections for stations HOT07, HOT08 & HOT09
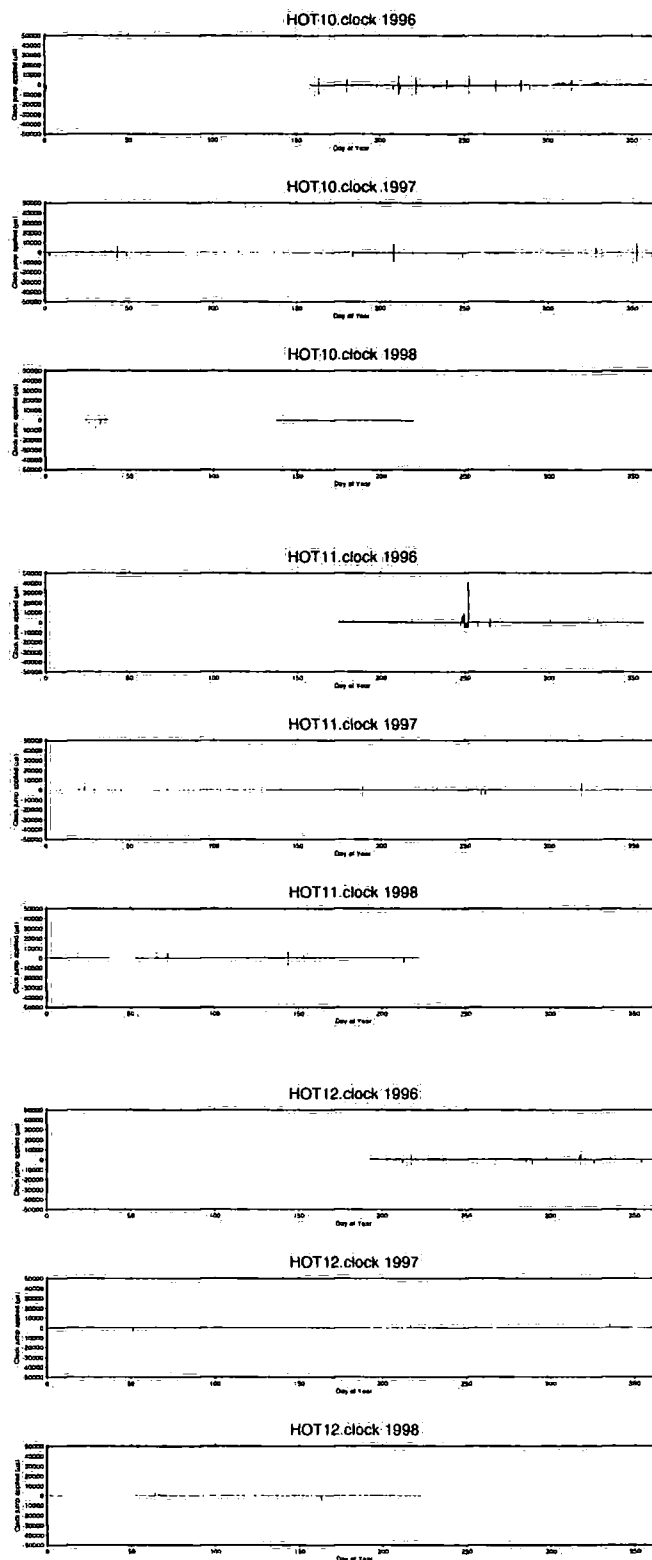
Clock corrections for stations HOT10, HOT11 & HOT12
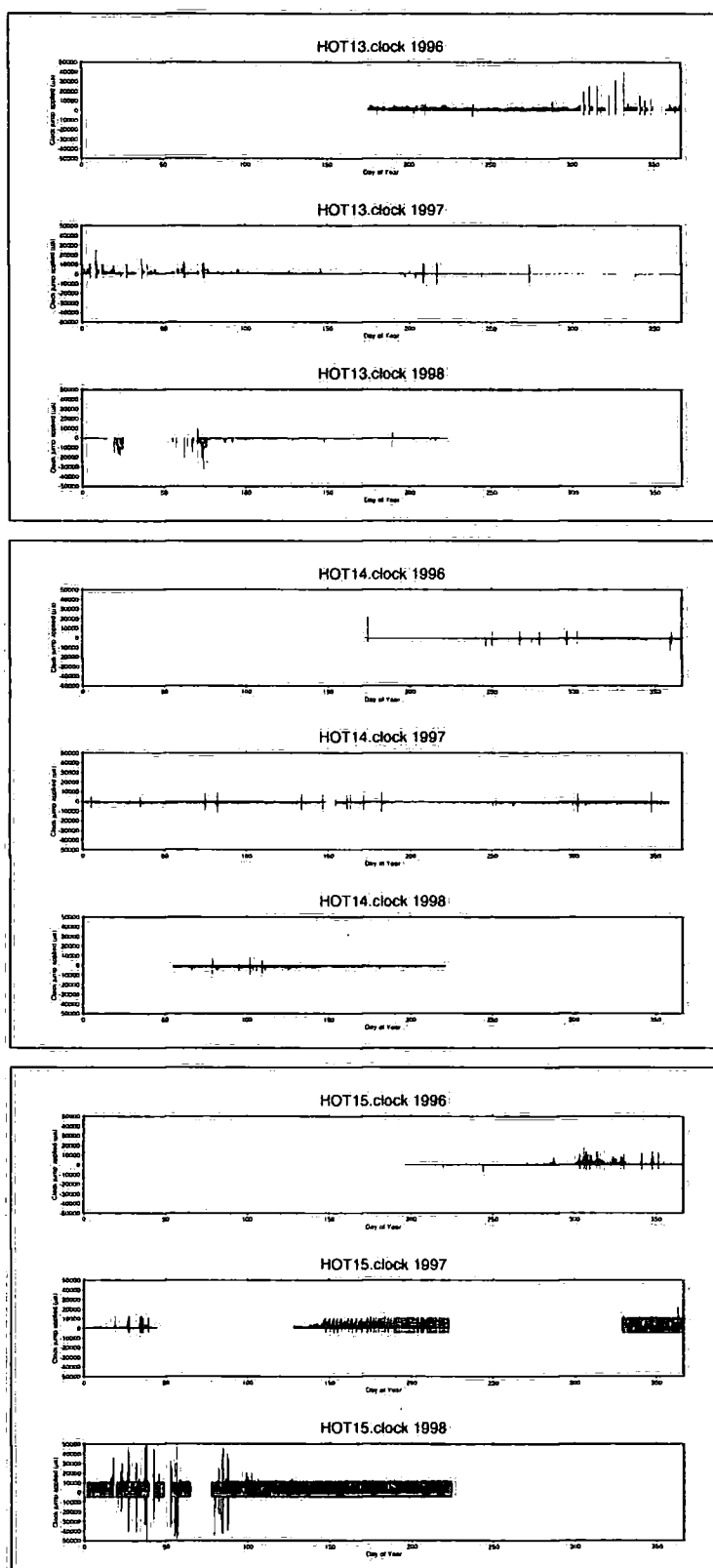
Clock corrections for stations HOT13, HOT14 & HOT15
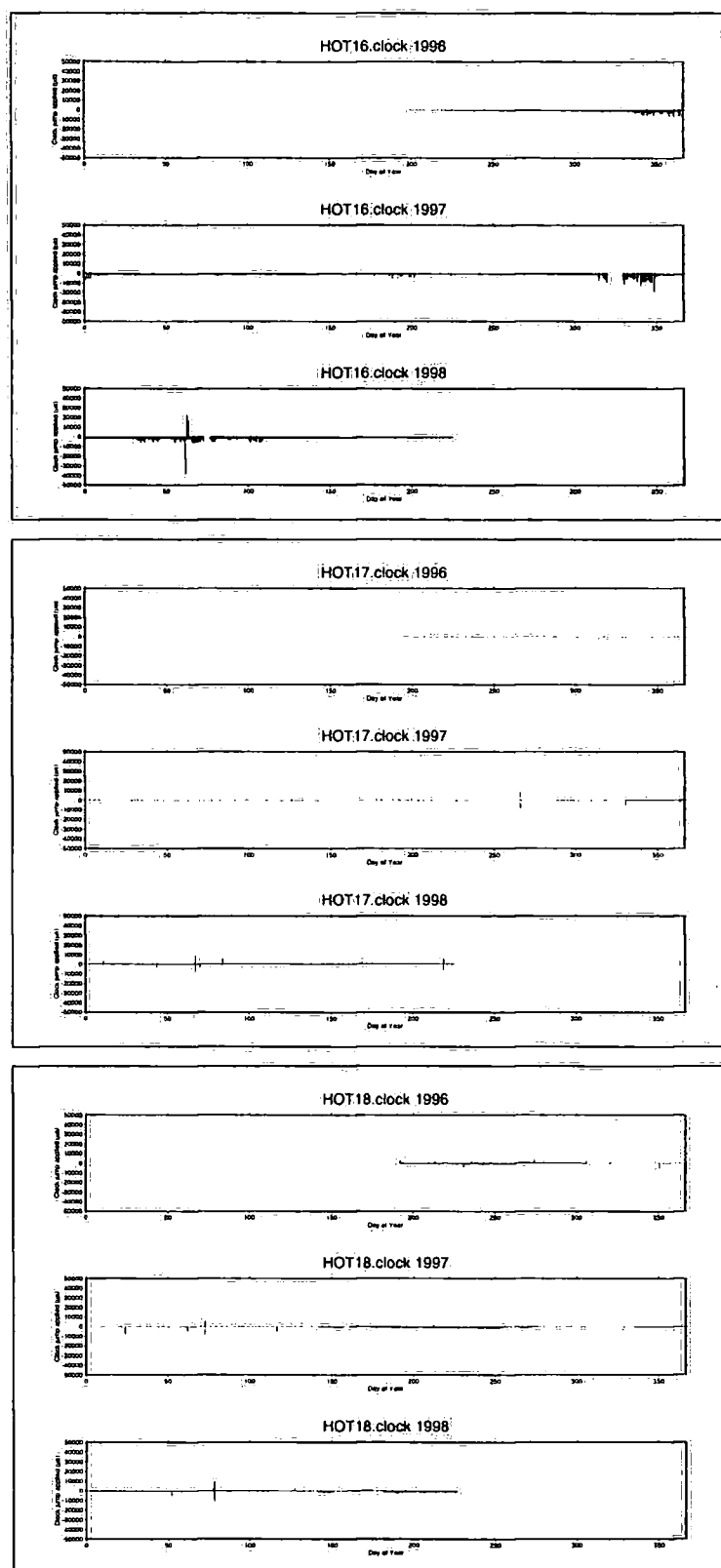
Clock corrections for stations HOT16, HOT17 & HOT18
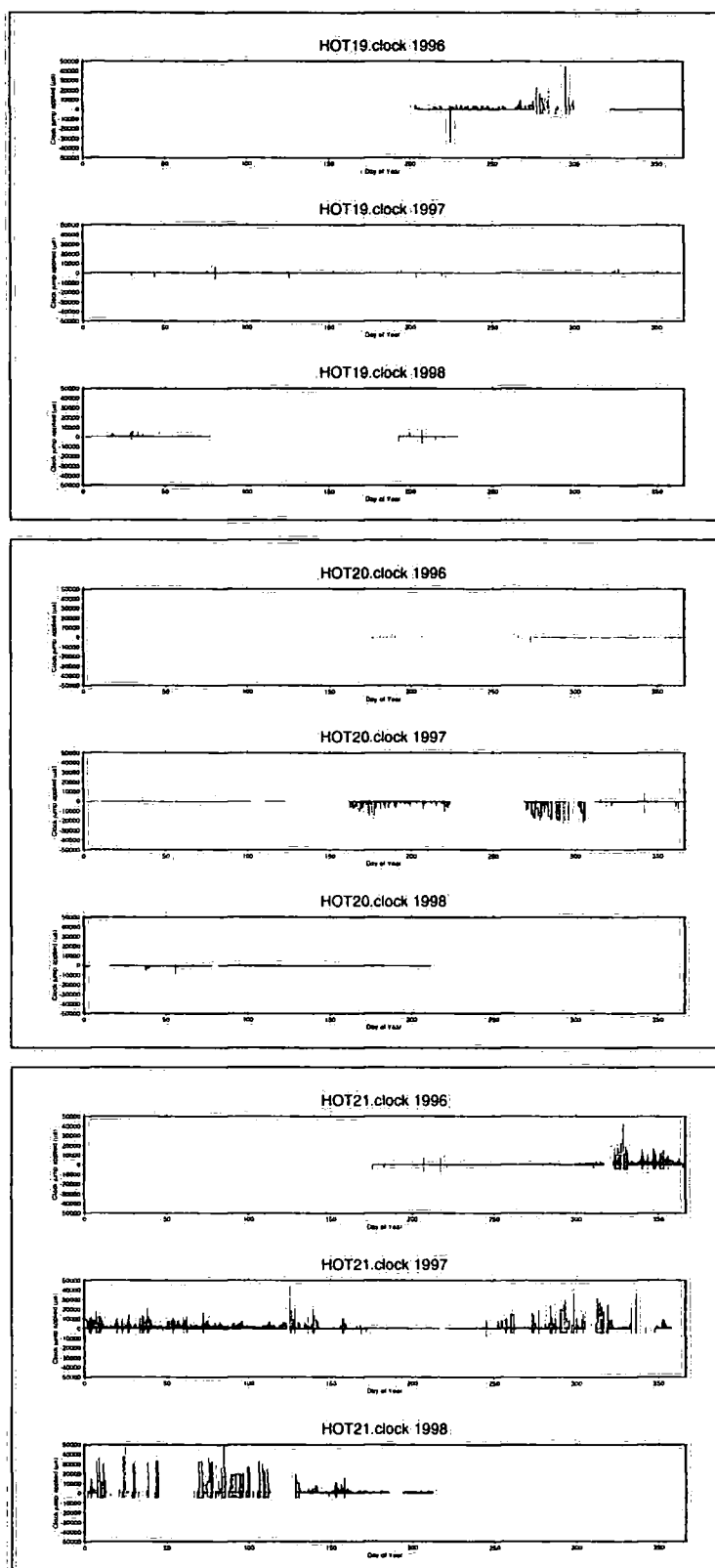
Clock corrections for stations HOT19, HOT20 & HOT21
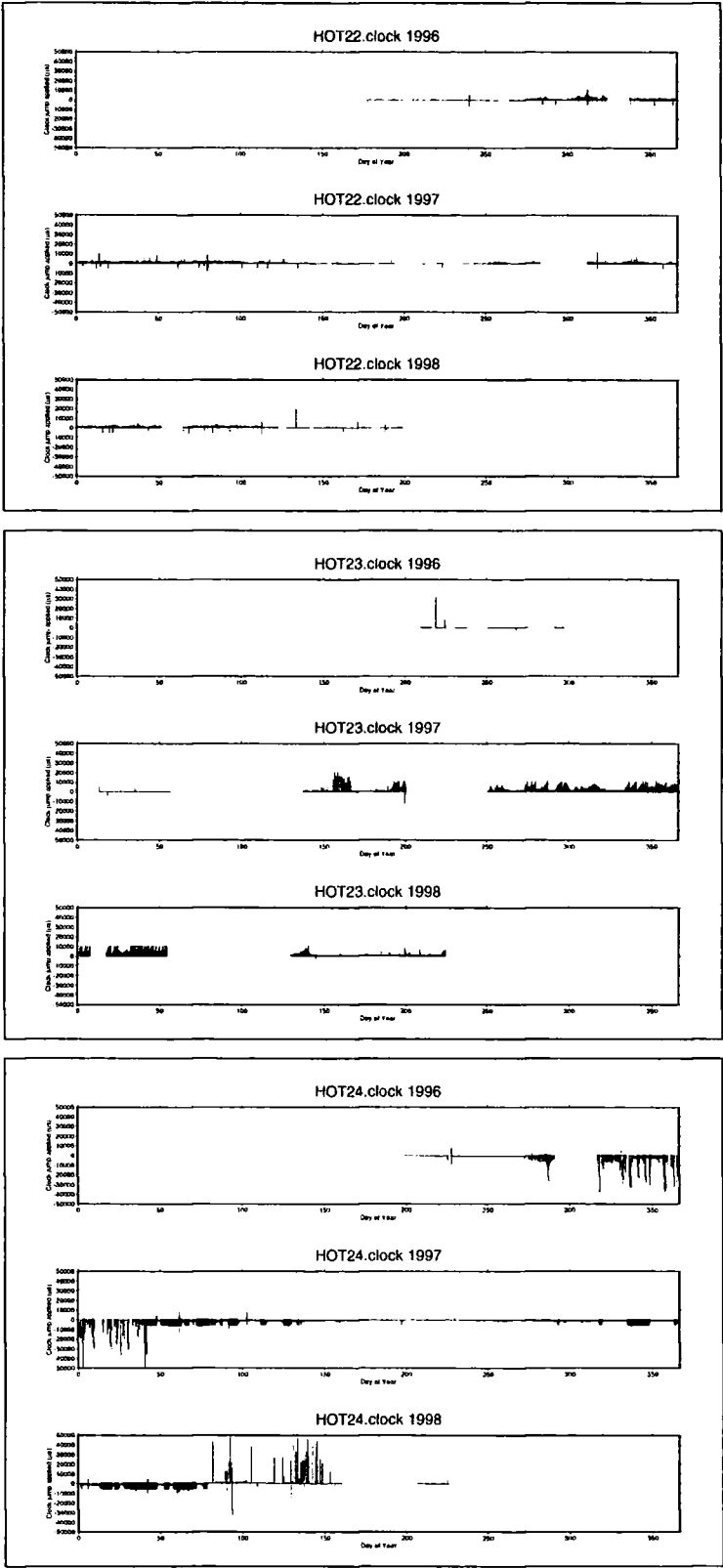
Clock corrections for stations HOT22, HOT23 & HOT24
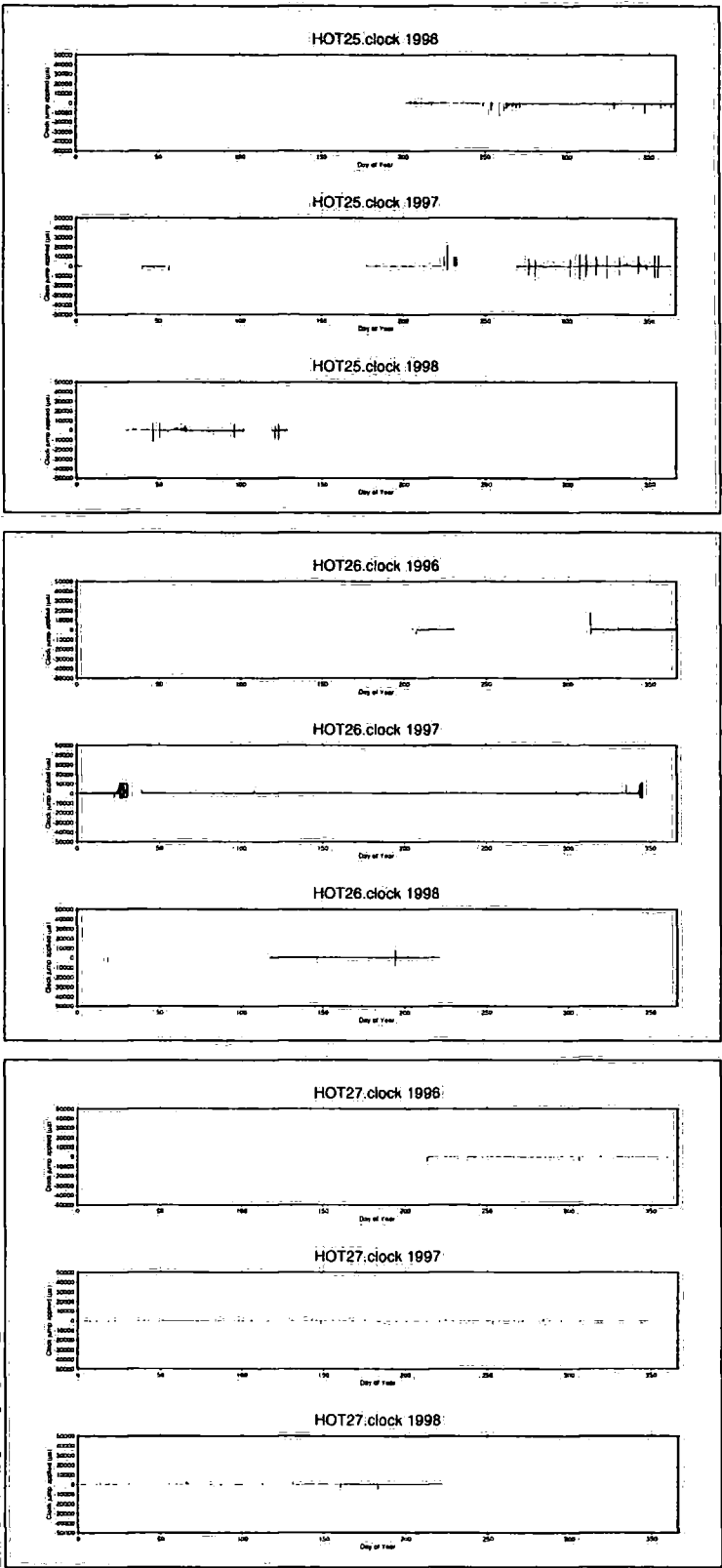
Clock corrections for stations HOT25, HOT26 & HOT27
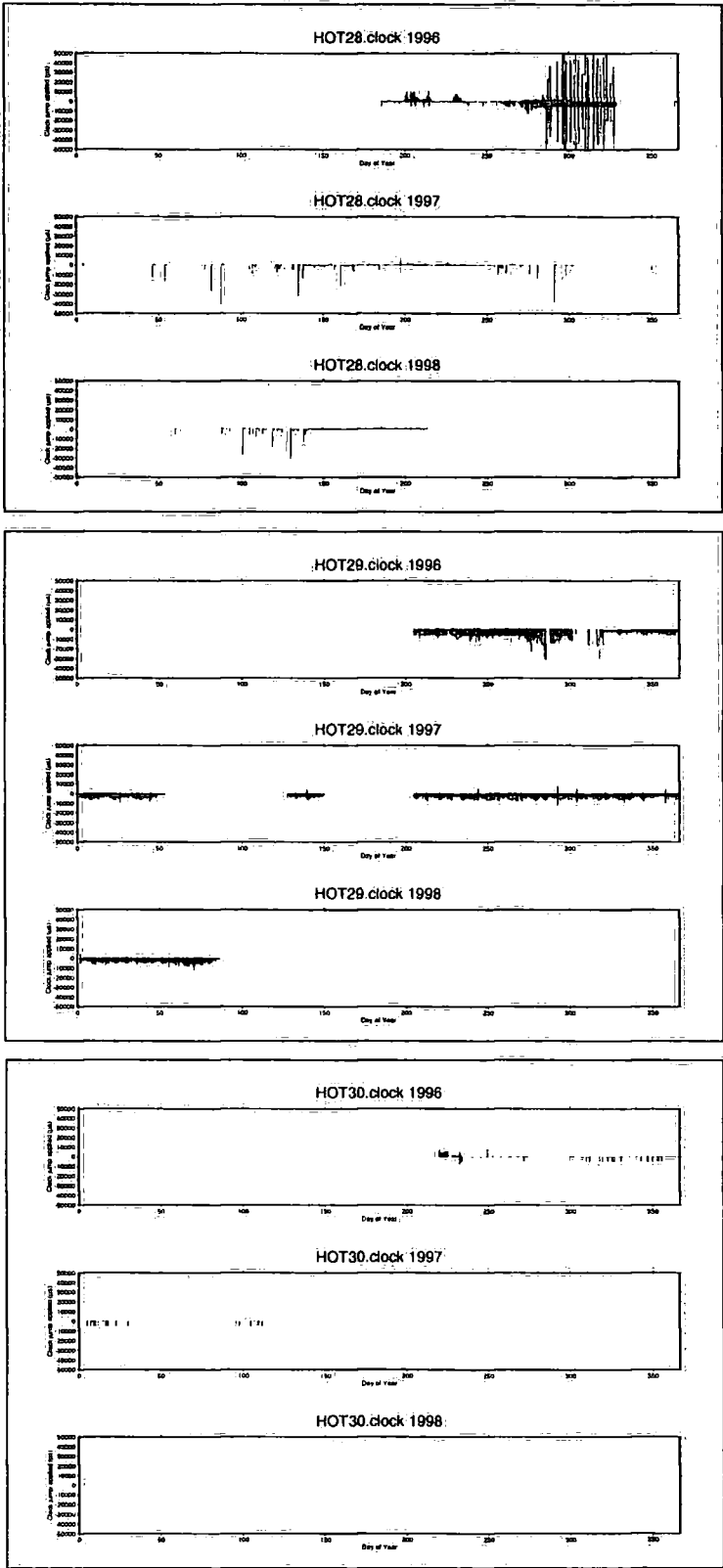
Clock corrections for stations HOT28, HOT29 & HOT30

Appendix 8.   PERL SCRIPT *tocsearch.pl*

This script was used to create lists of files to be extracted from tape using the table-of-contents file at the start of each HOTSPOT event tape.

```
#!/usr/local/perl/bin/perl
#Written by Matt Pritchard
#Check for 2 command line arguments:
#day in EYYYY.DDD
#time (directory) in HHMMSS format.

if (@ARGV < 2 ) {
die "Usage: $0 EYYYY.DDD HHMMSS\n";
}

$syearday=$ARGV[0];
$stime=$ARGV[1];
$tocno=0;
$n=0;
$i=0;

#Array containing names of HOTSPOT stations
@mfiles = (    'HOT01','HOT02','HOT03','HOT04','HOT05','HOT06',
          'HOT07','HOT08','HOT09','HOT10','HOT11','HOT12',
          'HOT13','HOT14','HOT15','HOT16','HOT17','HOT18',
          'HOT19','HOT20','HOT21','HOT22','HOT23','HOT24',
          'HOT25','HOT26','HOT27','HOT28','HOT29','HOT30'
          );

#Initialise flag labelling missing files
foreach(@mfiles) {
$missing{$_}=1;
}

#Open & read in lines of file "toclist"
#containing names of tape toc files.
open(TOCLIST,"EVENT_TAPES\/toclist");
@toclist=<TOCLIST>;
close(TOCLIST);

#Find relevant toc files to search:
#File daylist contains filenames, one per line
#of "day" files, which list
#one per line, the days covered by that tape.
open(DAYLIST,"EVENT_TAPES\/daylist");
while(<DAYLIST>) {
chop;
$dayfile=$_;
open(DAYFILE,"EVENT_TAPES\/$dayfile");
while(<DAYFILE>) {
        $dayline=$_;
        @dayfields=split(/:/,$dayline);
        $dyear=$dayfields[0];
        $dday=$dayfields[1];
        chop($dday);
        if(substr($syearday,1,4) == $dyear && substr($syearday,6,3) ==
$dday) {
                push(@uselist,$toclist[$i]);
                push(@usenos,$i+1);
        }
        $n++;
}
$i++;
}

#Match yearday & time; print matching files
$i=0;
foreach (@uselist) {
chop;
$tocfile=$_;
#print "$tocno\t$tocfile\t$syearday\t$stime\n";
open(TOCFILE,"EVENT_TAPES\/$tocfile");
```

```
        while(<TOCFILE>) {
            if (/$syearday/ && /$stime/) {
                    $line=$_;
                    @fields=split(/\//,$line);
                    if ($fields[1] == $stime && !/HOT31/) {
                            $file=substr($fields[3],0,5);
                            $missing{$file}=0;
                            print STDERR
"$usenos[$tocno]\t$tocfile\t$file\t$missing{$file}\t$line";
                            print STDOUT "$usenos[$tocno]\t$line";
                    }
            }
        }
        close(TOCFILE);
        $tocno++;
        }

        foreach(@mfiles) {
        if($missing{$_}) {
                print STDERR "Missing $_\n";
                print STDOUT "Missing $_\n";
        }
        }
```

Appendix 9.   PERL SCRIPT *dbrot.pl*

This script constructed commands for ahrotate, using sensor orientation information stored in the files dbname.sensor and dbname.instrument to ensure that seismograms were rotated using the appropriate correction for local magnetic north.

```
#!/usr/local/perl/bin/perl
#dbrot.pl
# Rotate seismograms from station (zne) to source (zrt) coordinates
#using file listing in dbname.wfdisc, epicentre info in dbname.origin

if (@ARGV < 3 ) {
        die "Usage: $0 dbname orid silpref\n";       #Must have 3
arguments: dbname orid and SIL prefix
    }


    #Arguments:
    $dbname = $ARGV[0];       #database name
    $orid = $ARGV[1];         #origin id (for lookup in dbname.origin)
    $silpref = $ARGV[2];      #prefix of SIL data filenames (prevents unwanted
files getting rotated)

    #Get EQ origin from dbname.origin

    open(ORIGIN,"$dbname.origin");
    while (<ORIGIN>) {
            @ofields = split;
            if ($ofields[4] == $orid) {                #Split origin line into
fields
                    $olat = $ofields[0];
                    $olon = $ofields[1];
            }
    }
    close(ORIGIN);

    open(SITE,"$dbname.site");
    while (<SITE>) {
    @sfields = split;
    $sta    = $sfields[0];

    #Decide whether the station is a hotspot or SIL station:

    if ($sta =~ /HOT/ ) {
            $HOT = 1;
```

```
                    $SIL = 0;
        } else {
                    $HOT = 0;
                    $SIL = 1;
        }

        #For HOTSPOT stations, NS sensor is aligned with Nmag, so look up
declination
        #for each stn in $DIR_HOT/HOTSPOT.sitechan, channel 5 (N):

        if($HOT) {
                    open(SITECHAN,
"/usr/local/seismic/hotspot/pritchard/hotspot/HOTSPOT.sitechan");
                    while (<SITECHAN>) {
                            @sitechanfields = split;
                            if (/$sta/ && $sitechanfields[1] == 5) {
                                    $hang{$sta} = $sitechanfields[7];
                            }
                    }
                    close (SITECHAN);
        } else {
                    $hang{$sta} = 0.0;
        }

        #Get channels, dir & filenames from wfdisc

        open(WFDISC,"$dbname.wfdisc");
        while (<WFDISC>) {
                    if (/$sta/) {
                            @wffields = split;
                            $chan = $wffields[1];
                            $dir  = $wffields[15];
                            $dfile= $wffields[16];
                            if($SIL && $dfile=~/$silpref/ || $HOT) {
                                    if ($chan == 4 || $chan eq "Z") {
                                            $zfile  = $dfile;
                                    } elsif ($chan ==5 || $chan eq "N") {
                                            $nfile = $dfile;
                                    } elsif ($chan ==6 || $chan eq "E") {
                                            $efile = $dfile;
                                    }
                            }
                    }
        }

        if($HOT) {
                    $zchan = 4;
                    $nchan = 5;
                    $echan = 6;
        } else {
                    $zchan = "Z";
                    $nchan = "N";
                    $echan = "E";
        }

        print "cat $dir/$zfile $dir/$nfile $dir/$efile | ahorient -chan $zchan
$nchan $echan -north $hang{$sta} -verbose |
/home/alice/julian/bin/sun4/ahrotate -ep $olat $olon -verbose -outchan ZRT >
$dir/$sta.rot\n";
        print "splitzrt $dir/$sta.rot\n";
        print "\\rm $dir/$sta.rot $dir/$sta.rot.Z\n\n";
        }
```

Appendix 10.   IASP91 EARTH MODEL

P- and S-wave velocities in the IASP91 standard Earth model (Kennet & Engdahl, 1991) are shown below to a depth of 700 km:
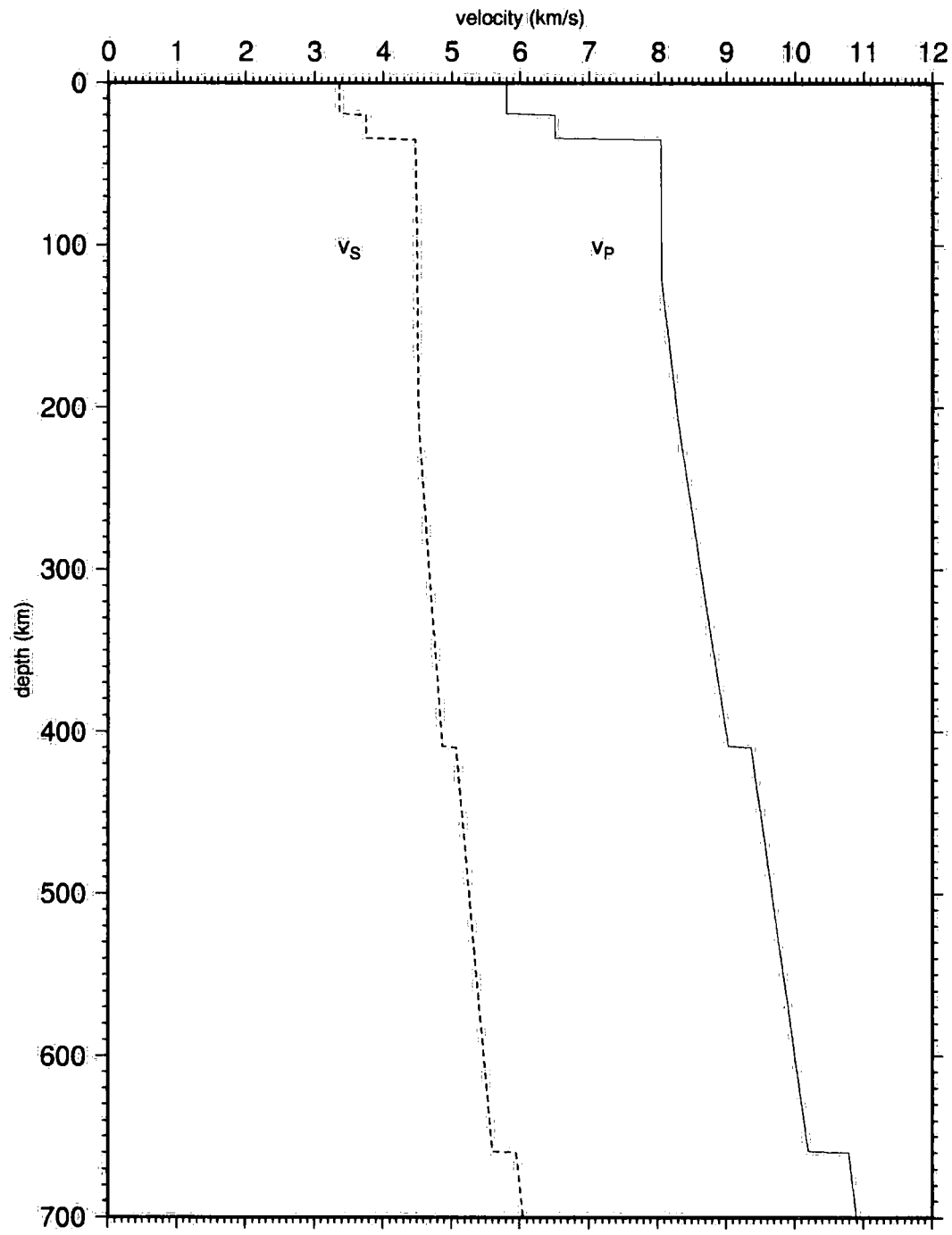
Appendix 11. TYPICAL LOG FILE ENTRY

The following extract of clock-related entries in a log file lists the times at which the GPS clock was locked, and the associated clock "jumps" which were then applied to the internal clock of the DAS recording instrument.

```
State of Health  96:171:23:47:39:197   ST: 0472
171:23:47:39 INTERNAL CLOCK PHASE ERROR OF 198 USECONDS
171:23:47:39 POSITION: N64:29:34.56 W021:10:07.20
171:23:52:09 EXTERNAL CLOCK IS UNLOCKED
171:23:52:20 NO EXTERNAL CLOCK INPUT
172:00:40:04 EXTERNAL CLOCK IS UNLOCKED
172:00:41:22 EXTERNAL CLOCK IS LOCKED
172:00:41:22 INTERNAL CLOCK PHASE ERROR OF 148 USECONDS
172:00:41:22 POSITION: N64:29:40.80 W021:09:59.14
172:00:42:12 EXTERNAL CLOCK IS UNLOCKED
172:00:44:00 EXTERNAL CLOCK IS LOCKED
172:00:44:00 INTERNAL CLOCK PHASE ERROR OF -15 USECONDS
172:00:45:28 EXTERNAL CLOCK IS UNLOCKED
172:00:48:27 EXTERNAL CLOCK IS LOCKED
172:00:48:27 INTERNAL CLOCK PHASE ERROR OF 14 USECONDS
172:00:52:57 EXTERNAL CLOCK IS UNLOCKED
172:00:53:08 NO EXTERNAL CLOCK INPUT
172:01:40:04 EXTERNAL CLOCK IS UNLOCKED
172:01:41:38 EXTERNAL CLOCK IS LOCKED
172:01:41:38 INTERNAL CLOCK PHASE ERROR OF 143 USECONDS
172:01:41:38 POSITION: N64:29:41.54 W021:09:58.55
172:01:46:08 EXTERNAL CLOCK IS UNLOCKED
172:01:46:20 NO EXTERNAL CLOCK INPUT
```

Appendix 12. AWK SCRIPT *getcron.awk*

This script takes the name of a log file as an argument, and extracts the lines containing clock lock information, to construct a file containing the clock corrections to be applied at specified times.

```
nawk '
BEGIN {
        TRUE = 1; FALSE = 0;
        sigma1 = 50.0;
        sigma2 = 500.0;
        locked = FALSE;
}
/DSP CLOCK SET/ {
year = 1900+substr($6,5,2)
}
/EXTERNAL CLOCK IS LOCKED/ {
        locked = TRUE;
}
/CLOCK PHASE ERROR OF/ {
        if ($8 == "MSECONDS")
                printf "%4d%s %10d  %s\n", year,":"$1, $7*1000, 500.0;
        if ($8 == "USECONDS")
                printf "%4d%s %10d  %s\n", year,":"$1, $7, sigma1;
}
/EXTERNAL CLOCK IS UNLOCKED/ {
        if (locked)
                printf "%4d%s %10d  %s\n", year,":"$1, 0, sigma2;
        locked = FALSE;
} ' $1
```

The output of *getcron.awk*, when run with the log file extract given in Appendix XX would be as follows (1st column = time, 2nd = correction in ms, 3rd = uncertainty in correction in ms):

```
1996:171:23:47:39      198 50
1996:172:00:41:22      148 50
1996:172:00:42:12        0 500
1996:172:00:44:00      -15 50
1996:172:00:45:28        0 500
1996:172:00:48:27       14 50
1996:172:00:52:57        0 500
1996:172:01:41:38      143 50
1996:172:01:46:08        0 500
```

This is in the format required for input by the C program *hotclock* (Appendix XX), which added or subtracted the appropriate correction to picks, after interpolation between the nearest two identified clock locks.

Appendix 13.   C PROGRAM *hotclock*

The C program *hotclock* is an adaptation of the program *clockcor* (B.R. Julian, *pers. comm.*) and is listed below. *hotclock* caclculates clock corrections by interpolation and applies them to picks.

```
#ifndef lint
static char rcsid[] = "$Header:
/we/crhet/julian/src/cmd/calib/RCS/calib.c,v 1.13 1997/10/30 00:32:16 julian
Exp $";
#endif lint
/* hotclock.c ... Some changes by Matt Pritchard to an original program
written by B.R. Julian (USGS)*/
 * Determine clock corrections at specified time.
 */
#include <stdio.h>
#include "local.h"
#include "cmd_opt.h"
#include "date_time.h"
#include "libq.h"

#define SIGMA_Y 1.0e-10

void    clkcor();        /* clkcor.c                        */
PRIVATE void    do_file();        /* Defined below                    */
void    fbsearch();      /* fbsearch.c                      */
void    interp2();       /* interp.c                        */

int     errno;
PRIVATE char    *clkfile;        /* Clock history file              */
double  sigma_y;         /* Std. dev. (Allan) of clock        */

/*---- C O M M A N D - L I N E  A R G U M E N T  P R O C E S S I N G
----*/
#define OPT_FUNCT(name) static void name(void)
OPT_FUNCT(qhelp){ if (eargc>2) prt_help(); else prt_doc("[file...]"); }
OPT_FUNCT(qclkfile){ clkfile = aarg(); }
OPT_FUNCT(qsig_y){ sigma_y = narg(); }

struct command cmd[] = {
    qhelp    , "-help"      , "[opt...]" , "Print documentation",
    qclkfile, "-clockfile", "file_name", "Clock history file",
    qsig_y  , "-allandev" , "value"    , "Clock's std. dev. (Allan)
(default 1e-10)",
};
```

```
main(argc, argv)
int argc;
char *argv[];
{
FILE    *fin;

/* Process command-line options */
clkfile = NULL;
sigma_y = SIGMA_Y;
CMD_OPTS;
if (clkfile == NULL )
        error("No clock history file specified.");

/* Process named files (standard input default) */
if (iarg >= argc) {
        do_file(stdin, stdout);
}
else
        for (; iarg<argc; iarg++) {
                fin = efopen(argv[iarg], "r");
                do_file(fin, stdout);
                fclose(fin);
        }
}
/*
 * Process one input file
 */
static void
do_file(fin, fout)
FILE    *fin, *fout;
{
int     d;              /* Day of year                        */
FILE    *fclk;          /* Clock-history file                 */
int     h;              /* Hour                               */
int     m;              /* Minute                             */
double  s;              /* Second                             */
int     y;              /* Year                               */
double  c;              /* Clock correction                   */
double  sigma_t;        /* Uncertainty in clock correction    */

/* Open history files */
if (clkfile != NULL) fclk = efopen(clkfile, "r");

/* Loop, reading times, computing and printing corrections */
while (fscanf(fin, "%d%d%d%d%lf", &y, &d, &h, &m, &s) == 5) {
        if (clkfile != NULL) {
                clkcor(fclk, y, d, h, m, s, &c, &sigma_t);
                fprintf(fout, "%g\t%g", c, sigma_t);
        }
        fprintf(fout, "\n");
}

/* Close history files */
if (clkfile != NULL) fclose(fclk);
}
```

Appendix 14.   PERL SCRIPT *ach.pl*

This program takes text files produced by dbpick and extracts pick
measurements from them, and calls programs which predict the travel time and
slowness for each arrival.

```
#!/usr/local/perl/bin/perl
#Written by Matt Pritchard
if (@ARGV < 4 ) {
die "Usage: $0 dbname orid phase rphase [f]\n";
}

#Perl script to produce model.dat file for Aki-Christoffersson-Husebye
(ACH)
```

```
#tomographic inversion program thrd (J.R.Evans, USGS)

#Searches for given origin id in dbname.origin
# & returns event parameters after converting epoch
# to human time.

#Then opens dbname.site & gets coordinates of stations

#Then opens dbname.picks & looks up given phase arrival
#again converting picktimes to from epoch to human

#Calculates epicentral distance & baz to event for each station
#using program achdistaz

#then predicts travel time for that arrival & outputs line with
#qSTA Delta baz ... predtime picktime reltime slowness

#Arguments:
$dbname = $ARGV[0];      #database name
$orid        = $ARGV[1];     #origin id (for lookup in dbname.origin)
$phase  = $ARGV[2];     #arrival table phase name ..might be P3
$rphase = $ARGV[3];     #real phase name eg P
$qual        = $ARGV[4];     #pick quality a,b,c,x
#               $ARGV[4]     #f : first event: don't print "NEWEVENT"
at start of output

if ($ARGV[5] eq "f") {
print "Iceland Hotspot Test Residuals\n";
} else {
print "NEWEVENT\n";
}

open(ORIGIN,"$dbname.origin");          #Open origin table
while (<ORIGIN>) {
@fields = split;
if ($fields[4] == $orid) {      #Split origin line into fields
        $olat = $fields[0];
        $olon = $fields[1];
        $odep = $fields[2];
        $N = "N";
        $E = "E";
        if ($olon < 0) {        #Need letter for hemisphere rather than
+/-
                $E = "W";
                $uolon = -$olon;
        } else {
                $uolon = $olon;
        }
        if ($olat < 0) {
                $N = "S";
                $uolat = -$olat;
        } else {
                $uolat = $olat;
        }
        $etime = $fields[3];

        #Convert epoch time to human
        open(ORTIME, "e2h -ymdHMS $etime|") || die "Can't convert epoch
time\n";
        $ortime = <ORTIME>;
        @orfields = split(/ /,$ortime);            #Split returned
human time to fields
        $year = $orfields[0];
        $month = $orfields[1];
        $day = $orfields[2];
        $hour = $orfields[3];
        $min = $orfields[4];
        $sec = $orfields[5];

printf("%s%s%02d%s%02d%s%4d%s\t%02d%s%02d%s%5.03f\t%5.03f%s\t%5.03f%s\t%5.03f\
n","
*$orid","$phase(",$day,"/",$month,"/",$year,"\)",$hour,":",$min,":",$sec,$uola
t,$N,$uolon,$E,$odep);
        }
        }
```

```perl
        close (ORIGIN);

        open(SITE,"/usr/local/seismic/hotspot/pritchard/hotspot/HOTSPOT.site");
        $relcount = 1;
        $mintime = 0;
        while (<SITE>) {
        @sitefields = split;
        $sta = $sitefields[0];
        $lat{$sta} = $sitefields[3];   #Use assoc. arrays for site coords
        $lon{$sta} = $sitefields[4];

        #       Read in picks from dbname.picks file:
        # (change this to .arrival for non-clock-corrected picks)
        open(PICKS,"$dbname.picks");
        while (<PICKS>) {
                @arrfields = split;
                if (($arrfields[7] eq $phase) && ($arrfields[0] eq $sta)) {
                        $gotarr{$sta} = 1;

        #                       Find delta, azimuth, backazimuth of event from
sta
                        open(DISTAZ, "achdistaz $olat $olon $lat{$sta}
$lon{$sta} |") || die "Can't calculate distaz\n";
                        $distaz = <DISTAZ>;
                        chop $distaz;
                        @distazfields = split(/\s+/,$distaz);
                        $delta{$sta} = $distazfields[1];
                        $azi{$sta} = $distazfields[2];
                        $baz{$sta} = $distazfields[3];

                        $predtime{$sta} = `taup_time $rphase $delta{$sta}
$odep`;

                        $obs_arr_time{$sta} = $arrfields[1]-$etime;

                        $reltime{$sta} = $obs_arr_time{$sta} - $predtime{$sta};
                        if ($reltime{$sta} < $mintime | $relcount == 1)  {
                                $mintime = $reltime{$sta};
                        }
                        $relsum += $reltime{$sta};
                        $relcount++;

                        $slowness{$sta} = `taup_slow $rphase $delta{$sta}
$odep`;

                        if(substr($slowness{$sta},0,9)=="taup_slow") {
                                print STDERR "Need manual phase time / slowness
for $sta\t$phase\t$delta{$sta}\t$odep\n";
                                $slowness{$sta} = 99.999;
                        }
                }
        }
        close (PICKS);
        }

        #Output results, making delay times relative to their mean

        $relav = $relsum / $relcount;
        foreach (sort keys %reltime) {
        if (length($_) > 3) {
                $psta = substr($_,2,3);
        } else {
                $psta = $_;
        }
        $q = $qual;

        printf("%s%3s%11.03f%10.03f%15.03f%10.3f%10.3f%10.3f%10.3f\n",$q,$psta
,$delta{$_},$baz{$_},0.0,$obs_arr_time{$_},$predtime{$_},$reltime{$_}-
$relav,$slowness{$_});
        }


        #Print newline to signify end of event:
        print "\n";
```

Appendix 15. OUTPUT FROM *ach.pl*

The following extract shows sample output from the script *ach.pl*. The command used to produce the following output was:

```
cd /usr/local/seismic/hotspot/pritchard/hotspot/db/1996/dec/22

ach.pl 15:03:00 96357004 P11 P a
```

```
NEWEVENT
 *96357004P11(22/12/1996) 14:53:27.600   43.208N 138.915E      226.000
 aT01    71.165    15.209        0.000   659.995  654.136      0.575    5.992
 aT02    71.038    14.421        0.000   658.910  653.376      0.250    6.001
 aT03    71.046    13.197        0.000   658.432  653.421     -0.272    6.000
 aT04    70.638    14.312        0.000   656.391  650.964      0.143    6.030
 aT05    70.563    15.320        0.000   656.040  650.517      0.240    6.035
 aT06    70.052    14.931        0.000   653.211  647.420      0.507    6.072
 aT07    70.241    14.283        0.000   653.903  648.570      0.050    6.059
 aT08    70.391    13.017        0.000   654.537  649.477     -0.224    6.048
 aT09    70.070    13.557        0.000   652.503  647.534     -0.315    6.071
 aT10    69.915    14.375        0.000   652.154  646.589      0.281    6.082
 aT12    69.853    16.520        0.000   651.797  646.211      0.303    6.087
 aT13    69.657    17.671        0.000   650.657  645.015      0.359    6.101
 aT14    70.042    17.509        0.000   653.130  647.358      0.489    6.073
 aT15    68.859    19.969        0.000   645.305  640.128     -0.107    6.159
 aT16    69.200    20.977        0.000   647.048  642.220     -0.456    6.134
 aT17    69.578    20.366        0.000   649.699  644.532     -0.116    6.107
 aT18    69.777    19.742        0.000   650.993  645.747     -0.037    6.092
 aT19    69.933    20.616        0.000   652.020  646.697      0.040    6.081
 aT21    71.183    18.581        0.000   659.950  654.240      0.426    5.990
 aT22    71.488    17.444        0.000   662.375  656.064      1.027    5.968
 aT24    70.047    19.673        0.000   652.663  647.388     -0.009    6.073
 aT25    70.069    18.705        0.000   653.071  647.523      0.264    6.071
 aT26    70.312    17.422        0.000   655.124  649.000      0.840    6.054
 aT27    70.303    16.480        0.000   655.072  648.944      0.845    6.054
 aT29    69.182    20.173        0.000   647.173  642.110     -0.221    6.135
 aT30    71.599    14.621        0.000   662.414  656.727      0.403    5.960
```

Further documentation for *thrd* and other programs used in the ACH method is available from their author (J.R. Evans, *pers. comm.*) on request from ftp://andreas.wr.usgs.gov/pub/outgoing/evans/

Appendix 16. C PROGRAMS *taup_time* AND *taup_slow*

These programs called routines included in the DSAP package (Harvey & Quinlan, 1996) to calculate travel times and slownesses assuming a specified Earth model (Buland & Chapman, 1983).

```
taup_time:

        /*      taup_time.c    */
        /*      Matt Pritchard */
        /*      24/3/97        */
        /*      Uses JSPC library routine "phasetime" to return phase travel
time */
        /*      given delta & source depth    */
```

```
        #include <stdio.h>
        #include
"/usr/local/geodata/hotspot/pritchard/jspc/3.2/solaris/include/tttaup.h"
        #include
"/usr/local/geodata/hotspot/pritchard/jspc/3.2/solaris/include/stock.h"

        main (argc, argv)

        int argc;
        char **argv;
        {
        char *phases;
        double delta, depth;
        char modname[256];

        if ( argc != 4 && argc !=5 ) {
                fprintf (stderr, "Usage: taup_time phase delta depth\n");
                exit (1);
        }

        phases = argv[1];
        delta = atof(argv[2]);
        depth = atof(argv[3]);

        if (argc == 5) {
                tt_taup_set_table (argv[4]);
        }

        if (!tt_taup_set_phases (phases)) {
                fprintf (stderr, "taup_time: Error return from
tt_taup_set_phases\n");
                exit (1);
        }

        if (!tt_taup_set_event_depth (depth)) {
                fprintf(stderr, "taup_time: Error return from
tt_taup_set_event_depth\n");
                exit (1);
        }

        /*      tt_taup_get_modname (modname); */

        /*      printf ("Travel time for %s\n", modname);    */
        /*      printf ("depth    delta  Traveltime (sec)\n"); */

        if(phasetime ( phases,delta, depth) != -1.0 ) {
                printf("%6.03f\n",phasetime (phases, delta, depth));
        } else {
                fprintf(stderr, "taup_slow: Error - no time found for
given phase/delta/depth\n");
                exit (1);
        }


        exit(0);

        }


taup_slow:

        /*      taup_slow.c    */
        /*      Matt Pritchard */
        /*      24/3/97        */
        /*      Uses JSPC library routine "slowness" to return phase slowness
*/
        /*      given delta & source depth    */

        #include <stdio.h>
        #include
"/usr/local/geodata/hotspot/pritchard/jspc/3.2/solaris/include/tttaup.h"
        #include
"/usr/local/geodata/hotspot/pritchard/jspc/3.2/solaris/include/stock.h"
```

```
                    main (argc, argv)

                    int argc;
                    char **argv;
                    {
                    char *phases;
                    double delta, depth;
                    char modname[256];

                    if ( argc != 4 && argc !=5 ) {
                             fprintf (stderr, "Usage: taup_slow phase delta depth
[model]\n");
                             exit (1);
                    }

                    phases = argv[1];
                    delta = atof(argv[2]);
                    depth = atof(argv[3]);

                    if (argc == 5) {
                             tt_taup_set_table (argv[4]);
                    }

                    if (!tt_taup_set_phases (phases)) {
                             fprintf (stderr, "taup_slow: Error return from
tt_taup_set_phases\n");
                             exit (1);
                    }

                    if (!tt_taup_set_event_depth (depth)) {
                             fprintf(stderr, "taup_slow: Error return from
tt_taup_set_event_depth\n");
                             exit (1);
                    }

                    if(phase_slowness (phases, delta, depth) != -1.0 ) {
                             printf("%6.03f\n",phase_slowness (phases, delta, depth));
                    } else {
                             fprintf(stderr, "taup_slow: Error - no slowness found for given
phase/delta/depth\n");
                             exit (1);
                    }
                    exit(0);
                    }
```

Appendix 17.   PERL SCRIPT *pickdb_azbin_data.pl*

```
#!perl

#pickdb_azbin_data.pl
#Written by Matt Pritchard

#Read in picks from ACH .dat files into hashes indexed by event id &
station.
#Assign azimuth-slowness bin number

@ARGV == 2 or die "usage: $0 datfile data_type\n";

open(DAT, $ARGV[0]);
$data_type = $ARGV[1];
if ($data_type eq "p") {
define_p_bins (\@pbin_min_az, \@pbin_max_az, \@pbin_min_slow,
\@pbin_max_slow);
     } elsif ($data_type eq "s") {
define_s_bins (\@sbin_min_az, \@sbin_max_az, \@sbin_min_slow,
\@sbin_max_slow);
     } else {
die "Specify data type: p or s\n";
     }

#Read lines giving event id & other info; count events.
@lines = <DAT>;          #slurp in whole file & close it
close (DAT);
```

```
        $lineno=0;
        $event=0;
        foreach (@lines) {
        if (/\*9/) {
                @headfields=split;
                $evid[$event]=$headfields[0];
                $eventstart[$event] = $lineno+1;
                $nevents=$event;
        }
        if ( substr($lines[$lineno],0,2) =~ /\n/) {
                $eventstop[$event]=$lineno-1;
                $event++;
        }
        $lineno++;
        }
        $nevents++;
        print STDERR "$nevents event/phase datasets\n";

        #Get station lat lons:

        open(DISTAZ,"/work/tomo/gmt/HOTSPOT.distaz");
        open(DELAYS,">delinfo.dat");
        while(<DISTAZ>) {
        @sitefields=split;
        $sta=$sitefields[0];
        $lat{$sta} = $sitefields[1];
        $lon{$sta} = $sitefields[2];
        $dnorth{$sta} = $sitefields[5];
        $deast{$sta} = $sitefields[4];
        $dist{$sta} = sqrt
($dnorth{$sta}*$dnorth{$sta}+$deast{$sta}*$deast{$sta});
        }

        #Deal with data lines

        $k=0;
        for ($i=0; $i<$nevents; $i++) {
        for ($j=$eventstart[$i]; $j<=$eventstop[$i]; $j++) {
                @evfields = split(/\s+/,$lines[$eventstart[$i]-1]);

                #Append sign of event lat, lon depending on hemisphere
                #(denoted by [NSEW] in dat file.

                unless (chop ($evfields[3]) eq N) {
                                        $evfields[3] = -$evfields[3];
                        }
                        unless (chop ($evfields[4]) eq E) {
                                        $evfields[4] = -$evfields[4];
                        }

                #If a HOTSPOT station, make name 5 chars long.
                $stn[$k] = substr($lines[$j],1,3);
                if (substr($stn[$k],0,1) eq "T") {
                        @chars = split(//,$stn[$k]);
                        @newchars = split(//,"HOT");
                        splice(@chars,0,1,@newchars);
                        $stn[$k] = join('',@chars);
                                $tobs{$evid,$stn} = substr($lines[$j],42,8);
                }

                #Assign each field to a hash element, uniquely id'd by
                # the evid & station.

                @datafields= split(/\s+/,$lines[$j]);
                $qual{$evid[$i],$stn[$k]}  = substr($lines[$j],0,1);

                $delta{$evid[$i],$stn[$k]} = $datafields[1];
#substr($lines[$j,8,7);
                $baz{$evid[$i],$stn[$k]}   = $datafields[2];
#substr($lines[$j],18,7);
                $tobs{$evid[$i],$stn[$k]}  = $datafields[4];
                $tpred{$evid[$i],$stn[$k]} = $datafields[5];
#substr($lines[$j],52,8);
                $delay{$evid[$i],$stn[$k]} = $datafields[6];
#substr($lines[$j],64,6);
```

```
                              $slow{$evid[$i],$stn[$k]}  = $datafields[7];
#substr($lines[$j],74,6);


                    #Addtional computed fields:

                    #Azimuth-slowness bin

                    if ($data_type eq "p") {
                            $azbin{$evid[$i],$stn[$k]} =
get_p_bin($baz{$evid[$i],$stn[$k]},$slow{$evid[$i],$stn[$k]});
                    } elsif ($data_type eq "s") {
                            $azbin{$evid[$i],$stn[$k]} =
get_s_bin($baz{$evid[$i],$stn[$k]},$slow{$evid[$i],$stn[$k]});
                    }
                    $k++;
          }
          }


          #Now any operation can be preformed on the set of arrivals.
          #Looping by event is done by
          #for ($i=0; $i<$nevents; $n++)
          #or
          #foreach $event (sort @evids)
          #
          #Looping over stations (in number order) can be done by
          #foreach $station (sort keys numerically %station_number)
          #
          #Loop over azimuth slowness bins:
          #for($i=0; $i<=$no_of_p_bins; $i++)

          #Output data for residual plots, grouped by azimuth-slowness bin.
          #First need to find:
          #        delay times relative to given datum (median or time from 1
station?)
          #        median of delay times for each event/phase subset
          #        deviations of each delay time from median
          #        median of these deviations
          #        n_times_deviation for each datapoint.

          #Loop over event ids
          foreach $event (@evid) {
          print ">\n";

          #Loop over stations listed for this event:
          @subset=();      #reset array
          foreach $i ( sort numerically values %station_number) {
                    if ( exists($tobs{$event,$stname[$i]}) ) {
                            $difftime{$event,$stname[$i]} =
$tobs{$event,$stname[$i]} - $tpred{$event,$stname[$i]};
                            push(@subset,$difftime{$event,$stname[$i]});
                    }
          }
          $med_difftime = median(@subset);

          #        if ( exists($tobs{$event,"HOT17"}) ) {
          #                $rel_to_stn = $station_number{"HOT17"};
          #        } elsif (exists($tobs{$event,"HOT28"}) ) {
          #                $rel_to_stn = $station_number{"HOT28"};
          #        } else {
                    $rel_to_stn = -1;       #### Leave this line uncommented ####
          #        }
          @devs=();
          foreach $i (sort numerically values %station_number) {
                    if ( exists($tobs{$event,$stname[$i]}) ) {
                            if ( $rel_to_stn >= 0 ) {
                                    $reldelay{$event,$stname[$i]}  =
$difftime{$event,$stname[$i]} - $difftime{$event,$stname[$rel_to_stn]};
                                    print STDERR "made relative to
$stname[$rel_to_stn]\n";
                            } else {
                                    $reldelay{$event,$stname[$i]}  =
$difftime{$event,$stname[$i]} - $med_difftime;
                                    print STDERR "made relative to median\n";
```

```
                                    }
                                    $deviation{$event,$stname[$i]} =
abs($reldelay{$event,$stname[$i]});
                                    push(@devs,$deviation{$event,$stname[$i]});
                         }
             }
             $med_dev = median(@devs);

             foreach $i (sort numerically values %station_number) {
                     if ( exists($tobs{$event,$stname[$i]}) ) {
                             if ($med_dev != 0) {
                                     $n_times_dev{$event,$stname[$i]} =
$deviation{$event,$stname[$i]};
                             } else {
                                     $n_times_dev{$event,$stname[$i]} = 999.9;
                             }
                     }
             }


             foreach $i (sort numerically values %station_number) {
                     if ( exists($tobs{$event,$stname[$i]}) ) {
                             printf STDOUT ("%d %s %d %s %9.5f %9.5f %9.5f %9.5f\n",
$azbin{$event,$stname[$i]}, $event, $station_number{$stname[$i]}, $stname[$i],
$baz{$event,$stname[$i]}, $slow{$event,$stname[$i]},
$reldelay{$event,$stname[$i]}, $n_times_dev{$event,$stname[$i]});
                     }
      }
}

sub median {
my @values = sort numerically @_;

my $n = scalar(@values);

if ($n % 2) {
        #odd number of elements
        return $values[($n-1)/2];
} else {
        #even number of elements
        return ($values[($n+1)/2]+$values[($n-1)/2])/2;
}
}

sub numerically {
        $a <=> $b;
}

sub get_p_bin {
my ($myaz, $myslow) = @_;
my $mybin;
my $j;
for ($j=0; $j<=$no_of_p_bins; $j++) {
        if (($myaz >= $pbin_min_az[$j] && $myaz < $pbin_max_az[$j]) &&
($myslow >= $pbin_min_slow[$j] && $myslow < $pbin_max_slow[$j])) {
                $mybin=$j;
        }
}
return $mybin;
}

sub get_s_bin {
my ($myaz, $myslow) = @_;
my $mybin;
my $j;
for ($j=0; $j<=$no_of_s_bins; $j++) {
        if (($myaz >= $sbin_min_az[$j] && $myaz < $sbin_max_az[$j]) &&
($myslow >= $sbin_min_slow[$j] && $myslow < $sbin_max_slow[$j])) {
                $mybin=$j;
        }
}
return $mybin;
}


sub define_p_bins (\@pbin_min_az, \@pbin_max_az, \@pbin_min_slow,
```

```
            sub define_p_bins (\@pbin_min_az, \@pbin_max_az, \@pbin_min_slow,
\@pbin_max_slow) {
            $no_of_p_bins = 10;

            #pbin 0
            $pbin_no = 0;
            $pbin_min_az[$pbin_no]          = 0;
            $pbin_max_az[$pbin_no]          = 360;
            $pbin_min_slow[$pbin_no]        = 0;
            $pbin_max_slow[$pbin_no]        = 4;

            #pbin 1
            $pbin_no = 1;
            $pbin_min_az[$pbin_no]          = 0;
            $pbin_max_az[$pbin_no]          = 50;
            $pbin_min_slow[$pbin_no]        = 4;
            $pbin_max_slow[$pbin_no]        = 6.5;


            #pbin 2
            $pbin_no = 2;
            $pbin_min_az[$pbin_no]          = 0;
            $pbin_max_az[$pbin_no]          = 50;
            $pbin_min_slow[$pbin_no]        = 6.5;
            $pbin_max_slow[$pbin_no]        = 12;

            #pbin 3
            $pbin_no = 3;
            $pbin_min_az[$pbin_no]          = 50;
            $pbin_max_az[$pbin_no]          = 90;
            $pbin_min_slow[$pbin_no]        = 4;
            $pbin_max_slow[$pbin_no]        = 12;

            #pbin 4
            $pbin_no = 4;
            $pbin_min_az[$pbin_no]          = 90;
            $pbin_max_az[$pbin_no]          = 150;
            $pbin_min_slow[$pbin_no]        = 4;
            $pbin_max_slow[$pbin_no]        = 12;

            #bin 5
            $pbin_no = 5;
            $pbin_min_az[$pbin_no]          = 135;
            $pbin_max_az[$pbin_no]          = 205;
            $pbin_min_slow[$pbin_no]        = 4;
            $pbin_max_slow[$pbin_no]        = 12;

            #pbin 6
            $pbin_no = 6;
            $pbin_min_az[$pbin_no]          = 205;
            $pbin_max_az[$pbin_no]          = 300;
            $pbin_min_slow[$pbin_no]        = 3.5;
            $pbin_max_slow[$pbin_no]        = 5.8;

            #pbin 7
            $pbin_no = 7;
            $pbin_min_az[$pbin_no]          = 205;
            $pbin_max_az[$pbin_no]          = 240;
            $pbin_min_slow[$pbin_no]        = 5.5;
            $pbin_max_slow[$pbin_no]        = 12;

            #bin 8
            $pbin_no = 8;
            $pbin_min_az[$pbin_no]          = 240;
            $pbin_max_az[$pbin_no]          = 300;
            $pbin_min_slow[$pbin_no]        = 5.5;
            $pbin_max_slow[$pbin_no]        = 12;

            #bin 9
            $pbin_no = 9;
            $pbin_min_az[$pbin_no]          = 300;
            $pbin_max_az[$pbin_no]          = 360;
            $pbin_min_slow[$pbin_no]        = 4;
            $pbin_max_slow[$pbin_no]        = 12;
            }
```

```
        sub define_s_bins (\@sbin_min_az, \@sbin_max_az, \@sbin_min_slow,
\@sbin_max_slow) {
        $no_of_s_bins = 9;

        #sbin 0
        $sbin_no = 0;
        $sbin_min_az[$sbin_no]          = 0;
        $sbin_max_az[$sbin_no]          = 360;
        $sbin_min_slow[$sbin_no]        = 0;
        $sbin_max_slow[$sbin_no]        = 8;

        #bin 1
        $sbin_no = 1;
        $sbin_min_az[$sbin_no]          = 0;
        $sbin_max_az[$sbin_no]          = 50;
        $sbin_min_slow[$sbin_no]        = 8;
        $sbin_max_slow[$sbin_no]        = 20;


        #sbin 2
        $sbin_no = 2;
        $sbin_min_az[$sbin_no]          = 50;
        $sbin_max_az[$sbin_no]          = 80;
        $sbin_min_slow[$sbin_no]        = 8;
        $sbin_max_slow[$sbin_no]        = 20;

        #bin 3
        $sbin_no = 3;
        $sbin_min_az[$sbin_no]          = 80;
        $sbin_max_az[$sbin_no]          = 170;
        $sbin_min_slow[$sbin_no]        = 8;
        $sbin_max_slow[$sbin_no]        = 20;

        #sbin 4
        $sbin_no = 4;
        $sbin_min_az[$sbin_no]          = 170;
        $sbin_max_az[$sbin_no]          = 215;
        $sbin_min_slow[$sbin_no]        = 8;
        $sbin_max_slow[$sbin_no]        = 20;

        #sbin 5
        $sbin_no = 5;
        $sbin_min_az[$sbin_no]          = 210;
        $sbin_max_az[$sbin_no]          = 245;
        $sbin_min_slow[$sbin_no]        = 4;
        $sbin_max_slow[$sbin_no]        = 12;

        #sbin 6
        $sbin_no = 6;
        $sbin_min_az[$sbin_no]          = 210;
        $sbin_max_az[$sbin_no]          = 245;
        $sbin_min_slow[$sbin_no]        = 12;
        $sbin_max_slow[$sbin_no]        = 20;

        #sbin 7
        $sbin_no = 7;
        $sbin_min_az[$sbin_no]          = 245;
        $sbin_max_az[$sbin_no]          = 280;
        $sbin_min_slow[$sbin_no]        = 8;
        $sbin_max_slow[$sbin_no]        = 20;

        #sbin 8
        $sbin_no = 8;
        $sbin_min_az[$sbin_no]          = 280;
        $sbin_max_az[$sbin_no]          = 360;
        $sbin_min_slow[$sbin_no]        = 8;
        $sbin_max_slow[$sbin_no]        = 20;
        }

        BEGIN {
        %station_number = (
        HOT01 => 11,
        HOT02 => 8,
        HOT03 => 7,
```

```
HOT04 => 5,
HOT05 => 10,
HOT06 => 4,
HOT07 => 3,
HOT08 => 0,
HOT09 => 1,
HOT10 => 2,
HOT11 => 6,
HOT12 => 22,
HOT13 => 21,
HOT14 => 20,
HOT15 => 29,
HOT16 => 32,
HOT17 => 33,
HOT18 => 34,
HOT19 => 37,
HOT20 => 39,
HOT21 => 40,
HOT22 => 41,
HOT23 => 38,
HOT24 => 35,
HOT25 => 36,
HOT26 => 18,
HOT27 => 19,
HOT28 => 15,
HOT29 => 30,
HOT30 => 12,
ASB    => 9,
GIL    => 28,
GRA    => 25,
GRI    => 24,
GRS    => 31,
HVE    => 16,
KRA    => 27,
KRO    => 14,
REN    => 26,
SIG    => 23,
SKR    => 17,
VOG    => 13 );

#Make array of station NAMES (note: array index starts at 1, not 0)
foreach $item (sort keys %station_number) {          #loop by NAME
        $stname[$station_number{$item}] = $item;
}
}
```

Appendix 18.   PERL SCRIPT *tpred_unix.pl*

```
#!perl

#pickdb_azbin_data.pl
#Written by Matt Pritchard

#Read in picks from ACH .dat files into hashes indexed by event id &
station.
#Assign azimuth-slowness bin number

@ARGV == 2 or die "usage: $0 datfile data_type\n";

open(DAT, $ARGV[0]);
$data_type = $ARGV[1];
if ($data_type eq "p") {
define_p_bins (\@pbin_min_az, \@pbin_max_az, \@pbin_min_slow,
\@pbin_max_slow);
    } elsif ($data_type eq "s") {
define_s_bins (\@sbin_min_az, \@sbin_max_az, \@sbin_min_slow,
\@sbin_max_slow);
    } else {
die "Specify data type: p or s\n";
    }
```

```perl
#Read lines giving event id & other info; count events.
@lines = <DAT>;        #slurp in whole file & close it
close (DAT);
$lineno=0;
$event=0;
foreach (@lines) {
if (/\*9/) {
        @headfields=split;
        $evid[$event]=$headfields[0];
        $eventstart[$event] = $lineno+1;
        $nevents=$event;
}
if ( substr($lines[$lineno],0,2) =~ /\n/) {
        $eventstop[$event]=$lineno-1;
        $event++;
}
$lineno++;
}
$nevents++;
print STDERR "$nevents event/phase datasets\n";

#Get station lat lons:

open(DISTAZ,"/work/tomo/gmt/HOTSPOT.distaz");
open(DELAYS,">delinfo.dat");
while(<DISTAZ>) {
@sitefields=split;
$sta=$sitefields[0];
$lat{$sta} = $sitefields[1];
$lon{$sta} = $sitefields[2];
$dnorth{$sta} = $sitefields[5];
$deast{$sta} = $sitefields[4];
$dist{$sta} = sqrt
($dnorth{$sta}*$dnorth{$sta}+$deast{$sta}*$deast{$sta});
}

#Deal with data lines

$k=0;
for ($i=0; $i<$nevents; $i++) {
for ($j=$eventstart[$i]; $j<=$eventstop[$i]; $j++) {
        @evfields = split(/\s+/,$lines[$eventstart[$i]-1]);

        #Append sign of event lat, lon depending on hemisphere
        #(denoted by [NSEW] in dat file.

        unless (chop ($evfields[3]) eq N) {
                                $evfields[3] = -$evfields[3];
                }
                unless (chop ($evfields[4]) eq E) {
                                $evfields[4] = -$evfields[4];
                }

        #If a HOTSPOT station, make name 5 chars long.
        $stn[$k] = substr($lines[$j],1,3);
        if (substr($stn[$k],0,1) eq "T") {
                @chars = split(//,$stn[$k]);
                @newchars = split(//,"HOT");
                splice(@chars,0,1,@newchars);
                $stn[$k] = join('',@chars);
                        $tobs{$evid,$stn} = substr($lines[$j],42,8);
        }

        #Assign each field to a hash element, uniquely id'd by
        # the evid & station.

        @datafields= split(/\s+/,$lines[$j]);
        $qual{$evid[$i],$stn[$k]}  =  substr($lines[$j],0,1);

        $delta{$evid[$i],$stn[$k]} = $datafields[1];
#substr($lines[$j,8,7);
        $baz{$evid[$i],$stn[$k]}   = $datafields[2];
#substr($lines[$j],18,7);
        $tobs{$evid[$i],$stn[$k]}  = $datafields[4];
        $tpred{$evid[$i],$stn[$k]} = $datafields[5];
```

```
#substr($lines[$j],52,8);
                $delay{$evid[$i],$stn[$k]} = $datafields[6];
#substr($lines[$j],64,6);
                $slow{$evid[$i],$stn[$k]}  = $datafields[7];
#substr($lines[$j],74,6);


                #Addtional computed fields:

                #Azimuth-slowness bin

                if ($data_type eq "p") {
                        $azbin{$evid[$i],$stn[$k]} =
get_p_bin($baz{$evid[$i],$stn[$k]},$slow{$evid[$i],$stn[$k]});
                } elsif ($data_type eq "s") {
                        $azbin{$evid[$i],$stn[$k]} =
get_s_bin($baz{$evid[$i],$stn[$k]},$slow{$evid[$i],$stn[$k]});
                }
                $k++;
        }
        }


        #Now any operation can be preformed on the set of arrivals.
        #Looping by event is done by
        #for ($i=0; $i<$nevents; $n++)
        #or
        #foreach $event (sort @evids)
        #
        #Looping over stations (in number order) can be done by
        #foreach $station (sort keys numerically %station_number)
        #
        #Loop over azimuth slowness bins:
        #for($i=0; $i<=$no_of_p_bins; $i++)

        #Loop over event ids
        foreach $event (@evid) {
        print ">\n";

        #Loop over stations listed for this event:
        @subset=();      #reset array
        foreach $i ( sort numerically values %station_number) {
                if ( exists($tobs{$event,$stname[$i]}) ) {
                        $difftime{$event,$stname[$i]} =
$tobs{$event,$stname[$i]} - $tpred{$event,$stname[$i]};
                        push(@subset,$difftime{$event,$stname[$i]});
                }
        }
        $med_difftime = median(@subset);

        #       if ( exists($tobs{$event,"HOT17"}) ) {
        #               $rel_to_stn = $station_number{"HOT17"};
        #       } elsif (exists($tobs{$event,"HOT28"}) ) {
        #               $rel_to_stn = $station_number{"HOT28"};
        #       } else {
                $rel_to_stn = -1;       #### Leave this line uncommented ####
        #       }
        @devs=();
        foreach $i (sort numerically values %station_number) {
                if ( exists($tobs{$event,$stname[$i]}) ) {
                        if ( $rel_to_stn >= 0 ) {
                                $reldelay{$event,$stname[$i]}  =
$difftime{$event,$stname[$i]} - $difftime{$event,$stname[$rel_to_stn]});
                                print STDERR "made relative to
$stname[$rel_to_stn]\n";
                        } else {
                                $reldelay{$event,$stname[$i]}  =
$difftime{$event,$stname[$i]} - $med_difftime;
                                print STDERR "made relative to median\n";
                        }
                        $deviation{$event,$stname[$i]} =
abs($reldelay{$event,$stname[$i]});
                        push(@devs,$deviation{$event,$stname[$i]});
                }
        }
```

```
            $med_dev = median(@devs);

            foreach $i (sort numerically values %station_number) {
                    if ( exists($tobs{$event,$stname[$i]}) ) {
                            if ($med_dev != 0) {
                                    $n_times_dev{$event,$stname[$i]} =
$deviation{$event,$stname[$i]} / $med_dev;
                            } else {
                                    $n_times_dev{$event,$stname[$i]} = 2; #Change
this!!
                            }
                    }
            }

            foreach $i (sort numerically values %station_number) {
                    if ( exists($tobs{$event,$stname[$i]}) ) {
                            printf STDOUT ("%d %s %d %s %9.5f %9.5f %9.5f %9.5f\n",
$azbin{$event,$stname[$i]}, $event, $station_number{$stname[$i]}, $stname[$i],
$baz{$event,$stname[$i]}, $slow{$event,$stname[$i]},
$reldelay{$event,$stname[$i]}, $n_times_dev{$event,$stname[$i]});
                    }
            }
        }
```

The following subroutines are omitted here but are the same as in pickdb_azbin_data.pl (Appendix 17).

```
        sub median {
        }

        sub numerically {;
        }

        sub get_p_bin {
         }


        sub get_s_bin {
        }


        sub define_p_bins (\@pbin_min_az, \@pbin_max_az, \@pbin_min_slow,
\@pbin_max_slow) {
            }

        sub define_s_bins (\@sbin_min_az, \@sbin_max_az, \@sbin_min_slow,
\@sbin_max_slow) {
            }
```

Appendix 19.   PERL SCRIPT *remake_ach.pl*

```
        #!perl

        #pickdb_azbin_data.pl
        #Written by Matt Pritchard

        #Read in picks from ACH .dat files into hashes indexed by event id &
station.
        #Assign azimuth-slowness bin number

        @ARGV == 2 or die "usage: $0 datfile data_type\n";

        open(DAT, $ARGV[0]);
        $data_type = $ARGV[1];
        if ($data_type eq "p") {
        define_p_bins (\@pbin_min_az, \@pbin_max_az, \@pbin_min_slow,
\@pbin_max_slow);
```

```perl
        } elsif ($data_type eq "s") {
        define_s_bins (\@sbin_min_az, \@sbin_max_az, \@sbin_min_slow,
\@sbin_max_slow);
        } else {
        die "Specify data type: p or s\n";
        }

        #Read lines giving event id & other info; count events.
        @lines = <DAT>;          #slurp in whole file & close it
        close (DAT);
        $lineno=0;
        $event=0;
        foreach (@lines) {
        if (/\*9/) {
                @headfields=split;
                $evid[$event]=$headfields[0];
                $eventstart[$event] = $lineno+1;
                $nevents=$event;
        }
        if ( substr($lines[$lineno],0,2) =~ /\n/) {
                $eventstop[$event]=$lineno-1;
                $event++;
        }
        $lineno++;
        }
        $nevents++;
        print STDERR "$nevents event/phase datasets\n";

        #Get station lat lons:

        open(DISTAZ,"/work/tomo/gmt/HOTSPOT.distaz");
        open(DELAYS,">delinfo.dat");
        while(<DISTAZ>) {
        @sitefields=split;
        $sta=$sitefields[0];
        $lat{$sta} = $sitefields[1];
        $lon{$sta} = $sitefields[2];
        $dnorth{$sta} = $sitefields[5];
        $deast{$sta} = $sitefields[4];
        $dist{$sta} = sqrt
($dnorth{$sta}*$dnorth{$sta}+$deast{$sta}*$deast{$sta});
        }

        #Deal with data lines

        $k=0;
        for ($i=0; $i<$nevents; $i++) {
        for ($j=$eventstart[$i]; $j<=$eventstop[$i]; $j++) {
                @evfields = split(/\s+/,$lines[$eventstart[$i]-1]);

                #Append sign of event lat, lon depending on hemisphere
                #(denoted by [NSEW] in dat file.

                unless (chop ($evfields[3]) eq N) {
                                        $evfields[3] = -$evfields[3];
                        }
                        unless (chop ($evfields[4]) eq E) {
                                        $evfields[4] = -$evfields[4];
                        }

                #If a HOTSPOT station, make name 5 chars long.
                $stn[$k] = substr($lines[$j],1,3);
                if (substr($stn[$k],0,1) eq "T") {
                        @chars = split(//,$stn[$k]);
                        @newchars = split(//,"HOT");
                        splice(@chars,0,1,@newchars);
                        $stn[$k] = join('',@chars);
                                $tobs{$evid,$stn} = substr($lines[$j],42,8);
                }

                #Assign each field to a hash element, uniquely id'd by
                # the evid & station.

                @datafields= split(/\s+/,$lines[$j]);
                $qual{$evid[$i],$stn[$k]}   = substr($lines[$j],0,1);
```

```
                       $delta($evid[$i],$stn[$k]) = $datafields[1];
#substr($lines[$j],8,7);
                       $baz($evid[$i],$stn[$k])   = $datafields[2];
#substr($lines[$j],18,7);
                       $tobs($evid[$i],$stn[$k])  = $datafields[4];
                       $tpred($evid[$i],$stn[$k]) = $datafields[5];
#substr($lines[$j],52,8);
                       $delay($evid[$i],$stn[$k]) = $datafields[6];
#substr($lines[$j],64,6);
                       $slow($evid[$i],$stn[$k])  = $datafields[7];
#substr($lines[$j],74,6);


                       #Addtional computed fields:

                       #Azimuth-slowness bin

                       if ($data_type eq "p") {
                               $azbin($evid[$i],$stn[$k]) =
get_p_bin($baz($evid[$i],$stn[$k]),$slow($evid[$i],$stn[$k]));
                       } elsif ($data_type eq "s") {
                               $azbin($evid[$i],$stn[$k]) =
get_s_bin($baz($evid[$i],$stn[$k]),$slow($evid[$i],$stn[$k]));
                       }
                       $k++;
               }
               }


        #Now any operation can be preformed on the set of arrivals.
        #Looping by event is done by
        #for ($i=0; $i<$nevents; $n++)
        #or
        #foreach $event (sort @evids)
        #
        #Looping over stations (in number order) can be done by
        #foreach $station (sort keys numerically %station_number)
        #
        #Loop over azimuth slowness bins:
        #for($i=0; $i<=$no_of_p_bins; $i++)

        #Output data for residual plots, grouped by azimuth-slowness bin.
        #First need to find:
        #        delay times relative to given datum (median or time from 1
station?)
        #        median of delay times for each event/phase subset
        #        deviations of each delay time from median
        #        median of these deviations
        #        n_times_deviation for each datapoint.

        #Loop over event ids
        foreach $event (@evid) {
        print ">\n";

        #Loop over stations listed for this event:
        @subset=();      #reset array
        foreach $i ( sort numerically values %station_number) {
                if ( exists($tobs($event,$stname[$i])) ) {
                        $difftime($event,$stname[$i]) =
$tobs($event,$stname[$i]) - $tpred($event,$stname[$i]);
                        push(@subset,$difftime($event,$stname[$i]));
                }
        }
        $med_difftime = median(@subset);

        #        if ( exists($tobs($event,"HOT17")) ) {
        #                $rel_to_stn = $station_number{"HOT17"};
        #        } elsif (exists($tobs($event,"HOT28")) ) {
        #                $rel_to_stn = $station_number{"HOT28"};
        #        } else {
                $rel_to_stn = -1;       #### Leave this line uncommented ####
        #        }
        @devs=();
        foreach $i (sort numerically values %station_number) {
```

```
                    if ( exists($tobs{$event,$stname[$i]}) ) {
                        if ( $rel_to_stn >= 0 ) {
                            $reldelay{$event,$stname[$i]}   =
$difftime{$event,$stname[$i]} - $difftime{$event,$stname[$rel_to_stn]};
                            print STDERR "made relative to
$stname[$rel_to_stn]\n";
                        } else {
                            $reldelay{$event,$stname[$i]}   =
$difftime{$event,$stname[$i]} - $med_difftime;
                            print STDERR "made relative to median\n";
                        }
                        $deviation{$event,$stname[$i]} =
abs($reldelay{$event,$stname[$i]});
                        push(@devs,$deviation{$event,$stname[$i]});
                    }
            }
            $med_dev = median(@devs);

            foreach $i (sort numerically values %station_number) {
                if ( exists($tobs{$event,$stname[$i]}) ) {
                    if ($med_dev != 0) {
                        $n_times_dev{$event,$stname[$i]} =
$deviation{$event,$stname[$i]} / $med_dev;
                    } else {
                        $n_times_dev{$event,$stname[$i]} = 2; #Change
this!!
                    }
                }
            }

            foreach $i (sort numerically values %station_number) {
                if ( exists($tobs{$event,$stname[$i]}) ) {
                    printf STDOUT ("%d %s %d %s %9.5f %9.5f %9.5f %9.5f\n",
$azbin{$event,$stname[$i]}, $event, $station_number{$stname[$i]}, $stname[$i],
$baz{$event,$stname[$i]}, $slow{$event,$stname[$i]},
$reldelay{$event,$stname[$i]}, $n_times_dev{$event,$stname[$i]});
                }
            }
        }
```

The following subroutines are omitted here but are the same as in pickdb_azbin_data.pl (Appendix 17)

```
        sub median {
        }

        sub numerically {
        }

        sub get_p_bin {
        }

        sub get_s_bin {
        }

        sub define_p_bins (\@pbin_min_az, \@pbin_max_az, \@pbin_min_slow,
\@pbin_max_slow) {
        }

        sub define_s_bins (\@sbin_min_az, \@sbin_max_az, \@sbin_min_slow,
\@sbin_max_slow) {
        }
```

Appendix 20.   SCRIPT *plot_azbin_delays_p_stnmed*

```
    #!bash

    #plot_azbin_delays_p_stnmed
    #Written by Matt Pritchard
```

```
#plot station vs residual for a set of data produced by
#azbin_divide_p.pl
#Substitute 's' for P in filenames for S-wave version, & change
#cutoff value to 1.5 sec.
rm .gmt*

if test "$1" == 0
then
rm event_keys_p.txt
echo "bin evno evid" > event_keys_p.txt
fi

gmtset MEASURE_UNIT cm
gmtset PAPER_MEDIA A4+
gmtset LABEL_FONT_SIZE 10p
gmtset HEADER_FONT_SIZE 15p
gmtset DEGREE_FORMAT 5
gmtset BASEMAP_TYPE PLAIN
gmtset PAGE_ORIENTATION LANDSCAPE
gmtset GRID_PEN 0.01

cat /work/tomo/gmt/pagemap_landscape.ps
psbasemap -R-1/42/-2/2 -JX25c/14c -X2c -Y2.5c -O -K -
Bf1g1/a1f1g0.1t:"Relative residual (s)":Wsen:."Residuals for azimuth-slowness
bin $1":

#plot lines
awk -v bin=$1 '
BEGIN {
        last_evid="blank"
        last_station=0
        event=0
}
NF>3 && $1==bin {
        if ($2 != last_evid || last_station+1 != $3) {
                print ">"
                event++
        }
        print $3,$7
        last_evid = $2
        last_station = $3
}' $2 |
psxy -R -JX -K -O -A -W0.01 -M

#plot dots
awk -v bin=$1 '
BEGIN {
        last_evid="blank"
        event=0
}
NF>3 && $1==bin {
        if ($2 != last_evid) {
                event++
        }
        print $3,$7,event
        last_evid=$2
}' $2 |
psxy -R -JX -K -O -A -Cevents.cpt -Sc0.3 -G0

#plot number label in middle of each dot
awk -v bin=$1 '
BEGIN {
        i=0
        last_evid="blank"
        event=0
}
NF>3 && $1==bin {
        if ($2 != last_evid) {
                event++
        }
        print $3,$7,8,0,1,"CM",event
        last_evid = $2
}' $2 |
pstext -R -JX -K -O -S0.01/0/0/0 -G255
```

```
awk -v bin=$1 '
BEGIN {
        i=0
        last_evid="blank"
        event=0
}
NF>3 && $1==bin {
        if ($2 != last_evid) {
                event++
                print bin,event,$2
        }
        last_evid = $2
}' $2 >> event_keys_p.txt

#Ring in red those data that have $n_times_dev greater than 0.6sec
awk -v bin=$1 "
NF>3 && $1==bin {
        if ($8 > 0.6) {
                print $3,$7
        }
}' $2 |
psxy -R -JX -O -K -Sc0.45 -W0.01/255/0/0

awk '
BEGIN {
        y=-2.2
        size=10
        angle=90
        fontno=0
        justify="MR"
}
NF>3 {
        stname[$3]=$4
        stnum[$3] =$3
}
END {
        for (i=0; i<42; i++) {
                print stnum[i],y,size,angle,fontno,justify,stname[i]
        }
} ' $2 |
pstext -R -JX -N -O
```

Appendix 21.   STATION PERFORMANCE CHART

Station	No of Days	Installed	Up (no problems)	Up but with non-fatal problem	Down (fatal problem)	Some problem		Up (no problems)	Up but with non-fatal problem	Down (fatal problem)	Some problem
Station reliability statistics											
1 Reykir	788	725	2	61	63		92.0	0.3	7.7	8.0
2 Ásbrún	785	704	2	79	81		89.7	0.3	10.1	10.3
3 Ingjaldshóll	781	627	2	152	154		80.3	0.3	19.5	19.7
4 Ormsstaðir	784	583	2	199	201		74.4	0.3	25.4	25.6
5 Brú	781	710	2	69	71		90.9	0.3	8.8	9.1
6 Hólmavík	793	756	2	35	37		95.3	0.3	4.4	4.7
7 Eyri	786	564	2	220	222		71.8	0.3	28.0	28.2
8 Ólafsviti	788	696	2	90	92		88.3	0.3	11.4	11.7
9 Þingeyri	791	694	2	95	97		87.7	0.3	12.0	12.3
10 Reykjanesskóli	793	665	2	126	128		83.9	0.3	15.9	16.1
11 Böðvarshólar	780	759	2	19	21		97.3	0.3	2.4	2.7
12 Hávík	781	735	2	44	46		94.1	0.3	5.6	5.9
13 Súlur	782	752	2	28	30		96.2	0.3	3.6	3.8
14 Hólsgerði	781	711	2	68	70		91.0	0.3	8.7	9.0
15 Finnafjörður	760	539	2	219	221		70.9	0.3	28.8	29.1
16 Borgarfjörður-eystri	760	748	2	10	12		98.4	0.3	1.3	1.6
17 Setberg	764	762	2	0	2		99.7	0.3	0.0	0.3
18 Grund	767	765	2	0	2		99.7	0.3	0.0	0.3
19 Fell	767	516	2	249	251		67.3	0.3	32.5	32.7
20 Hagi	768	702	2	64	66		91.4	0.3	8.3	8.6
21 Fagurhólsmýri	768	699	2	67	69		91.0	0.3	8.7	9.0
22 Hunkubakkar	766	702	2	62	64		91.6	0.3	8.1	8.4
23 Grímsfjall	747	454	2	291	293		60.8	0.3	39.0	39.2
24 Snæfell	758	753	1	4	5		99.3	0.1	0.5	0.7
25 Askja	757	438	2	317	319		57.9	0.3	41.9	42.1
26 Laugafell	746	458	2	286	288		61.4	0.3	38.3	38.6
27 Blöndulón	740	715	2	23	25		96.6	0.3	3.1	3.4
28 Leppistungur	760	758	2	0	2		99.7	0.3	0.0	0.3
29 Vatnsdalsgerði	752	538	2	212	214		71.5	0.3	28.2	28.5
30 Veðurstofa	756	579	0	177	177		76.6	0.0	23.4	23.4

Appendix 22. EVENTS USED IN THE TOMOGRAPHIC INVERSION

This table lists the phase sets picked from events in the final dataset prepared for the tomographic inversion. Events are identified by the "orid" (see section 4.1.4). In many cases, more than one phase was picked per event.

Orid	Date	hh	mm	ss	Lat	Lon	Delta	Baz	Dep (km)	Mag	Picked	Region
96204014	22/07/1996	14	19	35.77	0.8507	120.15	108.00	43.13	33	6.9	Pdiff	MINAHASSA PENINSULA
96204014	22/07/1996	14	19	35.77	0.8507	120.15	108.00	43.13	33	6.9	PP	MINAHASSA PENINSULA
96218016	05/08/1996	21	39	16.25	-1.8598	-80.80	80.04	243.11	33	5.9	P	NEAR COAST OF ECUADOR
96218016	05/08/1996	21	39	16.25	-1.8598	-80.80	80.04	243.11	33	5.9	PP	NEAR COAST OF ECUADOR
96218016	05/08/1996	21	39	16.25	-1.8598	-80.80	80.04	243.11	33	5.9	S	NEAR COAST OF ECUADOR
96223013	10/08/1996	18	12	17.35	38.8816	140.57	75.04	16.11	33	6	P	HONSHU, JAPAN
96223013	10/08/1996	18	12	17.35	38.8816	140.57	75.04	16.11	33	6	pP	HONSHU, JAPAN
96223013	10/08/1996	18	12	17.35	38.8816	140.57	75.04	16.11	33	6	S	HONSHU, JAPAN
96223014	10/08/1996	18	54	11.07	38.9232	140.56	74.99	16.11	33	5.7	P	HONSHU, JAPAN
96232007	19/08/1996	4	19	16.18	51.4311	-178.45	62.57	345.52	33	5.7	P	ANDREANOF ISL, ALEUTEAN IS.
96248002	04/09/1996	3	37	53.25	30.364	130.15	81.81	26.31	33	5.5	P	KYUSHU, JAPAN
96248020	04/09/1996	19	6	49.81	9.376	-84.26	71.05	250.94	33	5.9	P	COSTA RICA
96249001	05/09/1996	8	14	14.48	-22.2607	-113.41	111.79	263.78	10	7.1	Pdiff	EASTER ISLAND REGION
96249001	05/09/1996	8	14	14.48	-22.2607	-113.41	111.79	263.78	10	7.1	PP	EASTER ISLAND REGION
96249010	05/09/1996	20	44	9.29	42.8545	17.91	30.27	118.44	10	5.9	P	ADRIATIC SEA
96249010	05/09/1996	20	44	9.29	42.8545	17.91	30.27	118.44	10	5.9	S	ADRIATIC SEA
96249013	05/09/1996	23	42	6.15	21.9838	121.37	88.02	36.03	33	6.6	P	TAIWAN REGION
96249013	05/09/1996	23	42	6.15	21.9838	121.37	88.02	36.03	33	6.6	P	TAIWAN REGION
96249013	05/09/1996	23	42	6.15	21.9838	121.37	88.02	36.03	33	6.6	S	TAIWAN REGION
96255003	11/09/1996	2	37	14.99	35.5212	140.93	78.40	16.33	70.3	5.9	P	NEAR E COAST OF HONSHU, JAPAN
96255003	11/09/1996	2	37	14.99	35.5212	140.93	78.40	16.33	70.3	5.9	S	NEAR E COAST OF HONSHU, JAPAN
96258011	14/09/1996	13	10	53.97	-10.8442	165.83	125.84	353.79	65.9	6	PKIKP	SANTA CRUZ ISLANDS
96258011	14/09/1996	13	10	53.97	-10.8442	165.83	125.84	353.79	65.9	6	PP	SANTA CRUZ ISLANDS
96264001	20/09/1996	0	3	18.37	9.5792	126.37	101.24	34.54	33	6.2	Pdiff	MINDANAO, PHILIPPINE ISLANDS
96264001	20/09/1996	0	3	18.37	9.5792	126.37	101.24	34.54	33	6.2	PP	MINDANAO, PHILIPPINE ISLANDS
96264001	20/09/1996	0	3	18.37	9.5792	126.37	101.24	34.54	33	6.2	SKS	MINDANAO, PHILIPPINE ISLANDS
96264003	20/09/1996	4	10	27.68	9.46	126.24	101.32	34.70	33	6.4	Pdiff	MINDANAO, PHILIPPINE ISLANDS
96264003	20/09/1996	4	10	27.68	9.46	126.24	101.32	34.70	33	6.4	PP	MINDANAO, PHILIPPINE ISLANDS
96264009	20/09/1996	12	24	42.12	9.3593	127.28	101.67	33.71	33	6	PP	PHILIPPINE ISLANDS REGION
96264017	20/09/1996	19	24	57.3	9.5558	126.71	101.34	34.22	33	5.5	PP	MINDANAO, PHILIPPINE ISLANDS
96268001	24/09/1996	11	42	18.87	15.206	-61.41	57.23	230.33	147.5	5.6	P	LEEWARD ISLANDS
96268001	24/09/1996	11	42	18.87	15.206	-61.41	57.23	230.33	147.5	5.6	PcP	LEEWARD ISLANDS
96276015	02/10/1996	9	48	1.56	11.6848	125.58	99.01	34.78	33	6.4	PP	SAMAR, PHILIPPINE ISLANDS
96276015	02/10/1996	9	48	1.56	11.6848	125.58	99.01	34.78	33	6.4	S	SAMAR, PHILIPPINE ISLANDS
96276021	02/10/1996	11	24	48.42	44.8406	151.13	70.02	7.21	33	5.9	P	EAST OF KURIL ISLANDS, RUSSIA
96283014	09/10/1996	13	10	52.13	34.4923	32.12	43.03	109.26	33	6.8	P	CYPRUS REGION
96283014	09/10/1996	13	10	52.13	34.4923	32.12	43.03	109.26	33	6.8	S	CYPRUS REGION
96292009	18/10/1996	10	50	20.86	30.6302	131.06	81.72	25.47	33	6.6	P	KYUSHU, JAPAN
96292009	18/10/1996	10	50	20.86	30.6302	131.06	81.72	25.47	33	6.6	P	KYUSHU, JAPAN
96293014	19/10/1996	14	44	40.79	31.9166	131.42	80.53	24.90	33	6.7	P	KYUSHU, JAPAN
96293014	19/10/1996	14	44	40.79	31.9166	131.42	80.53	24.90	33	6.7	S	KYUSHU, JAPAN
96293015	19/10/1996	14	53	48.78	-20.294	-178.87	133.40	333.22	583.1	6	PKIKP	FIJI ISLANDS REGION
96309042	04/11/1996	17	24	57.43	7.2141	-77.55	70.41	243.57	33	6.1	P	PANAMA-COLOMBIA BORDER REGION
96309042	04/11/1996	17	24	57.43	7.2141	-77.55	70.41	243.57	33	6.1	S	PANAMA-COLOMBIA BORDER REGION

96310015	05/11/1996	9	41	34.77	-31.1276	179.96	144.20	331.15	369	6	PP	KERMADEC ISLANDS REGION
96311016	06/11/1996	20	0	58.85	28.0739	143.74	86.10	14.96	33	6.6	P	BONIN ISLANDS REGION
96324016	19/11/1996	10	44	46.06	35.2285	78.25	90.26	233.42	33	7.1	S	NEAR COAST OF PERU
96324016	19/11/1996	10	44	46.06	35.2285	78.25	61.52	67.11	33	7.1	P	EASTERN KASHMIR
96324016	19/11/1996	10	44	46.06	35.2285	78.25	61.52	67.11	33	7.1	S	EASTERN KASHMIR
96337021	02/12/1996	22	17	59.24	31.797	131.22	80.61	25.09	33	6.7	P	KYUSHU, JAPAN
96338020	03/12/1996	12	56	56.92	-18.2716	-172.48	130.06	325.97	33	6	PKIKP	TONGA ISLANDS REGION
96344022	09/12/1996	11	28	48.61	29.9496	-42.60	37.84	213.98	10	6.2	P	NORTHERN MID-ATLANTIC RIDGE
96345008	10/12/1996	8	36	18.7	0.7812	-29.98	64.57	191.85	10	6.2	S	CENTRAL MID-ATLANTIC RIDGE
96357004	22/12/1996	14	53	27.62	43.1898	138.94	70.59	16.66	226.6	6	P	EASTERN SEA OF JAPAN
96357004	22/12/1996	14	53	27.62	43.1898	138.94	70.59	16.66	226.6	6	PP	EASTERN SEA OF JAPAN
96357004	22/12/1996	14	53	27.62	43.1898	138.94	70.59	16.66	226.6	6	S	EASTERN SEA OF JAPAN
96357004	22/12/1996	14	53	27.62	43.1898	138.94	70.59	16.66	226.6	6	sS	EASTERN SEA OF JAPAN
97011009	11/01/1997	20	28	26.02	18.2465	-102.80	70.79	272.17	33	6.8	P	MICHOACAN, MEXICO
97011009	11/01/1997	20	28	26.02	18.2465	-102.80	70.79	272.17	33	6.8	S	MICHOACAN, MEXICO
97013013	13/01/1997	10	19	26.11	34.2321	32.33	43.35	109.22	33	5.5	S	CYPRUS REGION
97017006	17/01/1997	15	53	13.43	28.826	129.98	83.28	26.79	33	6.1	S	RYUKYU ISLANDS
97022012	22/01/1997	17	57	18.7	36.2426	36.01	43.10	103.96	33	5.5	S	JORDAN - SYRIA REGION
97023003	23/01/1997	2	15	22.97	-22.101	-65.74	94.00	222.31	276.2	6.4	P	JUJUY PROVINCE, ARGENTINA
97023003	23/01/1997	2	15	22.97	-22.101	-65.74	94.00	222.31	276.2	6.4	S	JUJUY PROVINCE, ARGENTINA
97035015	04/02/1997	10	37	47.14	37.394	57.35	51.11	83.24	33	6.9	P	IRAN-USSR BORDER REGION
97035015	04/02/1997	10	37	47.14	37.394	57.35	51.11	83.24	33	6.9	S	IRAN-USSR BORDER REGION
97052016	21/02/1997	23	40	24.14	43.8894	149.16	70.85	8.79	33	6.1	P	KURIL ISLANDS REGION
97058009	27/02/1997	21	8	2.36	29.8999	68.11	62.09	78.52	33	7.3	P	PAKISTAN
97058011	27/02/1997	21	30	36.57	30.022	67.90	61.90	78.63	33	6.3	P	PAKISTAN
97058011	27/02/1997	21	30	36.57	30.022	67.90	61.90	78.63	33	6.3	pP	PAKISTAN
97059010	28/02/1997	11	32	18.98	43.994	147.88	70.66	9.75	33	5.5	P	KURIL ISLANDS
97059011	28/02/1997	12	57	18.64	38.1038	47.79	46.47	91.23	33	6.1	P	NORTHWESTERN IRAN
97070030	11/03/1997	19	22	0.13	7.7897	127.42	103.22	33.96	33	6.7	PP	PHILIPPINE ISLANDS REGION
97070030	11/03/1997	19	22	0.13	7.7897	127.42	103.22	33.96	33	6.7	SP	PHILIPPINE ISLANDS REGION
97085003	26/03/1997	2	8	57.27	51.2631	179.58	62.93	346.86	33	6.4	P	RAT ISLANDS, ALEUTIAN ISLANDS
97091021	01/04/1997	18	33	32.2	-18.0228	-69.26	91.18	226.74	114	6	P	NORTHERN CHILE
97091021	01/04/1997	18	33	32.2	-18.0228	-69.26	91.18	226.74	114	6	pP	NORTHERN CHILE
97091021	01/04/1997	18	33	32.2	-18.0228	-69.26	91.18	226.74	114	6	S	NORTHERN CHILE
97091021	01/04/1997	18	33	32.2	-18.0228	-69.26	91.18	226.74	114	6	sS	NORTHERN CHILE
97091022	01/04/1997	18	42	14.06	-17.9688	-68.96	91.04	226.49	115	5.7	P	BOLIVIA
97091022	01/04/1997	18	42	14.06	-17.9688	-68.96	91.04	226.49	115	5.7	S	BOLIVIA
97091022	01/04/1997	18	42	14.06	-17.9688	-68.96	91.04	226.49	115	5.7	sS	BOLIVIA
97101007	11/04/1997	5	34	42.78	39.5042	76.97	57.30	65.70	23.5	6.1	P	SOUTHERN XINJIANG, CHINA
97101007	11/04/1997	5	34	42.78	39.5042	76.97	57.30	65.70	23.5	6.1	S	SOUTHERN XINJIANG, CHINA
97101007	11/04/1997	5	34	42.78	39.5042	76.97	57.30	65.70	23.5	6.1	sP	SOUTHERN XINJIANG, CHINA
97101007	11/04/1997	5	34	42.78	39.5042	76.97	57.30	65.70	23.5	6.1	SS	SOUTHERN XINJIANG, CHINA
97109005	19/04/1997	15	26	33.48	78.508	126.03	35.14	11.36	10	5.9	P	EAST OF SEVERNAYA ZEMLYA
97111007	21/04/1997	12	2	26.43	-12.4711	166.21	127.45	353.23	33	7.9	PKIKP	SANTA CRUZ ISLANDS
97111007	21/04/1997	12	2	26.43	-12.4711	166.21	127.45	353.23	33	7.9	PP	SANTA CRUZ ISLANDS
97111008	21/04/1997	12	11	27.86	-13.1065	166.24	128.08	353.15	33	6.1	PKIKP	VANUATU ISLANDS
97112020	22/04/1997	9	31	23.25	10.9683	-61.17	61.15	228.43	33	6.5	P	TRINIDAD
97112020	22/04/1997	9	31	23.25	10.9683	-61.17	61.15	228.43	33	6.5	S	TRINIDAD
97121009	01/05/1997	11	37	36.15	18.8687	-107.26	72.12	276.45	33	6.7	S	OFF COAST OF JALISCO, MEXICO
97123009	03/05/1997	16	46	2.02	-31.6549	-179.56	144.61	330.25	106.6	6.5	PP	KERMADEC ISLANDS REGION
97128001	08/05/1997	2	53	14.73	25.0668	92.19	75.94	60.33	33.5	5.7	P	INDIA-BANGLADESH BORDER REGION
97128001	08/05/1997	2	53	14.73	25.0668	92.19	75.94	60.33	33.5	5.7	S	INDIA-BANGLADESH BORDER REGION
97130003	10/05/1997	7	57	29.72	33.6542	59.74	55.32	83.59	33	7.3	P	IRAN

97130003	10/05/1997	7	57	29.72	33.6542	59.74	55.32	83.59	33	7.3	pP	IRAN
97130003	10/05/1997	7	57	29.72	33.6542	59.74	55.32	83.59	33	7.3	S	IRAN
97133004	13/05/1997	14	13	45.74	36.5343	71.00	57.50	72.31	196.2	6.1	P	HINDU KUSH REGION
97133004	13/05/1997	14	13	45.74	36.5343	71.00	57.50	72.31	196.2	6.1	pP	HINDU KUSH REGION
97133004	13/05/1997	14	13	45.74	36.5343	71.00	57.50	72.31	196.2	6.1	S	HINDU KUSH REGION
97141028	21/05/1997	22	51	28.73	23.075	80.02	73.04	71.65	36	6	P	INDIA
97141028	21/05/1997	22	51	28.73	23.075	80.02	73.04	71.65	36	6	PP	INDIA
97141028	21/05/1997	22	51	28.73	23.075	80.02	73.04	71.65	36	6	PP	INDIA
97141028	21/05/1997	22	51	28.73	23.075	80.02	73.04	71.65	36	6	S	INDIA
97142004	22/05/1997	7	50	53.52	18.618	-101.54	69.92	271.21	70	5.9	P	GUERRERO, MEXICO
97142004	22/05/1997	7	50	53.52	18.618	-101.54	69.92	271.21	70	5.9	PP	GUERRERO, MEXICO
97142004	22/05/1997	7	50	53.52	18.618	-101.54	69.92	271.21	70	5.9	S	GUERRERO, MEXICO
97161029	10/06/1997	21	53	55.02	-35.7156	-108.03	121.40	251.99	10	6.1	PP	EASTER ISLAND CORDILLERA
97161029	10/06/1997	21	53	55.02	-35.7156	-108.03	121.40	251.99	10	6.1	SS	EASTER ISLAND CORDILLERA
97168015	17/06/1997	21	3	40.26	51.3205	-179.35	62.77	346.13	33	6.6	P	ANDREANOF ISLANDS, ALEUTIAN IS.
97168015	17/06/1997	21	3	40.26	51.3205	-179.35	62.77	346.13	33	6.6	P	ANDREANOF ISLANDS, ALEUTIAN IS.
97168015	17/06/1997	21	3	40.26	51.3205	-179.35	62.77	346.13	33	6.6	S	ANDREANOF ISLANDS, ALEUTIAN IS.
97175042	24/06/1997	23	4	53.14	-1.7852	127.83	112.61	36.00	33	6.1	Pdiff	HALMAHERA
97175042	24/06/1997	23	4	53.14	-1.7852	127.83	112.61	36.00	33	6.1	Sdiff	HALMAHERA
97189004	08/07/1997	2	24	7.32	23.9494	142.70	90.07	16.41	33	5.9	P	VOLCANO ISLANDS REGION
97189004	08/07/1997	2	24	7.32	23.9494	142.70	90.07	16.41	33	5.9	PP	VOLCANO ISLANDS REGION
97189015	08/07/1997	12	11	15	51.34	-178.84	62.70	345.78	33	5.6	P	ANDREANOF ISLANDS, ALEUTIAN IS.
97190009	09/07/1997	19	24	13.17	10.4281	-63.49	62.41	230.67	10	6.8	P	NEAR COAST OF VENEZUELA
97190009	09/07/1997	19	24	13.17	10.4281	-63.49	62.41	230.67	10	6.8	S	NEAR COAST OF VENEZUELA
97196006	15/07/1997	11	5	31.34	24.7873	122.24	85.53	34.50	104.9	5.8	P	TAIWAN REGION
97196006	15/07/1997	11	5	31.34	24.7873	122.24	85.53	34.50	104.9	5.8	S	TAIWAN REGION
97200005	19/07/1997	14	22	8.75	15.8399	-98.19	70.99	266.86	33	6.2	P	OFF COAST OF GUERRERO, MEXICO
97200005	19/07/1997	14	22	8.75	15.8399	-98.19	70.99	266.86	33	6.2	S	OFF COAST OF GUERRERO, MEXICO
97201014	20/07/1997	10	14	22.8	-22.6888	-66.02	94.64	222.38	256.5	6	P	JUJUY PROVINCE, ARGENTINA
97201014	20/07/1997	10	14	22.8	-22.6888	-66.02	94.64	222.38	256.5	6	S	JUJUY PROVINCE, ARGENTINA
97201014	20/07/1997	10	14	22.8	-22.6888	-66.02	94.64	222.38	256.5	6	SP	JUJUY PROVINCE, ARGENTINA
97203036	22/07/1997	19	10	35.09	4.62	-32.69	61.02	195.31	10	5.4	P	CENTRAL MID-ATLANTIC RIDGE
97203036	22/07/1997	19	10	35.09	4.62	-32.69	61.02	195.31	10	5.4	pP	CENTRAL MID-ATLANTIC RIDGE
97203036	22/07/1997	19	10	35.09	4.62	-32.69	61.02	195.31	10	5.4	S	CENTRAL MID-ATLANTIC RIDGE
97208014	27/07/1997	10	7	52.55	35.512	21.12	37.91	120.80	10	5.7	P	MEDITERRANEAN SEA
97208014	27/07/1997	10	7	52.55	35.512	21.12	37.91	120.80	10	5.7	PcP	MEDITERRANEAN SEA
97208014	27/07/1997	10	7	52.55	35.512	21.12	37.91	120.80	10	5.7	S	MEDITERRANEAN SEA
97216013	04/08/1997	18	53	58.94	-15.0609	-175.43	127.59	330.46	33	6	SS	TONGA ISLANDS
97217006	05/08/1997	2	48	43.46	28.38	-43.73	39.62	214.81	10	5.3	P	NORTH ATLANTIC RIDGE
97217006	05/08/1997	2	48	43.46	28.38	-43.73	39.62	214.81	10	5.3	S	NORTH ATLANTIC RIDGE
97220015	08/08/1997	22	27	19.85	-15.4789	-179.40	128.77	335.12	33	6.6	PKIKP	FIJI ISLANDS REGION
97220015	08/08/1997	22	27	19.85	-15.4789	-179.40	128.77	335.12	33	6.6	PP	FIJI ISLANDS REGION
97222003	10/08/1997	9	20	30.98	-16.5171	123.58	125.58	45.36	33	6	PP	WESTERN AUSTRALIA
97222003	10/08/1997	9	20	30.98	-16.5171	123.58	125.58	45.36	33	6	SP	WESTERN AUSTRALIA
97222003	10/08/1997	9	20	30.98	-16.5171	123.58	125.58	45.36	33	6	SS	WESTERN AUSTRALIA
97232008	20/08/1997	13	51	16.62	-41.5432	80.19	130.76	102.95	10	6.4	SS	MID-INDIAN RISE
97241004	29/08/1997	6	54	0.24	-15.592	-175.53	128.13	330.44	33	6.3	PP	TONGA ISLANDS
97241004	29/08/1997	6	54	0.24	-15.592	-175.53	128.13	330.44	33	6.3	SS	TONGA ISLANDS
97241005	29/08/1997	8	14	9.97	-3.436	144.35	117.44	18.46	33	6.7	PP	NEAR N COAST OF PAPUA NEW GUINEA
97241005	29/08/1997	8	14	9.97	-3.436	144.35	117.44	18.46	33	6.7	Sdiff	NEAR N COAST OF PAPUA NEW GUINEA
97245012	02/09/1997	12	13	22.92	3.82	-75.74	72.88	240.47	231.6	6.4	P	COLOMBIA
97245012	02/09/1997	12	13	22.92	3.82	-75.74	72.88	240.47	231.6	6.4	S	COLOMBIA

97245012	02/09/1997	12	13	22.92	3.82	-75.74	72.88	240.47	231.6	6.4	SS	COLOMBIA
97245012	02/09/1997	12	13	22.92	3.82	-75.74	72.88	240.47	231.6	6.4	SS	COLOMBIA
97246004	03/09/1997	6	22	44.28	-55.1188	-128.75	145.45	251.96	10	6	SS	SOUTH PACIFIC CORDILLERA
97247003	04/09/1997	4	23	37.03	-26.4855	178.25	140.00	335.19	619.4	6.1	PKIKP	SOUTH OF FIJI ISLANDS
97247003	04/09/1997	4	23	37.03	-26.4855	178.25	140.00	335.19	619.4	6.1	PP	SOUTH OF FIJI ISLANDS
97253002	10/09/1997	12	57	7.07	-21.3223	-174.31	133.44	327.19	33	6.1	PP	TONGA ISLANDS
97253002	10/09/1997	12	57	7.07	-21.3223	-174.31	133.44	327.19	33	6.1	SS	TONGA ISLANDS
97263010	20/09/1997	16	11	32.15	-28.7022	-177.63	141.34	328.78	33	6.9	PKIKP	KERMADEC ISLANDS REGION
97263010	20/09/1997	16	11	32.15	-28.7022	-177.63	141.34	328.78	33	6.9	PP	KERMADEC ISLANDS REGION
97263010	20/09/1997	16	11	32.15	-28.7022	-177.63	141.34	328.78	33	6.9	SS	KERMADEC ISLANDS REGION
97277019	04/10/1997	15	29	46.28	16.01	-46.75	52.29	214.07	10	5.6	P	NORTHERN MID-ATLANTIC RIDGE
97277019	04/10/1997	15	29	46.28	16.01	-46.75	52.29	214.07	10	5.6	S	NORTHERN MID-ATLANTIC RIDGE
97278015	05/10/1997	18	4	30	-59.7029	-29.24	124.82	186.09	270.5	6.1	PKIKP	SOUTH SANDWICH ISLANDS REGION
97286013	13/10/1997	13	39	37.49	36.3372	22.11	37.54	119.02	10	6.6	P	SOUTHERN GREECE
97286013	13/10/1997	13	39	37.49	36.3372	22.11	37.54	119.02	10	6.6	S	SOUTHERN GREECE
97287008	14/10/1997	9	53	18.15	-21.9524	-176.92	134.63	330.27	166.2	6.5	PP	FIJI ISLANDS REGION
97287008	14/10/1997	9	53	18.15	-21.9524	-176.92	134.63	330.27	166.2	6.5	SS	FIJI ISLANDS REGION
97288001	15/10/1997	1	3	33.46	-30.9324	-71.01	103.88	223.91	33	6.8	Pdiff	NEAR COAST OF CENTRAL CHILE
97288001	15/10/1997	1	3	33.46	-30.9324	-71.01	103.88	223.91	33	6.8	PP	NEAR COAST OF CENTRAL CHILE
97288001	15/10/1997	1	3	33.46	-30.9324	-71.01	103.88	223.91	33	6.8	Sdiff	NEAR COAST OF CENTRAL CHILE
97301007	28/10/1997	6	15	17.33	-4.3189	-76.63	80.78	238.26	124.5	6.5	P	NORTHERN PERU
97301007	28/10/1997	6	15	17.33	-4.3189	-76.63	80.78	238.26	124.5	6.5	pP	NORTHERN PERU
97312006	08/11/1997	10	2	52.61	35.0443	87.31	65.12	59.86	10	7.9	P	TIBET
97312006	08/11/1997	10	2	52.61	35.0443	87.31	65.12	59.86	10	7.9	S	TIBET
97313010	09/11/1997	22	56	42.75	13.6488	-88.96	69.09	257.28	190.8	5.7	P	EL SALVADOR
97313010	09/11/1997	22	56	42.75	13.6488	-88.96	69.09	257.28	190.8	5.7	pP	EL SALVADOR
97313010	09/11/1997	22	56	42.75	13.6488	-88.96	69.09	257.28	190.8	5.7	S	EL SALVADOR
97313010	09/11/1997	22	56	42.75	13.6488	-88.96	69.09	257.28	190.8	5.7	sS	EL SALVADOR
97319007	15/11/1997	7	5	16.64	43.9092	144.94	70.51	11.98	160.9	5.7	P	HOKKAIDO, JAPAN REGION
97319014	15/11/1997	18	59	24.3	-15.1498	167.33	130.06	351.64	123.2	6.6	PKIKP	VANUATU ISLANDS
97322017	18/11/1997	13	7	41.73	37.618	20.64	35.86	119.78	33	6.4	P	IONIAN SEA
97322017	18/11/1997	13	7	41.73	37.618	20.64	35.86	119.78	33	6.4	pP	IONIAN SEA
97322017	18/11/1997	13	7	41.73	37.618	20.64	35.86	119.78	33	6.4	S	IONIAN SEA
97322018	18/11/1997	13	13	46.16	37.296	20.85	36.22	119.78	33	5.3	P	IONIAN SEA
97325003	21/11/1997	11	23	6.31	22.2137	92.83	78.79	60.97	56.9	6	P	INDIA-BANGLADESH BORDER REGION
97325003	21/11/1997	11	23	6.31	22.2137	92.83	78.79	60.97	56.9	6	pP	INDIA-BANGLADESH BORDER REGION
97327006	23/11/1997	3	51	0.44	40.1475	138.76	73.57	17.33	33	5.8	P	EASTERN SEA OF JAPAN
97332013	28/11/1997	22	53	41.53	-13.4425	-68.78	86.70	227.79	585.6	6.3	P	PERU-BOLIVIA BORDER REGION
97332013	28/11/1997	22	53	41.53	-13.4425	-68.78	86.70	227.79	585.6	6.3	PP	PERU-BOLIVIA BORDER REGION
97332013	28/11/1997	22	53	41.53	-13.4425	-68.78	86.70	227.79	585.6	6.3	PP	PERU-BOLIVIA BORDER REGION
97332013	28/11/1997	22	53	41.53	-13.4425	-68.78	86.70	227.79	585.6	6.3	S	PERU-BOLIVIA BORDER REGION
97339010	05/12/1997	11	26	54.69	54.9695	161.91	60.14	359.20	33	7.7	P	NEAR EAST COAST OF KAMCHATKA
97339010	05/12/1997	11	26	54.69	54.9695	161.91	60.14	359.20	33	7.7	pP	NEAR EAST COAST OF KAMCHATKA
97339011	05/12/1997	11	35	19.58	53.894	161.58	61.22	359.41	33	6	P	OFF EAST COAST OF KAMCHATKA
97339011	05/12/1997	11	35	19.58	53.894	161.58	61.22	359.41	33	6	pP	OFF EAST COAST OF KAMCHATKA
97339012	05/12/1997	11	37	9.32	54.376	162.34	60.73	358.91	33	5.7	P	NEAR EAST COAST OF KAMCHATKA
97339013	05/12/1997	11	48	40.96	54.439	162.53	60.67	358.79	33	5.8	P	NEAR EAST COAST OF KAMCHATKA
97339014	05/12/1997	11	51	10.39	54.133	161.56	60.98	359.43	33	5.4	P	NEAR EAST COAST OF KAMCHATKA
97339048	05/12/1997	18	48	22.79	53.9124	161.45	61.20	359.50	33	6.5	P	OFF EAST COAST OF KAMCHATKA
97339048	05/12/1997	18	48	22.79	53.9124	161.45	61.20	359.50	33	6.5	pP	OFF EAST COAST OF KAMCHATKA

97339048	05/12/1997	18	48	22.79	53.9124	161.45	61.20	359.50	33	6.5	S	OFF EAST COAST OF KAMCHATKA
97339051	05/12/1997	19	4	6.7	53.767	161.65	61.34	359.37	33	5.6	P	OFF EAST COAST OF KAMCHATKA
97345012	11/12/1997	7	56	28.85	3.9174	-75.72	72.78	240.49	150	5.8	P	COLOMBIA
97345012	11/12/1997	7	56	28.85	3.9174	-75.72	72.78	240.49	150	5.8	S	COLOMBIA
97351004	17/12/1997	4	38	51.46	51.2991	178.85	62.97	347.37	33	6.5	P	RAT ISLANDS, ALEUTIAN ISLANDS
97351007	17/12/1997	5	51	29.22	36.3392	70.79	57.58	72.60	201.6	5.6	P	HINDU KUSH REGION
97351007	17/12/1997	5	51	29.22	36.3392	70.79	57.58	72.60	201.6	5.6	sP	HINDU KUSH REGION
97352010	18/12/1997	15	2	0.32	13.5546	-88.97	69.17	257.25	179.4	5.7	P	EL SALVADOR
97352010	18/12/1997	15	2	0.32	13.5546	-88.97	69.17	257.25	179.4	5.7	pP	EL SALVADOR
97356004	22/12/1997	2	5	50.08	-5.5428	147.77	119.94	14.90	179.7	6.7	PKIKP	EAST PAPUA NEW GUINEA REGION
97356004	22/12/1997	2	5	50.08	-5.5428	147.77	119.94	14.90	179.7	6.7	PP	EAST PAPUA NEW GUINEA REGION
97356012	22/12/1997	10	3	45.18	13.6019	-90.32	69.69	258.54	33	5.5	P	NEAR COAST OF GUATEMALA
98001009	01/01/1998	6	11	22.64	23.995	141.99	89.94	17.04	33	6.7	P	VOLCANO ISLANDS REGION
98080018	21/03/1998	18	22	28.46	36.407	70.15	57.27	73.08	223.1	6	P	HINDU KUSH REGION
98088008	29/03/1998	7	14	58.98	-0.327	-17.88	65.33	178.77	10	5.5	P	NORTH OF ASCENSION ISLAND
98088008	29/03/1998	7	14	58.98	-0.327	-17.88	65.33	178.77	10	5.5	S	NORTH OF ASCENSION ISLAND
98088020	29/03/1998	19	48	16.21	-17.4152	-179.24	130.65	334.46	539	6.4	PKIKP	FIJI ISLANDS REGION
98088020	29/03/1998	19	48	16.21	-17.4152	-179.24	130.65	334.46	539	6.4	PP	FIJI ISLANDS REGION
98088020	29/03/1998	19	48	16.21	-17.4152	-179.24	130.65	334.46	539	6.4	pPKIKP	FIJI ISLANDS REGION
98088020	29/03/1998	19	48	16.21	-17.4152	-179.24	130.65	334.46	539	6.4	SS	FIJI ISLANDS REGION
98091012	01/04/1998	17	56	23.36	-0.5056	99.38	102.22	63.86	33	6.8	SS	SOUTHERN SUMATERA
98093022	03/04/1998	3	19	57.87	-8.1884	-74.22	83.54	234.61	164.5	6	P	PERU-BRAZIL BORDER REGION
98093022	03/04/1998	3	19	57.87	-8.1884	-74.22	83.54	234.61	164.5	6	PP	PERU-BRAZIL BORDER REGION
98093022	03/04/1998	3	19	57.87	-8.1884	-74.22	83.54	234.61	164.5	6	S	PERU-BRAZIL BORDER REGION
98100013	10/04/1998	15	0	53.14	32.5466	60.01	56.39	84.03	33	5.7	P	IRAN
98105013	15/04/1998	15	23	6.92	58.5105	164.60	56.57	357.57	33	5.5	P	KAMCHATKA
98105013	15/04/1998	15	23	6.92	58.5105	164.60	56.57	357.57	33	5.5	S	KAMCHATKA
98116037	26/04/1998	14	16	52.2	0.852	17.40	69.29	140.63	10	5.5	P	CONGO
98119003	29/04/1998	3	30	39.34	36.178	21.92	37.56	119.84	33	5.3	P	GREECE
98119003	29/04/1998	3	30	39.34	36.178	21.92	37.56	119.84	33	5.3	S	GREECE
98138013	18/05/1998	17	19	4.82	39.232	15.14	32.42	125.82	297	5.3	P	SOUTHERN ITALY
98138013	18/05/1998	17	19	4.82	39.232	15.14	32.42	125.82	297	5.3	S	SOUTHERN ITALY
98148001	28/05/1998	18	33	28.1	31.3723	27.67	43.99	116.59	10	5	P	ARAB REPUBLIC OF EGYPT
98148001	28/05/1998	18	33	28.1	31.3723	27.67	43.99	116.59	10	5	S	ARAB REPUBLIC OF EGYPT

Appendix 23. EXAMPLE OF AN ACH MODEL FILE

The following example of an ACH model file is for model p_10_75_225. The reader is referred to the ACH documentation for full details of the input format required by the ACH program *thrd*.

```
HOTSPOT       p_10_75_225
   64N53.26 019W17.57 00.0
    225.0     5   10     0 a 0.0500   b 0.1000   c 0.2000   x 9.9999   y 9.9999
z 99.9999
           0    1    0    0    1    0    0    1    0
           5.80000  10.00000    1  10.00000   42  10.00000      0.000      0.000
           8.04000  48.00000    8  75.00000   10  75.00000      0.000      0.000
           8.04550  48.00000   10  75.00000   12  75.00000      0.000      0.000
           8.08060  49.00000   12  75.00000   12  75.00000      0.000      0.000
           8.21670  49.00000   12  75.00000   12  75.00000      0.000      0.000
           8.37300  51.00000   12  75.00000   14  75.00000      0.000      0.000
           8.55910  51.00000   14  75.00000   16  75.00000      0.000      0.000
           8.74890  53.00000   16  75.00000   16  75.00000      0.000      0.000
           8.94240  53.00000   16  75.00000   18  75.00000      0.000      0.000
           9.46420  57.00000   20  75.00000   20  75.00000      0.000      0.000
           9.65570  57.00000   22  75.00000   22  75.00000      0.000      0.000
           9.85060  60.00000   26  75.00000   26  75.00000      0.000      0.000
          10.05550  60.00000   34  75.00000   34  75.00000      0.000      0.000

           ASB 6444.92N02119.92W 110
           GIL 6604.64N01621.64W 141
           GRA 6555.06N01734.06W  25
           GRI 6632.49N01800.49W  36
           GRS 6538.29N01607.29W 390
           HVE 6452.29N01933.29W 641
           KRA 6541.68N01646.68W 437
           KRO 6405.89N02107.89W 139
           REN 6538.82N01654.82W 345
           SIG 6607.94N01854.94W  16
           SKR 6433.62N01823.62W 812
           T01 6429.65N02110.65W 205
           T02 6444.75N02213.75W  40
           T03 6454.46N02351.46W  35
           T04 6510.83N02225.83W  40
           T05 6506.58N02105.58W  35
           T06 6542.30N02140.30W  25
           T07 6535.90N02230.90W  40
           T08 6536.59N02409.59W   8
           T09 6552.43N02329.43W  50
           T10 6555.60N02225.60W   7
           T11 6525.34N02043.34W 108
           T12 6540.24N01935.24W  38
           T13 6541.16N01805.16W  24
           T14 6518.17N01815.17W 245
           T15 6607.26N01510.26W  20
           T16 6532.45N01345.45W   5
           T17 6515.30N01430.30W  80
           T18 6509.96N01518.96W 342
           T19 6448.72N01405.72W  50
           T20 6417.27N01508.27W  15
           T21 6352.61N01638.61W  20
           T22 6346.19N01807.19W  65
           T23 6424.40N01715.40W1730
           T24 6453.18N01521.18W 600
           T25 6503.24N01639.24W 920
           T26 6501.74N01819.74W 740
           T27 6512.00N01935.00W 450
           T28 6431.93N01929.93W 600
           T29 6543.68N01450.68W  60
           T30 6407.80N02153.80W  50
           VOG 6358.11N02223.34W  12
```